Understanding the Roles of Promoters and Oxygen Species in Ethylene Epoxidation by Ex situ and In situ Spectroscopic Techniques

AMY RUBY MARSH

Understanding the Roles of Promoters and Oxygen Species in Ethylene Epoxidation by *Ex situ* and *In situ* Spectroscopic Techniques

Department of Chemistry, Durham University

2020 – 2024

Thesis submitted for the degree of Doctor of Philosophy

By

Amy Ruby Marsh

Declaration

This thesis is based on work carried out by the author in the Department of Chemistry at Durham University, during the period October 2020 – December 2023. All of the work detailed in this thesis is original unless specifically acknowledged in the text or references. None of this work has been submitted for another degree in this or any other university.

Copyright

Acknowledgements

Firstly, I would like to thank my supervisor, Dr. Simon Beaumont for all of his advice, support and guidance throughout my PhD. I would also like to acknowledge the EPSRC for providing the funding for this project.

I would also like to thank Prof. Georg Held and the other beamline scientists at B07, alongside Dr Luke Keenan and the other beamline scientists at B18, Diamond Light Source, for their guidance and advice with the NAP-XPS and EXAFS experiments. I wish to thank Dr Samuel Page for his help with data acquisition and data interpretation for the ^{133}Cs and ^{27}Al NMR and to Dr Monik Panchal for the XANES data collection. I wish to thank Dr Andrea Zarchariou and Zixuan Han for the collection of the TEM and STEM data. I also wish to acknowledge HarwellXPS for the *ex situ* XPS data collection. I wish to thank Dr Kathryn MacIntosh for the collection of the BET data.

Thank you to the excellent members of the workshops and technicians at Durham University, the support, knowledge and data collection was invaluable throughout my PhD.

Thank you to past and present members of the Beaumont group, for your constant support and help throughout the PhD, sharing your knowledge, laughs and a few drinks throughout the years.

To would like to specifically thank Andrea, Monik and Zixuan. Thank you for all the support, the laughs, the tears, the help with beamtime data collection, the night shifts and for all of your guidance, I could not have asked for a better group and could not have done it without you all.

I would like to thank my friends, from the friends I made throughout my PhD in Durham, to my friends from home, Cardiff and America, thank you for all your support throughout the years, you know who you are!

Thank you to my mum, dad, and brother Joe for never failing to believe in me and for the complete and utter support in helping me follow all my dreams always. Without your support, I would not be where I am today, and I am forever grateful. I would like to thank my grandparents, for their unconditional love and support, and for passing on my love of science.

Last – but by no means least – thanks to Ryan. The love, the support, the laughs and the home-cooked meals have carried me through my PhD, and I am forever thankful.

List of Abbreviations

AA – Acetaldehyde

ATR-IR – Attenuated Total Reflectance – Infrared

BET – Brunauer, Emmett and Teller

CCD – Charged Coupled Device

CO-DRIFTS – Carbon Monoxide - Diffuse Reflectance Infrared Fourier Transform Spectroscopy

CP – Cross Polarisation

DFT – Density-Functional Theory

DRIFTS – Diffuse Reflectance Infrared Fourier Transform Spectroscopy

DTGS – Deuterated Triglycine Sulfate

EDS – Energy-Dispersive X-ray Spectroscopy

ED-XRF – Energy Dispersive X-ray Fluorescence Spectroscopy

EO – Ethylene Oxide

EXAFS – Extended X-ray Absorption Fine Structure

FID – Flame Ionization Detector

FTIR – Fourier Transform Infrared Spectroscopy

FWHM – Full Width at Half Maximum

H_2-TPR – Hydrogen Temperature Programmed Reduction

ICP-OES – Inductively Coupled Plasma – Optical Emission Spectroscopy

NAP-XPS – Near-Ambient Pressure X-ray Photoelectron Spectroscopy

NEXAFS – Near-Edge X-ray Absorption Fine Structure

NMR – Nuclear Magnetic Resonance

MAS – Magic Angle Spinning

MCA – Multiple Component Analyser

MvK – Mars-van Krevelen

O_2-TPD – Oxygen Temperature Programmed Desorption

OMME / OME / OMC – Oxametallacycle

PMT – Photo Multiplier Tube

pXRD – Power X-ray Diffraction

SERS – Surface Plasmon Enhanced Raman Scattering

SEM – Scanning Electron Microscopy

SSD – Silicon Drift Detector

ss NMR – Solid State Nuclear Magnetic Resonance Spectroscopy

STEM – Scanning Transmission Electron Microscopy

TCD – Thermal Conductivity Detector

TEM – Transmission Electron Microscopy

TPD – Temperature Programmed Desorption

TPR – Temperature Programmed Reduction

UHV – Ultra-High Vacuum

XAFS – X-ray Absorption Fine Structure

XANES – X-ray Absorption Near-Edge Structure

XAS – X-ray Absorption Spectroscopy

XRF – X-ray Fluorescence

XPS – X-ray Photoelectron Spectroscopy

Contents Page

Abstract

Ethylene oxide (EO) is an important chemical intermediate and a valuable chemical building block to ethylene glycol needed to help make many everyday products including antifreeze, detergents, inks and pharmaceuticals. Industrially, EO is synthesised by direct catalytic oxidation of ethylene with air over supported silver catalysts. The employed Ag/Al_2O_3 catalysts use promoters, including Cs, Re or both to improve the EO selectivity. Understanding the role of promoters and oxygen species is still debated, but critical for improving the rational design of the catalysts. Here Ag/Al_2O_3-based catalysts with the addition of Cs and/or Re promoters have been thoroughly investigated with the use of *in situ* and *ex situ* spectroscopic and characterisation techniques. There are issues with *in situ* DRIFTS cells that are currently commercially available. Through the development and optimisation of an *in situ* DRIFTS cell, these problems have been solved and used to give more information on case studies and provide surface information. Indications of a hybrid atomic molecular oxygen structure of Ag_x–O_2 alongside atomic electrophilic oxygen was found to be present under ethylene epoxidation conditions on $Ag/\alpha\text{-}Al_2O_3$, where the Ag surface became more oxidised. The addition of 500 ppm of Re caused a decrease in EO selectivity, here Re weakened the Ag-O bond, however, an increase in acidity and hydroxyl groups caused the reduction in EO selectivity. Re was found to be as a +7, whilst 600 ppm of Cs was found to increase the EO selectivity by causing a decrease in Ag crystallite sizes, greater coverage of O_{ads} and a reduction in hydroxyl groups by titrating them. It was found that Cs is likely to be a layer where there is a mixture of peroxide and suboxide species. 600 ppm of Cs and 500 ppm of Re was found to cause a large increase in EO selectivity, due to the individual promotions working in tandem and the interaction between Cs and Re. The Cs and Re were found to weaken the Ag-O bond and increase the amount of O_{ads} whilst titrating the hydroxyl acidic groups on the support. The addition of Cs and Re together appeared to cause a change in the Re-O bonding and caused a significant amount of electron distortion of the Cs. Cs suboxide-like species were found to be present during ethylene epoxidation and the addition of Cs and Re showed an increase in the electrophilicity of oxygen. The use of Cu/Au catalysts is widely reported to give high propylene oxide (PO) selectivity; therefore, these were investigated for the production of EO. The Cu/Au-based catalysts were all found to be relatively active towards ethylene epoxidation. Cu was found in the +2 oxidation state, whilst the catalysts appeared to show metallic Au. The increase in temperature of the pretreatment to 450 °C was thought to be the reason for the reduction in the acidic hydroxyl groups. This thesis gives new insights into the role of different catalysts, promoters and oxygen species for ethylene epoxidation.

Chapter 1: Introduction

1.1 Ethylene Epoxidation

Ethylene oxide (EO) is an important chemical intermediate and a valuable chemical building block to ethylene glycol needed to help us make many everyday products, including antifreeze, pharmaceutics and detergents and as a monomer for producing plastics.[1] Therefore, ethylene oxidation is a very important reaction and has been extensively investigated over the past few decades, it has an annual turnover of $18 billion and estimated that an increase in 1% selectivity in ethylene epoxidation would generate around $180 million annually assuming the market value is directly proportional to the amount of ethylene oxide produced.[2]

1.1.1 Background of Ag/Al_2O_3 Catalysts

Industrially, ethylene oxide is synthesised with the direct catalytic oxidation of ethylene with air or oxygen over supported silver catalysts. Commonly, the catalyst support used for this is α-alumina, mainly due to the high selectivity that it provides to ethylene epoxidation compared to other supports.[3–6] Silver is used due to its uniqueness in the fact that oxygen can dissociatively adsorb on it and the relatively weak bond strength of oxygen to silver allows the formation of epoxide upon reaction with ethylene.[7]

The typical industrial reaction conditions employ a supported $Ag/\alpha\text{-}Al_2O_3$ catalyst at 200 – 280 °C and between 1 – 3 MPa.[1,8] Four main reactions occur during ethylene oxidation, these are shown in *Figure 1.1*. *Equation 1.1* shows selective ethylene oxidation of ethylene-to-ethylene oxide. *Equation 1.2* shows the unselective side reaction of ethylene over-oxidation. Here ethylene reacts with an excess of oxygen to produce carbon dioxide and water. The ethylene oxide formed can be recovered as a product but can also undergo consecutive oxidation via a two step-reaction: first, the isomerisation of ethylene oxide to acetaldehyde over acid support and then the oxidation of acetaldehyde to water and carbon dioxide over silver as shown in *Figure 1.1* due to the high reactivity of the aldehydic C-H bond as well as the three equivalent C-H species at the α-position.[5]

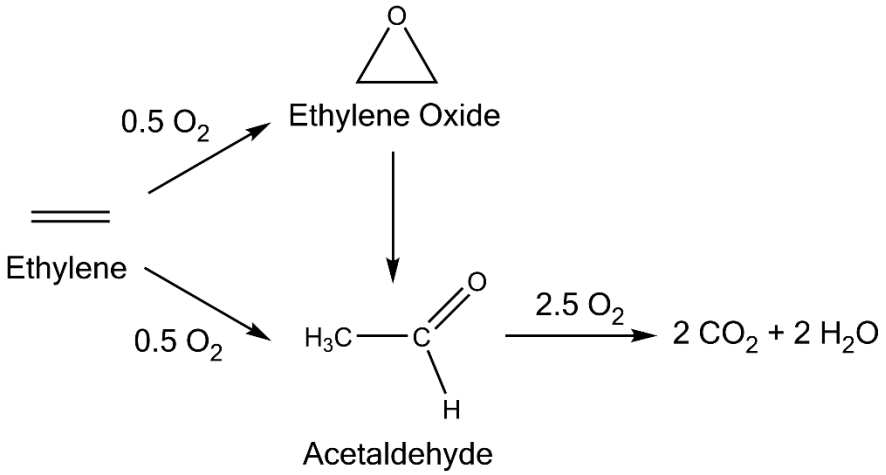

Figure 1.1: A pathway showing ethylene epoxidation to ethylene oxide, alongside the undesired reaction to acetaldehyde and the total combustion to carbon dioxide and water.

$$C_2H_4 + \frac{1}{2}O_2 \longrightarrow C_2H_4O$$ *Equation 1.1.*[1]

$$C_2H_4 + 3O_2 \longrightarrow 2CO_2 + 2H_2O$$ *Equation 1.2.*[1]

Commonly, supported Ag/Al_2O_3 catalysts for the EO process are synthesised by impregnation of the Al_2O_3 support by either aqueous silver nitrate or silver oxalate solutions.[9] The size of the silver particles on the α-Al_2O_3 is thought to influence the ethylene oxide selectivity, where the size effect for silver-catalysed ethylene epoxidation has been investigated by many authors.[9–12] There is no full agreement on how the particle size affects the ethylene oxide selectivity with disagreements occurring depending on the wt. % and reaction conditions.[9,13] The α-Al_2O_3 support has a small surface area (less than 10 $m^2\,g^{-1}$) and the silver particles have a high mobility, it is hypothesised in combination this means that the catalyst has large Ag particles with a low dispersion on the Al_2O_3 support.[3,14,15] Overall, there appears to be an increase in EO selectivity with an increase in Ag particle size up to a certain point, where there is then a decrease, this changes depending on wt. % and catalytic conditions and has not been found to be specific. This range includes, above 100 nm, between 50-60 nm, between 130-150 nm, above 400 nm and reaching a max at 60-70 nm.[12,16–20] However, it has been hypothesised that both the particle size and the dispersion of Ag (Ag: Al_2O_3) play a role in the EO selectivity and need to be taken into account when investigating EO selectivity. Where smaller particles often enhance selectivity, as there is an increase surface area, larger Ag particles provide more surface sites for oxygen adsorption, therefore an optimum is needed.[18,21]

It is common for the Ag/Al_2O_3 catalyst to have promoters to improve the EO selectivity.[3] Promoters are easily able to be added either after the silver impregnation step or with the silver precursor. In the case of halide promoters, they can also be added into the reactant stream (i.e. chlorine is typically added as alkyl chloride at ppm levels in the feed stream, which can be complicated).[22] For example, when there is an unprompted silver catalyst, the selectivity reaches 50%, however with promoters it can achieve an EO selectivity of 90%.[23] There are many different promotors used, however, the most common ones are chlorine (Cl), caesium oxides (CsO_x) and rhenium oxides (ReO_x). These promoters all have both individual proposed promoting effects and also synergistic effects when used in tandem.[24,25]

1.1.2 Arguments In The Literature

There are many arguments/disagreements in research about the complete mechanism of ethylene oxidation with many questions being left unanswered about the role of the promoters and oxygen in this mechanism. The examples below illustrate the current state of the discussions in the literature.

1.1.2.1 Oxygen Species and Mechanisms

There are many different arguments for the role of the oxygen species and different mechanisms. Over the past 50 years, the nature of the surface oxygen on Ag catalysts for selective ethylene epoxidation and nonselective total combustion has been extensively debated. In literature multiple oxygen species are proposed and investigated, ranging from nucleophilic and electrophilic to subsurface, molecular, atomic and hybrid oxygen.[1,26]

Kilty *et al.* were one of the first to try and attempt to predict the mechanism of ethylene oxidation using computational data, here they thought that two types of oxygen were present in this reaction, one was atomic oxygen O and the second was charged molecular oxygen, O_2^-.[27] They thought that the molecular oxygen was responsible for the selective route by being chemisorbed onto the silver catalyst surface and that the atomic oxygen causes the unselective route, therefore they found that the maximum achievable selectivity would be 86%.[27]

However, Grant and Lambert invalidated this by achieving selectivities of over 86%, here they used temperature-programmed reaction (TPR) measurements to remove the molecular oxygen from the Ag(1 1 1) surface, when doing this they found no change when looking at the production of EO, therefore, they concluded that the reaction occurred through the atomically absorbed oxygen. They suggested that there were two types of

adsorbed atomic oxygen, one is a type which had a low valence charge, which makes it electrophilic and therefore selective whilst the other which was unselective was electronegative and had a high valence charge.[28]

For metallic silver surfaces with low oxygen coverage, Linic and Barteau investigated using density-functional theory (DFT) on metallic Ag that there was an intermediate oxametallacycle that existed. This is shown in *Figure 1.2*, here the oxametallacycle is either OME or OMME (where M is for metal and E is for ethylene). They suggested that when the ethylene is oxidised it produces different oxametallacycles. It can then follow two different mechanisms, the first one is going straight to the epoxidation, whilst the second mechanism is forming another intermediate which then forms CO_2 and H_2O, known as combustion.[29]

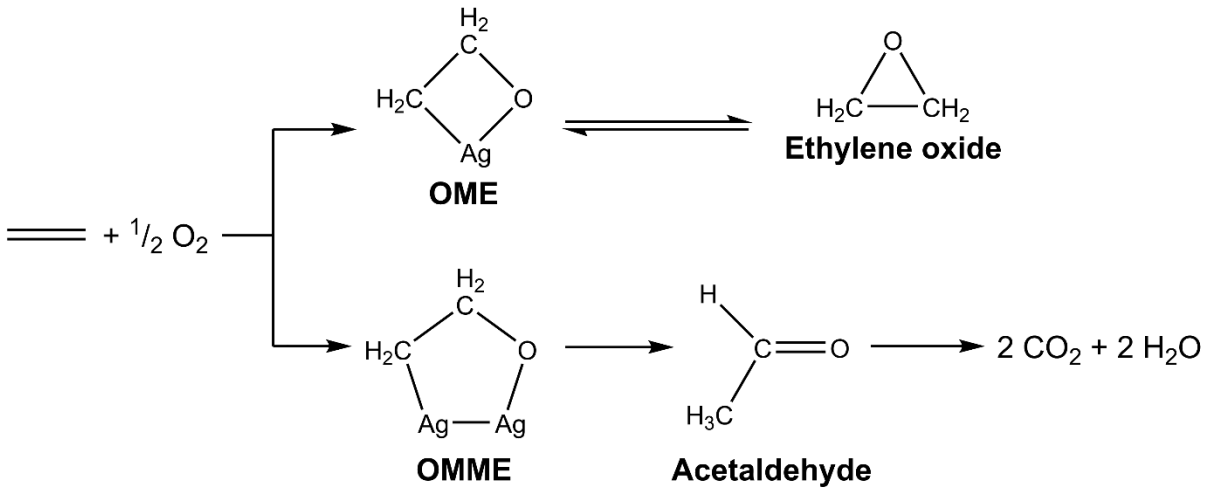

Figure 1.2: A reaction mechanism for the ethylene epoxidation modified by Linic and Barteau. The OME and the OMME both represent the two oxametallacycles that they predicted.[29]

Whilst the EO selectivities around 50% observed with model catalysts fit the competitive formation of acetaldehyde and EO, the observed increase in selectivity with increasing oxygen coverage cannot be explained by the OMC mechanism. Starting from the 1970s, investigations of oxygenated Ag surfaces revealed the formation of complex structures on the catalyst surface, commonly referred to as surface oxides.[30] Here it is suggested that the silver catalyst is likely to be not purely metallic and possess a thin silver oxide layer. Although the majority of these studies focus on the structure and the properties of these surface-oxides, a few computational studies – DFT calculations were testing the OMC mechanism at higher oxygen coverage. No significant changes in the reactivity of the OMC intermediate were reported as long as a surface vacancy was available to stabilize the OMC complex.[1,23]

After this, Waugh, Hauge and co-workers using O_2 temperature programmed desorption alongside computational studies suggested that the selectivity had to do with the Ag-O bond strength and therefore a weaker Ag-O bond is more selective.[31] They contradict the oxametallacycle mechanism which was proposed by Linic and Barteau and they proposed a new molecular model where a reaction intermediate is adsorbed onto a fully oxidised Ag surface and the selectivity results from competitive reactions of cyclisation to EO and H abstraction. The conclusions they gained from their experiments were that the selectivity and unselective reactions of EO occur by energetic pathways to the CH_2-CH_2-O-Ag intermediate. The first pathway consists of stretching the Ag-O bond and the intermediate of CH_2-CH_2-O-Ag cyclises. The next pathway consists of hydrogen bonding of the intermediate to the oxygen atoms on the surface of the Ag which results in the hydrogen abstraction from the intermediate to form water and then CO_2. This mechanism is shown in *Figure 1.3*.

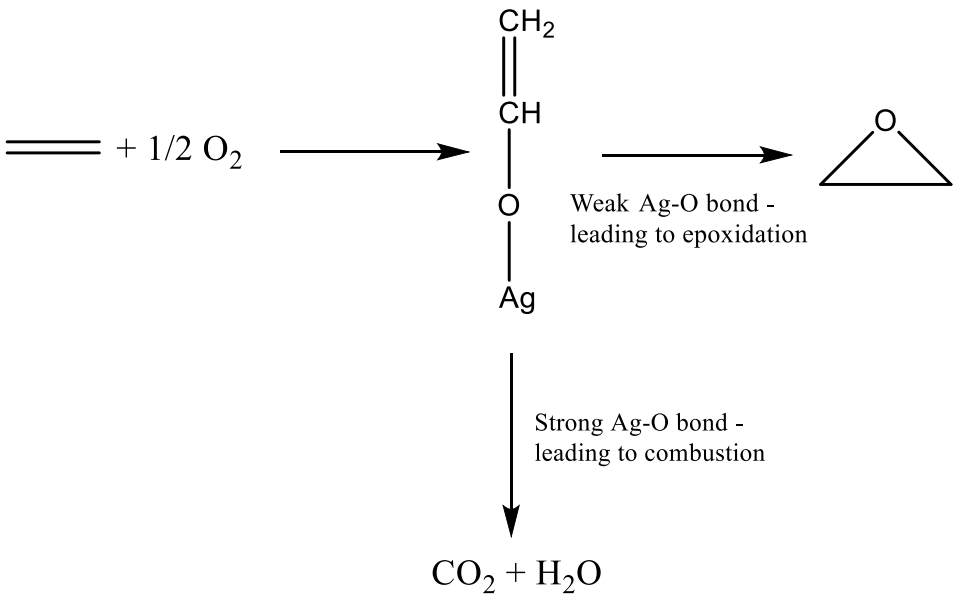

Figure 1.3: A reaction mechanism for the ethylene epoxidation modified by Waugh and Hauge. The Ag-O-CH_2-CH_2 intermediate is suggested in this mechanism.[31]

Van Santen and co-workers studied the mechanism of ethylene epoxidation on silver oxide surfaces using DFT calculations. Here they indicated that the direct oxidation of ethylene is likely possible in the absence of an oxygen vacancy. Here they found that an electrophilic oxygen that can attack the C=C bond to directly form EO. However, in the presence of an oxygen vacancy, the formation of the OMC is more favourable which would lead to total combustion since the activation barrier of acetaldehyde formation is much smaller than that of EO.[23,32–35]

Three different oxygen species (molecular, atomic and subsurface) can be found on the catalyst surface.[7,36] However, there is still discussion over the structure of the O/Ag system during ethylene epoxidation. It is now widely accepted that the surface species of strongly bound nucleophilic oxygen, an electron-rich oxygen has been proposed to activate C-H bond breaking and participates in the complete oxidation of ethylene.[26,37] Whilst the weakly bound electrophilic, electron-rich oxygen has been proposed for to open the C=C double bond of ethylene, forming the COC ring through O insertion.[23,26] However, some believe that the high selectivity is thought to derive from the electrophilic nature of particular surface oxygen species, whose properties are modified by subsurface oxygen.[9] If the silver surface is partially oxidized, the nature of the adsorbed and subsurface oxygen is believed to play an important role in the fate of an ethylene molecule.[18] There have been suggestions that the effect from the subsurface oxygen arises from an $O_{(sb)}$-induced upshift of the d-band centre of the Ag surface and becomes more pronounced at higher $O_{(sb)}$ coverage. This refers to the change in the position of the d-band energy level relative to the Fermi level. When the d-band shifts up the ability to adsorb and the activity improves due to the electrons being more likely to participate.[38] It stabilises the adsorption of H, C, N, O, O_2, CO, NO, C_2H_2, and C_2H_4 on Ag(1 1 1) and enhances the kinetics of H_2, O_2, and NO dissociation substantially.[39]

Recently, hybrid species have been identified on Ag oxide surfaces. Here, very little work has been undertaken with the investigation of these species due to the recent identification.[40,41] These hybrid species form, when one adsorbed O atom reacts with one lattice O atom on the surface or in the subsurface of Ag. These hybrid structures require the dissociation of adsorbed molecular oxygen into O atoms but still possess the O-O bond. They have been found to not form by recombination of two adsorbed O atoms because one of the O atoms in the hybrid structure must be embedded into the Ag lattice. Recent publications looking at Raman spectroscopy, DFT calculations and XPS have suggested these species are the active species in selective oxidation reactions on Ag catalysts.[16,40–43]

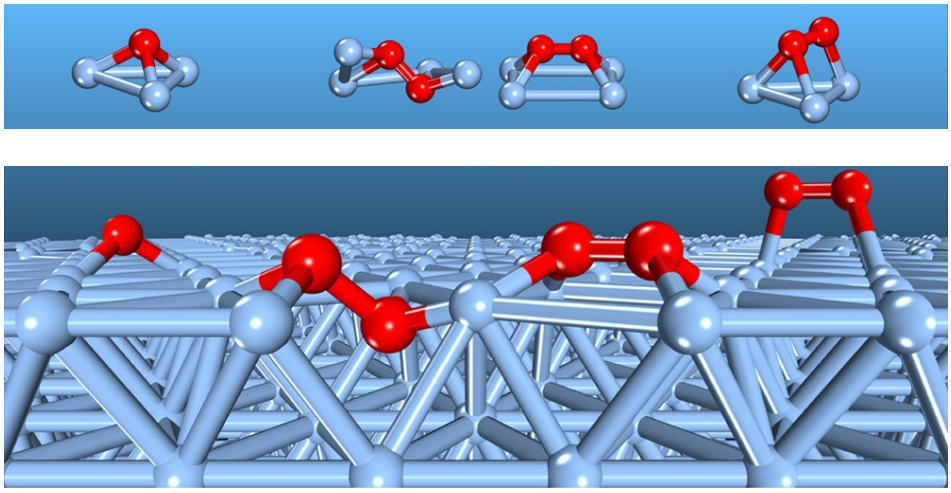

Figure 1.4: Three different species, thought to play a role in ethylene epoxidation. The numbers show their corresponding Raman peaks. Reprinted with permission from Tang et al.[40] *Copyright 2024 American Chemical Society.*

There is much to debate about the actual mechanism, the oxygen, and the silver surface. Therefore, the role of oxygen in EO is thought to be an important candidate to study by spectroscopic techniques.

1.1.2.2 Chlorine

Chlorine was tested among other halogens and compounds for the use of ethylene epoxidation due to their properties as a strong oxidising agent and being widely used in various oxidation reactions.[44,45] However, as discussed below chlorine was found to cause the largest selectivity, therefore commonly chlorine is used as a promoter for ethylene epoxidation.[24] Whilst it is commonly used, there are still many arguments in the literature into the role of the chlorine species.

Frequently, the co-feeding of dichloroethane or vinyl chloride with the reactants is used to deposit chlorine onto the catalyst. A large amount of research has been undertaken into identifying the role of Cl. It is thought that chlorine affects the silver epoxidation catalyst in various ways. Lambert *et al.* with the use of XPS suggested that halogen-induced selectivity in heterogeneous epoxidation is an electronic effect where the chlorine withdraws electrons causing an increase in the adsorbed electrophilic oxygen. Here Cl has a high electron affinity and highly electronegative meaning it can readily accept electrons giving rise to these electronic effects. They found that selectivity promotion in the catalysts corresponded with the halogen electron affinity, therefore confirming that it is an electronic phenomenon rather than a steric or geometrical effect. They found that chlorine causes the largest selectivity, whereas fluorine, bromine and iodine only show modest improvements. This trend follows the electron affinities of the halogens, which shows a maximum at chlorine.

The charge withdrawal causes more electrophilic oxygen that is proposed to increase the EO selectivity.[24] Next, Rocha *et al.* using XPS suggested that the addition of chlorine, increased the amount of "electrophilic oxygen" species, which are involved in the oxidation of ethylene to ethylene oxide, therefore meaning there is an increase in selectivity.[46] The decrease of both CO_2 and nucleophilic oxygen suggested that Cl acts as site blockers which promotes selectivity by the removal of nucleophilic oxygen species that are involved in the unselective oxidation pathway. They also suggested that Cl influences the selective oxidation pathways by enhancing the electrophilic oxygen. Therefore they believe that Cl overall increases the selectivity due to a combination of structural and electronic effects, which act together to modify the balance of electrophilic and nucleophilic oxygen species on the silver surface and in turn the active sites.[46] Here the chlorine is fed in in the gas phase and is more complex to do experimentally as there needs to be a low concentration of the chlorine gas phase.[1] Therefore, this promoter has not been investigated in this thesis.

1.1.2.3 Caesium

Caesium has unique properties that make it effective in oxidation reactions, it typically exhibits a +1 oxidation state making it highly reactive and effective in forming ionic compounds, it has a low ionisation energy and high electropositivity meaning that is can easily lose its single valence electron to form Cs^+ ion, enhancing its ability to modify the electron environment of catalysts.[47,48] When comparing to other alkali metals such as potassium and sodium, there is an advantage of using caesium, here, caesium has a larger atomic radius and lower ionisation energy making it more effective in modifying catalyst surfaces.[49]

Whilst the use of Cs as a promoter has been discussed, its specific role in the selective oxidation of ethylene is still a subject of much debate, with no role being conclusive. Lambert and co-workers suggested that Cs promotion was mainly electronic in nature.[28,50,51] They suggested with using DFT calculations that Cs affected the secondary chemistry by decreasing the rate of ethylene oxidation isomerisation to acetaldehyde, which during typical reaction conditions combusts immediately in the presence of Ag.[51] Epling and co-workers using XPS also suggested that the presence of Cs neutralises the acid sites on the support that are active for the isomerisation of EO to form acetaldehyde.[52] This work was then contradicted by Waugh and co-workers using O_2 temperature programmed desorption and computational experiments who suggested that the role of Cs is geometric in nature and that Cs is preferentially bound to Ag on unselective stepped silver sites.[25] With this, they believe that Cs is responsible for blocking the adsorption of oxygen onto the less

selective sites.[31,53–55] Minahan *et al.* and Bal'zhinimaev *et al*. using SEM and XPS suggested that the reason there is an improved EO selectivity is due to Cs being able to distribute the silver particles more uniformly on the support.[52,56] Diao *et al*. using kinetic studies and XPS found that Cs lowers the Ag binding energy to facilitate the desorption of the EO precursor to form gas phase EO.[57] Ren *et al*. using DFT calculations, TPD, XRD and XPS found that Cs both decreases the adsorption strength of oxygen on Ag and shifts the Ag binding energy to facilitate the desorption of the EO precursor to form gas EO. Cs was found to weaken the adsorption of atomic oxygen which thereby enhances the electrophilic attack by atomic oxygen at the electron-rich C=C bond of ethylene using DFT calculations, XPS and O_2 temperature programmed desorption.[58]

Caesium oxide based species (Cs_2O, CsO_2 and Cs_2O_2) are strong bases because they contain oxide ions (O^{2-}) which readily react with hydrogen ions to form CsOH.[59,60] When they come into contact with hydroxyl groups, they can neutralise them by forming water, the reaction produces caesium hydroxide which is a strong base and can further neutralise any acidic species present.[61,62]

To describe the neutralisation clearly, based on the well-established chemistry of solid-base zeolite catalysts, some equations can be drawn to derive a pathway for caesium hydroxide formation on the alumina surface.[63] *Equation 1.3* shows the simple interaction of a Cs ion with a hydroxyl ion to form caesium hydroxide. *Equations 1.4* and *1.5* show the interaction of caesium oxide with the alumina surface, generating caesium hydroxide, alumina and water.

$$Cs^+ + OH^- \longrightarrow CsOH \qquad \textit{Equation 1.3}$$

$$Cs_2O + 2Al - OH \longrightarrow 2CsOH + Al - O - Al \qquad \textit{Equation 1.4}$$

$$2Cs_2O + 2Al(OH)_3 \longrightarrow 4\,CsOH + Al_2O_3 + H_2O \qquad \textit{Equation 1.5}$$

According to the density function theory (DFT) method, Linic and Barteau found that Cs leads easily to the formation of an oxametallacycle (OMC) intermediate, which reacts through a transition state to form EO and acetaldehyde. It has been suggested that the Cs cations increase the selectivity by long-range electrostatic interactions that stabilise the transition state for the EO formation.[64] This effect can be understood where the transition state involved in the selective pathway has a favourable dipole orientation compared to the transition state involved in combustion.[64] Lastly when looking at the role of Cs,

Carvalho *et al*., using BET, SEM, XRD, TGA and diffuse-reflectance UV/Vis suggested that Cs promoted the formation of very small silver particles which increased the selectivity of ethylene oxide by increasing the contact with the reactants.[65]

The reason why there are so few papers looking at the Cs-O compounds involved in the catalytic reaction is due to the “material gap problem”, where there are discrepancies like bulk and dispersed silver so that results have been obtained in the model experiments with Cs doped Ag foil or single crystals cannot be directly applied to support silver catalysts.[66] Secondly, there are likely various Cs-O structures on the surface of the silver catalyst. Podgornov *et al*. using XPS, TPD and TPR investigated the Cs-O structures on the Ag/Al_2O_3 catalysts.[66] They found that Cs peroxide appears to suppress the total oxidation whilst the Cs suboxide causes the promotion of ethylene epoxidation.[66]

Therefore, due to the large arguments into the role and little literature on the structure of the Cs, it was thought to be useful to investigate both the role and the structure with the addition of a Cs promoter to Ag/Al_2O_3.

1.1.2.4 Rhenium

Rhenium is known for its unique properties that make it highly effective in oxidation reactions these include, rhenium exhibiting a wide range of oxidation states from -1 to +7, allowing rhenium to participate in various oxidation reactions, making it very flexible, being generally stable under reaction conditions, which is crucial for maintaining catalytic activity over extended periods, and examples of rhenium catalysts such as methyltrioxorhenium are highly effective in oxidation reactions such as olefin epoxidation and alcohol oxidation.[67–69] When comparing to other metals, whilst platinum is a highly effective oxidation catalyst it is often more expensive and can be prone to deactivation, whilst Re tends to be more resistant, compared to palladium it is widely used in oxidation reactions but normally operates at a lower oxidation state and lastly when compared to manganese rhenium’s higher oxidation states and stability often make it more effective in harsh reaction conditions.[70–73] Therefore it used as a promoter for ethylene epoxidation, however as stated before, the role of the Re is still not completely understood.

The use of Re as a promotor is much less understood compared to the other promoters. Jun *et al.* using O_2 temperature programmed desorption argued that the addition of Re competes with the adsorbed oxygen for the silver outer electrons which therefore reduces the electron density of the adsorbed oxygen and enhances the EO selectivity.[74] Dellamorte *et al.* using high-throughput reactor and SEM with EDS suggested that Re can cause a

redistribution of the Ag into a trimodal particle size distribution.[75] Diao *et al.* agree with Jun *et al*. and have suggested that the electronic effect of Re is connected with making the Ag sites more electron-deficient, therefore increasing the interaction with the electron-rich C=C double bond of ethylene and lowering the nucleophilic attack at one of the four C-H bonds which leads to the combustion to CO_2 and H_2O using kinetic studies and XPS. From SEM analysis they suggested that the presence of Re does not change either the morphology or particle sizes of the Ag particles relative to the catalysts without Re as a promotor. However, they suggested that the Re makes the Ag sites more electron-deficient and the resulting O adsorbed on Ag more electrophilic.[57] Barteau and co-workers using oxygen temperature programmed desorption contradicted this by saying it was a geometric effect, where the Re is connected to the blocking of the step and defect sites on Ag which results in a transition of oxygen adsorption and reaction towards Ag terraces.[76]

Very little work has been undertaken with investigations into the structure of the rhenium on the Ag/Al_2O_3, however, some work has been undertaken with looking at rhenium on different alumina without silver. Hardcastle *et al.* using laser Raman spectroscopy and XANES investigated the interaction of rhenium oxide with an alumina support, where they found that supported rhenium oxide on alumina is present as an atomically dispersed surface $[ReO_4]_{ads}$ species coordinated to the alumina support.[77] They found that the $[ReO_4]_{ads}$ species possessed C_{3v} symmetry which was consistent with the presence of three equivalent terminal Re-O bonds and one inequivalent Re-O bond as part of the Re-O-Al linkage to the alumina support. They found that there was a drop in the surface coverage of the $[ReO_4]_{ads}$ with increasing calcination temperature as the surface rhenium oxide species can recombine at elevated temperatures to give gaseous dimeric Re_2O_7.[77] Okal *et al*. using XPS, TEM and O_2 uptake measurements investigated Re on γ-Al_2O_3 they found that rhenium was present as a highly nonuniform phase, which consisted of very small clusters and metallic particles.[78] With the addition of oxygen, at room temperature, the clusters and small particles of Re are completely oxidised to Re^{4+} - Re^{7+} species. At 150 °C, the rhenium oxide spreads over the alumina support, where some particles of rhenium form a surface oxide phase. At 300 °C, the process of oxidation accelerates, and all rhenium transforms into a highly dispersed surface phase with chemical composition between Re^{4+} and Re^{7+}. At or above 500 °C rhenium undergoes complete oxidation to Re^{7+} species.[78] Okal using H_2 chemisorption, O_2 uptake, BET, XPS and Raman spectroscopy also found that after O_2 treatment at 500 °C, the rhenium particle as a Re^{7+} species, forms some kind of surface complex with an $Al\text{-}O\text{-}ReO_3$ or $Al\text{-}(O\text{-}ReO_3)_3$ structure, which stops the surface migration of rhenium and its loss from the oxidised catalyst.[79]

Greiner *et al*. using *in situ* XPS examined the oxidising rhenium species that form on a metallic rhenium foil during different reaction conditions.[68] Here, they found that in an oxidising environment, a Re_2O_7 film forms on the metal surface, with buried layers of sub-oxides that contain Re^{4+}, Re^{2+} and Re^{+} species at the Re_2O_7/Re interface. The Re^{2+} containing sub-oxide is not a known bulk oxide and is only known to exist on rhenium-metal surfaces. The Re_2O_7 film sublimes at a very low temperature (150 °C), while the Re^{4+}, Re^{2+} and Re^{+} species remain stable in oxidizing conditions up to at least 450 °C. Under conditions for partial oxidation of ethylene, they found that the active rhenium catalyst surface contains no bulk-stable oxides but consists of mainly Re^{2+} species and small amounts of Re^{4+} species. When the catalyst was cooled and in-active, Re_2O_7 was found to form on the surface. These results suggested that Re^{2+} and Re^{4+} species may be active species in heterogeneous rhenium catalysts.[68]

A few papers have investigated the Re oxide species on the surface of the Ag/Al_2O_3, however only the oxidation state was investigated, with little research undertaken on the structure. Dellamorte and Diao *et al*. using XPS and SEM found that Re on Ag/α-Al_2O_3 and Cs-Ag/α-Al_2O_3 was found to be in oxidation state +7.[57,76] Ren *et al*. using XPS found that the rhenium oxides with a valence of +4 to +7 are distributed around the Ag particles.[80]

1.1.2.5 Rhenium and Caesium

Compared to Cs and Re, a lot less work has been undertaken with investigations into the promotion of Cs and Re together on Ag/α-Al_2O_3. Ren *et al*. found that when adding Cs and Re, the impregnated catalyst has improved catalytic performance of both activity and selectivity compared to the individual Cs and Re catalysts. Using DFT calculations they attributed this to higher concentrations of weakly adsorbed oxygen and lower concentrations of strongly adsorbed oxygen.[80] Salaev and co-workers using DFT calculations showed that experimentally observed enhancement of performance of Re and Cs co-promoted catalysts can be caused by the formation of $CsReO_x$ species, where the Cs stabilises the Re to promote ethylene epoxidation and prevents Re loss from the Ag catalyst surface.[81] Jingfa and co-workers suggested that using both ReO_x and CsO_x reduces the potential energy between the surface and the subsurface oxygen, therefore this allows oxygen to transfer and move easily between the two areas.[82] Diao *et al*. using XPS found that whilst Re causes the Ag binding energy to increase, which makes the Ag sites more electron-deficient and therefore the resulting O adsorbed on Ag more electrophilic, the Cs lowers the desorption energy of the EO precursor which is strongly bound.[57] In the absence of Cs, the strongly bound EO undergoes combustion to CO_2 and H_2O, therefore the Re and

Cs promote two different steps of the overall mechanism. Re increases the rate of electrophilic attack by Ag-O at the C=C bond of C_2H_4, while Cs lowers the desorption energy of the adsorbed EO precursor to form EO.[57] Zhang *et al*. using DFT calculations found that Re in the form of ReO_4 increases the dispersion of Cs, which maximised the promotional effects of Cs, alongside combing the electron-withdrawing Re and the electron-donating Cs balances the amount of charge transferred to the catalyst, therefore maximised EO selectivity by preventing the formation of overly nucleophilic oxygen species that facilitate ethylene combustion and overly electrophilic Ag centres that accelerate EO isomerisation.[8]

Therefore, it was thought to be useful to investigate both the role and structure of Cs and Re together on both Ag/α-Al_2O_3 and Ag/γ-Al_2O_3.

1.1.3 Use of Gold and/or Copper Catalysts for Ethylene Epoxidation

Propylene epoxidation contains all the same challenges as ethylene epoxidation however due to the presence of allylic hydrogen in propylene the selectivity towards the epoxide is generally much lower for propylene than for ethylene. Due to the ease of the abstraction of H atoms resulting in combustion rather than selective oxidation, the heterogeneous epoxidation of alkenes other than ethylene is very difficult. In addition to Au, it is well known that Cu-based catalysts are particularly effective for alkene epoxidation when allylic hydrogen atoms are present because Cu favours metallacycle formation instead of allylic hydrogen stripping, which is the main obstacle for epoxidation.[83] The use of gold and copper catalysts are used for propylene epoxidation with little work investigated with these catalysts for ethylene epoxidation, it was thought that the use of gold, copper and a mixture as catalysts could be investigated to see if they are selective towards ethylene epoxidation.[84]

Initially, it was thought that gold was catalytically unreactive, however, the same chemistry that is observed in silver and copper is also observed on gold. Commonly, gold is used for oxidation reactions.[85] Nijhuis *et al*. using IR spectroscopy, TEM and XRF investigated gold on titania and found that a peroxide species provided by Au facilitates the epoxidation of propene on the titania sites, therefore generating propylene oxide.[86] They found that the presence of gold nanoparticles on the titania catalyses a reaction between propene and the titania sites where a bidentate propoxy species is formed.[86] Wang *et al*. also investigated the use of Au as a catalyst for propylene epoxidation using computational calculations and they found that when molecular oxygen is used, there is a higher selectivity to OOMMP (shown in *Figure 1.5)* and therefore, an improved overall selectivity to propylene oxide (PO).[87] This OOMMP can cleave the O-O bond and transform into OMMP.[87]

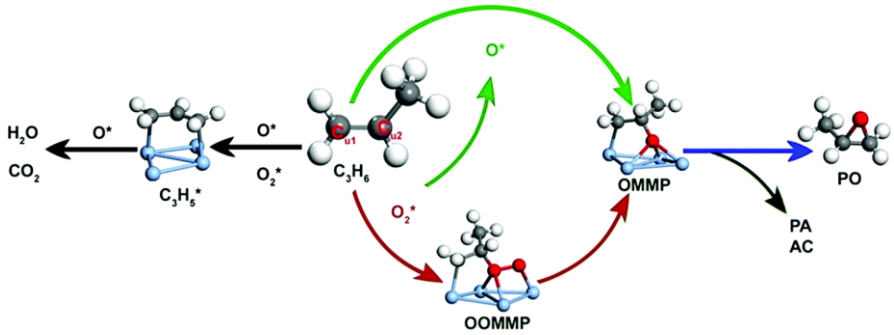

Figure 1.5: A diagram to show the suggested mechanism to PO, reproduced from Wang et al.[87]

Chen *et al*. investigated theoretically using DFT calculations the adsorption and reaction of ethylene and O_2 on a gold cluster, here they found that the Au nanoparticle is much more selective for ethylene epoxidation compared to the Au (1 1 1) surface. Due to the inversion of the activation energy barriers for cyclisation to epoxide versus the H-shift to acetaldehyde relative to the Au (1 1 1) surface.[88,89]

Copper is also used for alkene epoxidation. The use of copper as a catalyst has been tested extensively for propylene oxidation. It has been found that under propylene epoxidation conditions, copper is present predominately as Cu_2O as well as CuO.[90] Djinović *et al*. investigated the use of Cu for propylene epoxidation for a review and produced the reaction pathways shown in *Figure 1.6* with the participation of lattice or surface chemisorbed oxygen species.[91] To conclude, it is thought that the Cu^+ is the predominant oxidation state and there is often a mixture of Cu^{2+} and Cu^+. It is thought that the presence of different adsorbed oxygen species (O_2^-, O^- and O^{2-}) originate from molecular oxygen activation which allows for a parallel occurrence of epoxidation reactions via lattice or adsorbed oxygen species.[91]

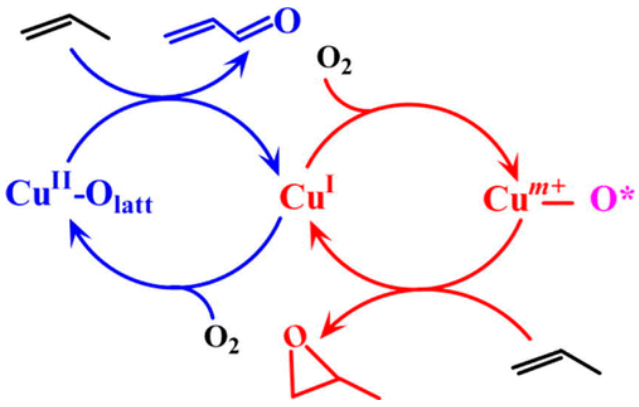

Figure 1.6: A diagram to show the suggested mechanism of Cu reproduced from Djinović et al.[91]

Greiner *et al*. found that using *in situ* XPS and DFT calculations, close to the Cu_2O-CuO phase transition there is an increase in activity towards ethylene epoxidation.[92] They found

that the metastable O precursors to the CuO phase can account for the selectivity enhancements near the phase transition. When fully oxidized to CuO, or when present as Cu_2O, but far away from the phase transition, catalysts exhibit a reduction in epoxide selectivity.[92] Another paper from Greiner *et al*. using XPS, XAFS, SEM and DFT calculations found that both oxides exhibited some activity for partial oxidation with Cu_2O exhibiting slightly higher partial oxidation selectivity than CuO.[93] Cu_2O was found to produce equal amounts of acetaldehyde as epoxide, whilst CuO produced roughly ten times more epoxide than aldehyde.[93] Santra *et al*. using TPR and XPS stated that due to the copper's strong bonding to oxygen and relatively weak bonding to carbon the reaction pathway to the epoxide is favoured over the pathway to the acetaldehyde.[94] For high selectivity epoxidation to occur on copper, both metallic copper sites and adsorbed oxygen sites are required.[94] Lastly, Jayamurthy *et al*. using XRD, SEM and TEM found that Cu(I) is an active species in epoxidation.[95] Where a decrease in selectivity is due to this change from Cu(I) to Cu(II).[95]

Llorca *et al*. using HRTEM, XPS and TPR investigated the use of propene epoxidation with Au-Cu catalysts and found that there was an increase in the activity and selectivity of propene oxide due to an alloy compared to monometallic Au or Cu samples.[83] For ethylene epoxidation, Tseng *et al*. using periodic first-principles computations found that Cu-Au core-shell nanoclusters are more reactive than pure Cu and Au nanoclusters due to a lower activation energy for ethylene oxide formation compared to acetaldehyde formation.[96]

Cu-promoted Ag/Al_2O_3 catalysts for ethylene epoxidation have been investigated in the literature, however, the results are mainly theoretical rather than experimental. Fortunelli *et al*. theoretically investigated ethylene epoxidation with Cu-Ag catalysts.[97] Here they found that the relative bond strength between the C-O and the O-metal bonds in the oxametallacycle (OMC) intermediate affects the selectivity to EO, where there is a volcano like relationship as a function of surface Cu content.[97] Stampfl *et al*. using DFT found that in the formation of a surface alloy where copper oxide is formed, both Cu(I) and Cu(II) are present at the surface as thin overlays on top of the silver particles.[98] Nguyen *et al.* using first-principles density functional theory found that under reaction conditions, Cu tends to oxidise and form thin Cu oxide layers on top of the Ag particles, causing O_{sub} to migrate to the catalyst surface.[99,100] Saten *et al*. using electronic structure calculations found that the O_{sub} weakens the bond strength of surface oxygen O_{surf} therefore facilitating the binding of the C=C double bond of ethylene to O_{surf} forming EO.[101] Jankowiak and Dellamorte *et al*. using DFT and selectivity data found that Ag keeps the copper in an oxidation state that provides a selective pathway to epoxide via alloying.[76,102] Piccinin used DFT alongside XPS and XRD and found the coexistence of thin CuO and AgO-CuO films on the Ag substrate.

The active O species, rather than the O atoms chemisorbed on a metal surface, are O atoms which are part of an oxide layer.[103]

Therefore, as the Cu and Au-based catalysts are used widely in propylene epoxidation, and the majority of work undertaken with investigations into these catalysts are with DFT calculations and computation work, it was thought to be interesting to investigate these catalysts experimentally for ethylene epoxidation.

1.2 Catalyst Characterisation and *Ex situ* Spectroscopic Techniques

Catalyst characterisation refers to the process of understanding and describing the properties, structure, and behaviour of catalysts. Here, the aim is to gain insight into the fundamental features of a materials composition, morphology, crystal structure and physical properties. Characterisation techniques can be undertaken both *in situ* and *ex situ* and give information into the catalyst post preparation and under reaction conditions. Spectroscopic techniques are a subset of characterisation techniques that specifically involve the interactions of electromagnetic radiation and matter.

Ex situ characterisation refers to methods in which the material is investigated in an ambient or static environment, often under a different environment to the environment in which the catalyst would be exposed in its application. These are typically conducted pre- or post-process to determine catalyst properties and observe any changes that have occurred under reaction conditions. Some advantages of using *ex situ* spectroscopic techniques include detailed analysis alongside the use of carefully controlled conditions (e.g. temperatures and atmosphere), whilst allowing access to a broader range of analysis, as not all instruments can be applied *in situ*.[104,105]

There are many different characterisation and *ex situ* spectroscopic techniques used to analyse catalysts. Examples of those used in this project include transmission electron microscopy (TEM), powder X-ray diffraction (pXRD), diffuse reflectance infrared Fourier transform spectroscopy (DRIFTS), X-ray photoelectron spectroscopy (XPS) and elemental analysis, e.g. inductively coupled plasma – optical emission spectroscopy (ICP-OES).

TEM is an electron microscopy technique that uses the interaction of an electron beam with a sample to form an image of the sample. TEM instruments can be used to provide morphologic, but also compositional and crystallographic information on different samples.[106] There are many advantages of using TEM, offering powerful magnification to provide information on elemental composition (when paired with EDX analysis) and compound structure.[106]

Powder X-ray diffraction (pXRD) is a technique used to determine the atomic and molecular structure and phase of a crystalline material.[107] XRD works by irradiating a material with incident X-rays and then measuring the intensities and scattering angles of the X-rays that leave the material.[108] pXRD has many advantages, for example, it is a rapid technique for identifying unknown materials with only minimal preparation and at least at a basic level interpreting the resulting data is easy/straightforward.[108]

Inductively Coupled Plasma – Optical Emission Spectroscopy (ICP-OES) is used to determine elemental compositions and can be used on a variety of different elements. It has many advantages over other elemental analysis techniques. Firstly, it has a wide linear dynamic range, secondly, it has a high matrix tolerance and lastly, it has a short timescale of analysis.[109]

Fourier Transform Infrared Spectroscopy (FTIR) is a method of IR spectroscopy used to determine the structures of molecules and materials when a sample has absorbed IR radiation.[110] When the radiation is absorbed it is converted into rotational and/or vibrational energy by the sample molecules. By analysing an IR spectrum it is possible to determine structural information about a sample.[110] The spectrum produced by a FTIR represents a molecular “fingerprint” of the sample, different chemical structures and molecules have unique spectral fingerprints. There are many advantages of using FTIR as a characterisation technique, one of the main ones is that it can analyse virtually any sample in any state, for example, liquids, powders, gases and surfaces can all be analysed, except water, as this can affect the IR spectrum.[111]

Attenuated total reflectance (ATR-IR) is a form of infrared (IR) analysis, it gives information on both the different structures and also the environment of the different adsorbed molecules. This technique is normally used alongside traditional IR spectroscopy.[110] It is a technique which is useful in many different applications as it is able to probe single or multiple layers of adsorbed species at a solid/liquid interface.[112]

DRIFTS is also an infrared spectroscopy sampling technique which is used on powder samples. It studies the surface chemistry of high surface area powders, normally in the form of heterogeneous catalysts.[113] DRIFTS gives information regarding the chemical and physical structures of adsorbates on materials. An advantage of using DRIFTS is that it can analyse almost any sample form, solid, liquid or gas with minimum preparation, where the sample can be loaded into the sample cup, therefore making it an easy and useful technique.[114] It also has a fast and easy clean-up as the contents of the cup are discarded and then rinsed clean.

Raman Spectroscopy is a vibrational spectroscopic technique that can be used to determine chemical structure, phase, crystallinity, and molecular interaction. A Raman spectrum shows a distinct chemical fingerprint for a particular substance, therefore meaning that identification of chemicals is both easy and quick. Raman spectral libraries are used for the identification of materials where they contain thousands of spectra to find a match for the spectrum of the material.[115] Raman spectroscopy has many advantages, firstly both organic and inorganic materials are suitable, in solids, liquids, polymers or vapours. There is no sample preparation required and the technique is less susceptible to interference than IR, particularly from water, whilst remaining a non-destructive technique.[116]

X-ray photoelectron spectroscopy (XPS) is a technique that can be used for analysing the surface chemistry of a material. It can measure the chemical state and the electronic state of the elements.[117] XPS also has many advantages, firstly it is effective across a range of both organic and inorganic materials. No other analytical technique provides the same useful combination of surface sensitivity and quantifiable elemental and chemical information. It provides information on both elemental composition and chemical bonding. It is a non-destructive technique with a high surface sensitivity.[117]

X-ray absorption spectroscopy (XAS) is a technique that is used for determining the local geometric and/or electronic structure of matter, where it is element specific. XAS has many advantages including, looking at the oxidation state, gaining coordination environment information and it is not limited by the state of the sample.[118] Another important advantage of using XAS is that it can penetrate the surface of samples to allow for analysis of the bulk.

Therefore, this shows that *ex situ* spectroscopic techniques and different characterisation techniques are useful for giving more understanding of catalysts.

1.3 *In Situ* Spectroscopy – Why Is It Useful for Studying Catalysis?

Whilst *ex situ* methods allow us to characterise the catalyst pre- and post-process, there are sometimes important changes that occur under reaction conditions. Therefore, there is a need for *in situ* spectroscopic techniques to observe changes.

In situ spectroscopy are analytical techniques where the spectroscopic characterisation of a material occurs during the reaction process.[119] The definition of "*in situ*" refers to a collection of spectra being collected using several different techniques simultaneously to characterise the catalyst under reaction conditions.[120] The main aim of *in situ* spectroscopy is to observe the structure-reactivity/selectivity relationships of catalysts or identify surface species present to find information about the mechanism of the process taking place.[121]

This provides invaluable information for designing new catalysts and improving existing catalytic processes.[120]

Some spectroscopy methods are more easily adapted to *in situ* studies, such as DRIFTS, Raman, and XAS, facilitated either by the penetration of the spectroscopic probe through the reaction medium or through conducting the reaction using a spectroscopic cell.[122] The development of *in situ* methods for techniques routinely conducted using high vacuum systems, such as near ambient pressure-XPS (NAP-XPS) and electron microscopy, have both proven more challenging but have undergone significant advances in recent years, therefore making them much easier to use.[123]

It should be noted that with near ambient pressure techniques, the investigation of model catalysts contained under high vacuum systems can give insightful information to the fundamental surface science, however, these do not represent the real catalytic systems used in industry. This concept is often referred to as the materials and pressure gap, i.e. the difference between the surface studied in ambient conditions compared to the 'real' industrial catalyst in its operating environment.[123]

Therefore, the combined use of characterisation techniques, *ex situ* and *in situ* spectroscopy is important to give an overall understanding of the catalysts and how the catalyst behaves under reaction conditions.

1.4 Diffuse Reflectance Infrared Fourier Transform Spectroscopy (DRIFTS)

Diffuse reflectance infrared Fourier transform spectroscopy (DRIFTS) is a technique that can be used for studying surface species.[124] The methodology of DRIFTS can be found in **Chapter 2.1.3**. DRIFTS is an infrared spectroscopy technique, which is used on powder samples. It is used for studies of the surface chemistry of high surface area powders, normally in the form of heterogeneous catalysts, where optionally the temperature and the environment of the catalyst can be controlled *in situ* in a DRIFTS cell.[124] An advantage of using DRIFTS is that it can analyse almost any sample form, solid, liquid or gas with minimum preparation as it can be placed in the sample cup or cell, therefore making it an easy and useful technique.[124]

The ability to conduct *in situ* experiments can provide information on the surface structure of the metal or species at the metal and the chemical intermediates present on the catalyst during catalysis. Therefore, *in situ* experiments will need the use of a DRIFTS cell rather than a simple sample cup.[124] Whilst there are commercially available cells already that can be used in carrying out *in situ* DRIFTS experiments, there are some issues with them

including gas by-passing the sample bed, inaccurate temperature readings and in particular difficulty in accurate backgrounding.[125] These problems can lead to inaccurate results, therefore the design of a suitable DRIFTS cell for *in situ* measurements will be discussed in this thesis.

1.4.1 Limitations with DRIFTS

Despite finding widespread utility in catalysis studies, several researchers have found significant limitations with *in situ* DRIFTS cells. In particular, these limitations and possible workarounds have been studied in detail by Meunier and Drochner.[113,126]

The first problem with many commercial DRIFTS cells is that the gas can bypass the sample bed.[113] *Figure 1.7* shows a schematic of the Spectra-Tech® DRIFTS cell and shows the issue of a small gap between the bottom of the ceramic crucible and the metal base. Therefore, this means that gas can leave the cell without passing through the sample bed. Whilst there have been updated versions of this cell, where they have sealed this gap with PTFE tape, it is subjected to large temperature changes so overall an acceptable seal cannot be achieved.[125]

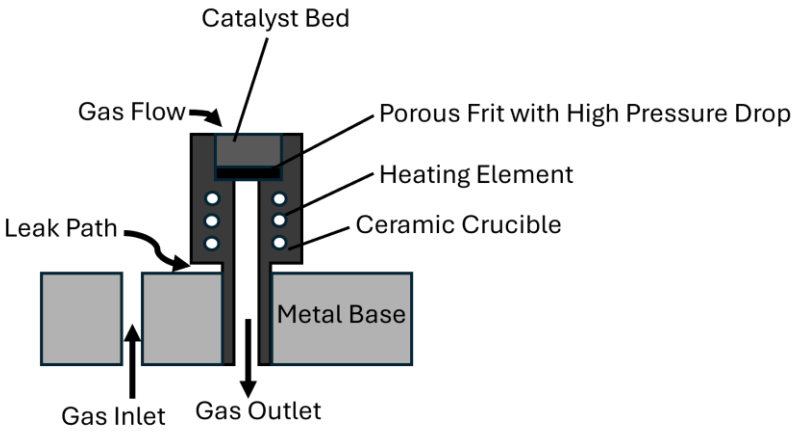

Figure 1.7: Schematic representation of the Spectra-Tech® DRIFTS cell modified from Cumming et al. with permission from the Royal Society of Chemistry.[125]

Another reported problem in commercial DRIFTS cells, is the accuracy of the temperature readings.[113] By looking at both the Harrick and the Spectra-Tech cell, as shown in *Figure 1.8*, when the temperature is below 100 °C, both the cells' thermocouples provide reasonably accurate readings when compared to an optical temperature measurement of the powder surface. However, at higher temperatures, there are quite substantial deviations. This is likely to be due to the thermocouple not being placed close to the sample

bed. Therefore, ideally, the thermocouple should be placed in a position that sits within the catalyst bed.[113]

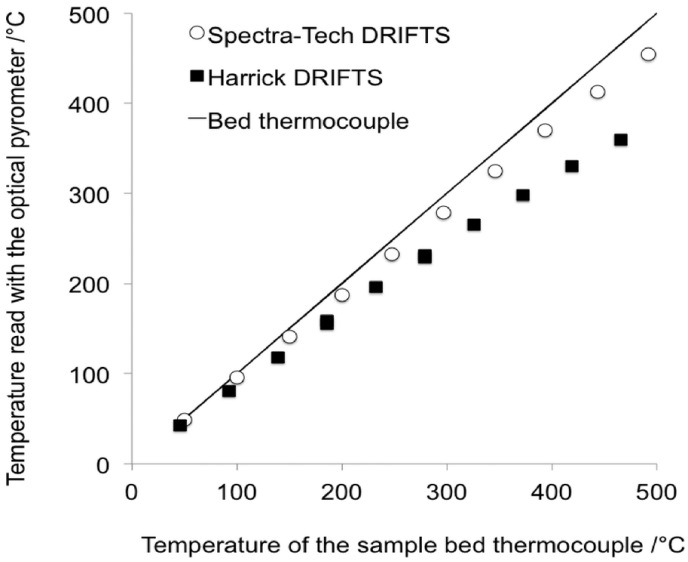

Figure 1.8: A comparison of the temperature readings of the sample bed thermocouple with the optical pyrometer for the Harrick DRIFTS cell, the Spectra-Tech DRIFTS cell and the bed thermocouple reproduced from Meunier with permission from the Royal Society of Chemistry.[113]

The last main problem with commercial cells is that only one material can be measured at one time. Therefore, this means that the background spectrum must be taken separately from the sample which can lead to problems as the atmosphere in the DRIFTS instrument chamber can change significantly throughout a long *in situ* measurement, meaning that the backgrounding becomes unreliable.[113] It has been found that adsorbed species with short lifetimes can desorb and change, therefore the backgrounding needs to account for the presence of gas-phase species. Another issue is caused by high boiling species condensing on the windows in constantly changing amounts, due to the issue of the window being cooler. During IR adsorption, H_2O and CO_2 gas phases are constantly changing and it is not possible to reliably subtract the peaks after measurements. Therefore, improvements are needed to fix these problems.

1.5 Improvements to *In Situ* DRIFTS Cells

1.5.1 Previous Work Undertaken in the Literature to Improve *In Situ* Cells

Firstly, Drochner *et al.* constructed a new cell (shown in *Figure 1.9*) where the catalyst as well as a reference substance are in the same reaction chamber. Therefore, both of the substances are exposed to the same reaction gas, meaning that the gas phase molecules in the reaction chamber can now be eliminated as well as the changes that occur as a result

of the condensation of by-products on the window. Therefore meaning, adsorbates were able to be detected under *in situ* conditions.[126]

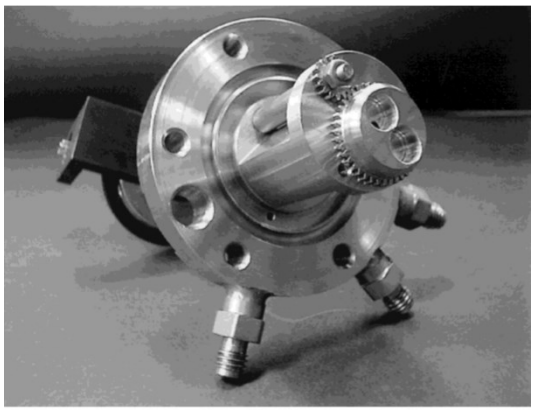

Figure 1.9: An image of the cell reproduced by Drochner et al.[126]

Whilst the idea of the sample and the reference being in the same reaction chamber was important and groundbreaking, the design is fairly complex, using gear mechanisms to move from sample to reference. There are also potential pitfalls of the design, including the thermocouple position and the gas flow, where the outlet position means that gas will only pass through one bed at a time.[126]

Meunier *et al*. also investigated improving the Spectra-Tech cell with ZnSe windows (shown in *Figure 1.10*). The modified cell was obtained by replacing the original crucible with a custom-made one. Although this is a commonly used cell, the cell presents some bypass of the catalyst bed, and it is due to the gas present between the stem of the ceramic crucible and the metallic base plate. Secondly, the ZnSe dome is very close to the rim of the crucible, therefore meaning the void above the catalyst bed can become a dead zone with a very slow diffusion pathway to the circulating gas passing through the cell.[127]

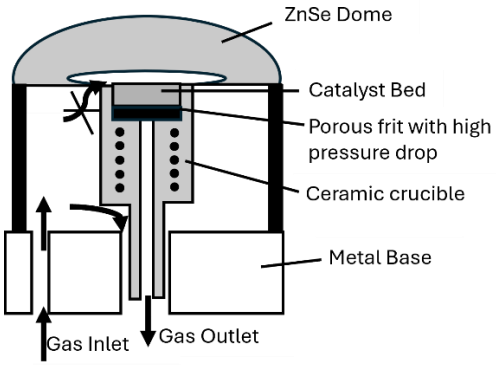

Figure 1.10: Schematic representation of the Spectra-Tech high temperature/high-pressure DRIFTS cell chamber modified from Meunier et al. with permission from the Royal Society of Chemistry.[127]

Therefore, they have modified the cell by replacing the original crucible with a custom-made ceramic reactor, which is shown in *Figure 1.11*. Here the crucible presented no significant

pressure drop as a metallic mesh was used to support the catalyst instead of the ceramic porous frit of the original cell. Whilst this has fixed the pressure issue for the Spectra-Tech cell, the reference and sample being taken under different conditions has not been solved.[128]

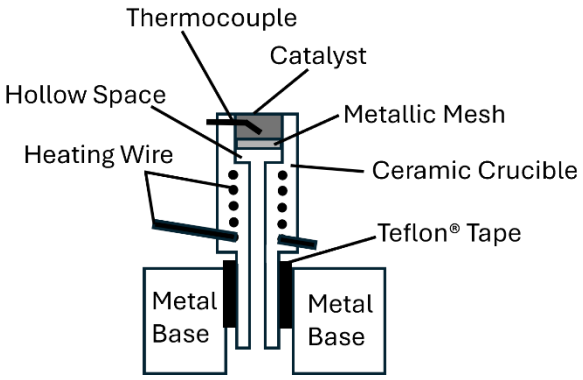

Figure 1.11: Schematic representation of the modified Spectra-Tech high temperature/high-pressure DRIFTS cell chamber modified from Meunier et al.[128]

Dr Ellie Dann developed an *in situ* DRIFTS cell for combined XAFS and DRIFTS.[129] Here a DRIFTS cell was made, with a single flat window allowing the gas to flow through the cell. This therefore minimises the cell dead volume within the cell. The design of the cell also allows for no gaps for the bypass of the gas flow, therefore improving some of the issues above. However, it did have some problems with thermal expansion and temperature inhomogeneity within the sample bed.[129]

This has therefore led to the need for the development of a modified *in situ* DRIFTS cell.

1.5.2 Previous Work Undertaken by the Beaumont Group to Improve Previous *In situ* Cells.

An updated DRIFTS cell is required to carry out accurate and reliable *in situ* DRIFTS experiments.

Initial ideas of an updated DRIFTS cell included:

- Two-bed sections, one for the sample and one for reference material.
- A mechanism that can move between the two without opening the DRIFTS cell or the instrument chamber - no release of gases.
- A thermocouple in the bed.

Initial development of a DRIFTS cell and “sliding mechanism” to move between reference and sample beds was previously undertaken by members of the Beaumont group. Images of the cell and the shelf are shown below in *Figures 1.12, 1.13 and 1.14*.

Other members of the Beaumont group developed the initial DRIFTS cell (shown in *Figure 1.12a*) to the second DRIFTS cell design (shown in *Figure 1.12b*). Here they improved the signal, by reducing the depth of the section where the window would be screwed in, increasing the signal intensity, and providing smooth edges of the cell to make sure that the cell reached the sample height that resulted in the best signal. Secondly, they found a way of separating the bed into two sections – one for the sample and the other for a reference material that can be used in backgrounding, whilst allowing gas flow through the beds. Here the design consisted of inserting two thin pieces of metal, with numerous small holes to ensure an even gas flow and putting a small amount of quartz wool, to stop any sample transfer and to prevent the sample and the background from moving around. As shown in both *Figure 1.12a* and *1.12b*, there is a gap in the side of the cell to allow a thermocouple to enter the middle of the bed so that the temperature of the bed can be read. A schematic of the DRIFTS cell is shown in *Figure 1.13.*

The aim of this *in situ* DRIFTS cell is to take background measurements continually throughout experiments, with the backgrounding material under the same conditions as the sample.[130] Therefore, a sliding mechanism is required (shown in *Figure 1.14*), here they found that metal wires could be attached to t (b) ing section, which allows the cell to be moved back and forth between the sample and the background, without opening the DRIFTS instrument, which would admit cause changing in CO_2 and H_2O in the beam path. Here a pull-pull sliding mechanism is used to switch between the two positions.

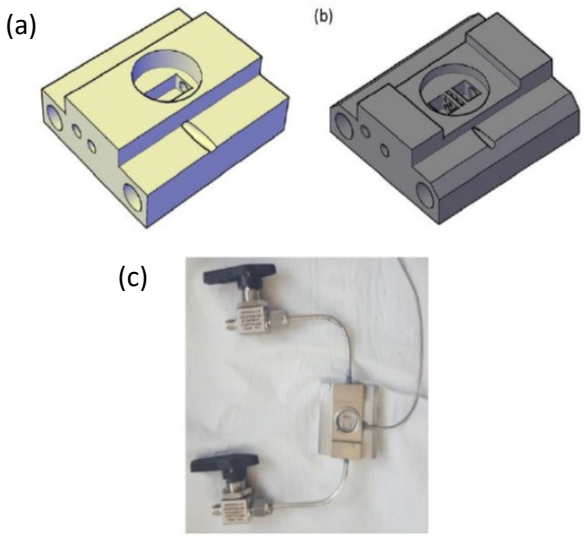

Figure 1.12: (a) the initial DRIFTS cell design, (b) the second DRIFTS cell design with sides cut away to allow better optical throughput and (c) the produced DRIFTS cell including the necessary fittings reproduced from Kathryn MacIntosh.[131]

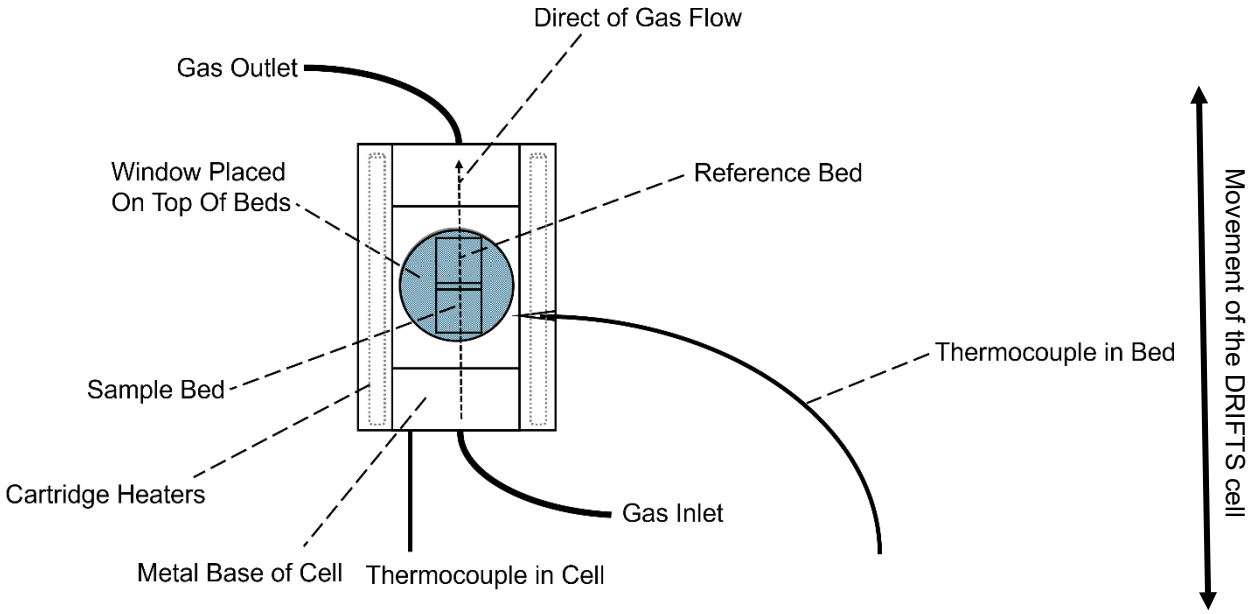

Figure 1.13: A schematic diagram of the DRIFTS cell.

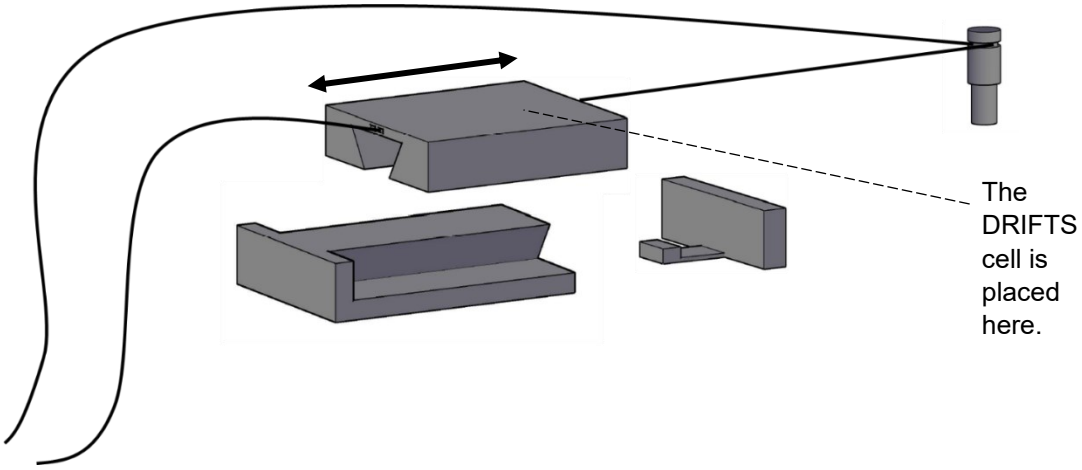

Figure 1.14: Schematic of sliding mechanism for use with the DRIFTS cell. Reproduced and modified from Kathryn MacIntosh.[131]

Whilst an *in situ* DRIFTS cell had been previously produced, there were several further improvements required. The issues included:

- Reduction in the signal of around 30% between the commercial sample cup that is used routinely for *ex situ* measurements and the cell. This must originate from not all the signals being collected, which reduced signal intensity.
- Initial attempts to flow gases through the cell led to the sample and the reference material being disturbed as there seemed to be a slight build-up of pressure, which occurred whilst attaching the gas line. A slight build-up in pressure was released when the valves to the cell were opened, which resulted in the beds being disturbed.
- Difficulties with being able to seal the cell completely due to the metal ring not catching correctly on the cell as the thread kept giving which led to the leaking of gases. With the circular motion of having to screw in the metal ring, with some materials it caused the o-ring to move and shift which also led to not forming a proper seal. This window sealed to the cell is shown in *Figures 1.15* and *1.16*.
- No *in situ* reactions have been undertaken in the DRIFTS cell.

Therefore, in the current work, a new improved cell is described.

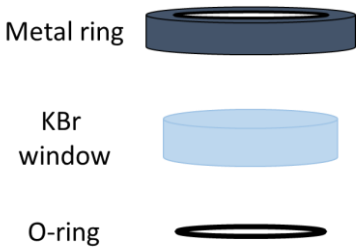

Figure 1.15: Schematic representation of the window sealing mechanism. Reproduced from Kathryn MacIntosh.[131]

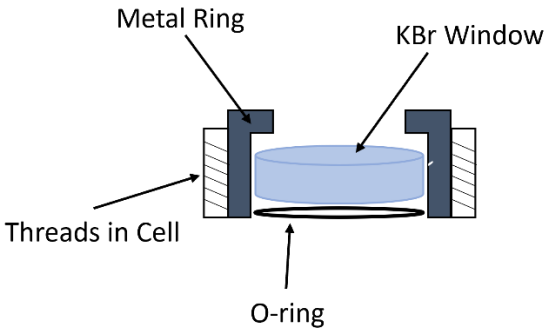

Figure 1.16: A side profile of the cell, showing how the metal ring screwed into the threads in the cell.

1.6 Aims and Objectives

As discussed in **Chapter 1**, the use of *ex situ* and *in situ* characterisation and spectroscopic techniques are useful for gaining more information on improving the understanding of catalysis. Whilst *in situ* DRIFTS is commonly used to give an more information during catalytic reactions, there are current issues with commercially available *in situ* DRIFTS cells which lead to inaccurate and unreliable results. One catalytic reaction that would be useful to gain an improved understanding from the use of these techniques is ethylene epoxidation. Whilst the ethylene epoxidation reaction is widely used in the literature and industry, the role of the mechanism and the oxygen species are still widely debated. The use of promoters, caesium and rhenium have been known to improve the conversion and selectivity towards ethylene oxide, however the exact role of the promoters is still unknown with large disagreements. The use of copper and gold catalysts have been widely used as successful for propylene epoxidation however have not currently been investigated for the use of ethylene epoxidation.

Based on the key results from the literature review, this thesis aims to:

1. Develop and optimise an *in situ* DRIFTS cell which solves the limitations of current commercial DRIFTS cells. Improving the previously developed DRIFTS cell by the Beaumont group, optimising, and developing the setup so that case studies are able to be undertaken. Show the improvement of this new developed DRIFTS cell compared to the old one – indicating why there is a need for an improvement of these limitations. Finally using this developed DRIFTS cell to give more information on surface species during *in situ* O_2 pretreatment and ethylene epoxidation.
2. Improve the understanding of the Ag/α-Al_2O_3 catalyst and compare it to Ag/γ-Al_2O_3, where the Ag/α-Al_2O_3 catalyst can be used as a basis to understand the role the promoters have on ethylene epoxidation. To develop a greater understanding the role of the oxygen species during *in situ* oxygen pretreatment and ethylene epoxidation on the Ag/α-Al_2O_3 catalyst through the use of *in situ* and *ex situ* characterisation techniques. Alongside investigating the role of the Re promoter with comparison to the literature, and how the Re has an effect on the ethylene epoxidation reaction. The structure of the Re on the surface of the catalyst will also be investigated, giving more information into the role of Re as a promoter in ethylene epoxidation.
3. To understand the role of the Cs promoter and to find out why the addition of Cs to Ag/Al_2O_3 causes an increase in ethylene oxide selectivity. Using both *in situ* and *ex situ* characterisation techniques to identify the structure of the Cs on the surface of the catalyst alongside investigating the geometric and electronic effects that the Cs gives to improve the EO selectivity. To improve the understanding on why the Cs and Re promoter together gives the most selective catalyst towards ethylene epoxidation, and how they work both separately and synergistically to provide this result. To investigate the structure on the surface of the catalyst and how the Cs and Re interact with both each other and the Ag using both *ex situ* and *in situ* characterisation techniques to investigate this.
4. Whilst Cu and Au-based catalysts have been investigated for propylene epoxidation, currently there is very limited experimental data present of using these catalysts for ethylene epoxidation. Therefore, an aim is to investigate if Cu and Au-based catalysts could be used for ethylene epoxidation and investigate their selectivity and conversion towards ethylene epoxidation. Give an insight into why these catalysts could be used for ethylene epoxidation using both *in situ* and *ex situ* spectroscopic and characterisation techniques, taking into consideration the metals alongside the support and pretreatments. Looking at the structure of the catalysts and a combination of metals in their different environments.

1.7 References

1 T. Pu, H. Tian, M. E. Ford, S. Rangarajan and I. E. Wachs, *ACS Catal.*, 2019, **9**, 10727–10750.
2 K. C. Waugh and M. Hague, *Catal. Today.*, 2010, **157**, 44–48.
3 S. Rojluechai, S. Chavadej, J. W. Schwank and V. Meeyoo, *Catal. Commun.*, 2007, **1**, 57–64.
4 C. J. Keijzer, L. C. J. Smulders, D. Wezendonk, J. W. de Rijk and P. E. de Jongh, *Catal. Today.*, 2024, **428**, 114447.
5 J. E. van den Reijen, W. C. Versluis, S. Kanungo, M. F. d'Angelo, K. P. de Jong and P. E. de Jongh, *Catal. Today.*, 2019, **338**, 31–39.
6 A. Ayame, Y. Uchida, H. Ono, M. Miyamoto, T. Sato and H. Hayasaka, *Appl. Catal. A Gen.*, 2003, **244**, 59–70.
7 D. Lafarga, M. A. Al-Juaied, C. M. Bondy and A. Varma, *Ind. Eng. Chem. Res.*, 2000, **39**, 2148–2156.
8 B. W. J. Chen, B. Wang, M. B. Sullivan, A. Borgna and J. Zhang, *ACS Catal.*, 2022, **12**, 2540–2551.
9 A. J. F. van Hoof, E. A. R. Hermans, A. P. van Bavel, H. Friedrich and E. J. M. Hensen, *ACS Catal.*, 2019, **9**, 9829–9839.
10 J. K. Lee, X. E. Verykios and R. Pitchai, *Appl. Catal.*, 1989, **50**, 171–188.
11 X. E. Verykios, F. P. Stein, R. W. Coughlin and R. W. Coughlin, *J. Catal.*, 1980, **66**, 368–382.
12 B. T. Egelske, W. Xiong, H. Zhou and J. R. Monnier, *J. Catal.*, 2022, **410**, 221–235.
13 K. R. Iyer and A. Bhan, *J. Catal.*, 2023, **420**, 99–109.
14 J. E. van den Reijen, S. Kanungo, T. A. J. Welling, M. Versluijs-Helder, T. A. Nijhuis, K. P. de Jong and P. E. de Jongh, *J. Catal.*, 2017, **356**, 65–74.
15 C. J. Keijzer, L. C. J. Smulders, D. Wezendonk, J. W. de Rijk and P. E. de Jongh, *Catal. Today.*, 2024, **428**, 114447.
16 H. A. Alzahrani and J. J. Bravo-Suárez, *J. Catal.*, 2023, **418**, 225–236.
17 A. J. F. van Hoof, I. A. W. Filot, H. Friedrich and E. J. M. Hensen, *ACS Catal.*, 2018, **8**, 11794–11800.
18 C. J. Keijzer, L. C. J. Smulders, D. Wezendonk, J. W. de Rijk and P. E. de Jongh, *Catal. Today.*, 2024, **428**, 114447.
19 S. N. Goncharova, B. S. Bal'zhinimaev, S. V. Tsybulya, V. I. Zaikovskii and A. F. Danilyuk, in *Studies in Surface Science and Catalysis*, eds. G. Poncelet, J. Martens, B. Delmon, P. A. Jacobs and P. Grange, Elsevier, 1995, vol. 91, pp. 915–922.
20 J. Lu, J. J. Bravo-Suárez, A. Takahashi, M. Haruta and S. T. Oyama, *J. Catal.*, 2005, **232**, 85–95.
21 P. Mäki-Arvela and D. Yu. Murzin, *Appl. Catal. A Gen.*, 2013, **451**, 251–281.
22 J. W. Harris and A. Bhan, *J. Catal.*, 2018, **367**, 62–71.
23 M. O. Özbek and R. A. van Santen, *Catal Lett.*, 2013, **143**, 131–141.
24 R. M. Lambert, R. L. Cropley, A. Husain and M. S. Tikhov, *Chem. Commun.*, 2003, 1184–1185.
25 Kenneth. C. Waugh and M. Hague, in *Mechanisms in Homogeneous and Heterogeneous Epoxidation Catalysis*, Elsevier, Amsterdam, Netherlands, 2008, pp. 233–263.
26 V. I. Bukhtiyarov, M. Hävecker, V. V. Kaichev, A. Knop-Gericke, R. W. Mayer and R. Schlögl, *Phys. Rev. B.*, 2003, **67**, 235422.
27 P. A. Kilty and W. M. H. Sachtler, *Rev. Catal.*, 1974, **10**, 1–16.
28 R. B. Grant and R. M. Lambert, *J. Catal.*, 1985, **92**, 364–375.
29 S. Linic and M. A. Barteau, *J. Am. Chem. Soc.*, 2002, **124**, 310–317.
30 G. Rovida, F. Pratesi and E. Ferroni, *Appl. Surf. Sci.*, 1980, **5**, 121–132.
31 K. C. Waugh and M. Hague, *Catal. Today.*, 2010, **157**, 44–48.
32 M. O. Ozbek, I. Onal and R. A. V. Santen, *J. Phys.: Condens. Matter.*, 2011, **23**, 404202.

33 M. O. Ozbek, I. Onal and R. A. van Santen, *Top Catal.*, 2012, **55**, 710–717.
34 M. O. Ozbek, I. Onal and R. A. van Santen, *J. Catal.*, 2011, **284**, 230–235.
35 M. O. Özbek, I. Önal and R. A. van Santen, *ChemCatChem.*, 2011, **3**, 150–153.
36 van Santen R. A. and H. P. C. E. Kuipers, *Adv. Catal.*, 1987, **35**, 265–321.
37 V. I. Bukhtiyarov, A. I. Nizovskii, H. Bluhm, M. Hävecker, E. Kleimenov, A. Knop-Gericke and R. Schlögl, *J. Catal.*, 2006, **238**, 260–269.
38 J. Yu, J. Li, C.-Y. Xu, Q. Li, Q. Liu, J. Liu, R. Chen, J. Zhu and J. Wang, *Nano Energy.*, 2022, **98**, 107266.
39 Y. Xu, J. Greeley and M. Mavrikakis, *J. Am. Chem. Soc.*, 2005, **127**, 12823–12827.
40 Z. Tang, T. Chen, K. Liu, H. Du and S. G. Podkolzin, *Langmuir.*, 2021, **37**, 11603–11610.
41 T. Pu, A. Setiawan, A. C. Foucher, M. Guo, J.-M. Jehng, M. Zhu, M. E. Ford, E. A. Stach, S. Rangarajan and I. E. Wachs, *ACS Catal.*, 2024, **14**, 406–417.
42 T. Pu, A. Setiawan, B. Mosevitzky Lis, M. Zhu, M. E. Ford, S. Rangarajan and I. E. Wachs, *ACS Catal.*, 2022, **12**, 4375–4381.
43 C. Liu, D. P. Wijewardena, A. Sviripa, A. Sampath, D. W. Flaherty and C. Paolucci, *J. Catal.*, 2022, **405**, 445–461.
44 P. Drogui and R. Daghrir, in *CO2 Sequestration, Biofuels and Depollution*, eds. E. Lichtfouse, J. Schwarzbauer and D. Robert, Springer International Publishing, Cham, 2015, pp. 1–32.
45 T. J. Korstanje and R. J. M. K. Gebbink, in *Organometallics and Renewables*, eds. M. A. R. Meier, B. M. Weckhuysen and P. C. A. Bruijnincx, Springer, Berlin, Heidelberg, 2012, pp. 129–174.
46 T. C. R. Rocha, M. Hävecker, A. Knop-Gericke and R. Schlögl, *J. Catal.*, 2014, **312**, 12–16.
47 D. Sneed, M. Pravica, E. Kim, N. Chen, C. Park and M. White, *J. Phys.: Conf. Ser.*, 2017, **950**, 042055.
48 H. G. Limberger and T. P. Martin, in *Small Particles and Inorganic Clusters*, eds. C. Chapon, M. F. Gillet and C. R. Henry, Springer, Berlin, Heidelberg, 1989, pp. 439–442.
49 Atomic and physical properties of Periodic Table Group 1, https://www.chemguide.co.uk/inorganic/group1/properties.html, (accessed 16 October 2024).
50 S. A. Tan, R. B. Grant and R. M. Lambert, *J. Catal.*, 1987, **106**, 54–64.
51 R. B. Grant and R. M. Lambert, *Langmuir.*, 1985, **1**, 29–33.
52 D. M. Minahan, G. B. Hoflund, W. S. Epling and D. W. Schoenfeld, *J. Catal.*, 1997, **168**, 393–399.
53 S. T. Oyama, *Mechanisms in Homogeneous and Heterogeneous Epoxidation Catalysis*, Elsevier, Amsterdam, 1st edn., 2008.
54 J. Couves, M. Atkins, M. Hague, B. H. Sakakini and K. C. Waugh, *Catal Lett.*, 2005, **99**, 45–53.
55 M. Atkins, J. Couves, M. Hague, B. H. Sakakini and K. C. Waugh, *J. Catal.*, 2005, **235**, 103–113.
56 S. N. Goncharova, E. A. Paukshtis and B. S. Bal'zhinimaev, *Appl. Catal. A: Gen.*, 1995, **126**, 67–84.
57 W. Diao, C. D. DiGiulio, M. T. Schaal, S. Ma and J. R. Monnier, *J. Catal.*, 2015, **322**, 14–23.
58 D. Ren, H. Xu, J. Li, J. Li and D. Cheng, *Mol. Catal.*, 2017, **441**, 92–99.
59 A. Simon, *Coordination Chemistry Reviews*, 1997, **163**, 253–270.
60 Oxide - Phosphorus, Chemical, Compounds | Britannica, https://www.britannica.com/science/oxide/Oxides-of-phosphorus, (accessed 15 October 2024).
61 V. Calvino-Casilda, R. Martin-Aranda, I. Sobczak and M. Ziolek, *Appl. Catal. A Gen.*, 2006, **303**, 121–130.
62 L. Lisi and S. Cimino, *Catalysis.*, 2020, **10**, 1475.
63 R. J. Davis, *J. Catal.*, 2003, **216**, 396–405.

64 S. Linic and M. A. Barteau, *J. Am. Chem. Soc.*, 2004, **126**, 8086–8087.
65 M. C. N. A. Carvalho, C. A. Perez, R. A. Simão, F. B. Passos and M. Schmal, *An. Acad. Bras. Ciênc.*, 2004, **76**, 19–27.
66 E. A. Podgornov, I. P. Prosvirin and V. I. Bukhtiyarov, *J. Mol. Catal. A Chem.*, 2000, **158**, 337–343.
67 F. M. Harth, B. Likozar and M. Grilc, *Mater. Today Chem.*, 2022, **26**, 101191.
68 M. T. Greiner, T. C. R. Rocha, B. Johnson, A. Klyushin, A. Knop-Gericke and R. Schlögl, *Z. Phys. Chem.*, 2014, **228**, 521–541.
69 F. E. Kühn, A. Scherbaum and W. A. Herrmann, *J. Organomet. Chem.*, 2004, **689**, 4149–4164.
70 N. R. C. (US) C. S. Roundtable, in *The Role of the Chemical Sciences in Finding Alternatives to Critical Resources: A Workshop Summary*, National Academies Press (US), 2012.
71 A. Schwartz, L. L. Holbrook and H. Wise, *J. Catal.*, 1971, **21**, 199–207.
72 P. J. M. Dijkgraaf, M. J. M. Rijk, J. Meuldijk and K. van der Wiele, *J. Catal.*, 1988, **112**, 329–336.
73 D. Sun, L. Peng, K. Cheng, Y. Zheng and S. P. Jiang, *J. CO2 Util.*, 2023, **68**, 102382.
74 Y. Jun, D. Jingfa, Y. Xiaohong and Z. Shi, *Appl. Catal. A: Gen.*, 1992, **92**, 73–80.
75 J. C. Dellamorte, J. Lauterbach and M. A. Barteau, *Ind. Eng. Chem. Res.*, 2009, **48**, 5943–5953.
76 J. C. Dellamorte, J. Lauterbach and M. A. Barteau, *Catal. Today.*, 2007, **120**, 182–185.
77 F. D. Hardcastle, I. E. Wachs, J. A. Horsley and G. H. Via, *Mol. Catal.*, 1988, **46**, 15–36.
78 J. Okal, W. Tylus and L. Kępiński, *J. Catal.*, 2004, **225**, 498–509.
79 J. Okal, *Appl. Catal. A: Gen.*, 2005, **287**, 214–220.
80 D. Ren, G. Cheng, J. Li, J. Li, W. Dai, X. Sun and D. Cheng, *Catal. Letters.*, 2017, **147**, 2920–2928.
81 M. A. Salaev, A. A. Salaeva and O. V. Vodyankina, *Catal. Today.*, 2021, **375**, 585–590.
82 D. Jingfa, Y. Jun, Z. Shi and Y. Xiaohong, *J. Catal.*, 1992, **138**, 395–399.
83 J. Llorca, M. Domínguez, C. Ledesma, R. J. Chimentão, F. Medina, J. Sueiras, I. Angurell, M. Seco and O. Rossell, *J. Catal.*, 2008, **258**, 187–198.
84 W. N. Porter, Z. Lin and J. G. Chen, *Surf. Sci. Rep.*, 2021, **76**, 100524.
85 G. J. Hutchings, *ACS Cent. Sci.*, 2018, **4**, 1095–1101.
86 T. A. Nijhuis, T. Visser and B. M. Weckhuysen, *Angew. Chem. Int. Ed. Engl.*, 2005, **44**, 1115–1118.
87 Y. Dai, Z. Chen, Y. Guo, G. Lu, Y. Zhao, H. Wang and P. Hu, *Phys. Chem. Chem. Phys.*, 2017, **19**, 25129–25139.
88 H.-T. Chen, J.-G. Chang, S.-P. Ju and H.-L. Chen, *J. Phys. Chem. Lett.*, 2010, **1**, 739–742.
89 C.-C. Lee and H.-T. Chen, *J. Phys. Chem. A.*, 2015, **119**, 8547–8555.
90 J. Teržan, P. Djinović, J. Zavašnik, I. Arčon, G. Žerjav, M. Spreitzer and A. Pintar, *Appl. Catal. B-Environ.*, 2018, **237**, 214–227.
91 J. Teržan, M. Huš, B. Likozar and P. Djinović, *ACS Catal.*, 2020, **10**, 13415–13436.
92 M. T. Greiner, T. E. Jones, A. Klyushin, A. Knop-Gericke and R. Schlögl, *J. Am. Chem. Soc.*, 2017, **139**, 11825–11832.
93 M. T. Greiner, T. E. Jones, B. E. Johnson, T. C. R. Rocha, Z. J. Wang, M. Armbrüster, M. Willinger, A. Knop-Gericke and R. Schlögl, *Phys. Chem. Chem. Phys.*, 2015, **17**, 25073–25089.
94 A. K. Santra, J. J. Cowell and R. M. Lambert, *Catal Lett.*, 2000, **67**, 87–91.
95 M. Jayamurthy, P. Hayden and A. K. Bhattacharya, *J. Catal.*, 2014, **309**, 309–313.
96 J.-Y. Tseng and H.-T. Chen, *Theor Chem Acc.*, 2020, **139**, 57.
97 A. Fortunelli, D. Cheng, J. Zhu, Y. Xie, Y. Nan, L. Zhu and H. Xu, *Ind. Eng. Chem. Res.*, 2019, **58**, 12996–13006.
98 C. Stampfl and S. Piccinin, *J. Mater. Chem.*, 2010, **20**, 10521–10527.
99 N. L. Nguyen, S. de Gironcoli and S. Piccinin, *J. Chem. Phys.*, 2013, **138**, 184707.

100 N. L. Nguyen, S. Piccinin and S. de Gironcoli, *J. Phys. Chem. C.*, 2011, **115**, 10073–10079.
101 P. J. Van den Hoek, E. J. Baerends and R. A. Van Santen, *J. Phys. Chem.*, 1989, **93**, 6469–6475.
102 J. T. Jankowiak and M. A. Barteau, *J. Catal.*, 2005, **236**, 379–386.
103 S. Piccinin, S. Zafeiratos, C. Stampfl, T. W. Hansen, M. Hävecker, D. Teschner, V. I. Bukhtiyarov, F. Girgsdies, A. Knop-Gericke, R. Schlögl and M. Scheffler, *Phys. Rev. Lett.*, 2010, **104**, 035503.
104 F. F. Tao and M. Salmeron, *Science.*, 2011, **331**, 171–174.
105 G. A. Somorjai, *Langmuir.*, 1991, **7**, 3176–3182.
106 D. B. Williams and C. B. Carter, *Transmission Electron Microscopy*, Springer US, Boston, MA, 2009.
107 C. F. Holder and R. E. Schaak, *ACS Nano.*, 2019, **13**, 7359–7365.
108 Y. Waseda, E. Matsubara and K. Shinoda, *X-Ray Diffraction Crystallography: Introduction, Examples and Solved Problems*, Springer, Berlin, Heidelberg, 2011.
109 J. W. Olesik, *Anal. Chem.*, 1991, **63**, 12A-21A.
110 F. Berna, in *Encyclopedia of Geoarchaeology*, ed. A. S. Gilbert, Springer Netherlands, Dordrecht, 2017, pp. 285–286.
111 L. El Fels, M. Zamama and M. Hafidi, in *Biodegradation and Bioremediation of Polluted Systems - New Advances and Technologies*, InTech, London, UK, 2015.
112 A. Subramanian and L. Rodriguez-Saona, in *Infrared Spectroscopy for Food Quality Analysis and Control*, ed. D.-W. Sun, Academic Press, San Diego, 2009, pp. 145–178.
113 F. C. Meunier, *React. Chem. Eng.*, 2016, **1**, 134–141.
114 M. B. Mitchell, in *Structure-Property Relations in Polymers*, American Chemical Society, 1993, vol. 236, pp. 351–375.
115 I. E. Wachs, *Top. Catal.*, 1999, **8**, 57–63.
116 E. Smith and G. Dent, *Modern Raman Spectroscopy: A Practical Approach*, John Wiley & Sons, 2019.
117 D. R. Baer, K. Artyushkova, C. R. Brundle, J. E. Castle, M. H. Engelhard, K. J. Gaskell, J. T. Grant, R. T. Haasch, M. R. Linford, C. J. Powell, A. G. Shard, P. M. A. Sherwood and V. S. Smentkowski, *J. Vac. Sci. Technol. A: Vac. Surf. Films.*, 2019, **37**, 031401.
118 J. Yano and V. K. Yachandra, *Photosynth. Res.*, 2009, **102**, 241–254.
119 B. M. Weckhuysen, *Phys. Chem. Chem. Phys.*, 2003, **5**, 6.
120 X. Li, X. Yang, J. Zhang, Y. Huang and B. Liu, *ACS Catal.*, 2019, **9**, 2521–2531.
121 Y. Zhu, J. Wang, H. Chu, Y.-C. Chu and H. M. Chen, *ACS Energy Lett.*, 2020, **5**, 1281–1291.
122 Z. Xu, Z. Liang, W. Guo and R. Zou, *Coord. Chem. Rev.*, 2021, **436**, 213824.
123 L. Zhong, D. Chen and S. Zafeiratos, *Catal. Sci. Technol.*, 2019, **9**, 3851–3867.
124 P. Larkin, in *Infrared and Raman Spectroscopy*, ed. P. Larkin, Elsevier, Oxford, 2011, pp. 27–54.
125 D. J. Cumming, C. Tumilson, S. F. R. Taylor, S. Chansai, A. V. Call, J. Jacquemin, C. Hardacre and R. H. Elder, *Faraday. Discuss.*, 2015, **182**, 97–111.
126 A. Drochner, M. Fehlings, K. Krauß and H. Vogel, *Chem. Eng. Technol.*, 2000, **23**, 319–322.
127 F. C. Meunier, *Chem. Soc. Rev.*, 2010, **39**, 4602–4614.
128 F. C. Meunier, A. Goguet, S. Shekhtman, D. Rooney and H. Daly, *Appl. Catal. A: Gen.*, 2008, **340**, 196–202.
129 E. K. Dann, University College London, 2019.
130 R. L. White, in *Encyclopedia of Spectroscopy and Spectrometry*, ed. J. C. Lindon, Elsevier, Oxford, 1999, pp. 288–293.
131 K. L. MacIntosh, Durham University, 2022.

Chapter 2: Methodology and Experimental

The main aim of this thesis is to use *in situ* and *ex situ* techniques to improve the understanding of the role of oxygen, the promoters and the catalysts used in ethylene epoxidation. This has required catalyst preparation and reactor testing as well as the use of advanced characterisation techniques to understand the roles. The various techniques that have been employed to prepare and analyse the catalysts are discussed below.

2.1 Methodology

2.1.1 Powder X-ray Diffraction (pXRD)

Powder X-ray diffraction (pXRD) is a technique used to determine the atomic and molecular structure and phase of a crystalline material.[1] Electrons in an atom scatter X-rays, the strength with which an atom scatters the X-rays is proportional to the number of electrons around the atom.[1]

The atoms in a crystalline material are arranged in a periodic array and therefore can diffract light.[2] The scattering of X-rays from atoms produces diffraction patterns which contain information about the atomic arrangements within materials. X-rays enter the lattice at an angle of θ, here they are diffracted, as shown in *Figure 2.1*. When the waves that have been diffracted are in phase with each other, it produces constructive interference and when they are out of phase it produces destructive interference. The constructive interference increases the amplitude of the signal. When the electrons are diffracted with the angle of incidence of θ, to give constructive interferences this satisfies the Bragg Equation shown in *Equation 2.1*.[2]

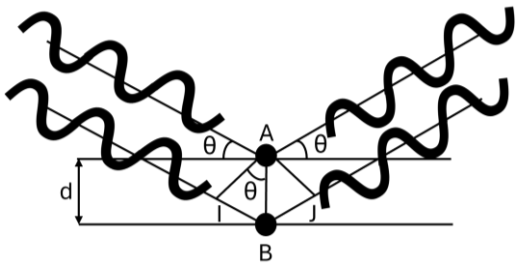

Figure 2.1: A diagram showing X-ray beams being scattered from successive planes in the crystal. Here the constructive interference results in an increase in the amplitude of the signal, modified from the Encyclopedia of Spectroscopy and Spectrometry (Second Edition).[3]

$$n\lambda = 2dsin\theta$$

Where n is an integer, λ is the wavelength of the electrons, d is the spacing of the crystal planes and θ is the angle of incidence.

Equation 2.1.[3]

Powder diffraction produces a distinctive diffraction pattern for each crystal structure, because the angle of diffraction is characteristic of the lattice plane separation, a set of diffraction reflections will be produced at different angles.[2] This produces a pattern which can then be used to identify the phase and structure of varied materials. Currently in this project, pXRD has been used to refer to database patterns for providing a "fingerprint" for comparison to known reference materials and also to estimate particle sizes with the Scherrer equation (*Equation 2.2*).[2] The crystallite sizes obtained using the Scherrer equation can only be considered as an estimate as the dimensionless shape factor is often assumed to be 0.9, however, this value varies with the shape of the crystallite. Smaller crystallites have a larger full width at half maximum value and therefore broader signals. The value of chosen 2θ is important as larger angles will result in increased broadening.[4]

$$\beta(2\theta) = \frac{K\lambda}{L\cos(\theta)}$$

Where $\beta(2\theta)$ = full width half maximum of the reflection at angle 2θ in radians, K = dimensionless shape factor, which is taken to be 0.9, λ = wavelength of radiation in nm, L = average crystallite size in nm and θ = angle of reflection in radians.

Equation 2.2.[4]

Whilst XRD is a powerful technique for giving important information, it does have some limitations. pXRD is not very effective for studying amorphous materials, where it is more accurate and reliable for crystalline materials.[5] It has been found that if the crystallites in the sample are too small, the diffraction patterns may be too weak or difficult to interpret. Samples which contain multiple phases or complex mixtures normally contain overlapping diffraction peaks, which can make it challenging to identify individual components.[6,7]

2.1.2 Inductively Coupled Plasma – Optical Emission Spectroscopy (ICP-OES)

Inductively coupled plasma–optical emission spectroscopy (ICP-OES) is commonly used as an analytical technique for the detection and quantification of chemical elements. It is used to determine elemental compositions and can be used on a variety of different elements. ICP-OES is a type of emission spectroscopy, which uses inductively coupled plasma to transfer energy to a sample which causes the atomisation, ionisation and electronic excitation of atoms within a sample. Inductively coupled plasma (ICP) is a type

of plasma source where the energy is supplied by electric currents, where the electron currents are caused by electromagnetic induction.[8]

A plasma is formed from argon, where it is ionised so that it is overall neutral and has an equal number of positively and negatively charged particles. Argon is used as it has a high ionisation energy, and chemical inertness, produces a simple emission spectrum and also does not usually form any compounds with the elements being analysed. Argon gas is passed through a plasma torch with electrons, the electrons are then accelerated and collide with the argon atom releasing more electrons to form argon ions. The sample being analysed is then added and atoms of elements in the sample become excited, when they return from the excited states to the lower energy states electromagnetic radiation is emitted. The photons that have been emitted are separated and the radiation is emitted by wavelength with the characteristic energies of their respective elements they appear as spectral lines. When looking at the spectra, the concentration of the elements in the samples is shown by the intensity of the lines.[8]

The sample preparation of ICP-OES needs to be in the solution state so that the content of the solid supported catalyst can be analysed, the metals need to be removed from the support through a process commonly referred to as digestion. The digestion method is typically by heating the sample in a concentrated acid and filtering out any solids forming a solvated sample suitable for analysis by ICP-OES.[9]

Whilst ICP-OES gives very accurate elemental analysis it does have some limitations. ICP-OES can have spectral overlaps, where the emission lines from the different elements interfere with each other making the analysis more complicated.[10] The samples are atomized and destroyed during the analysis; therefore they cannot be recovered post analysis. Finally, the presence of other substances in the sample can affect the accuracy of the measurements, therefore leading to signal suppression or enhancement.[10]

2.1.3 Diffuse Reflectance Infrared Fourier Transform Spectroscopy (DRIFTS)

Diffuse Reflectance Infrared Fourier Transform Spectroscopy (DRIFTS) is a type of infrared (IR) spectroscopy which is used to identify vibrational modes in solids or of adsorbates on solid materials, from which it may be possible to deduce their chemical structure or binding modes. It is a technique that is often used for studying surface species.[11] When the IR beam reaches the sample, it can either be reflected or transmitted. The IR energy that is reflected is typically lost, however, the IR beam that is transmitted can either reflect off the next particle or can be transmitted through the next particle. The IR radiation interacts with the

particles and reflects off their surfaces, causing the light to diffuse or scatter as it moves through the sample. This transmission-reflection event can occur many times which increases the path length. This scattered IR energy is then collected by the mirror which then focuses it onto the IR detector, via a Michelson interferometer. The detected IR light is therefore partially absorbed by particles of the sample, encoding sample information. The IR light on the sample is reflected and transmitted at different amounts depending on the absorbance of the material.[12] DRIFTS studies the surfaces of powders, commonly heterogeneous catalysts, in which case it may be used "*in situ*" by controlling the temperature and the environment in a "DRIFTS cell".[12] In DRIFTS, the IR energy is directed into a sample cup which is filled with the sample. Sometimes an IR transparent matrix is added, a common example is KBr. Commonly, a background is collected and subtracted from the sample to remove atmospheric content (CO_2 and H_2O), so that only the sample is being viewed and analysed.[12] *Figure 2.2* shows a typical DRIFTS set up.

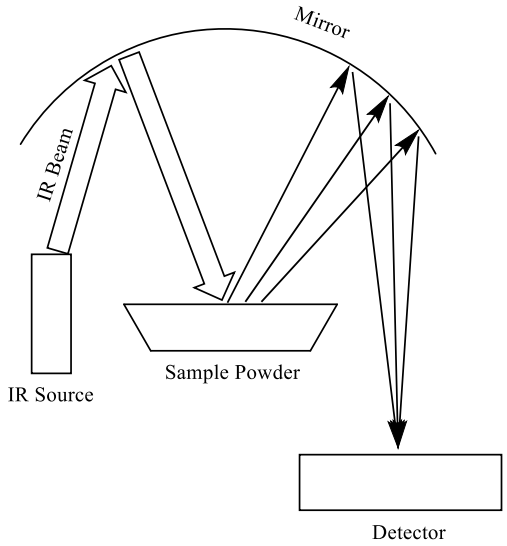

Figure 2.2: A DRIFTS set up, here the IR beam is focused onto the powdered samples and then the scattered light is collected by a mirror and then relayed onto a detector. This is modified from Manzoli.[13]

Quantitative analysis of DRIFTS is complicated, as there is a non-linear relationship between band intensity and the concentration of the associated species in the sample.[12] The most commonly used expression in the Kubelka-Munk equation (*Equation 2.3*), which is a simplified model based on the limiting case of an infinitely thick sample.

$$\frac{k}{s} = \frac{(1 - R_\infty)^2}{2R_\infty}$$

Equation 2.3: Kubelka-Munk equation where R_∞ is the absolute reflectance of an infinitely thick sample, k is the absorption coefficient and s is the scattering coefficient.[14]

The Kubelka-Munk transform of the measured spectroscopic observable is approximately proportional to the absorption coefficient and therefore is approximately proportional to the concentration. This allows for semi-quantitative analysis of DRIFTS data. However, for the analysis of surface adsorbates (except for highly absorbing adsorbates), experiments suggest absorbance to provide a more quantitative measure of concentration.[14] Therefore, Pseudo-transmission rather than Kubelka-Munk has been used in this thesis.

Whilst DRIFTS is a very useful technique giving a large amount of information, it does have some limitations. These include, having to finely ground the sample to ensure uniformity and to minimise the scattering effects, being able to achieve accurate quantitative results can be challenging due to the complex relationship between reflectance and concentration.[12] DRIFTS primarily probes the surface of the sample which can be a limitation if the bulk properties are of interest and there can be spectral interferences if the sample contains multiple components with overlapping adsorption bands. Water can absorb strongly in certain regions of the infrared spectrum, which can interfere with spectroscopic measurements.[15]

2.1.4 Brunauer-Emmett-Teller (BET) Theory

BET theory is used to measure the surface area of materials, giving the specific surface area and porosity distribution of solid materials. The specific surface area is determined by the physisorption of an inert gas, commonly nitrogen. The main steps of the process for BET measurements are as described:

1. Degas – Before the determination of an adsorption isotherm over the BET region, the sample must be degassed.
2. Evacuate – The BET sample tubes are evacuated.
3. Volume – The dead volume is measured with an inert gas. This result is used to correct the quantity of adsorbate adsorbed.
4. Evacuate – The dead-volume gas is then removed.
5. Adsorption – The gas is admitted into the tubes in doses or as a slow continuous flow. After each dose of nitrogen gas, the relative pressure (P/P_0) is allowed to equilibrate, and the amount of nitrogen adsorbed is determined. This step gives the adsorption isotherm over a selected range of P/P_0.

BET theory extends the Langmuir theory, which explains monolayer molecular adsorption to multilayer adsorption through several mathematical assumptions. These assumptions include, gas molecules physically adsorb on a solid in layers infinitely, there is no interaction

between each adsorption layer and the Langmuir theory can be applied to each layer. BET theory allows for a materials specific surface area to be calculated by using a linear range of P/P_0 values and their respective gas adsorption quantities.[16]

Whilst the BET method is widely used for surface area analysis of materials, it does have some limitations. These include, assuming that gas molecules form a monolayer on the surface before multilayer adsorption begins, which is not always the case. BET is also less effective for materials with very small or very large pores, leading to inaccurate results.[17]

2.1.5 Transmission Electron Microscopy (TEM)

TEM is an electron microscopy technique that uses the interaction of an electron beam with a sample to form an image of the sample.[18] TEM instruments can be used to provide morphologic, but also compositional and crystallographic information on different samples. A beam of electrons is transmitted through a sample to form an image of the transmitted electrons. TEM operates on the same principle as a light microscope but uses electrons instead of light. As the wavelength of electrons is much smaller than the wavelength of light the resolution of the TEM images have a much higher order of magnitude compared to light microscopy, therefore TEM can identify many finer details and allows nanometre sized objects to be imaged.[18]

The role of components in a typical TEM can be summarised as follows.[18] An electron gun generates a beam of electrons, which go through a condenser lens to focus into a small, thin coherent beam. The beam then hits the material, and some electrons are transmitted depending upon the thickness and electron transparency of the material. When the sample is exposed to the electron beam, the electrons collide with the electrons in the sample causing elastic or inelastic scattering. During bright field transmission electron microscopy, (the mode analogous to standard optical microscopy), the electrons that have been scattered do not contribute to the image and the ones that did not interact with the sample are the ones that are detected. When looking at the image there are darker and lighter parts of it, the darker areas are the parts of the samples that few electrons are transmitted through, whilst the lighter areas of the image are those where more electrons are transmitted through the sample. The image is formed by the transmitted electrons being focused by an objective lens into an image on a charge coupled device (CCD) camera or a phosphor screen. The electron microscope relies on magnetic fields to focus the electron beam rather than conventional lenses used in light microscopy, which must be carefully aligned and stable to form images for long enough to be recorded by the CCD camera.

Typically, the sample thickness is less than 100 nm as TEM measures transmitted electrons and the mean free path of electrons is small.[18]

Whilst TEM is a powerful imaging technique it does have several disadvantages. TEM machines are large and expensive instruments where the preparation of samples is labour intensive and can introduce artifacts. Here, they can only analyse samples that are under and can withstand the vacuum environment, which means they're unable to be under reaction conditions.[19]

2.1.6 Scanning Transmission Electron Microscopy (STEM)

STEM is remarkably similar to TEM. As with TEM, the images are produced by electrons passing through a thin specimen, however with STEM, the electron beam is focused to a focal point which is then scanned over the sample in a raster, the signal is collected as a function of the beam location.[20] As the electron beam is focussed on a spot on the sample surface EDX (energy-dispersive X-ray spectroscopy) can be used to find the elemental composition of the sample. Elemental maps of specific areas of the sample can be generated where locations of specific elements can be found.[21] When a vacancy is created in the electron orbital of the inner shell of an atom by an incident electron, electrons with a higher electron level are transferred from the outer shell to stabilise it. The X-rays emitted in this process have a specific energy value for each element. From the energy of the characteristic X-ray obtained, the presence of the element in the sample can be identified. The intensity of the X-rays can also be used to measure the content of each element and analyse the dispersion within the field of view.[22]

The disadvantages of STEM are very similar to TEM, where the instrument is highly complex and expensive where operating the STEM requires training and expertise. STEM requires very thin samples and needs to operate under a high vacuum conditions.[23]

2.1.7 Raman Spectroscopy

Raman spectroscopy is a technique that uses the interaction of light with the vibrational modes of chemical bonds in a material to measure vibrational energies and intensities and determine from this information, chemical structure, phase, crystallinity and molecular interactions.[24]

Raman scattering is based off the Raman Effect. The Raman scattering or the Raman Effect occurs when the light interacts with molecular vibrations, relying on the inelastic scattering

of photons.[25] A source of monochromatic light which is usually from a laser interacts with molecular vibrations and results in the laser photons being shifted up or down in energy. The energy changes that occur during Raman spectroscopy give the frequency of the vibrational modes in the system. When a photon interacts with a sample it causes an excitation to a short-lived virtual state, relaxation then occurs which releases energy in the form of a photon which is shown in a Raman spectrum.[26]

As shown in *Figure 2.3*, some incident photons collide with the sample and give up some of their energy to the sample and decrease in frequency to give Stokes radiation.[25] Other incident photons collide with the sample and gain energy from the sample causing an increase in frequency therefore giving a higher frequency anti-Stokes radiation. Scattering without changing the frequency results in Rayleigh radiation. Raman spectroscopy can be regarded as the excitation of a sample to a wide range of different virtual states, and then the subsequent return to a lower state, of either a lower, higher or the same energy; the net energy change is then carried away by the photon, as shown in *Figure 2.3*.[25] Anti-Stokes Raman light is less intense than the Stokes as Anti-Stokes relies on the initial population of excited states, only samples that are vibrational excited prior to irradiation can give rise to the anti-Stokes line.[27] Therefore Stokes radiation is more commonly used in Raman spectroscopy (especially vibrational spectroscopy). Raman scattering is a linear spectroscopic technique, therefore the Raman signal is proportional to the intensity of the pump laser and therefore to the electric field squared, the intensity of a spectrum is also directly proportional to concentration.[28]

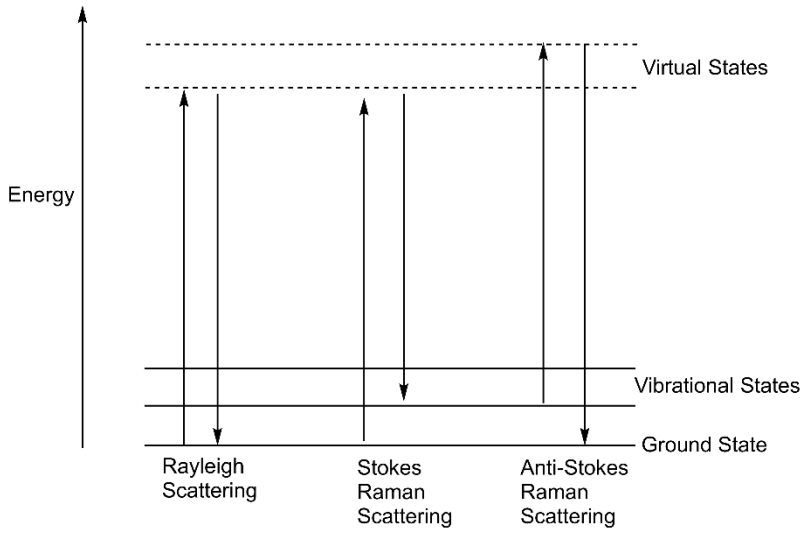

Figure 2.3: A diagram showing the changes in frequencies with Rayleigh, Stokes Raman and Anti-Stokes Raman scattering, reproduced and modified from Matousek et al.[28]

A Raman spectrum shows the intensity, and the wavelength position of the Raman scattered light. Each peak corresponds to a specific molecular bond vibration. Different substances typically have a characteristic Raman 'fingerprints'.[24]

Raman spectroscopy has selection rules for a Raman transition, the main overall selection rule is that the molecular polarisability must change during the molecular vibration. For non-linear molecules with N atoms, the number of vibrational modes is given by 3N-6. Where the 3N is the total degrees of freedom for the molecule, and the 6 is 3 translational and 3 rotational degrees of freedom. For linear molecules, there is one less rotational degree of freedom, and the number of vibrational modes is 3N-5. This selection rule complements the dipole moment rule for infrared. Where vibrations are only active if the molecular dipole moment changes during the vibration.[29] Not all vibrational modes can be detected using Raman Spectroscopy. Raman spectroscopy is often said to be complementary to IR spectroscopy. With symmetrical molecules with a centre of inversion, bonds that are IR-active will not be Raman-active and bonds that are Raman-active will not be IR-active. Other molecules may have bonds that are Raman-active, IR-active, neither or both.[29] The situation for molecular adsorbates and solids dealt with in this project is often more complicated due to the breaking of symmetry at a surface.

Whilst Raman spectroscopy is a valuable analytical technique it does have some limitations. The Raman effect is weak; therefore, it is difficult to detect low concentrations of a substance without highly sensitive and optimised equipment. Fluorescence from impurities or the sample itself can overwhelm the Raman signal, therefore making it challenging to obtain a clear spectra.[30] The intense laser radiation which is used in Raman spectroscopy, can cause heating of the sample, which is likely to damage or alter the Raman spectrum.[31] Lastly, Raman spectroscopy is generally not effective for analysing metals and alloys because they do not produce a significant Raman signal.[32]

2.1.8 Solid State Nuclear Magnetic Resonance Spectroscopy (ss NMR)

NMR is an analytical technique that can give information on the structure and composition of a sample. The principle behind NMR is that many nuclei have spin, and all nuclei are electrically charged. NMR involves placing a sample where the nuclei have a non-zero spin in an external magnetic field B_0, here two spin states exist.[33,34] The magnetic moment of the lower energy state is aligned with the external field, whilst the one with the higher energy is opposed to the external field. The two spin states have the same energy when the external field is zero but diverges as the field increases. This leads to a net magnetisation along the same axis and in the same direction as the magnetic field. By applying a pulse of radio

frequency, the net magnetisation can be moved into the xy plane, and relaxation back to the z-axis is monitored as a free induction decay (FID). Fourier transform of this produces an NMR spectrum. In solution NMR, rapid random tumbling causes the averaging of anisotropic NMR interactions, therefore the spectra show a series of very sharp transitions. However, with solid-state NMR, the orientation-dependent interactions are observed in the spectrum, therefore giving very broad peaks.[33,34]

Due to the orientation of molecules in solids being mostly fixed, there are some challenges and limitations that occur with solid-state NMR. Common issues include quadrupolar interactions causing peak splitting due to the different distribution of charge around the nucleus, magnetic dipole moments of nuclei causing small localised magnetic fields and chemical shift anisotropy, which occurs by the electron distribution being anisotropic, therefore meaning the electron density and shielding of a nucleus is not equal in all orientations. These issues can lead to peak broadening of the spectrum or the spectrum having orientational dependence.[33,34]

Two important techniques used in ss NMR that can help solve some of the problems caused by fixed orientations. Firstly, a technique used to help with reducing the chemical shift anisotropy is magic angle spinning (MAS), which allows for an average reading across the sample with minimised quadrupolar interactions therefore meaning there is no orientational dependence. Magic angle spinning is where the sample is rapidly spinning at the magic angle B_0. Here the sample and rotor are spun at 54.736 ° with respect to B_0. This therefore means that the quadrupolar interactions due to the non-spherical distribution of charge around a nucleus get reduced.[33,34] Secondly, cross polarisation can give shorter relaxation times and an increased signal intensity. Cross polarisation is a technique where magnetisation is transferred from an abundant nuclei to a dilute nuclei with the same spin. The relaxation times for dilute spins are normally very long, which leads to longer experiment times to gain a good signal to noise ratio. However, with cross-polarisation, the relaxation time is dependent on the abundant nuclei, this is normally shorter and therefore can reduce the experimental time and still gain a good signal-to-noise ratio.[33,34]

2.1.9 X-ray Photoelectron Spectroscopy (XPS)

X-ray photoelectron spectroscopy (XPS) is a technique that can be used for analysing the surface chemistry of a material. It can measure the elemental composition, empirical formula, chemical state and the electronic state of the elements. It reveals which chemical elements are present at the surface and the nature of the chemical bond that exists between these elements.[35] It is a surface characterisation technique that can analyse a sample to a depth of 2 to 5 nm.[36] XPS works by incoming electromagnetic radiation (X-rays) being absorbed by an atom or molecule and an electron being ejected. The kinetic energy of the electron depends on the photon energy and the binding energy of the electron, which is the energy required to remove the electron from the surface.[36] XPS is based upon the photoelectric effect which is shown in *Figure 2.4*.

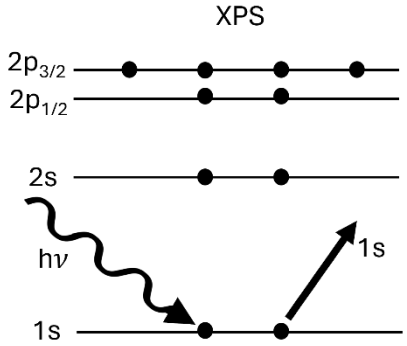

Figure 2.4: The Photoelectric Effect, an example of an oxygen atom modified from Donley et al.[36]

Measuring the kinetic energy of the emitted photons means it is possible to determine which elements are near the material's surface, their chemical states and the binding energy of the electron, using *Equation 2.4*.

$$E_{\mathrm{k}}=h\nu-(E_{\mathrm{B}}-\phi)$$

Where E_K is the kinetic energy, $h\nu$ is the energy of the incident photons where h is Plank's constant and ν is the frequency, E_B is the binding energy and ϕ is the work function (where the work function is defined as the minimum energy required to release a photoelectron from the surface of a material).[37]

Equation 2.4.[38]

The binding energy depends on the element from which the electron is emitted, the orbital from which the electron is ejected and the chemical environment of the atoms from which the electron was emitted. These differ for different elements and therefore the technique is very element specific.[39] To be able to measure the kinetic energy, it is important that the system is under ultra-high vacuum (UHV) so that none of the gas molecules can interact with the electrons, causing attenuations. However, UHV can cause problems, especially for catalysis and therefore instruments have been developed for near-ambient pressure XPS (NAP-XPS), where small amounts of gas can be present. This occurs by placing a small

aperture very close to the sample, the pressure is then reduced before the photoelectrons reach the detector.[40]

In general, there are 2 common backgrounding techniques employed when looking at XPS data. Firstly, is the Shirley background. Here, the background intensity at any binding energy is proportional to the intensity of the total peak area above the background in the lower binding energy peak range. The second is the Tougaard background. Here, the intensity of the background is integrated at a given binding energy from the spectral intensities to higher kinetic energies. Whilst the Tougaard background is the most accurate, it gets quite difficult if multiple peaks overlap, therefore commonly the Shirley background is used.[41]

The cross sections of the elements being studied can be determined based on the work done by Yeh and Lindau, where the cross sections are calculated for a large number of elements at a variety of different energies.[42] The inelastic mean free path (IMFP) can be roughly estimated for most materials using a universal curve, as described by the equations detailed in a paper by Seah and Dench.[43] Lastly, the extent of signal attenuation which is from the presence of gas molecules in near-ambient pressure experiments is based on the instrument used to carry out the experiments and so cannot be calculated. Held *et al*. details relevant data for the instrument used at B07 is investigated where correction factors for the signal attenuation due to the presence of gases for the NAP-XPS experiments can be estimated.[40]

Whilst XPS is a powerful surface analysis technique is has several limitations. These include, poor spatial resolution which limits its ability to analyse very small features, not being able to detect hydrogen and helium, the sample being under ultra-high vacuum conditions and that it is highly surface specific where it analyses only the top few nanometres of a sample.[44]

2.1.10 X-ray Absorption Spectroscopy (XAS)

XAS is an analysis technique which gives valuable information on the oxidation state, geometry and nature of neighbouring atoms about an element of interest.[45] By providing the sample with an incident X-ray with a photon energy that is tuned around the distinct elemental electron binding energy, the energy of the incoming photon can be close to the ionisation energy of the elements inner shell electrons. The basis of XAS is due to the photon being absorbed through the photo-electric effect, which results in energy absorption to the core electron, the electron can undergo a transition to an empty orbital or be ejected

from the atom. This results in an abrupt energy rise (absorption edge, E_0). Commonly, XAS is performed using synchrotron radiation, due to the need of an intense and energy-tunable source of X-rays, although XAS studies have been shown to be possible using laboratory-based radiation sources.[45,46]

In transmission XAS, the absorption of X-rays is directly measured by analysing what passes through the sample, following Beer-Lamberts law. Whilst in fluorescence XAS the re-filling of deep core holes is detected. When the X-rays are absorbed by the sample, they create core holes, and as these holes are filled by electrons from higher energy levels, characteristic X-ray fluorescence is emitted. Fluorescence XAS is used when the samples have a low loading (< 1 wt. %) of the element of interest, therefore the transmission intensity may not be high enough to obtain useable data, if the sample is too thick to observe any changes in the transmission spectra or if the total adsorption of the material is too high leading to self-adsorption effects.[47]

The x-ray absorption spectrum is normally divided into two parts, the x-ray absorption near-edge spectroscopy (XANES) and the extended x-ray absorption fine-structure spectroscopy (EXAFS), as shown in *Figure 2.5* and *Figure 2.6*.[48]

XANES typically covers the energy range where the potential is approximately 10 eV below the adsorption edge and 50 eV above the adsorption edge, here the photoelectron path is dominated by multiple scattering and transitions into unoccupied orbitals. XANES is strongly sensitive to oxidation states and coordination chemistry of the absorbing atom, it is the pre-edge adsorption as well as the edge itself. The pre-edge features arise from transitions into unoccupied orbitals, whilst the E_0 position can be used to identify the oxidation states of the element.[49]

EXAFS corresponds to the potential between 50 eV and 1000 eV above the edge, here the contribution is mainly by single scattering paths. EXAFS is normally used to determine the distances, the coordination number and the species of the neighbours of the absorbing atom. The extended edge describes the oscillating region of the EXAFS spectrum that is at higher energies than the edge. If the electron has enough energy to leave the atom it will proceed to scatter off neighbouring atoms. The increase and decrease in absorption found in EXAFS correspond to constructive and destructive interference of the outgoing photoelectron waves with the back-scattered photoelectron waves produced respectively.[45]

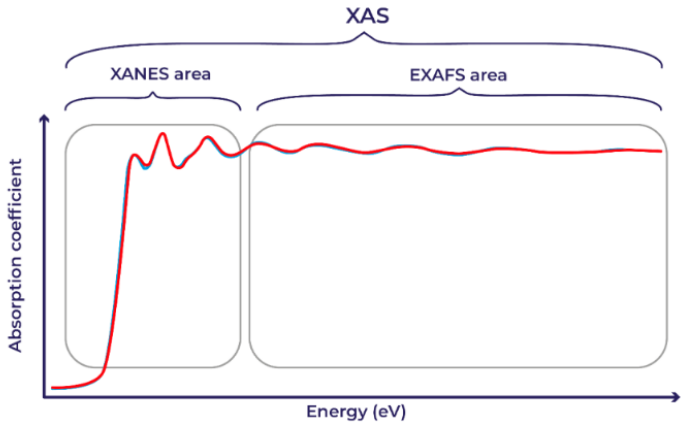

Figure 2.5: A diagram reproduced showing an XAS spectrum, which shows where the XANES and EXAFS reproduced from Butakova et al.[48]

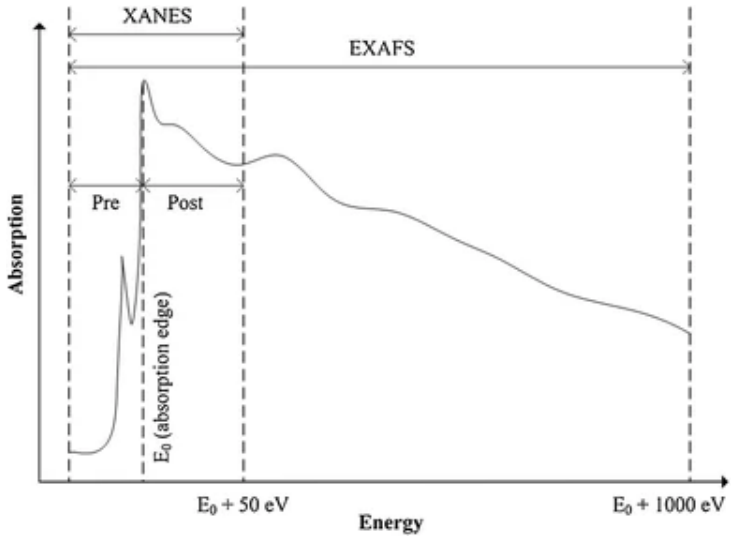

Figure 2.6: A diagram showing the pre, post and E_0 adsorption edge for XANES reproduced from Monteiro et al.[50]

For the EXAFS area, data fitting can be performed where the coordination number and the distances of neighbouring atoms can be determined.

Whilst XAS is a versatile technique it does have some limitations. These include, sometimes there is a poor signal to noise ratio due to low catalyst concentration and background absorption, alongside deconvoluting data from samples with mixed structures of the absorber element can be challenging.[51,52]

2.1.11 Temperature Programmed Desorption (TPD) / Reduction (TPR)

Temperature programmed desorption is used to determine the interactions between a surface and adsorbed species. TPD's can be used to give information to gain an improved understanding of catalytic reactions including surface reactions and desorption. Commonly, for TPD's the sample is dosed with the gas being used to probe and then inert gas is used

to remove the free gas, the sample is then increased in temperature at a linear ramp rate and the desorption products are analysed.[53]

In contrast, for TPR's the sample is placed in a stream of flowing H_2 and then the sample is increased in temperature at a linear ramp rate and the hydrogen is measured. Here TPR can be used as a characterisation technique to investigate the metal or metal oxide. Commonly for TPR a detector such as a thermal conductivity detector (TCD) is used to indicate when the H_2 consumption occurs during the heating process, therefore the reduction temperature is able to be found. Calibration is able to occur of the detector which allows the consumption of the reducing gas to be quantified, which when related to the number of moles of metal present in the sample can provide additional information about the reduction process or processes that are occurring.[54]

Whilst temperature programmed desorption and temperature programmed reduction are valuable techniques in surface science and catalysis, but they do have some limitations. The main limitation from these techniques is overlapping peaks, making it challenging to identify and quantify different processes.[55]

2.2 Experimental

2.2.1 Materials

Ultra-high purity (UHP) water was obtained from a Elga Veolia PURELAB® Chorus 1 in the Chemistry Department, Durham University and had a resistivity ≥18.2 MΩ. Oxygen, hydrogen, nitrogen, ethylene and argon gases were obtained from BOC and had a minimum purity of 99.99%. Caesium hydroxide hydrate (90% - 99.5%), α-aluminium oxide, (99.9%) γ-aluminium oxide (99.9%), ethylenediamine (99%), silver nitrate (99%), and oxalic acid (99%) were purchased from Sigma Aldrich. Ammonium perrhenate (99%), tetrachloroauric(III) acid trihydrate (49%), acetaldehyde (99.5%), nickel (II) nitrate hexahydrate (98%) and copper(II) nitrate trihydrate (99%) were purchased from Fisher Scientific. The silica support was obtained from commercial sources, Cab-O-Sil M5 silica (CABOT).

2.2.2 Catalysts Preparation

2.2.2.1 Synthesis of Ag/α-Al_2O_3 and Ag/γ-Al_2O_3

To prepare either Ag/α-Al_2O_3 or Ag/γ-Al_2O_3, a sample of α- or γ-alumina (~2 g, 19.6 mmol) was calcined overnight at 550 °C. α-Alumina was used as purchased whilst the γ-alumina was crushed using a pestle and mortar and then put through a sieve of 180 microns where

the smaller fraction was collected to use. Silver oxalate was then synthesised by dissolving silver nitrate (5 g, 29.4 mmol) and oxalic acid (50 g, 555.4 mmol) into 100 mL of deionised water. The sample was held at room temperature and stirred for 10 min. A suspension formed and it was then filtered and washed with deionised water three times. The sample was then dried under vacuum overnight, here silver oxalate was formed. Ethylenediamine (130 µL, 1.9 mmol) was added to 5 mL of deionised water. Next silver oxalate (0.58 g, 1.91 mmol) was also added to 5 mL of deionised water. The ethylenediamine solution was then added dropwise to the silver oxalate solution. The α-/γ-alumina support (1.84 g, 18.1 mmol) was impregnated with the silver oxalate/ethylenediamine solution. The catalyst precursor was then dried at room temperature with a rotary evaporator with no heating and a cooling trap in place to condense the water. The catalyst precursor was then calcined at 225 °C with a heating rate of 10 °C/min, for 4 h in a quartz tubular flow reactor. Here the catalyst precursor was added to a quartz tube, supported with quartz wool, placed inside a tube furnace and connected to gas lines *via* Ultra-torr type fittings. Gas flows were set to 5 mL min^{-1} of O_2 and 45 mL min^{-1} of N_2. Heating was measured by a thermocouple and temperature controller, shown in *Figure 2.7*.

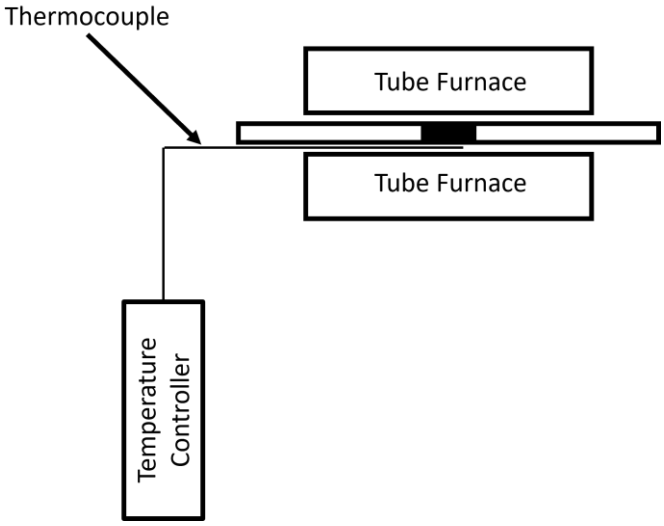

Figure 2.7: Heating Setup – showing how a thermocouple and a temperature controller measured the heating of the catalyst.

2.2.2.2 Synthesis of Cs promoted Ag/α-Al_2O_3 and Ag/γ-Al_2O_3

To prepare both Cs promoted Ag/α-Al_2O_3 and Ag/γ-Al_2O_3, the catalysts were prepared as in **Section 2.2.2.1**, but with the addition of caesium hydroxide hydrate. Caesium hydroxide hydrate (0.023 g, 0.15 mmol) was added with the silver oxalate (0.58 g, 1.91 mmol) to the 5 mL of deionised water.

2.2.2.3 Synthesis of Re promoted Ag/α-Al_2O_3 and Ag/γ-Al_2O_3

To prepare both Re promoted Ag/α-Al_2O_3 and Ag/γ-Al_2O_3, the catalysts were prepared as in **Section 2.2.2.1**, but with the addition of ammonium perrhenate. Ammonium perrhenate (0.027 g, 0.10 mmol) was added with the silver oxalate (0.58 g, 1.91 mmol) to the 5 mL of deionised water.

2.2.2.4 Synthesis of Cs-Re promoted Ag/α-Al_2O_3 and Ag/γ-Al_2O_3

To prepare both Cs-Re promoted Ag/α-Al_2O_3 and Ag/γ-Al_2O_3, the catalysts were prepared as in **Section 2.2.2.1**, but with the addition of caesium hydroxide hydrate and ammonium perrhenate. Ammonium perrhenate (0.027 g, 0.10 mmol) and caesium hydroxide hydrate (0.023 g, 0.15 mmol) was added with the silver oxalate (0.58 g, 1.91 mmol) to the 5 mL of deionised water.

2.2.2.5 Synthesis of Cu/α-Al_2O_3

The catalyst was prepared by the wet impregnation method. Copper(II) nitrate trihydrate (0.155 g, 0.64 mmol) was dissolved in 10 mL of deionised water. The α-alumina support (2 g, 19.6 mmol) was impregnated with this solution and then vigorously stirred for 2 h. The catalyst precursor was then dried at 80 °C with a heating rate of 10 °C/min, for 16 h in a static furnace. The catalyst precursor was then calcined in a static furnace at 450 °C with a heating rate of 10 °C/min, for 4 h.

2.2.2.6 Synthesis of Au/α-Al_2O_3

The catalyst was prepared by the wet impregnation method. Tetrachloroauric(III) acid trihydrate (0.11 g, 0.28 mmol) was dissolved in 10 mL of deionised water. The α-alumina support (2 g, 19.6 mmol) was impregnated with this solution and then vigorously stirred for 2 h. The catalyst precursor was then dried at 80 °C with a heating rate of 10 °C/min, for 16 h in a static furnace. The catalyst precursor was then calcined in a static furnace at 450 °C with a heating rate of 10 °C/min, for 4 h.

2.2.2.7 Synthesis of Cu-Au/α-Al_2O_3

The catalyst was prepared by the wet impregnation method. Tetrachloroauric(III) acid trihydrate (0.11 g, 0.28 mmol) and copper(II) nitrate trihydrate (0.155 g, 0.64 mmol) was dissolved in 10 mL of deionised water. The α-alumina support (2 g, 19.6 mmol) was impregnated with this solution and then vigorously stirred for 2 h. The catalyst precursor

was then dried at 80 °C with a heating rate of 10 °C/min, for 16 h in a static furnace. The catalyst precursor was then calcined in a static furnace at 450 °C with a heating rate of 10 °C/min, for 4 h.

2.2.2.8 Synthesis of Cu-Ag/α-Al_2O_3

The catalyst was prepared by the wet impregnation method. Copper(II) nitrate trihydrate (0.155 g, 0.64 mmol) and silver nitrate (0.09 g, 0.53 mmol) was dissolved in 10 mL of deionised water. The α-alumina support (2 g, 19.6 mmol) was impregnated with this solution and then vigorously stirred for 2 h. The catalyst precursor was then dried at 80 °C with a heating rate of 10 °C/min, for 16 h in a static furnace. The catalyst precursor was then calcined in a static furnace at 450 °C with a heating rate of 10 °C/min, for 4 h.

2.2.2.9 Synthesis of $Ni(NO_3)_2/SiO_2$

The 5wt. % $Ni(NO_3)_2/SiO_2$ catalyst was prepared by Thomas Ha, a master's student.[56] The procedure used was as follows. Cab-O-Sil was dried overnight in a static oven at 120 °C and then subsequently dried in a vacuum oven for a least 4 h at 120 °C. Nickel (II) nitrate hexahydrate (1.07 g, 5.9 mmol) was dissolved in 12.7 mL of deionised water (as determined by the pore volume of the support). This solution was added dropwise to the dried Cab-O-Sil (4.10 g, 68.2 mmol) with frequent mixing using a vortex mixer to ensure an even distribution. The catalyst precursor was then dried in a static air oven overnight at 120 °C and dried further in a vacuum oven for a least 4 h at 120 °C.

2.3 Characterisation Techniques

2.3.1 Powder X-ray Diffraction (pXRD)

Samples for pXRD were prepared by spreading a thin layer of Vaseline on a low background silicon sample holder (silicon wafer (100)-cut off orientation 9 ° towards (001), Sil'tronix Silicon Technologies mounted in a plastic puck) and sprinkling a small amount of the sample onto the Vaseline layer. All pXRD samples were run by the author.

pXRD patterns were acquired using a Bruker AXS D8 Advance diffractometer, fitted with a Lynxeye Soller PSD detector and controlled by Diffrac and XRD commander software. Copper $K\alpha_1$ (λ = 1.5406 Å) and $K\alpha_2$ (λ = 1.5444 Å) radiation was used. Patterns were recorded with a 2θ range of 10 – 90 ° and a typical scan lasted around 40 min.

For the Ag and Au based catalyst's pXRD patterns, an exponential background was applied to the section of the data in the 2θ range of 63.5 – 65.5 ° using MATLAB. MATLAB was also used to fit a Gaussian function to an Ag reflection at 64.5 ° and the Au reflection at 64.6 °. This gives the full-width half-maximum (FWHM) of the reflection used for the estimation of the crystallite size, which was undertaken with the Scherrer equation (shown in *Equation 2.5*):

$$\beta(2\theta) = \frac{K\lambda}{L\cos(\theta)}$$

Where $\beta(2\theta)$ = full width half maximum of the reflection at angle 2θ in radians, K = dimensionless shape factor, which is taken to be 0.9, λ = wavelength of radiation in nm, L = average crystallite size in nm and θ = angle of reflection in radians.

Equation 2.5.

For the Scherrer equation, three repeats were undertaken, where the average was found, and the errors were calculated based on the error from fitting the Gaussian functions. Unreliability from the Scherrer equation comes from the assumption that the particles are a uniform size and a single average size.

2.3.2 Inductively Coupled Plasma – Optical Emission Spectroscopy (ICP-OES)

Samples were prepared by digesting a small amount of carefully weighed catalyst, typically approximately 15-20 mg, in around 3 mL of nitric acid at 80 °C for 1 h. The solutions were then cooled to room temperature and then diluted with UHP water using volumetric flasks to achieve a solution with a metal concentration expected to be nominally around 8 mg L^{-1}. Standards were prepared from water-soluble salt precursors of silver nitrate, ammonium perrhenate, caesium chloride, tetrachloroauric(III) acid trihydrate and copper(II) nitrate trihydrate used to confirm the reliability of a particular experimental run. The standards were prepared the same as the samples, by being dissolved and diluted in aqua regia and UHP water. The acid concentrations of the standards matched the same as the sample acid concentrations. All the samples were prepared in duplicate. All ICP-OES samples were digested by the author, however ICP-OES data collection was carried out by Dr Emily Unsworth at the Elemental Analysis service in Durham University.

A Thermo iCAP 6000 series instrument was used to carry out the ICP-OES analysis. The instrument comprises of a sequential monochromator, a vertical torch, a cyclonic spray chamber, a concentric nebuliser and a high dynamic detector. The silver content was determined from the emission lines at 224.641 nm, the rhenium content was determined from the emission lines at 221.426 nm, and the caesium content was determined from the emission line at 455.531 nm. The copper content was determined from the emission lines

at 213.598 nm and the gold content was determined from the emission lines at 267.594 nm. The instrument was calibrated before the samples were measured using commercial calibration standards of known metal content. All standards run were found to be within experimental error.

2.3.3 Diffuse Reflectance Infrared Fourier Transform Spectroscopy (DRIFTS)

DRIFTS measurements were carried out on a Nicolet IS10 FTIR spectrometer, fitted with a Praying Mantis diffuse reflection accessory. Samples were analysed for 64 scans with a resolution of 0.5 cm^{-1}. Samples were backgrounded against KBr unless otherwise stated. Whilst *ex situ* DRIFTS was undertaken using a cup, *in situ* DRIFTS was undertaken using an in-house developed DRIFTS cell, described in **Chapter 3**.

For the *in situ* DRIFTS experiments in **Chapter 3**, when undertaking a reduction, 10% of H_2 in Ar at a flow of 20 mL min^{-1} was flowed through the cell. The temperature was increased from 25 °C to 300 °C at a ramp rate of 2 °C min^{-1}, whilst recording spectra every 2 min. When undertaking CO adsorption, the catalyst was reduced using 10% of H_2 in Ar at a flow of 20 mL min^{-1} at 300 °C with a ramp rate of 2 °C min^{-1} for 3 h. After 3 h, the sample was cooled, and 20 mL min^{-1} of Ar was flowed for 30 min to purge the cell. 5% CO in Ar at a flow of 40 mL min^{-1} flowed through the cell for 60 min, the cell was then purged with 40 mL min^{-1} of Ar for 20 min. After this, the spectrum was recorded with 10 mL min^{-1} Ar.

For the *in situ* DRIFTS experiments undertaken in **Chapter 3**, **Chapter 4**, **Chapter 5** and **Chapter 6** when looking at the O_2 pretreatment, 10% of O_2 in Ar at a flow of 20 mL min^{-1} was flowed through the cell. The temperature was increased from 25 °C to 225 °C at a ramp rate of 2 °C min^{-1}, whilst recording spectra every 2 min. The temperature was held at 225 °C for 20 min. The temperature was then increased from 225 °C to 275 °C at a ramp rate of 2 °C min^{-1}, whilst recording spectra every 2 min at 275 °C the temperature was held for 20 min. When undertaking ethylene epoxidation in the *in situ* DRIFTS cell, the samples were heated under 10% O_2 to 225 °C at a rate of 10 °C min^{-1}, at a total flow rate of 20 mL min^{-1}. The samples were held at 225 °C under 10% O_2 for 2 h. There was then an introduction of 5% C_2H_4, and 10% O_2 at a total flow rate of 20 mL min^{-1} this was held for 2 h. Next, the C_2H_4 was removed and heated to 275 °C at a rate of 10 °C min^{-1}. C_2H_4 was then added back in at 5% and held at 275 °C for 30 min. The spectra were recorded every 2 min. All *in situ* and *ex situ* DRIFTS measurements were untaken by the author.

2.3.4 Brunauer-Emmett-Teller (BET)

The BET surface area of Al_2O_3 was measured by nitrogen adsorption and desorption at 77 K using a Micromeritics ASAP 2020 volumetric adsorption analyser. Samples were degassed at 350 °C (ramp rate: 10 °C min^{-1}) for 4 h under dynamic vacuum before analysis. P/P_0 values between 0.05-0.25 were used in the BET calculation for evaluation of the surface area. All BET surface areas were measured by Dr Kathryn MacIntosh a previous member of the Beaumont group.

2.3.5 Transmission Electron Microscopy (TEM)

TEM imaging was carried out using a JEOL 2100F FEG microscope with a Schottky field emitter at 200 kV and Gatan Rio16 CMOS camera. The necessary instrument alignments were performed to carry out high resolution transmission electron microscopy (HR-TEM).

The catalysts were prepared for TEM analysis by adding a small amount of the sample (ground in a pestle and mortar) into a vial, followed by a small volume of HPLC-grade ethanol. This suspension was then sonicated to ensure an even dispersion of the solid. One drop of each sonicated sample was then deposited onto a 300-mesh copper grid with a carbon film (EM Resolutions) for the Ag based catalysts and onto a 300-mesh nickel grid with a carbon film (EM Resolutions) for the Cu and Au based catalysts. At least 6 areas were sampled to ensure the images selected were representative of the sample. Further image analysis and measurements of crystallite sizes were carried out using ImageJ. All TEM data collection was undertaken by Dr Andrea Zarchariou and Zixuan Han.

2.3.6 Scanning Transmission Electron Microscopy (STEM)

STEM imaging and EDX analysis (including elemental mapping) of the catalyst were carried out using the same microscope used for TEM, with the addition of a JEOL HAADF/dark field photomultiplier tube (PMT) and Gatan ADF/bright field PMT (imaging carried out at 200 keV).

The catalysts were prepared for STEM analysis by adding a small amount of the sample (ground in a pestle and mortar) into a vial, followed by a small volume of HPLC grade ethanol. This suspension was then sonicated to ensure an even dispersion of the solid. One drop of each sonicated sample was then deposited onto a 300-mesh copper grid with a carbon film (EM Resolutions). At least 4 areas were sampled to ensure the images selected were representative of the sample. EDX spectra were also recorded, to ensure there were no crossovers of different elements. All STEM data collection was undertaken by Zixuan Han.

2.3.7 Hammett Indicators

The solid samples were dispersed in dry toluene (3 mL). Methyl red and methyl yellow indicator solutions were prepared by dissolving methyl red (10 mg) or methyl yellow (10 mg) in dry toluene (10 mL). 1-2 drops of either the methyl red or methyl yellow indicator solution were added to the catalyst/toluene suspensions. Methyl red changes colour from yellow above pH 6.2 through orange to red at pH 4.4.[57] Between pH 4.4 and 6.2, it exhibits various shades of orange. While methyl yellow changes colour from below pH 2.9 red to above pH 4.0 yellow.[58] Colourless solutions where the catalyst has changed colour indicate a stronger acidity, whilst coloured solutions indicate weaker acidity, where orange indicates lower acidity and red indicates higher acidity. The author undertook all testing using Hammett indicators.

2.3.8 Oxygen Temperature Programmed Desorption (O_2-TPD)

The O_2 TPD measurements were performed in the in-house Hiden Catlab Microreactor with an integrated Hiden Quadrupole mass spectrometer (HPR-20 EGA). Temperature-programmed desorption of oxygen was undertaken on all synthesised catalysts before the ethylene oxidation reaction. 10% Oxygen in argon at a flow of 20 mL min^{-1} flowed at 225 °C at a ramp rate of 10 °C min^{-1} for 2 h. Next, the flow was changed to argon only at a flow of 50 mL min^{-1} and cooled to 50 °C, the catalyst was held at 50 °C for 2 h. The reactor was heated to 500 °C at a ramp rate of 5 °C min^{-1}. Oxygen analysis was carried out by mass spectrometry. Once the reactor reached 500 °C the reactor was cooled to room temperature, whilst still undertaking oxygen analysis. Here the mass used for this measurement was 32 m/z. The experimental data was background subtracted due to the signal not becoming completely zero at higher temperatures. All oxygen temperature programmed desorption's were untaken by the author.

2.3.9 Solid State Nuclear Magnetic Resonance Spectroscopy – ^{133}Cs (ss NMR)

Caesium-133 magic-angle spinning measurements were undertaken at 52.45 MHz using a Varian VNMRS spectrometer on a Bruker Avance III HD and a 6 mm rotor o.d. probe. Spectra were acquired at a spin rate of 6 kHz. All direct excitation ^{133}Cs spectra were acquired with a 1 us 30 degree solid pulse which was determined from a 12 us solution pulse determined on 1 M CsCl. The spectra were acquired with a recycle delay of 1 s determined on the sample. Caesium spectral referencing is relative to 1 M $CsNO_3$. The type

of measurement undertaken was cross polarisation (CP). All ^{133}Cs ss NMR data collection was undertaken by Dr Samuel Page at the Solid State NMR service at Durham University.

2.3.10 Solid State Nuclear Magnetic Resonance Spectroscopy – ^{27}Al (ss NMR)

Aluminium-27 magic-angle spinning measurements were carried out at 128.39 MHz using a Bruker Avance III HD 500 spectrometer and a 3.2 mm rotor o.d. probe. Spectra were acquired at a spin rate of 20 kHz. All direct excitation ^{27}Al spectra were acquired with a 1 us 30 degree solid pulse which was determined from a 9 us solution pulse determined on 1M aq. $Al(NO_3)_3$. The spectra were acquired with a recycle delay of 1 s determined on the sample. Aluminium spectral referencing is relative to 1M aq. $Al(NO_3)_3$. Peak fitting was conducted using QuadFit.[59] All ^{27}Al ss NMR data collection was undertaken by Dr Samuel Page at the Solid State NMR service at Durham University.

^{27}Al has a quadrupolar moment leading to broad NMR lines due to quadrupolar interactions, whilst ^{133}Cs has a spin ½ nucleus and does not have a quadrupolar moment.[60] Higher spinning speeds and smaller rotors is crucial where it helps to average out the anisotropic interactions, leading to better spectral resolution, therefore compared to ^{133}Cs ssNMR, there is an increase in the spin rate and a decrease in the rotor probe.[61]

2.3.11 Ammonia Temperature Programmed Desorption (NH_3-TPD)

A schematic representation of the NH_3 TPD set-up is shown in *Figure 2.8*. The catalyst (100 mg) was added to a quartz tube, supported with quartz wool, placed inside a tube furnace, and connected to gas lines *via* Ultra-torr type fittings. Pre-treatment of 20% O_2/Ar (2.4 mL/min of O_2 and 9.6 mL/min of Ar) at 225 °C for 2 h with a ramp rate of 10 °C min^{-1}. The temperature was then reduced to 50 °C and the setup was purged with argon for 2 h. Next, the gas was switched to NH_3 and controlled with the use of a needle value for 1 h. The setup was purged with argon for 30 min and then the temperature was increased to 400 °C at a ramp rate of 5 °C min^{-1} then cooled down. Both m/z 16 and m/z 17 were recorded for the ammonia peak, however, m/z of 16 could likely be contaminated with water.[62] Therefore, the ammonia is monitored by mass spec using m/z 17. The experimental data was background subtracted due to the signal not becoming completely zero at higher temperatures. Author undertook all ammonia temperature programmed desorption experiments.

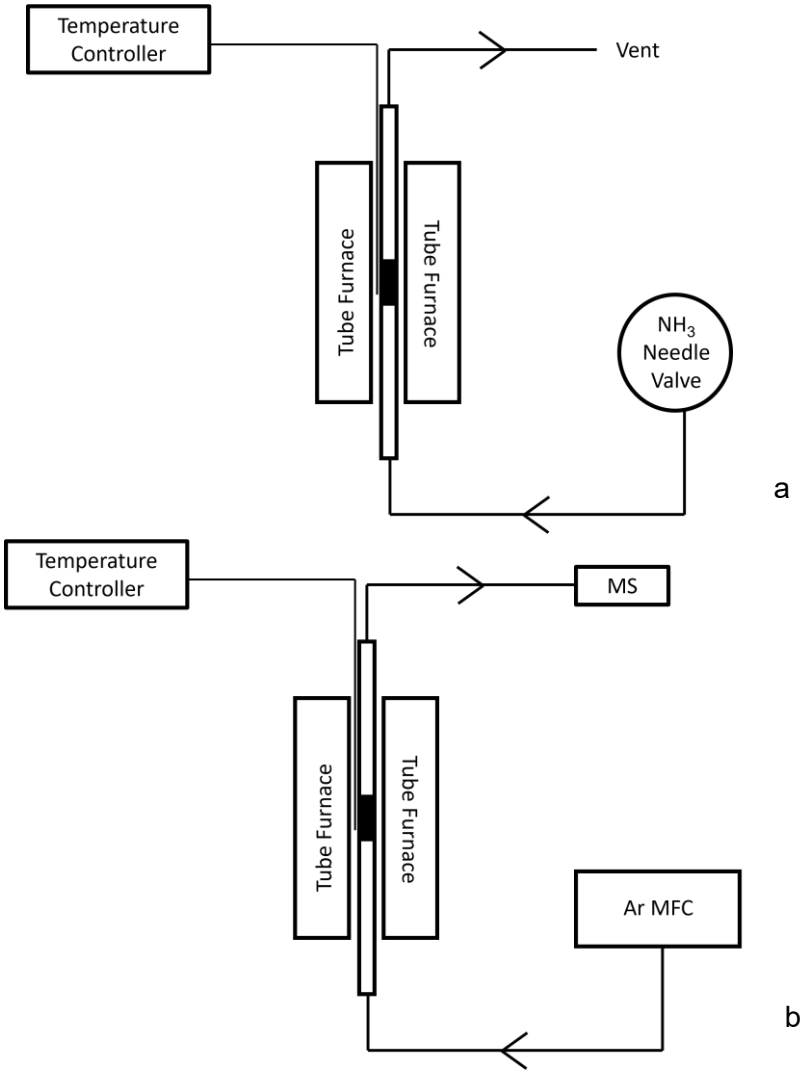

Figure 2.8: Ammonia desorption setup – a) shows the setup when flowing ammonia, whilst b) is a diagram of the setup when flushing and recording the ammonia desorbed.

2.3.12 Hydrogen Temperature Programmed Reduction (H_2-TPR)

The catalyst (100 mg) was added to a quartz tube, supported with quartz wool, placed inside a tube furnace, and connected to gas lines *via* Ultra-torr type fittings. Pre-treatment of 20% O_2/Ar (10 mL/min of O_2 and 40 mL/min of Ar) at 225 °C for 1 hr with a ramp rate of 10 °C min^{-1}. The temperature was then reduced to 30 °C and the setup was purged with argon for 30 min. Next, the gas was switched to 20% H_2/Ar (10 mL/min of H_2 and 40 mL/min of Ar) and then the temperature was increased to 700 °C at a ramp rate of 5 °C min^{-1} then cooled down. The hydrogen was monitored by TCD. The experimental data was background subtracted due to the signal not becoming completely zero at higher temperatures. The hydrogen amount represented by TPR peaks was calibrated by TPR of known masses of CuO diluted in SiC ($CuO + H_2 \longrightarrow Cu + H_2O$; 3 different masses, each run in duplicate). The author undertook all hydrogen temperature programmed reduction experiments.

2.3.13 *Ex situ* X-ray Photoelectron Spectroscopy (XPS)

XPS data collection was performed at the EPSRC National Facility for XPS ('HarwellXPS'), operated by Cardiff University and UCL. Samples were prepared by being affixed to copper tape. Spectra were recorded with photon energies of 1486.7 eV. The binding energy was calibrated using the Al 2p peak. After the subtraction of a Shirley background, the integral areas of the peaks were used to determine the molar ratios of the different elements. Cross sections for the chosen elements were obtained from data reported by Yeh and Lindau using the values at $h\nu$ = 1486.7 eV. The instrument function was assumed to be unity. All *ex situ* XPS data collection was undertaken by HarwellXPS. Peak fitting of the XPS spectra occurred using Origin Pro Peak Analyser when necessary.

2.3.14 *In situ* X-ray Photoelectron Spectroscopy (XPS)

NAP-XPS experiments were performed at beamline B07, Diamond Light Source, Oxfordshire, UK. Details of the NAP-XPS apparatus and B07 beamline are described elsewhere.[40] Samples were prepared by drop-casting the catalysts onto silicon wafers from solutions of catalysts dispersed in ethanol. Firstly, all samples were recorded at room temperature under a flow of Ar. The samples were then heated under 10% O_2 in Ar at a total flow rate of 1.2 mL min^{-1} to 225 °C at a ramp rate of 10 °C min^{-1} where the spectra were recorded. The spectra were recorded at 3 different ethylene environments, firstly there was then an introduction of a 5:1 ratio (oxygen-rich) of 1 mL min^{-1} of O_2 and 0.2 mL min^{-1} of C_2H_4, next, there was an introduction of a 2:1 ratio (practical) of 0.8 mL min^{-1} of O_2 and 0.4 mL min^{-1} of C_2H_4 and lastly there was an introduction of a 1:1 ratio (fuel rich) of 0.6 mL min^{-1} of O_2 and 0.6 mL min^{-1} of C_2H_4. The samples were then cooled down to room temperature. During these reactions, 0.25 mbar O_2 was used for comparison to work by Schlögl and co-workers but was increased to ~ 10 mbar.[63]

Spectra were recorded with photon energies of 1200 eV for all elements, 695 eV for Ag 3d, 365 eV for Re 4f and Si 2p, 605 eV for C 1s, 1060 eV for Cs 3d and 865 eV for O 1s. The samples were analysed using higher and lower photon energies so that analysis was able to occur at different sample depths and the reason these photon energies were selected was so where possible, the kinetic energies were approximately equal. The binding energy was calibrated using the Al 2p peak. After the subtraction of a Shirley background, the integral areas of the peaks were used to determine the molar ratios of the different elements. Cross-sections for the chosen elements were obtained from data reported by Yeh and Lindau.[42] All *in situ* XPS data collection was undertaken by author, alongside other members of the Beaumont group – including, Dr Andrea Zarchariou, Zixuan Han and Dr Monik

Panchal. Peak fitting of the XPS spectra occurred using Origin Pro Peak Analyser when necessary.

2.3.15 *Ex situ* XANES

Ex situ XANES were undertaken using lab-based XAS at Durham X-ray Absorption Facility. Samples were pelletised prior to analysis, using cellulose as a binder, and pressed into 13 mm diameter pellets using a die and a hydrolytic press. The composition of the pelletised sample was calculated to achieve sufficient absorption from the element of interest without absorbing too strongly overall. *Ex situ* XANES were collected at the Cu K-edge and Au L3-edge. Pellets were placed onto the spectrometer using polymer containing adhesive tape. Experiments were conducted under transmission mode on the EasyXAFS300+ laboratory-scale spectrometer, using an Ag anode X-ray source. For Cu K-edge XANES a Si (5 5 3) spherically bent crystal analyser was used and for Au L3-edge XANES a Si (7 3 3) spherically bend crystal analyser was used.[64] Ag was unable to be investigated on the EasyXAFS300+ laboratory-scale spectrometer as the K and L edges are out of the range of the instrument.

Data collection and processing were undertaken by the Durham X-ray Absorption Facility, this included deadtime corrections, which were performed by the silicon drift detector (SSD) and multiple component analyser (MCA) within the instrument. Data collected from the instrument was background corrected, and energy shifted using the Python-based EasyXAFS software (EasyXAFS, WA). Cu energies were calibrated using a Cu foil standard and Au energies were calibrated using an Au foil standard. All *ex situ* XANES data collection was undertaken by Dr Monik Panchal.

2.3.16 *In situ* EXAFS

In situ EXAFS were performed at beamline B18, Diamond Light Source, Oxfordshire, UK. Details of the B18 beamline are described elsewhere.[65] Samples were prepared by the catalyst being added to a quartz capillary (2.9 mm inner diameter), supported with quartz wool and placed inside a furnace shown in *Figure 2.9*. These capillaries were then mounted onto the cell with ultra-torr fittings. Gas lines were fitted to the inlet and outlet of the capillary using Swagelok fittings, and a K-type thermocouple was inserted through the outlet side of the capillary and was positioned in the middle of the catalyst bed.

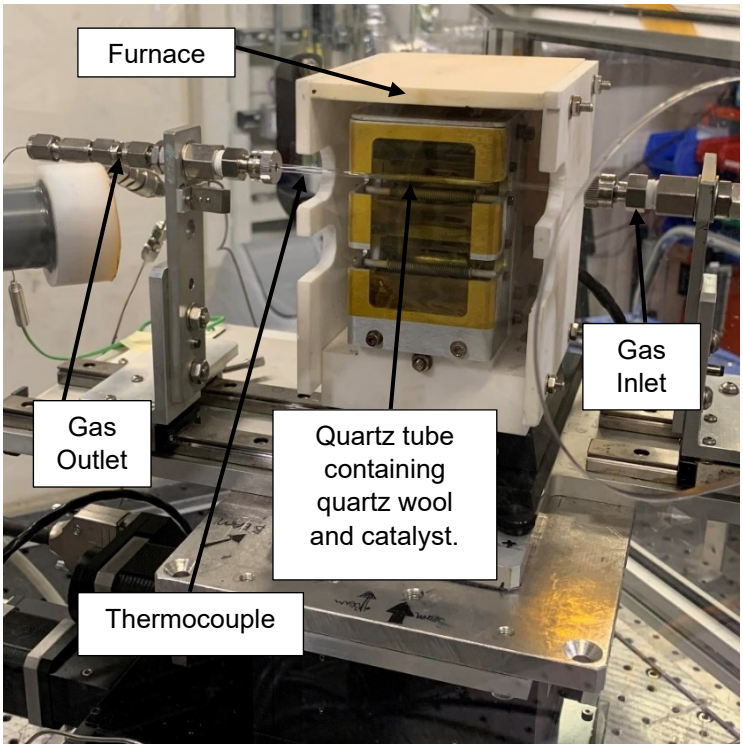

Figure 2.9: A diagram showing the sample setup used for the reactions on B18.

Synchrotron XAFS using B18 were performed to understand the changes in the Re speciation under operation conditions, using a capillary flow microreactor. Approximately 100 mg of each α-Al_2O_3 catalyst and 45 mg of each γ-Al_2O_3 catalyst were sieved to a particle size range of 150-250 μm and loaded into the quartz capillary, giving a bed length of ~ 14 mm, corresponding to a gas hourly space velocity of approximately 12977 h^{-1}. Re K-edge XAFS were acquired at all stages of the pre-treatment and reaction. Firstly, all samples were recorded at room temperature under a flow of Ar (20 mL min^{-1}). The samples were then heated under 10% O_2 to 225 °C at a rate of 10 °C min^{-1}, at a total flow rate of 20 mL min^{-1}. The samples were held at 225 °C under 10% O_2 for 2 h. There was then an introduction of 5% C_2H_4, and 10% O_2 at a total flow rate of 20 mL min^{-1} this was held for 2-6 h. Next, the C_2H_4 was removed and heated to 275 °C at a rate of 10 °C min^{-1}. C_2H_4 was then added back in at 5% and held at 275 °C for 2 h. The samples were then cooled down to room temperature.

Once the XAS data was acquired, it was compiled and EXAFS and XANES studies were performed using IFEFFIT with the Demeter package (Athena and Artemis).[66] The raw data collected was imported into Athena and averaged, from at least 10 spectra in order to improve the signal to noise ratio. The spectra were normalised (removal of parabolic background of spectra), aligned to the calibrated W foil standard and deglitched if needed. Background correction and energy shifts were conducted on Athena. EXAFS fitting models

were created on Artemis against the experimental data collected, here the radial distances were modelled with known values, which were found by using known crystal structures from the Inorganic Crystal Structure Database (ICSD).[67] E_0 values were derived using a modelled W foil, alongside estimations on the *N*, *R* and σ^2 values. Models were created for the data where values of E_0 (energy of the adsorption edge), coordination number, radial distance, and mean-squared disorder of neighbouring atoms. The amplitude reduction factor, S_0^2, of 0.78 was determined from EXAFS of W foil. Fourier transformed analysis was limited to the first shell scattering paths between Re-O(1) (1.73 Å) and Re-O(2) (2.05 Å) found in Re_2O_7 and Re-Re (2.80 Å) found in ReO_2.[68,69]

All fits were performed using multiple k-weight fitting, k^3 weighted data is shown in figures. K-space analysis was performed between k = 2.8 $Å^{-1}$ and k = 12.5 $Å^{-1}$, and this region was Fourier transformed to return the representative R-space plots given. All *in situ* XAFS data collection was undertaken by author, alongside other members of the Beaumont group – including, Dr Andrea Zarchariou, Zixuan Han and Dr Monik Panchal.

2.3.17 Raman Spectroscopy

Raman spectroscopy was conducted at Durham University. Unfortunately, due to health and safety reasons and COVID, there were significant delays in being able to turn the laser on. The correct enclosures and agreement of the H&S service was needed to be able to start the laser, which was not possible until September 2021 due to factors beyond our group's control. *Figure 2.10* shows the schematic of the set up used for Raman spectroscopy and *Figures 2.11-2.13* show photos of key sections of the system.

One laser was used throughout this thesis. Laser Quantum gem 660 nm diode laser was used with a laser power of 80 mW (unless stated otherwise). The mirrors in Enclosure 1 were used to point and steer the beam, ensuring that the beam went through the centre of the aligner and the shutter. The beam was expanded to around 9 mm with the use of a beam expander and directed to the sample by a series of mirrors. The laser power for alignment is reduced by a filter wheel containing a number of different optical density filters. A Fresnel Rhomb λ/2 optic is used on the incident path to rotate the polarisation of the incident light by 90 °. The incident beam is then focussed onto the sample using two cylindrical lenses which are both before the final alignment mirror to cause beam shaping. There is a beam block placed behind the sample to ensure that there is a safe collection of the unabsorbed laser beam. The Raman scattered light was then collected using an objective lens, and an additional camera and lamp mean that visual alignments of the sample can take place. A mirror and a beam splitter which are both installed on flip mounts

were incorporated into the system so these elements could be optionally included behind the objective. The confocal iris regulates how much light can be let through. A wire grid polariser enables either p or s polarised light to be collected. Edge filters are then used to remove the Rayleigh scattered light. These edge filters are two Semrock 664 nm Razor Edge Ultrasteep long-pass edge filters used in series. A depolariser is placed before the slit focusing lens to prevent polarisation dependence of the spectrograph influencing the observed intensity. Lastly, an Andor Shamrock 303i which is fitted with 3 grating, is then used to disperse light which is collected onto the CCD. An Andor Newton 920 BE2X-DD CCD camera was used to mean there was efficient collection at longer wavelengths.

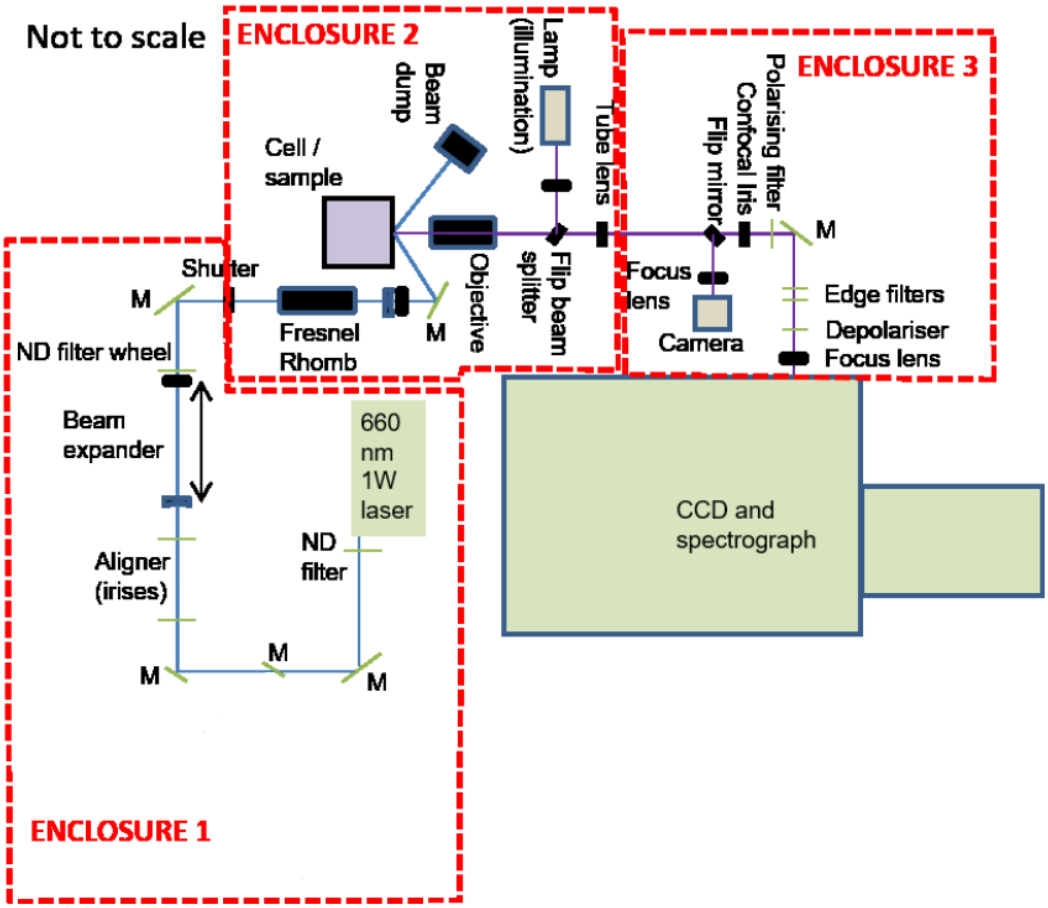

Figure 2.10: Schematic of the set-up used for Raman spectroscopy of 660 nm 1 W laser. When M are mirrors and ND is neutral density.

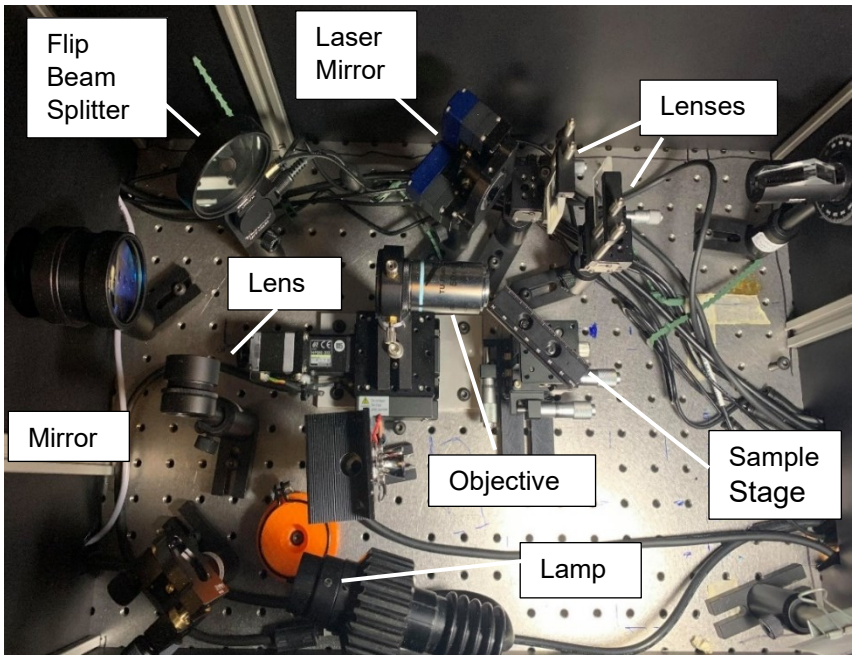

Figure 2.11: Photo of the sample chamber of the Raman setup, showing the sample stage, lenses, objective, laser mirror, flip beam splitter, mirror, lamp, and Fresnel rhomb.

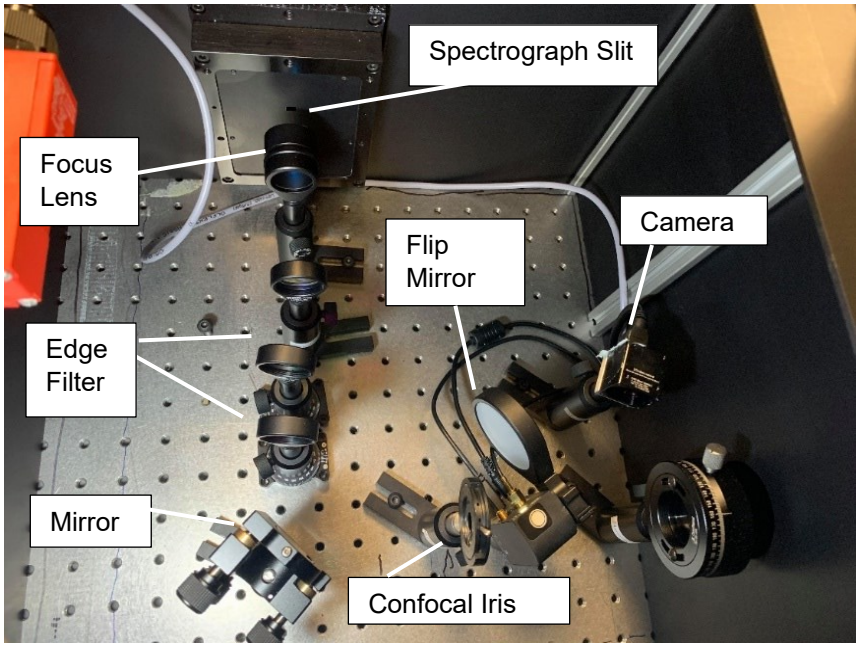

Figure 2.12: Photo of the spectrograph antechamber of the Raman setup, showing the spectrograph slit, lens, depolariser, filters, mirror, iris, camera mirror, polarising filter, and the camera.

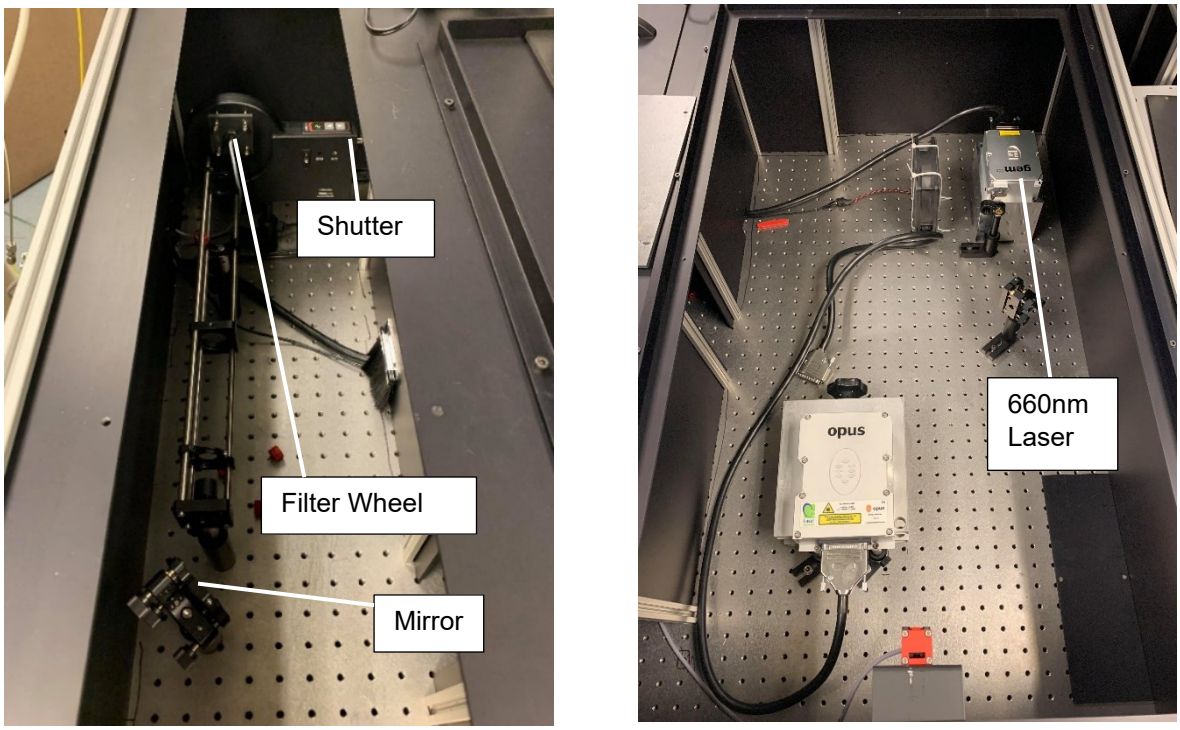

Figure 2.13: Photos of the laser chamber of the Raman setup, showing the lasers, filter wheel and shutter.

To prepare a sample, the sample was stuck to the orange sample holder via double-sided sticky tape as shown in *Figure 2.14* and mounted on a dovetail stage for ease of positioning on the XYZ linear stage.

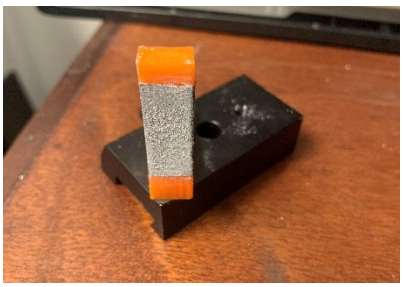

Figure 2.14: Silicon wafer holder with double-sided sticky tape where the sample is attached.

For experimental acquisitions, measurements were undertaken with a slit width of 150 µm, an exposure time of 20 seconds, with 10 accumulation and a kinetic series length of 10, unless otherwise stated. The experimental data was background subtracted due to the signal not becoming completely zero due to fluorescence. The author undertook all Raman spectroscopy experiments.

2.4 Ethylene Epoxidation Reaction Data

Catalytic activity measurements were undertaken on all synthesised catalysts. The catalytic activity measurements were performed on the in-house Hiden Catlab Microreactor with an integrated Hiden Quadrupole mass spectrometer (HPR-20 EGA). This catalyst testing was based on methods outlined by Waugh and co-workers.[70] The capillary was loaded with 150 mg of catalyst. The pretreatment gas mixture consisted of 10 vol % oxygen in argon, and a total flow of 20 mL min^{-1} was maintained by mass flow controllers. The reactor was then heated to 225 °C at a rate of 10 °C min^{-1} and dwelled for 2 h in the pretreatment gas. The pretreatment gas was then replaced by the reaction feed mixture. The reaction feed mixture consisted of 10 vol % oxygen and 5 vol % ethylene balanced by argon, at a total flow of 20 mL min^{-1}. Online gas analysis was carried out by mass spectrometry, the fragments investigated were oxygen, argon, ethylene, ethylene oxide, carbon dioxide, acetaldehyde, and water. After 8 h, the reaction was stopped by replacing the feed mixture with argon and cooling the reactor to room temperature. The m/z used were 18, 27, 28, 29, 32, 40, 42, 43 and 44. Calibrations were undertaken with water, acetaldehyde, ethylene, argon, oxygen, and carbon dioxide.

There is a large overlap of the fragment m/z values between acetaldehyde and ethylene oxide in their cracking patterns, making the quantification of acetaldehyde and ethylene oxide using a single m/z value impossible. To overcome this a least squares fitting approach was used to fit the data to concentrations of each species (H_2O, CO_2, ethylene, ethylene oxide, argon, acetaldehyde), based on assuming cracking patterns were those obtained experimentally for the isolated or argon diluted species of all the reaction effluent components (except ethylene oxide discussed below). The intensities for different concentrations were assumed to be linear relative to the concentration in these measurements. All species for which experimentally obtained cracking patterns were obtained show a strong similarity to the reference spectra obtained from the NIST database, as shown in **Appendix 1**. For ethylene oxide, due to the toxicity of this gas and constraints of where the catalyst test rig was located, obtaining an experimental cracking pattern was not possible. However, given the good agreement of the rest of the species cracking patterns with those in the NIST database, the NIST spectra for ethylene oxide and acetaldehyde were used to simulate a set of experimental intensities for ethylene oxide assuming the two species have comparable cross-sections (a reasonable assumption for similar size molecules containing same atoms). This was then used instead of the experimental cracking pattern. The analysis was performed in Microsoft Excel using the Solver add-in. The concentrations of the sum of all species were normalised to 100% to account for differences in the chamber pressure of the mass spectrometer between reaction

test runs. The NIST spectra and calibration data can be found in **Appendix 1**. All selectivities were extrapolated after 2 h under ethylene epoxidation conditions. An example of a time on stream for the catalysts investigated in **Chapters 4** and **5** is shown in **Appendix 1**, where all catalysts in these chapters behaved similarly. The author collected all ethylene epoxidation reaction data.

The reaction data of 8 other catalysts are included in **Appendix 1**, where a comparison of different Ag, Cs and Re wt. % were investigated. The catalysts which displayed the most favourable catalytic activity towards ethylene epoxidation were chosen for investigation in this thesis.

2.5 References

1 C. F. Holder and R. E. Schaak, *ACS Nano.*, 2019, **13**, 7359–7365.
2 R. Prins, A. Wang and X. Li, *Introduction To Heterogeneous Catalysis*, World Scientific Publishing Company, Singapore, 2016.
3 D. D. Le Pevelen, in *Encyclopedia of Spectroscopy and Spectrometry (Second Edition)*, ed. J. C. Lindon, Academic Press, Oxford, 2nd edn., 2010, pp. 2559–2576.
4 V. S. Vinila and J. Isac, in *Design, Fabrication, and Characterization of Multifunctional Nanomaterials*, Elsevier, Oxford, 2022, pp. 319–341.
5 X-ray diffraction (XRD) basics and application, https://chem.libretexts.org/Courses/Franklin_and_Marshall_College/Introduction_to_Materials_Characterization__CHM_412_Collaborative_Text/Diffraction_Techniques/X-ray_diffraction_(XRD)_basics_and_application, (accessed 6 October 2024).
6 XRD Basics, https://www.physics.upenn.edu/~heiney/datasqueeze/basics.html, (accessed 6 October 2024).
7 V. Ramaswamy, in *Studies in Surface Science and Catalysis*, eds. T. S. R. P. Rao and G. M. Dhar, Elsevier, 1998, vol. 113, pp. 683–688.
8 J. W. Olesik, *Anal. Chem.*, 1991, **63**, 12A-21A.
9 S. Ashoka, B. M. Peake, G. Bremner, K. J. Hageman and M. R. Reid, *Anal Chim Acta.*, 2009, **653**, 191–199.
10 J. Olesik, 2020, **35**, 18–21.
11 D. Peak, in *Reference Module in Earth Systems and Environmental Sciences*, Elsevier, Oxford, 2013.
12 T. Armaroli, T. Bécue and S. Gautier, *Oil Gas Sci. Technol.*, 2004, **59**, 215–237.
13 M. Manzoli, *Catalysis.*, 2019, **9**, 30.
14 J. Sirita, S. Phanichphant and F. C. Meunier, *Anal. Chem.*, 2007, **79**, 3912–3918.
15 F. C. Meunier, *React. Chem. Eng.*, 2016, **1**, 134–141.
16 S. Brunauer, P. H. Emmett and E. Teller, *J. Am. Chem. Soc.*, 1938, **60**, 309–319.
17 S. Lowell, J. E. Shields, M. A. Thomas and M. Thommes, *Characterization of Porous Solids and Powders: Surface Area, Pore Size and Density*, Springer Netherlands, Dordrecht, 2004, vol. 16.
18 Ph. Sciau, in *Advances in Imaging and Electron Physics*, ed. P. W. Hawkes, Elsevier, Oxford, 2016, vol. 198, pp. 43–67.
19 P. Choudhary and O. P. Choudhary, *Int.J.Curr.Microbiol.App.Sci.*, 2018, **7**, 743–747.
20 J. J. P. Peters, T. Mullarkey, E. Hedley, K. H. Müller, A. Porter, A. Mostaed and L. Jones, *Nat. Commun.*, 2023, **14**, 5184.
21 S. Nasrazadani and S. Hassani, in *Handbook of Materials Failure Analysis with Case Studies from the Oil and Gas Industry*, eds. A. S. H. Makhlouf and M. Aliofkhazraei, Butterworth-Heinemann, Oxford, 2016, pp. 39–54.
22 M. Scimeca, S. Bischetti, H. K. Lamsira, R. Bonfiglio and E. Bonanno, *Eur J Histochem.*, 2018, **62**, 2841.
23 O. P. Choudhary and Priyanka, *Int.J.Curr.Microbiol.App.Sci.*, 2017, **6**, 1877–1882.
24 H. Szymanski, *Raman Spectroscopy: Theory and Practice*, Springer Science & Business Media, Berlin, 2013.
25 P. Atkins, *Atkins' Physical Chemistry, Oxford University Press*, Oxford, 10th edn., 2014.
26 D. Long, in *The Raman Effect*, John Wiley & Sons, Ltd, Hoboken, 2002, pp. 31–48.
27 D. Long, in *The Raman Effect*, John Wiley & Sons, Ltd, Hoboken, 2002, pp. 85–152.
28 S. Mosca, C. Conti, N. Stone and P. Matousek, *Nat. Rev. Methods Primers.*, 2021, **1**, 1–16.
29 P. O. P. Ts'o, *Basic Principles in Nucleic Acid Chemistry V1*, Elsevier, Oxford, 2012.
30 D. Cebeci-Maltaş, M. A. Alam, P. Wang and D. Ben-Amotz, *Eur. Pharm. Rev.*, 2017, **22**, 18–21.
31 F. Hanke, U. Böttger, A. Pohl, K. Irmscher and S. G. Pavlov, *J. Raman Spectrosc.*, 2024, **55**, 26–42.

32 A. Orlando, F. Franceschini, C. Muscas, S. Pidkova, M. Bartoli, M. Rovere and A. Tagliaferro, *Chemosensors*, 2021, **9**, 262.
33 B. Reif, S. E. Ashbrook, L. Emsley and M. Hong, *Nat. Rev. Methods Primers.*, 2021, **1**, 1–23.
34 D. C. Apperley, R. K. Harris and P. Hodgkinson, *Solid-State NMR: Basic Principles and Practice*, Momentum Press, New York, 2012.
35 P. van der Heide, in *X-Ray Photoelectron Spectroscopy*, John Wiley & Sons, Ltd, Hoboken, 2011, pp. 1–12.
36 F. A. Stevie and C. L. Donley, *J. Vac. Sci. Technol. A: Vac. Surf. Films.*, 2020, **38**, 063204.
37 A. Kiejna, in *Encyclopedia of Interfacial Chemistry*, ed. K. Wandelt, Elsevier, Oxford, 2018, pp. 319–326.
38 J. Yarwood, R. Douthwaite and S. Duckett, *Spectroscopic Properties of Inorganic and Organometallic Compounds: Techniques, Materials and Applications, Volume 42*, Royal Society of Chemistry, London, 2011.
39 D. R. Baer, K. Artyushkova, C. R. Brundle, J. E. Castle, M. H. Engelhard, K. J. Gaskell, J. T. Grant, R. T. Haasch, M. R. Linford, C. J. Powell, A. G. Shard, P. M. A. Sherwood and V. S. Smentkowski, *J. Vac. Sci. Technol. A: Vac. Surf. Films.*, 2019, **37**, 031401.
40 G. Held, F. Venturini, D. C. Grinter, P. Ferrer, R. Arrigo, L. Deacon, W. Quevedo Garzon, K. Roy, A. Large, C. Stephens, A. Watts, P. Larkin, M. Hand, H. Wang, L. Pratt, J. J. Mudd, T. Richardson, S. Patel, M. Hillman and S. Scott, *J. Synchrotron Radiat.*, 2020, **27**, 1153–1166.
41 G. Greczynski and L. Hultman, *Prog. Mater. Sci.*, 2020, **107**, 100591.
42 J. J. Yeh and I. Lindau, *At. Data Nucl. Data Tables.*, 1985, **32**, 1–155.
43 M. P. Seah and W. A. Dench, *Surf. Interface Anal.*, 1979, **1**, 2–11.
44 D. N. G. Krishna and J. Philip, *Appl. Surf. Sci.*, 2022, **12**, 100332.
45 Q. Wang and A. I. Frenkel, in *Studies in Surface Science and Catalysis*, eds. P. Fornasiero and M. Cargnello, Elsevier, Oxford, 2017, vol. 177, pp. 149–183.
46 R. Zou, G. A. Bramley, S. Xu, S. Chansai, M. Panchal, H. Chen, Y. Zhou, P. Gao, G. Hou, S. M. Holmes, C. Hardacre, Y. Jiao, A. J. Logsdail and X. Fan, *Catal. Sci. Technol.*, 2024, **14**, 164–173.
47 A. S. Hoffman, L. M. Debefve, A. Bendjeriou-Sedjerari, S. Ould-Chikh, S. R. Bare, J.-M. Basset and B. C. Gates, *Rev. Sci. Instrum.*, 2016, **87**, 073108.
48 O. O. Kartashov, A. V. Chernov, D. S. Polyanichenko and M. A. Butakova, *Materials.*, 2021, **14**, 7884.
49 A. A. Guda, S. A. Guda, A. Martini, A. N. Kravtsova, A. Algasov, A. Bugaev, S. P. Kubrin, L. V. Guda, P. Šot, J. A. van Bokhoven, C. Copéret and A. V. Soldatov, *npj. Comput. Mater.*, 2021, **7**, 1–13.
50 S. R. Chae, J. Moon, S. Yoon, S. Bae, P. Levitz, R. Winarski and P. J. M. Monteiro, *Int. J. Concr. Struct. Mater.*, 2013, **7**, 95–110.
51 R. Ortega, A. Carmona, I. Llorens and P. L. Solari, *J. Anal. At. Spectrom.*, 2012, **27**, 2054–2065.
52 G. J. Sherborne and B. N. Nguyen, *Chem. Cent. J.*, 2015, **9**, 37.
53 J. L. Falconer and J. A. Schwarz, *Catal. Rev. - Sci. Eng.*, 1983, **25**, 141–227.
54 J. A. Moulijn, in *Studies in Surface Science and Catalysis*, eds. P. W. N. M. van Leeuwen and R. A. van Santen, Elsevier, Amsterdam, 1993, vol. 79, pp. 401–417.
55 S. Da Ros, K. A. Valter Flores, M. Schwaab, E. Barbosa-Coutinho, N. R. C. Fernandes and J. C. Pinto, *J. Ind. Eng. Chem.*, 2021, **94**, 425–434.
56 T. Ha, Durham University, 2023.
57 Methyl Red, ACS, https://www.thermofisher.com/order/catalog/product/036682.22, (accessed 9 March 2024).
58 Methyl Yellow, indicator, https://www.thermofisher.com/order/catalog/product/B21145.14, (accessed 9 March 2024).

59 T. F. Kemp and M. E. Smith, *Solid State Nucl. Magn. Reson.*, 2009, **35**, 243–252.
60 M. Haouas, F. Taulelle and C. Martineau, *Prog. Nucl. Magn. Reson. Spectrosc.*, 2016, **94–95**, 11–36.
61 M. Deschamps, in *Annual Reports on NMR Spectroscopy*, ed. G. A. Webb, Academic Press, 2014, vol. 81, pp. 109–144.
62 C.-A. Trujillo, N.-T. Ramírez-Marquez and J.-S. Valencia-Rios, *Thermochim. Acta.*, 2020, **689**, 178651.
63 T. C. R. Rocha, A. Oestereich, D. V. Demidov, M. Hävecker, S. Zafeiratos, G. Weinberg, V. I. Bukhtiyarov, A. Knop-Gericke and R. Schlögl, *Phys. Chem. Chem. Phys.*, 2012, **14**, 4554–4564.
64 Products, https://www.easyxafs.com/products-1, (accessed 12 March 2024).
65 Welcome to B18 - - Diamond Light Source, https://www.diamond.ac.uk/Instruments/Spectroscopy/B18.html, (accessed 12 March 2024).
66 B. Ravel and M. Newville, *J. Synchrotron Radiat.*, 2005, **12**, 537–541.
67 Inorganic Crystal Structure Database (ICSD) | Physical Sciences Data science Service, https://www.psds.ac.uk/icsd, (accessed 13 April 2024).
68 A. L. Ivanovskii, T. I. Chupakhina, V. G. Zubkov, A. P. Tyutyunnik, V. N. Krasilnikov, G. V. Bazuev, S. V. Okatov and A. I. Lichtenstein, *Phys. Lett. A.*, 2005, **348**, 66–70.
69 B. Krebs, A. Mueller and H. H. Beyer, *Inorg. Chem.*, 1969, **8**, 436–443.
70 A. J. F. van Hoof, E. A. R. Hermans, A. P. van Bavel, H. Friedrich and E. J. M. Hensen, *ACS Catal.*, 2019, **9**, 9829–9839.

Chapter 3: Development and Optimisation of a DRIFTS Cell for *In situ* Experiments

3.1 Improvements to the DRIFTS Cell

As discussed in **Chapter 1.4.1**, there are many limitations with current commercial DRIFTS cells. These problems include gas bypassing the sample bed, inaccurate temperature readings and only one material being measured at a time, leading to inaccurate background measurements.[1] Whilst previous work has been undertaken in the literature to improve these problems, they have not been completely solved, therefore there is a need to develop a modified *in situ* DRIFTS cell.[2–4] As discussed in **Chapter 1.5.2** work was undertaken by a previous group member to develop a modified DRIFTS cell, which included two-bed sections and a mechanism to allow for movement between the sample and reference bed.[5] Whilst a new *in situ* cell was made successfully, where background measurements could be taken continually throughout experiments, there were some problems. There was a large reduction in the intensity of the signal of around 30% between the sample cup and the cell, therefore not all the signal was collected. It was found that there were leaks where the window was sealed to the cell, here there was difficulty getting a gas-tight seal due to the metal ring not catching correctly on the cell, and also causing the o-ring to move with the circular motion of having to screw in the metal ring. Whilst the cell had been developed no *in situ* reactions had been tested or run where the temperature and gas flow (reaction conditions) had not been investigated. Therefore, there was a need to make improvements and optimisations to the cell.

The window sealing mechanism was investigated, here a new cell was designed to clamp a metal structure on top of the window to compress the o-ring, as shown in *Figure 3.1*. This metal top was clamped onto the cell with screws, rather than using a circular motion, therefore reducing the problems with the leaking previous cell.

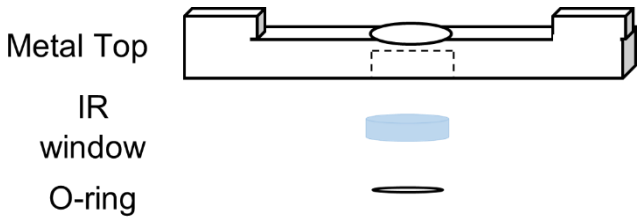

Figure 3.1: Schematic representation of the window sealing mechanism.

Pipes were added with a 1/8” Swagelok fitting meaning gases were able to flow between the reference and the sample chambers, as shown in *Figure 3.2*.

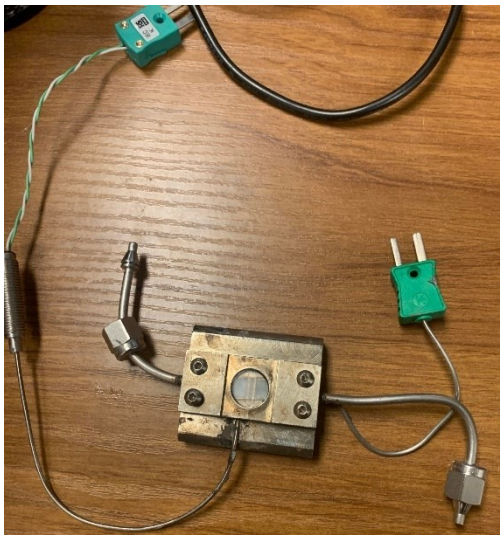

Figure 3.2: New in situ DRIFTS cell.

Figure 3.3 shows a side view of the updated DRIFTS cell (within the IR setup), showing the new gas-tight seal with the metal top being screwed into the cell.

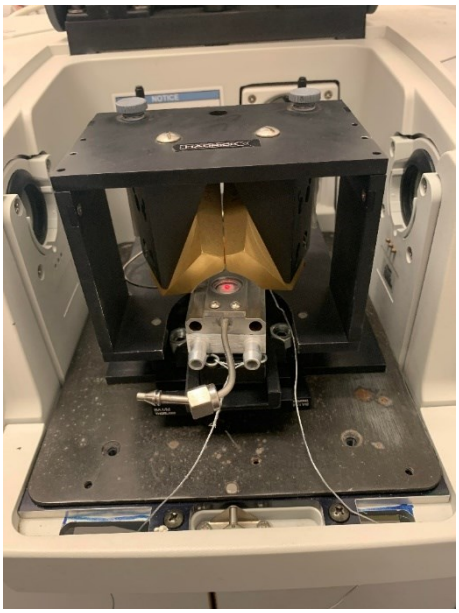

Figure 3.3: New in situ DRIFTS cell and setup without gases and heating added.

3.2 Comparison and Optimisation of the DRIFTS Cell to the Sample Cup

Another limitation of the previously developed DRIFTS cell was that the signal intensity had substantially decreased in the cell compared to in the cup, therefore meaning a loss in signal. This was investigated; Ag/α-Al_2O_3 was chosen as the sample, where the single beam intensity was investigated. As a comparison, the *ex situ* sample cup was used to obtain spectra for the Ag/α-Al_2O_3. Initially, the optical throughput was considered, as the cell could

obstruct some of the optical path. As shown when comparing *Figure 3.4* and *Figure 3.5*, there is a large decrease in the intensity when using the cell compared to using the *ex situ* sample cup, the likely reason for this is that the cell could not be at its optimum position, i.e., not being completely aligned.

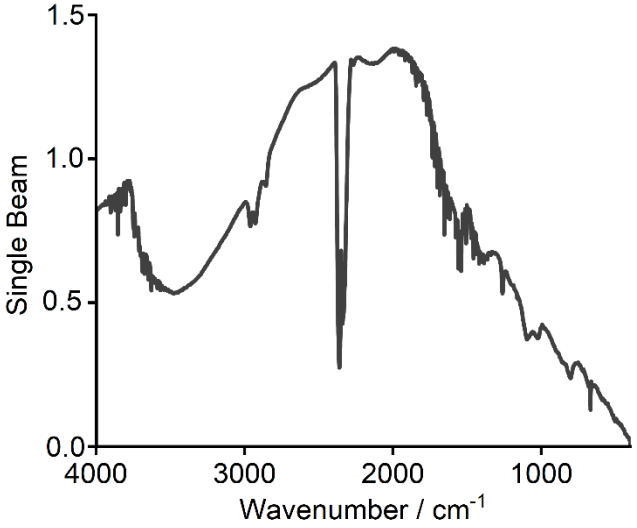

Figure 3.4: DRIFTS of α-Al_2O_3 in the DRIFTS sample cup.

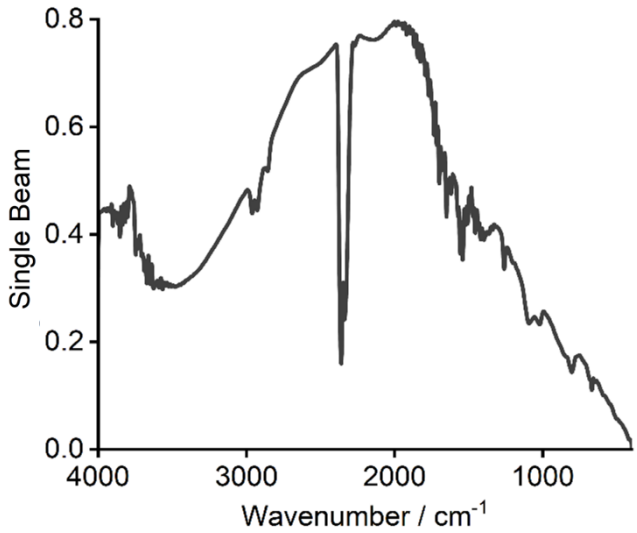

Figure 3.5: DRIFTS of α-Al_2O_3 in the DRIFTS cell.

In the attempt to improve and increase this single beam intensity, it was thought that compressing the o-ring using a pellet press would decrease the space between the sample and the KBr window, allowing the metal clamp to be lowered down relative to the sample and obstruct less of the beam (shown in *Figure 3.6*). It was found that practically 0.3 mm (decreasing from 1.0 mm to 0.7 mm) was the optimum amount that it could be compressed, any more and the o-ring split and lost its shape, therefore meaning the cell would no longer be leak-tight.

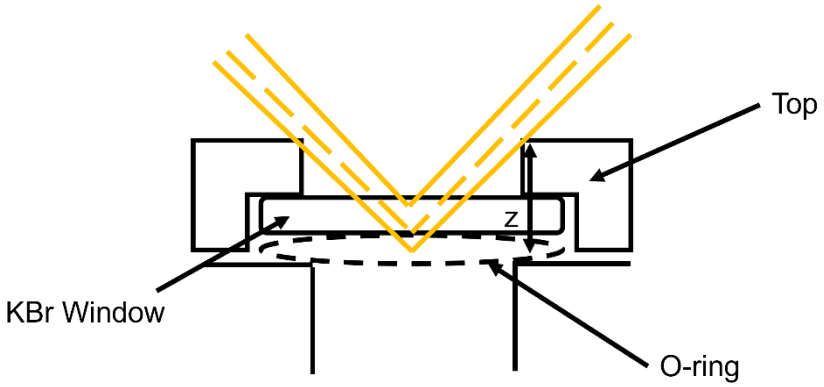

Figure 3.6: Schematic showing how compressing the o-ring and lowering the top to reduce z increases the optical throughput.

Comparing *Figure 3.7* and *Figure 3.5*, there is an increase in the intensity of the signal (for this set of experiments, the gain is always fixed), which corresponds to using a compressed o-ring in the cell. However, whilst there is an increase in intensity, it does not match the intensity of the sample cup.

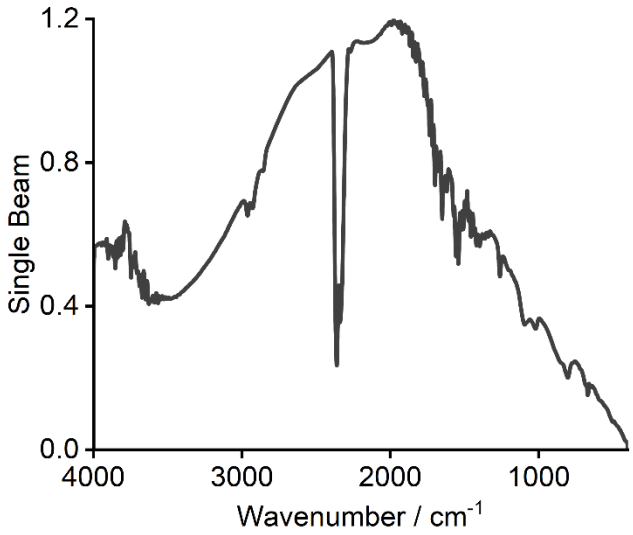

Figure 3.7: DRIFTS of α-Al_2O_3 with the compressed o-ring in the DRIFTS cell.

Another way to improve the intensity was to adjust the height and movement of the cell. The previous cell support on which the metal cell rests, commonly referred to as the shelf made by the other members of the Beaumont group produced a fixed-height shelf, therefore there was a need to be able to move the shelf in the vertical axis to improve the alignment.[5] *Figure 3.8* shows the shelf that was developed by 3D printing which could successfully hold the cell in place. Using the screws (shown in *Figure 3.9*) and a hex key the DRIFTS cell was able to be moved up and down, therefore meaning different samples in the cell could be aligned correctly to its maximum intensity to improve the measurements. By making these changes to the shelf, an increase was made (as shown in *Figure 3.10*), which is likely to correlate to the DRIFTS cell being more aligned to gain a higher intensity.

Figure 3.8: DRIFTS shelf

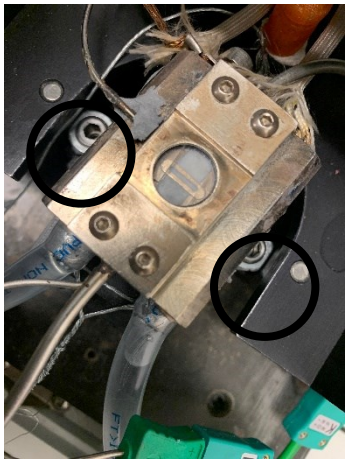

Figure 3.9: Movement of the height of the cell

As shown in *Figure 3.10*, there is a significant increase in single beam intensity compared to *Figure 3.5*. The single beam intensity of the DRIFTS cell is now larger than the cup, which shows the improvements have increased the intensity and therefore allowed better alignment of the cell.

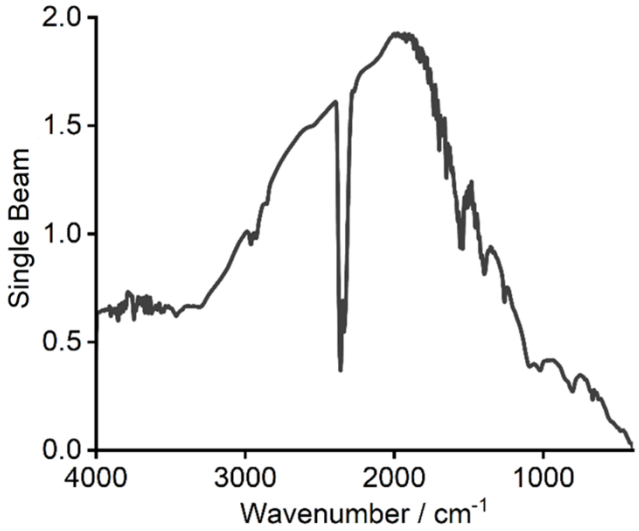

Figure 3.10: DRIFTS of α-Al_2O_3 with the compressed o-ring in the DRIFTS cell and the new shelf setup.

3.3 Testing the Mechanism for Obtaining Background Measurements

With the changing of both the shelf and the cell, it was important to assess the backgrounding mechanism to ensure that it was operating appropriately. Here Ag/α-Al_2O_3 was chosen as the sample, with α-Al_2O_3 being used as the background material. As the comparison, the *ex situ* sample cup was used to obtain spectra for Ag/α-Al_2O_3 and α-Al_2O_3 separately. As shown in *Figure 3.11*, the sliding mechanism and the backgrounding were successful, there was also a reduction in the noise of the *in situ* DRIFTS cell compared to the cup. There has also been the removal of the CO_2 band (2450 cm^{-1}) in the *in situ* DRIFTS spectrum compared to the DRIFTS cup. This is likely to be due to the reduction in the changes in atmospheric conditions as the IR setup did not need to be opened during the measurement of both sample and reference in the cell due to the sliding mechanism, however, with the *ex situ* sample cup, this needed to be opened when changing from reference to sample.

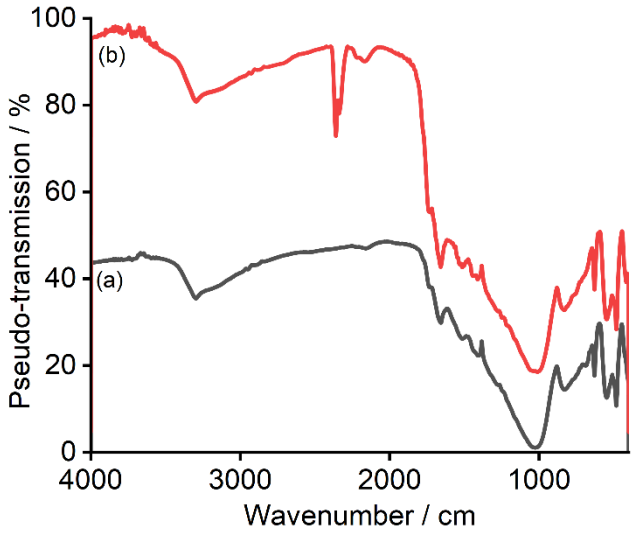

Figure 3.11: DRIFTS spectra for Ag/α-Al_2O_3; (a) using DRIFTS cell with sliding mechanism and (b) using DRIFTS cup for backgrounding. Spectra have been offset for clarity.

Once the optimisation of the cell had occurred, the development of the use of the cell with temperature and gases then needed to be investigated.

3.4 Optimising Heating and Water Cooling

Due to the temperature inaccuracies in commercial setups which were described in **Chapter 1.4.1**, there was a need to investigate the large changes in temperatures between the thermocouple in the sample bed and the temperature of the cell. It was therefore thought that two thermocouples, one in the catalyst bed monitoring the temperature and one controlling the cell temperature (shown in *Figure 3.12*) would solve this problem. This means the temperature of the catalyst bed can be controlled to be exactly the temperature

required for the catalytic reaction. The reason for not controlling the temperature of the cell from the bed gives better control externally from the metal cell.

Temperature heating within this DRIFTS cell was provided by cartridge heaters and a PID controller with feedback from the control thermocouple. By looking at both the maximum operating temperature of the o-rings (Kalrez o-rings) and the reactions that would be undertaken it was thought that the temperature of the catalyst bed could get to 300 °C. A phase-regulating output on the PID controller was autotuned at 300 °C. The use of the phase-regulating output was due to the short heating duty cycle as this limits the expansion and contraction of the cell for the heater's lifetime.

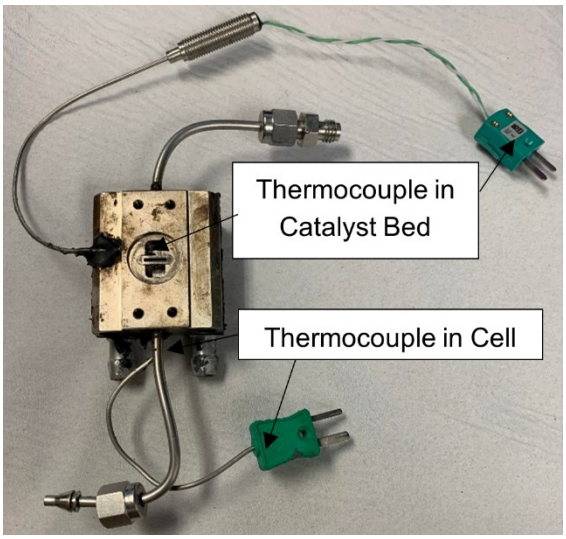

Figure 3.12: The new DRIFTS cell, showing the two thermocouples, one in the bed and the other in the cell.

The temperature of the bed thermocouple was recorded against the temperature of the cell thermocouple to give the values in *Table 3.1*. It can be shown that the catalyst bed can be successfully heated and can get to the temperature that was required for the experiments. As expected, there is a difference between the temperature of the cell thermocouple and the bed thermocouple, where this difference is greater as the temperature increases. This gives evidence showing that the use of two thermocouples can be used to control and get a more accurate temperature reading which is needed to run *in situ* catalytic reactions.

Table 3.1: This table shows the temperature input, the temperature of the cell thermocouple reader, and the temperature of the bed thermocouple reader.

Temperature Input / °C	Temperature of the Bed Thermocouple / °C	Temperature of the Cell Thermocouple / °C
Nothing Set	21.0	23.2
30	29.6	31.1
50	49.7	51.3
60	59.0	59.3
80	79.3	81.3
120	119.3	122.9
150	149.6	154.3
200	199.2	208
250	250.6	261
270	270.6	285
280	280.2	292
300	300.4	313

Due to the cell needing to be heated, a cooling system was required to make sure that the shelf and the IR setup were not being damaged by the heating of the cell. A water pump was used to flow water underneath the cell to cool, but also to make sure the cell would get to the required temperature. A water-cooling block was purchased, shown in *Figure 3.13*, this was attached to the bottom of the DRIFTS cell using high-temperature epoxy with a piece of insulating board (polystyrene foam) between them, where the setup is shown in *Figure 3.14*.

Figure 3.13: The water bath used for the cooling of the DRIFTS system.

Figure 3.14: The cell is connected to the water-cooling system by epoxy.

For the cooling system, a plastic box was used as a reservoir containing water, a water pump was used and plastic pipes running from the box to the DRIFTS cell were connected. This setup is shown in *Figure 3.15*. Here, the water flows from the water pump, up through the water pipe into the water-cooling block, around the water-cooling block and out through a second water pipe back down to the water container.

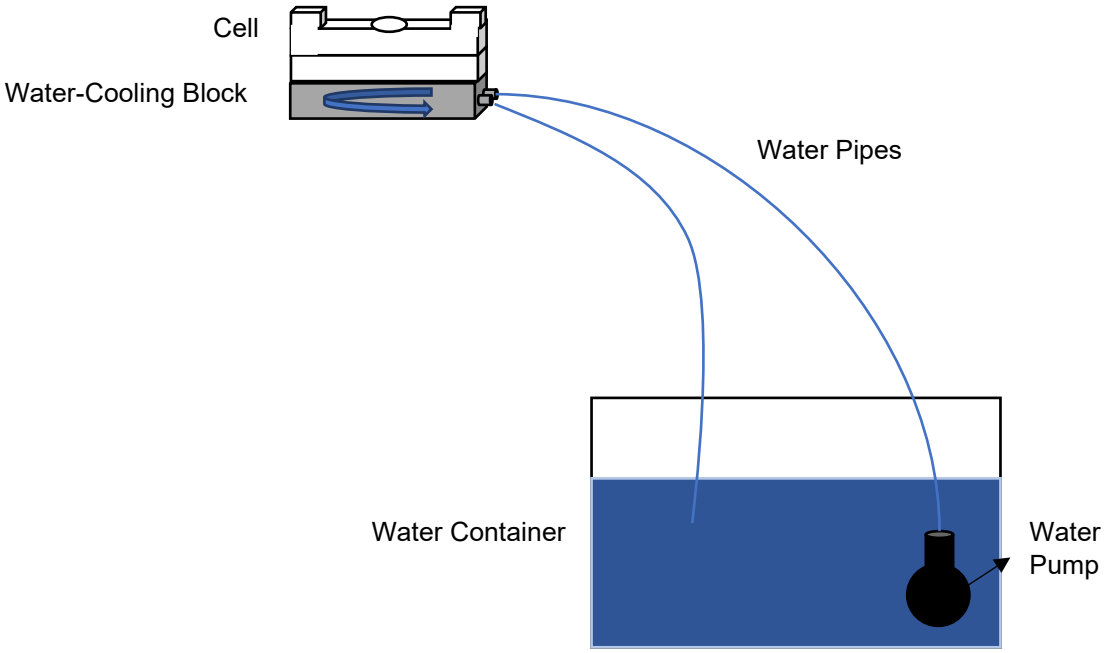

Figure 3.15: DRIFTS cooling setup system.

Initial testing of the temperature found that the water pump was too powerful for the cell heating, therefore leading to the cell only being able to reach 150 °C. A less powerful water pump was found, which meant the cell was able to reach 300 °C for the $Ni(NO_3)_2/SiO_2$ experiments discussed in **Chapter 3.8**. Epoxy connects the water cooler to the DRIFTS cell; however, the epoxy was found to smoke at 250 °C, therefore there was a need to change the connection between the cell and the water cooler. It was thought that a "clamp" could be used, meaning the two would be connected with the insulating board in the middle which would not interfere with the beam path. This is shown in *Figure 3.16*, here the water cooler and the cell are "clamped" together, therefore meaning separation can occur easily without damaging or affecting the cell.

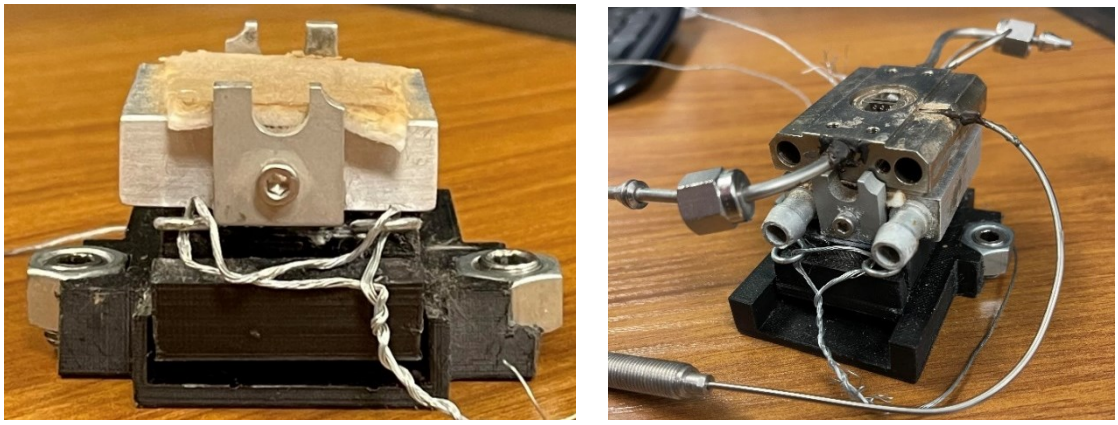

Figure 3.16: The clamp connecting the water cooler to the cell.

3.5 Optimising Gas Flow

Once the cell had been assessed, checked, and made sure it could reach 300 °C, the next step was to check the cell was leakproof. Here the cell was leak-checked with a flow of 5-50 mL min^{-1} of Ar. It was found that no gas leak could be detected in this cell with leak detection spray.

1/8 ” stainless steel gas lines were attached to the cell by Swagelok fittings by the inlet and outlet. Ar, H_2, C_2H_4 and O_2 using Alicat Scientific mass flow controllers (MFCs) were attached using stainless steel gas lines to the inlet of the cell (shown in *Figure 3.17*). With the outlet of the cell being connected to a ventilated fume hood.

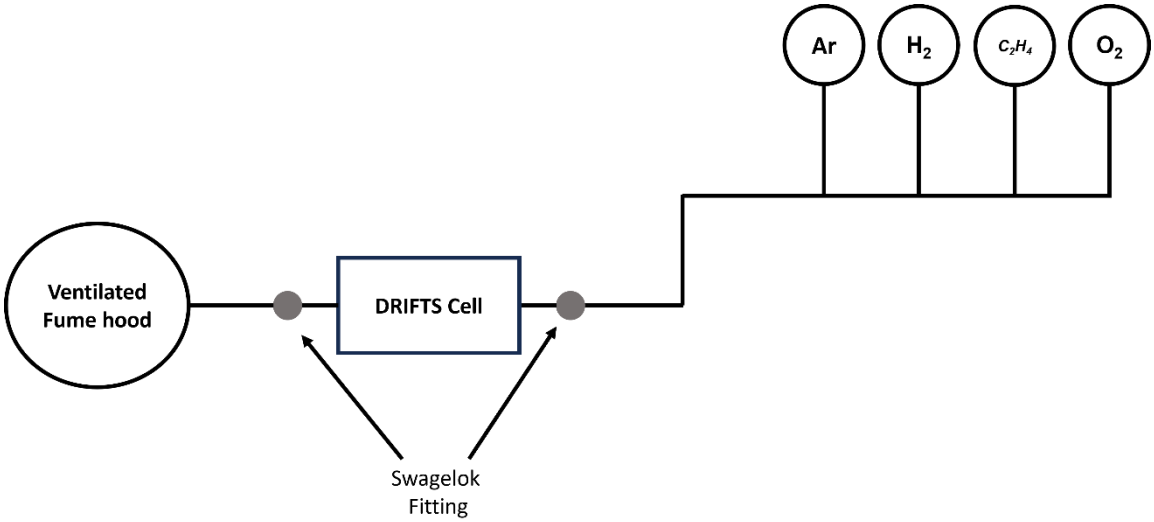

Figure 3.17: Gases setup going into and out of the cell.

Once, the gas system had been set up, calibrations of H_2, C_2H_4, O_2 and Ar mass flow controllers were undertaken. These are shown in **Appendix 2**.

To conclude it was found that with this new design of the cell if the cell was compressed correctly and screwed together tightly, there was no accidental leaking of gases, the intensity increased to *ex situ* samples was achieved, translation between background and sample worked and heating could readily be achieved.

3.6 Optimising using KBr and CaF_2

For initial experiments, KBr was used as the window for the majority due to widespread use and availability. However, it was found that after some time the KBr windows were both cracking and becoming foggy. It was found that the KBr windows were getting to the reaction temperature, whilst this meant that no high boiling species were condensing on the window (giving an improvement to this cell), it meant that a slow cool down was needed. Whilst slow cooling stopped the cracking of the window, the problem of the fogginess of the KBr window still occurred. As the KBr window needed to be a specific size for the cell, it meant that the window was expensive, therefore other materials were investigated. Whilst zinc selenide (ZnSe) was suggested, it oxidised significantly at 300 °C, and should not be used above 250 °C, due to its toxicity.[6] Therefore, CaF_2 was investigated. Although CaF_2 cannot be used under 1000 cm^{-1}, it is largely cheaper than KBr and the detector used for this infrared spectrometer is a fast recovery deuterated triglycine sulfate (DTGS) detector, therefore it is very unreliable under 1000 cm^{-1}.[7] As shown in *Figure 3.18* and *Figure 3.19*, Ag/α-Al_2O_3 was chosen as the sample, with α-Al_2O_3 being used as the background material, a comparison was undertaken between using the cheaper CaF_2 and the more expensive KBr window. As expected, CaF_2 is unable to be used for below 1000 cm^{-1}, however above 1000 cm^{-1}, CaF_2 can be used for a cheaper version of KBr.

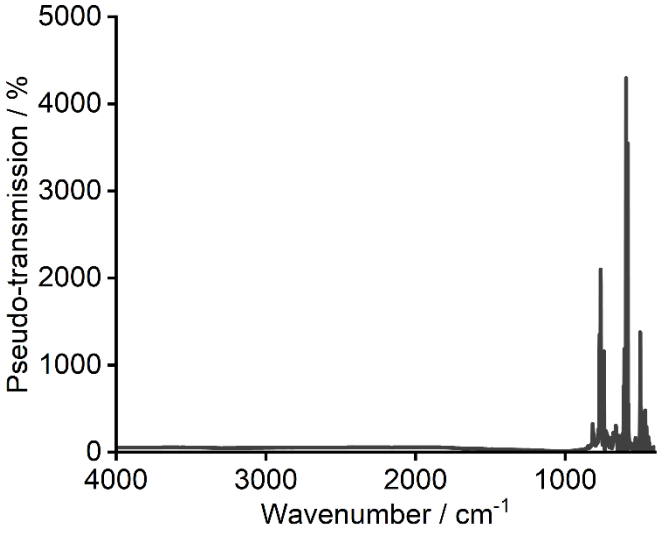

Figure 3.18: A graph showing a CaF_2 window, between 400 and 4000 cm^{-1}.

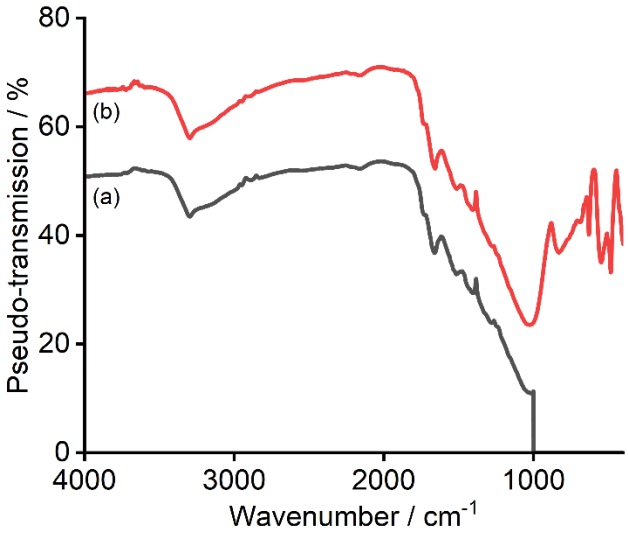

Figure 3.19: A graph showing a comparison of using a KBr or a CaF_2 window. Where (a) is CaF_2 above 1000 cm^{-1} and (b) is KBr. Spectra offset for clarity.

3.7 How Modifications Undertaken Address Limitations of Commercial Cells

Figure 3.20 shows the developed DRIFTS cell. As shown, there are two beds, one is the sample, one is the reference bed and there is a translation between the two meaning both the reference and the sample can be recorded alternately in quick succession. There is both an outlet and an inlet for the gases so that they can flow through both beds. Two thermocouples, one in the cell and one in the bed, mean that the temperature of the bed can be recorded and controlled by the thermocouple in the cell.

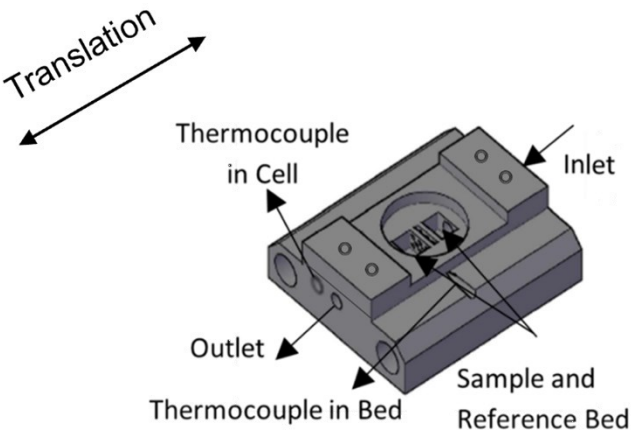

Figure 3.20: The developed DRIFTS cell. Diagram created with the help of Kathryn MacIntosh and Thomas Ha.[5,8]

Sections 3.7.1, **3.7.2** and **3.7.3**, describe how the developed DRIFTS cell is improved compared to the commercial cells available.

3.7.1 Gas By-Passing the Sample Bed

The design of this cell, where the two beds are connected with a slit of metal with holes in, allows an easy flow of gas. As shown in *Figure 3.21*, the gas flows through the inlet, through the centre of the reference bed then through the centre of the sample bed and out through the outlet. This allows for an easy flow of gas and makes sure that the gas does not bypass the beds. Therefore, even if there was headspace available, the gases have to travel through the sample and reference bed to get there.

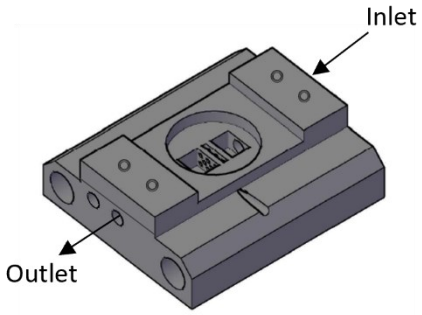

Figure 3.21: The developed DRIFTS cell, showing the inlet for the gas is in the middle of the sample and reference beds.

3.7.2 Accuracy of Temperature Readings

As discussed in **Chapter 1.4.1**, a reported problem in commercial DRIFTS cells is the accuracy of the temperature readings. With looking at both the Harrick and the Spectra-Tech cell, as shown in *Figure 3.22*, when the temperature is below 100 °C, both the cells' thermocouples provide reasonably accurate readings when compared to the temperature measurement of the sample.[1] However, at higher temperatures, there are quite substantial deviations. This could lead to a large number of problems as during catalysis the accuracy of reaction temperature is very important. It was thought that this problem could be due to the thermocouple not being placed close to the sample bed.

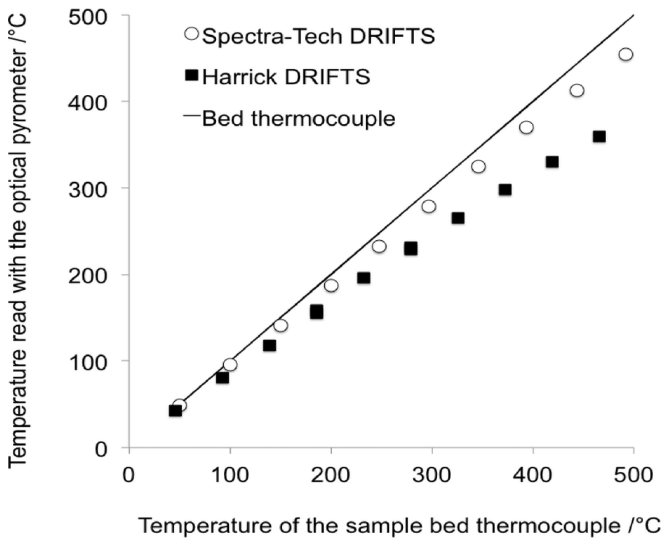

Figure 3.22: A comparison of the temperature readings of the sample bed thermocouple with the optical pyrometer for the Harrick DRIFTS cell, the Spectra-Tech DRIFTS cell and the bed thermocouple reproduced from Meunier with permission from the Royal Society of Chemistry.[1]

Therefore, in this developed DRIFTS cell, two thermocouples were used, one being used to control the temperature of the cell and the second being used to record the temperature of the bed. This allowed the beds to get to the accurate and correct temperature of the catalytic reactions that were taking place. To conclude, this issue with the accuracy of temperature readings gives more accurate temperature readings, however, it is still possible that there are temperature gradients, especially if the reaction is strongly endo or exothermic. This is mitigated in part by putting the thermocouple in the sample rather than the reference bed as this might be expected to undergo a larger temperature change.

3.7.3 Inaccurate Backgrounding

To solve this problem, this new cell contains two beds, one being the reference bed and the other being the sample bed. Translation can occur between the two, meaning that the DRIFTS of the reference can be taken under the same conditions as the sample. This idea comes from a more complex design put forward by Drochner *et al*. as discussed in **Chapter 1.5.1**.[3] This therefore reduces the differences in the atmosphere (CO_2 and H_2O gas phases) in the DRIFTS instrument and improves the backgrounding.

Other commercial cells, for example, the Spectra-Tech® DRIFTS cell (as shown in *Figure 3.23*), use a dome shape for attaching the KBr window, which gives a large amount of dead volume above the sample bed in the optical path length.[1] The gas phase species need to be subtracted from the DRIFTS spectrum of the surface species so that the catalyst can be understood, which is currently difficult in commercial DRIFTS cells.

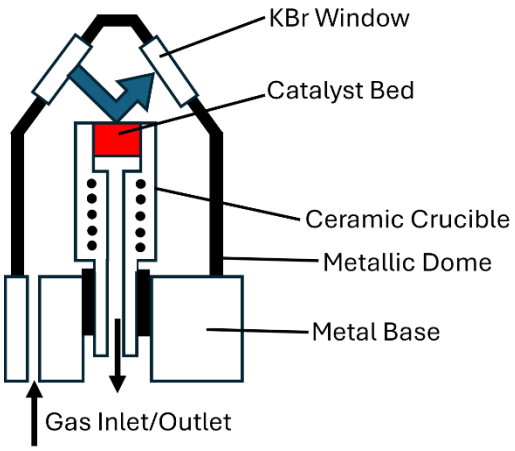

Figure 3.23: Schematic representation of the Spectra-Tech® DRIFTS cell modified from Meunier with permission from the Royal Society of Chemistry.[1]

It has been found that although these species are well known, the rovibrational spectra of gas-phase water and methanol have been mistaken for adsorbates, therefore leading to inaccurate results.[9,10] This developed DRIFTS cell, has a flat window with a flat cover (shown in *Figures 3.24 and 3.25*), allowing for a reduction in the dead volume therefore meaning there is a reduction in the gas phase species in this cell. The dead volume of the cell was calculated as 0.495 cm^3.

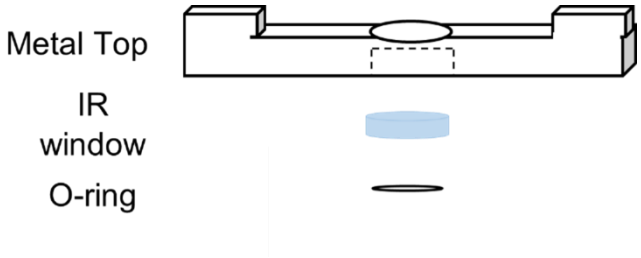

Figure 3.24: A diagram showing the flat cover allowing a reduction in the dead volume.

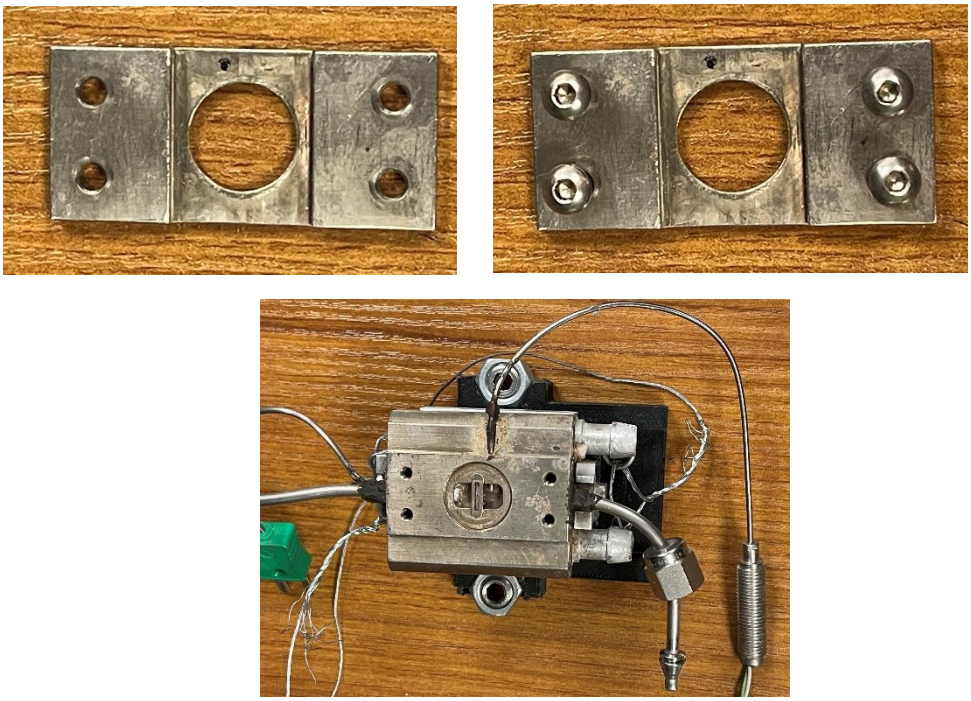

Figure 3.25: The top cover, showing the screws and how it screws into the cell.

Another issue with commercial cells is the issue with high boiling point species adsorbing on the surface of the window, which will again cause problems with accurate backgrounding.[1] However, due to the flat IR window and the reduced dead volume between the metal top and the cell, the IR window gets very hot. It has been found to get to the reaction temperature and caused problems with cracking and fogging (discussed previously in **Chapter 3.6**), however, this meant that high boiling point species were less likely to condense on the window. However, if these species do condense, backgrounding occurs immediately rather than in an entirely separate experiment, allowing us to remove such artefacts.

3.8 Case Study 1: *In situ* Reduction of $Ni(NO_3)_2/SiO_2$

A case study was used to investigate the improvements of this DRIFTS cell compared to the conventional backgrounding in a separate experiment and to show how this newly designed cell would work during experiments. Here the reduction of 5 wt. % $Ni(NO_3)/SiO_2$ was investigated. It should be noted that the data collection from this section was undertaken with Thomas Ha, a master's student in Simon Beaumont's group, however, the author solely undertook interpretation and analysis of the data. The catalyst Ni/SiO_2 is used widely in industry and has been investigated by previous group members, therefore it was thought to be a useful starting point.[11] The synthesis of this catalyst is shown in

Equation 3.1, where step 1 is an incipient wetness impregnation (IWI) and step 2 uses H_2 in the *in situ* reduction.

$$SiO_2 + Ni(NO_3)_2\,(aq.) \longrightarrow Ni(NO_3)_2/SiO_2 \xrightarrow{H_2} Ni/SiO_2$$

Equation 3.1: Synthesis of Ni/SiO_2 catalyst.[11]

The method of catalyst preparation is a key parameter which needs to be optimised and will result in different structural and textural properties of Ni-based catalysts, there is a debate in the literature, regarding the reduction step of $Ni(NO_3)_2$, therefore this catalyst was the first case study to be investigated on this new DRIFTS cell.

Firstly, the reduction of the 5 wt. % $Ni(NO_3)_2/SiO_2$ catalyst was investigated using the "old backgrounding", where the reference used (KBr) stayed at 25 °C over the entire reaction, shown in *Figure 3.26a*. The second reaction undertaken on this new DRIFTS cell was the reduction of the 5 wt. % $Ni(NO_3)_2/SiO_2$ catalyst using the "new backgrounding", here the reference (KBr) was measured before every sample measurement (shown in *Figure 3.26b)*. Therefore, a spectrum was taken at every temperature and condition recorded translating between reference and sample. The region shown spans the nitrate bands and its evolution from 1290 cm^{-1} to 1420 cm^{-1} as it changes form.

As shown in *Figure 3.26*, there are some large differences between a and b. Firstly, in the "old background" conditions, there has been a large problem with the background at 97 °C. This is likely to be due to the differences in the atmosphere and the conditions, however with the "new backgrounding," this has been solved.

In *Figure 3.26b*, at 269 °C, there is a clear shoulder at 1400 cm^{-1} which was not able to be resolved in the "old backgrounding". This shows the benefit of the new backgrounding in improving the signal-to-noise so that otherwise unresolved features can be identified unambiguously.

NO_3^- is shown at approximately 1380 cm^{-1}.[12,13] The reduction in the intensity of the band as a function of temperature indicates the reduction of the Ni species after shifting to lower wavenumbers. This shift in wavenumber could be due to the increase in temperature alongside the reduction that is occurring. Brockner *et al*. investigated the thermal decomposition of $Ni(NO_3)_2$ and found HNO_3 to be produced at 250 °C.[14] A shoulder at 1400 cm^{-1} at 269 °C is likely to correspond to δ(OH) in HNO_3.[15] At 301 °C there is a very reduced peak, indicating that most of the NO_3^- has been removed, likely to be in the form of HNO_3. Here, the temperature decomposition agrees with *Figure 3.26b*. Unfortunately, due to the temperature of the cell only reaching 301 °C, the sample had not been completely reduced, however, the reduction profile was able to be shown.

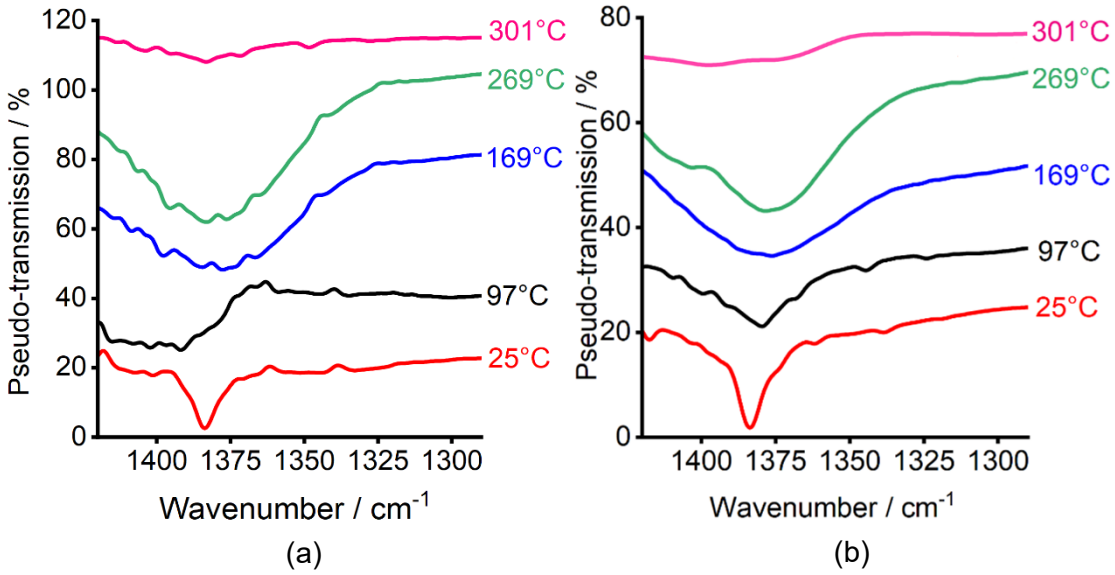

Figure 3.26: In situ DRIFTS of (a) reduction of $Ni(NO_3)_2/SiO_2$ catalyst, under the old backgrounding conditions and (b) reduction of $Ni(NO_3)_2/SiO_2$ catalyst, under the new backgrounding conditions. Spectra have been offset for clarity.

3.9 Case Study 2: CO Adsorption of Ni/SiO_2

A common use of *in situ* DRIFTS is CO-DRIFTS, therefore it was thought this experiment would be another useful technique to investigate with the use of the new *in situ* DRIFTS cell. Here CO-DRIFTS provides a method to detect the available surface of metal and metal oxide using CO as a probe molecule.[16] Due to another member of the group requiring more information regarding the structure of the Ni/SiO_2 catalyst, the CO adsorption of Ni/SiO_2 was investigated. Here both the post-reduced Ni/SiO_2 catalyst and KBr reference were exposed to CO and flowed at 10 mL min^{-1} for 1 h, then switched to Ar for 30 min to remove the atmospheric and free CO at room temperature.

CO typically binds linearly on the edge and corner sites of the surface of catalysts, since there is enough space for a CO molecule to bind to every site, whereas CO typically binds in bridging modes on flat surfaces of catalysts (except at higher pressures of CO) since there is more crowding.[17]

As shown in *Figure 3.27*, there are two key peaks, one is at 1850 cm^{-1} and the second one at 2000 cm^{-1}, which corresponds to the bridging and linear CO respectively on Ni.[18,19] There is also a small peak at 1625 cm^{-1}, which corresponds to an adsorbed carbonate species formed from CO interacting with the support or NiO.[5,19] Sharp oscillations below 1800 cm^{-1} are likely to be due to the incomplete removal of signals due to CO_2's rovibrational spectrum. This therefore shows that there are more bridging rather than linear CO species adsorbed on the Ni-based catalyst. This is indicative that there are a high fraction of flat surface sites on this catalyst suggestion of quite small (few nm) particles.

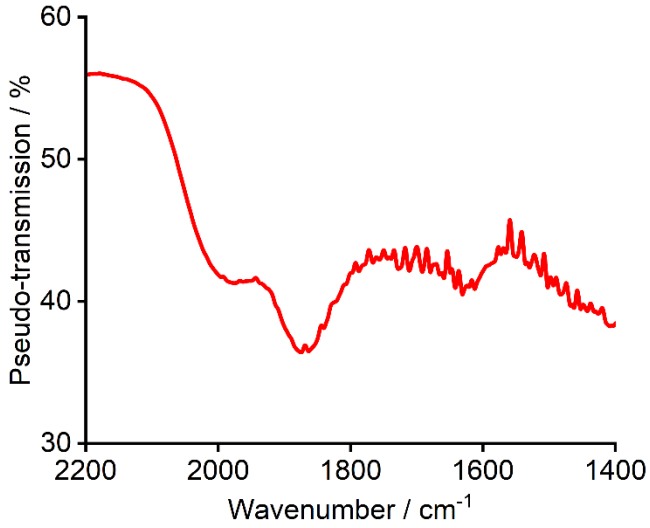

Figure 3.27: CO adsorption of Ni/SiO_2 catalyst

3.10 Case Study 3: Oxidation of $Ag/\alpha\text{-}Al_2O_3$

The last case study to be investigated was the oxidation of $Ag/\alpha\text{-}Al_2O_3$. As discussed in **Section 1.6**, this project investigates the use of $Ag/\alpha\text{-}Al_2O_3$-based catalysts. Therefore, the oxidation of $Ag/\alpha\text{-}Al_2O_3$ using the "old backgrounding" was compared to the "new backgrounding". This is shown in *Figure 3.28a* and *b*.

Again, *Figure 3.28a* shows the "old backgrounding" where the reference used (KBr) stayed at 25 °C throughout the entire reaction, whilst *Figure 3.28b*, shows the "new backgrounding" where the reference used (KBr) was taken before every sample measurement at the same temperature and conditions using the translation mechanism. As shown in *Figure 3.28a* there is a large amount of noise in comparison to *Figure 3.28b*, therefore indicating that any small changes in the spectra could be missed and therefore not picked up on the DRIFTS spectrum. This indicates that the use of the translation mechanism and the correct backgrounding can reduce the amount of noise in the spectrum.

Figure 3.28b, can indicate the role of the hydroxyl groups at 3300 cm^{-1}, here there is a shape change at 3500 cm^{-1} from 25 °C to 87 °C in *Figure 3.28b*, which is likely to be adsorbed water being removed from heating the sample.[20] Temperatures between 87 °C and 257 °C indicate that the pretreatment of oxygen does not affect the hydroxyl groups. However, at 275 °C in *Figure 3.28b*, there appears to be a slight increase in the hydroxyl groups that was unable to be identified in *Figure 3.28a*.

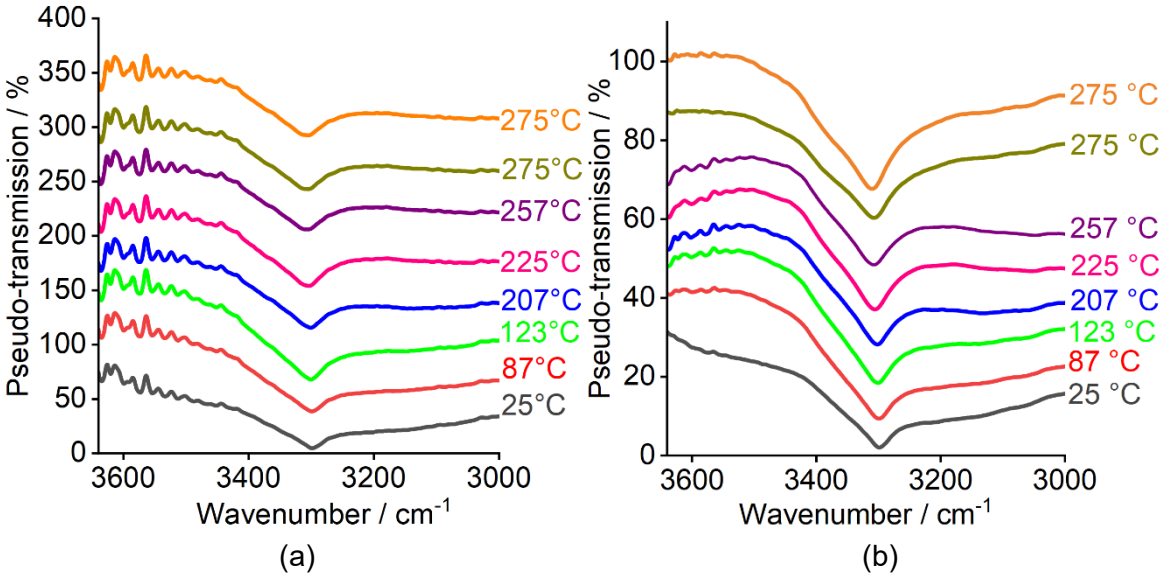

Figure 3.28: In situ DRIFTS (a) oxidation of Ag/Al_2O_3 catalyst, under the old backgrounding conditions and (b) oxidation of Ag/Al_2O_3 catalyst, under the new backgrounding conditions. The second 275 °C shown is after 20 min of being held at 275 °C. Spectra have been offset for clarity.

3.11 Conclusion

To conclude, an *in situ* DRIFTS cell has been successfully designed and developed. Improvements to the previous DRIFTS cell, including a new window sealing mechanism, a new shelf and a new thinner o-ring were made to optimise and make a leak-tight cell. The heating and water cooling were optimised giving an *in situ* DRIFTS cell that can undertake reactions up to 300 °C. Optimisation of gas flow occurred, including ensuring the cell was leakproof for reactions including argon, ethylene, oxygen and hydrogen to be performed. Although fracture and fogging occurred using KBr as a window, another window (CaF_2), was found to be suitable.

As described in the literature, there were some limitations with the current commercial DRIFTS cells. These problems included gas by-passing the sample bed, inaccurate temperature readings and only one material being measured at a time, leading to inaccurate backgrounding and in turn incorrect results.[1] In the new DRIFTS cell, there are two beds, one is the sample bed, and the other is the reference bed, and there is a translation between

the two meaning that both the reference and the sample can be taken in quick succession under the same gas atmosphere. This means that the reference can be taken under the same conditions as the sample therefore reducing the differences in the atmosphere (CO_2 and H_2O gas phases) in the DRIFTS instrument and improving the backgrounding. The flat window with a flat cover allows for a reduction in the dead volume and, in turn, a reduction in the gas phase species in this cell, therefore improving the backgrounding due to this being removed. Lastly, this also causes the IR window to get to reaction temperature, whilst this led to the problems with cracking and fogging, it did reduce the issue with high boiling point species condensing on the window. Whilst not all the issues that are described in the literature have been solved (including qualitative issues that occur when undertaking DRIFTS and the cell temperature being limited to 300 °C), the main ones focused on in this chapter have been investigated and show improvement to current commercial *in situ* DRIFTS cells.

Two thermocouples, one in the cell and the other in the bed, mean that the temperature of the bed can be recorded and controlled by the thermocouple in the cell, giving accurate and correct temperature readings of the bed during reactions. The design of this cell allows an easy flow of gas between both beds and using a new flat top screwed into the cell allows a gas-tight DRIFTS cell.

Three case studies have been conducted using this new DRIFTS cell and have shown that the cell is successful under reaction conditions and has also improved the backgrounding by reducing noise and identifying features that could not be seen before.

Case Studies 1 and 2 give more information regarding the Ni/SiO_2 catalyst, giving evidence to decomposition steps and giving information on the structural properties of the resulting metal catalyst, where there are more flat surfaces on the catalyst. Case Study 3 gives information on the pre-treatment of O_2 on $Ag/\alpha\text{-}Al_2O_3$ with investigations into the hydroxyl groups.

After the development and optimisation of this *in situ* DRIFTS cell was successful, this cell was used in other sections of this thesis and was a key part in giving more information regarding the role of the promoters and Au and Cu-based catalysts.

Contribution of the author to the development of the DRIFTS cell:

- Designed, developed and optimised a new top for the DRIFTS cell – reducing the dead volume.
- Added in pipes for the flow of gases and thermocouples to record temperatures.

- Improved the signal intensity of the cell – by compressing the o-ring and designing and developing a shelf to be able to adjust the height and movement of the cell.
- Tested the mechanism of the back and forth between reference and sample *in situ* under reaction conditions.
- Optimised the heating and water cooling – investigated the optimal temperature by designing the setup and also thought about and developed the water cooling system so that the setup could stay cool. Recorded and optimised the heating and temperature controls.
- Designed and developed a clamp which connected the water cooler to the cell.
- Designed, developed and optimised the gas flow setup, making sure that the gases could flow through the cell easily and without problem.
- Optimised the IR window – looking at both KBr and CaF_2 as two separate cases showing the advantages and disadvantages of using both.
- Undertaken a case study looking at the *in situ* reduction of $Ni(NO_3)_2/SiO_2$ where improvements of the new DRIFTS setup were shown and more evidence regarding the decomposition steps were found.
- Undertook a case study looking at CO adsorption of Ni/SiO_2 where information regarding the structure of the catalyst was found, giving indication of a higher fraction of flat surfaces on the catalyst.
- Finally, looked at a case study of $Ag/\alpha\text{-}Al_2O_3$ where improvements of the new DRIFTS cell were also found, with evidence being shown of the pre-treatment of O_2 looking at the hydroxyl groups.

3.12 Challenges and Next Steps

Although an improved *in situ* DRIFTS cell compared to the literature and commercially available cells have been designed, developed, optimised and tested, there is some next steps to further improve the cell and some challenges that still remain.

Firstly, due to the o-rings, the developed DRIFTS cell is only able to reach 300 °C, therefore high temperature reactions are unable to be undertaken in this cell. This DRIFTS cell is only able to be used under atmospheric conditions, where pressures are unable to be changed inside the cell. Being able to get to different pressures inside the cell would allow for more accurate *in situ* experiments under actual and accurate industrial conditions. Whilst currently, the shifting/moving between the reference and the sample is done manually before every spectrum, a motor could be added, to mean that the shifting between the two is done electronically, therefore speeding up and making date collection easier. Lastly,

whilst the high temperature of the KBr gave more reliable results due to less adsorbates absorbing, there was problems with fogginess, therefore there is a need to improve this so that the expensive KBr was able to be used for all high-temperature long reactions.

3.13 References

1 F. C. Meunier, *React. Chem. Eng.*, 2016, **1**, 134–141.
2 D. J. Cumming, C. Tumilson, S. F. R. Taylor, S. Chansai, A. V. Call, J. Jacquemin, C. Hardacre and R. H. Elder, *Faraday. Discuss.*, 2015, **182**, 97–111.
3 A. Drochner, M. Fehlings, K. Krauß and H. Vogel, *Chem. Eng. Technol.*, 2000, **23**, 319–322.
4 F. C. Meunier, A. Goguet, S. Shekhtman, D. Rooney and H. Daly, *Appl. Catal. A: Gen.*, 2008, **340**, 196–202.
5 K. L. MacIntosh, Durham University, 2022.
6 Zinc Selenide (ZnSe), https://www.continentaltrade.com.pl/en/our-offer/technical-glass/types-of-materials/zinc-selenide-znse, (accessed 12 January 2024).
7 R. A. Spragg, in *Encyclopedia of Spectroscopy and Spectrometry (Third Edition)*, eds. J. C. Lindon, G. E. Tranter and D. W. Koppenaal, Academic Press, Oxford, 2017, pp. 419–427.
8 T. Ha, Durham University, 2023.
9 F. C. Meunier and W. Li, *Korean J. Chem. Eng.*, 2011, **28**, 1495–1496.
10 M. Adnan Saqlain, A. Hussain, M. Siddiq and A. A. Leitão, *RSC Adv.*, 2015, **5**, 47066–47073.
11 K. L. MacIntosh and S. K. Beaumont, *Top. Catal.*, 2020, **63**, 1446–1462.
12 S. He, L. Zhang, S. He, L. Mo, X. Zheng, H. Wang and Y. Luo, *J. Nanomater.*, 2015, 1–8.
13 S.-C. Ho and T.-C. Chou, *Ind. Eng. Chem. Res.*, 1995, **34**, 2279–2284.
14 W. Brockner, C. Ehrhardt and M. Gjikaj, *Thermochim. Acta.*, 2007, **456**, 64–68.
15 A. L. Goodman, E. T. Bernard and V. H. Grassian, *J. Phys. Chem. A*, 2001, **105**, 6443–6457.
16 C. C. Zhang, J. Shi, S. Hartlaub, J. P. Palamara, I. Petrovic and B. Yilmaz, *Catal. Commun.*, 2021, **150**, 106273.
17 R. P. Eischens, S. A. Francis and W. A. Pliskin, *J. Phys. Chem.*, 1956, **60**, 194–201.
18 M. Agnelli, H. M. Swaan, C. Marguez-Alvarez, G. A. Martin and C. Mirodatos, *J. Catal.*, 1998, **175**, 117–128.
19 J. Zarfl, D. Ferri, T. J. Schildhauer, J. Wambach and A. Wokaun, *Appl. Catal. A: Gen.*, 2015, **495**, 104–114.
20 X. Kang, A. Chatzitakis, T. Aarholt, X. Sun, C. Negri and T. Norby, *J. Mater. Chem. A.*, 2022, **10**, 218–227.

Chapter 4: Understanding the Role of the Oxygen and the Re Promoter For Ethylene Epoxidation

Ag/α-Al_2O_3 is commonly used as the catalyst for ethylene epoxidation.[1] As discussed in **Chapter 1.1.2**, the role of the oxygen species and promoters, especially Re is still debated in the literature.[2] In this chapter, Ag/α-Al_2O_3 has been investigated to give information regarding the oxygen species, this includes, what oxygen species are present on the surface of the catalyst, how the oxygen species change throughout ethylene epoxidation and showing how different conditions change the presence of the oxygen species. This Ag/α-Al_2O_3 is then compared to Re-Ag/α-Al_2O_3 to give more information on the role and the structure of the Re promoter. Whilst commonly α-Al_2O_3 is used as the support for the catalysts for ethylene epoxidation, where it is well established that α-Al_2O_3 performs more effectively in this reaction compared to γ-Al_2O_3. It was thought to be useful to compare to γ-Al_2O_3 to understand what role the support, Ag and oxygen species have in the reaction. Comparing to γ-Al_2O_3 helped to give more evidence into how much of a role the support plays in ethylene epoxidation and to be able to give more evidence of the ethylene epoxidation reaction on the surface of the catalyst independent of the support and how these species change. These catalysts have been characterised with both *in situ* and *ex situ* techniques and the activity and selectivity profiles of these catalysts have been determined with comparison to the literature. The role of the O species, the support, the conditions, the O_2 pre-treatment and the Re promoter have been discussed and provide information to improve the understanding of the catalysts used in ethylene epoxidation.

4.1 Comparison of α-Al_2O_3 versus γ-Al_2O_3

The comparison of Ag/α-Al_2O_3 and Ag/γ-Al_2O_3 was investigated. Whilst this section is a comparison of α-Al_2O_3 and γ-Al_2O_3 to understand why α-Al_2O_3 is used as a support, the use of the pretreatment and why the Ag/α-Al_2O_3 is selective, some of the details in **Chapter 4.1**, will be used as a comparison to understand the roles of the promoters (Cs and Re) therefore due to the large arguments in the literature, understanding the Ag/α-Al_2O_3 catalyst is firstly required. As discussed by Minahan *et al*. the Ag metal loadings are typically high around 10 wt. %.[3] Therefore, both Ag/α-Al_2O_3 and Ag/γ-Al_2O_3 catalysts were made using incipient wetness impregnation with 10 wt. % Ag. To confirm that the elemental composition of the catalysts was as expected, ICP-OES was conducted on both. The elemental composition of the catalysts is shown in *Table 4.1*. The silver contents of the two catalysts were close to the expected values, with small value fluctuations and low errors.

Table 4.1: Summary of ICP-OES results. The results reported are the average results of the duplicate samples where errors are one standard deviation calculated based on the duplicate samples for each material. Standards are run in the same batch to confirm no significant anomalies or deviations in the instrumental analysis of the samples.

Catalyst	Metal	Expected Metal Content / wt. %	Metal Content by ICP-OES / wt. %	Error in Metal Content by ICP-OES/ wt. %
Ag/α-Al_2O_3	Ag	10	9.86	±0.69
Ag/γ-Al_2O_3	Ag	10	10.12	±0.84

Both Ag/α-Al_2O_3 and Ag/γ-Al_2O_3 were evaluated for ethylene epoxidation, with the results displayed in *Figure 4.1*. The reactions were undertaken at laboratory scale using 150 mg of catalyst where the online gas analysis was carried out with a mass spectrometer and a least squares fitting approach was used to fit the data to concentrations of each species. These calculated selectivities agree with typical selectivities of ethylene oxide reported on unpromoted Ag/α-Al_2O_3, ranging from 25 to 80%, depending on the reaction conditions (between 220 to 275 °C) and reactant partial pressures (between 1 to 17 bar).[2,4–12] As discussed in **Chapter 1** typical reaction conditions are between 200 – 280 °C and 1 – 3 mPa, therefore the reaction conditions differ significantly in terms of operating pressure from industrial ones, however are similar to other literature conditions. As shown in *Figure 4.1*, there is a clear decrease in EO selectivity when comparing Ag/γ-Al_2O_3 to Ag/α-Al_2O_3, indicating why α-Al_2O_3 is used compared to γ-Al_2O_3. There is also a large increase in acetaldehyde, when catalysed with Ag/γ-Al_2O_3 showing that the Ag/α-Al_2O_3 is the more selective catalyst as expected.[11]

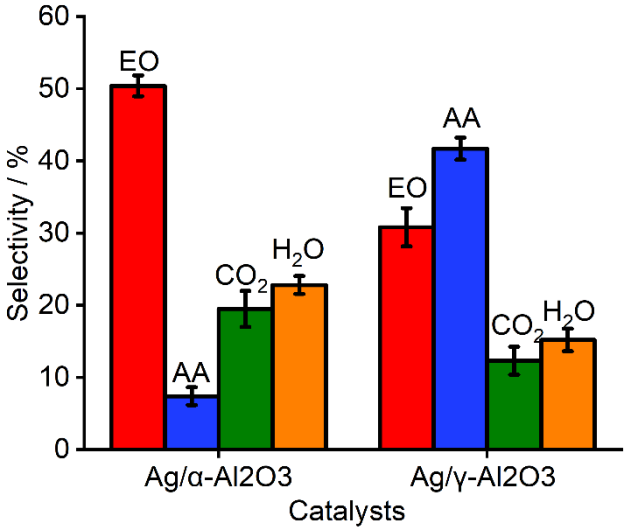

Figure 4.1: A comparison of selectivity between Ag/α-Al_2O_3 and Ag/γ-Al_2O_3. Errors are based on 3 repeat measurements.

Ethylene conversion was calculated and displayed in *Table 4.2*. The range of ethylene conversion in the literature is typically reported under these conditions to be between 1.5 to

12.5% depending on the reaction conditions and reactant partial pressures, therefore indicating that the conversions of 7.71% and 3.69% are in the correct range.[2] There is a decrease in ethylene conversion between Ag/α-Al_2O_3 and Ag/γ-Al_2O_3. The access to the silver may be limited by the increase in porosity of the Ag/γ-Al_2O_3 compared to the Ag/α-Al_2O_3 causing a decrease in conversion.

Table 4.2: A table showing the ethylene conversion and percentage error based on 3 repeat measurements for both Ag/α-Al_2O_3 and Ag/γ-Al_2O_3.

Catalyst	Ethylene Conversion / %	% Error
Ag/α-Al_2O_3	7.7	0.4
Ag/γ-Al_2O_3	3.7	0.1

Minahan *et al*. state that the α-Al_2O_3 must have low surface area (< 2 m^2 g^{-1}) and low acidity to prevent the complete oxidation of ethylene and EO.[3] Therefore, BET was undertaken to investigate the surface area. Commonly in literature, it is suggested that the α-Al_2O_3 surface area is much lower than the γ-Al_2O_3 surface area, as shown in *Table 4.3*, it confirms that the surface area of α-Al_2O_3 is much lower and below 2 m^2 g^{-1} compared to γ-Al_2O_3.[13] This supports the larger surface area of γ-Al_2O_3 giving rise to the isomerisation of EO to AA and therefore a reduction in EO selectivity.

Table 4.3: BET surface areas of two catalysts, Ag/α-Al_2O_3 and Ag/γ-Al_2O_3.

Catalyst	BET Surface Area / m^2 g^{-1}
Ag/α-Al_2O_3	1.4
Ag/γ-Al_2O_3	206.9

Pore size analysis was also conducted at the same time as the surface area was measured, these results are shown in *Table 4.4*.

Table 4.4: Pore size analysis of two catalysts, Ag/α-Al_2O_3 and Ag/γ-Al_2O_3.

Catalyst	Adsorption Average Pore Diameter / Å
Ag/α-Al_2O_3	30.5
Ag/γ-Al_2O_3	60.4

The surface chemistry of α-Al_2O_3 and γ-Al_2O_3 differs mainly due to their crystalline structures and surface properties. α-Al_2O_3 is an ordered material, has a hexagonal crystal structure, lower surface area, less chemically reactive and less porous whilst γ-Al_2O_3 is a disordered material, has a cubic or spinel-like structure, a much higher surface area, more chemically reactive and is generally more porous.[14] However there are also differences in α-Al_2O_3 and γ-Al_2O_3 regarding their acidity, Lewis acid sites are locations on the surface where

aluminium atoms can accept electron pairs and are typically associated with tetrahedral and penta coordinated Al^{3+} whilst Brønsted acid sites are located where aluminium atoms are bonded to hydroxyl groups which can donate protons, therefore these sites are often associated with tetrahedrally coordinated Al in the presence of bridging OH groups.[15,16] Due to the inherent order of α-Al_2O_3, the acid sites present are mainly Brønsted acid sites with Lewis acidity present from the tetrahedral and penta coordinated Al^{3+}. This contrasts γ-Al_2O_3 where the inherent disorder of the material leads to higher Lewis acid and Brønsted acid sites, with the increase in Brønsted acid sites due to the increase in hydroxyl groups and the increase in Lewis acidity arising from the increasing quantity of unsaturated aluminium ions present in the material.

4.1.1 Particle Sizes and Morphology

As discussed in **Chapter 1.1.1**, there are arguments for how the size of the Ag crystallite affects ethylene epoxidation.[2] XRD analysis was conducted to be able to both estimate the particle sizes of Ag and to confirm the crystallinity of the material. *Figure 4.2* shows the pattern obtained of the α-Al_2O_3 after calcination at 225 °C. This was taken for reference and to be able to compare with the patterns obtained from the samples of the catalysts. The crystal planes for the α-Al_2O_3 have been assigned to the individual reflections.[17]

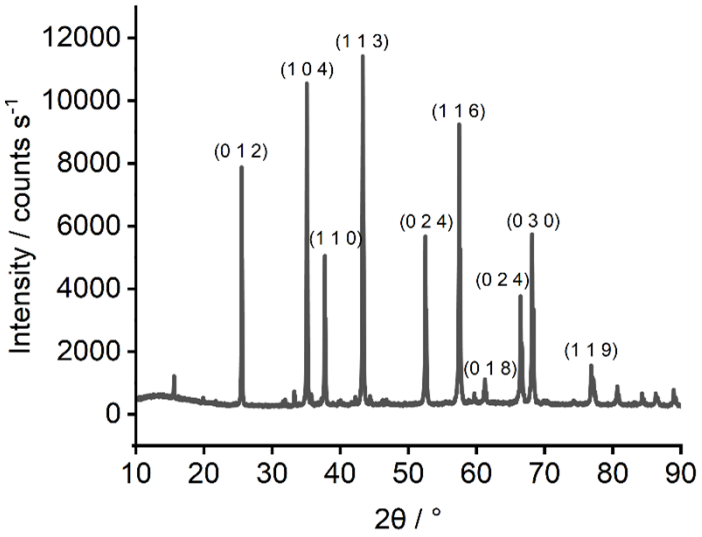

Figure 4.2: pXRD pattern of 225°C calcined α-Al_2O_3.

Ag/α-Al_2O_3 was analysed by pXRD and compared to α-Al_2O_3. As shown in *Figure 4.3*, many of the reflections from metallic silver are hidden by the α-Al_2O_3 as they overlap. The metallic Ag^0 reflections should be at 38.1 ° (1 1 1), 44.3 ° (2 0 0), 64.4 ° (2 2 0), 77.4 ° (3 1 1) and 81.5 ° (2 2 2).[17] These have been indicated by the arrows shown in *Figure 4.3*. There is some overlap between the Ag and the α-Al_2O_3 reflections, however, pXRD can confirm that

the Ag/α-Al_2O_3 catalyst contains additional reflections consistent with the presence of metallic Ag^0. With the addition of Ag to α-Al_2O_3 there appears to be a shift in the relative intensity of the reflections at around 38 °, this shift is likely to be due to the addition of Ag reflection overlapping with the α-Al_2O_3 reflection.

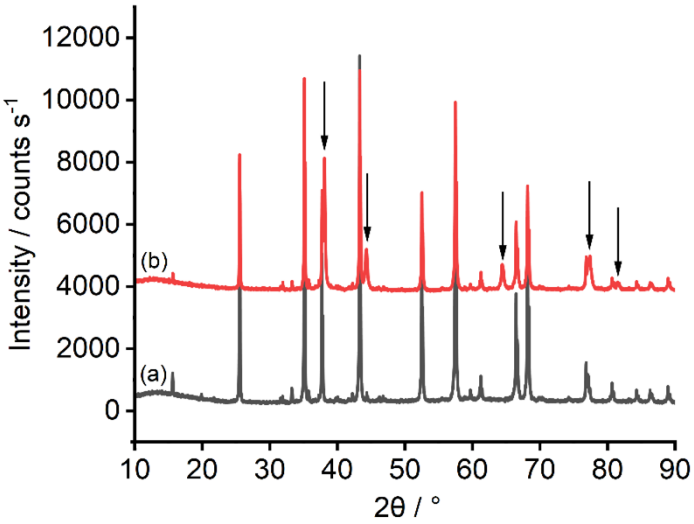

Figure 4.3: pXRD pattern of (a) α-Al_2O_3 and (b) Ag/α-Al_2O_3 both calcined at 225 °C. Patterns offset vertically for clarity.

The pXRD of Ag/γ-Al_2O_3 is shown in *Figure 4.4*, however, it is difficult to identify the silver reflections within the broad background from γ-Al_2O_3, as expected with γ-Al_2O_3 being less crystalline and a disordered material structure.[18] However, ICP-OES (*Table 4.1*) has shown that there is Ag present in the Ag/γ-Al_2O_3 catalyst. It is however possible that the silver features seen in the case of the Ag/α-Al_2O_3 are due to larger silver particles and therefore sharper (easier to see in the presence of the alumina background). This is reinforced by the sharp features in Ag/α-Al_2O_3 being around 1000 counts s^{-1} high, which would be readily visible above the γ-Al_2O_3 baseline. As shown in the BET analysis, γ-alumina has a much higher surface area than α-alumina, so smaller particles may have resulted in the case of this γ-alumina support. The disorder, high surface area and smaller Ag particles of γ-Al_2O_3 highlights significant differences from the α-Al_2O_3 commonly used as the support for ethylene epoxidation.

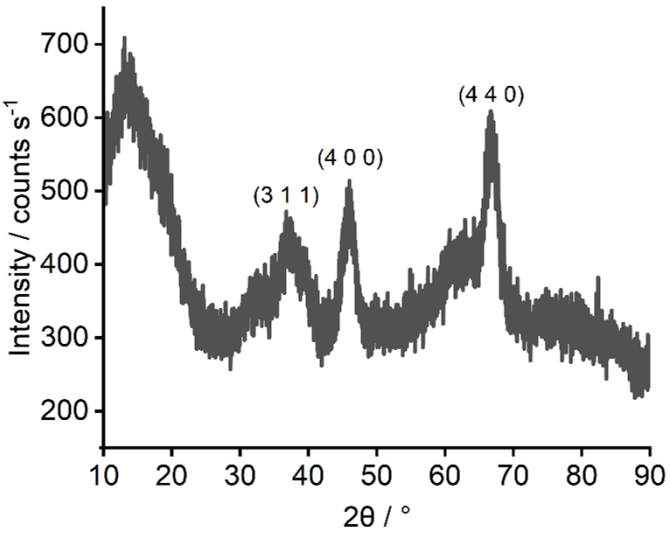

Figure 4.4: pXRD pattern of Ag/γ-Al_2O_3.

Comparisons between the Ag/α-Al_2O_3 catalyst before the reaction, after O_2 pretreatment and after ethylene epoxidation was investigated using pXRD to show how the crystallinity and the silver crystallite sizes change. As shown in the pXRD in *Figure 4.5*, the patterns are remarkably similar with slight differences in intensities. The graph was expanded at the Ag (2 2 0) reflection to investigate the reflection broadenings as there is no overlap of α-Al_2O_3 here. As shown in the pXRD in *Figure 4.6*, it suggests that ethylene epoxidation influences the size of the Ag crystallites due to the changes in the reflection widths. With the addition of the O_2 pretreatment to Ag/α-Al_2O_3, there appears to be a shift in the relative intensity of the reflections at around 38 °, this shift could be for a few different reasons. Suggestions include internal stresses, strains or defects within the crystal structure which can alter the diffraction pattern therefore affecting the relative intensities of the peaks, the presence of different phases or impurities is able to lead to shift in peak intensities, instrumental factors including sample preparation, or a preferred orientation, where a change in crystallographic plans may be more aligned with the X-ray beam, leading to higher intensities for those planes.[19,20]

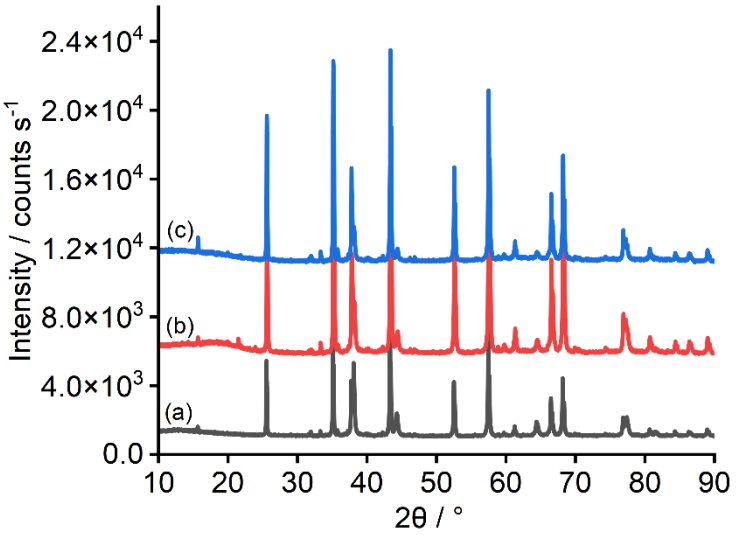

Figure 4.5: pXRD pattern where (a) is Ag/α-Al_2O_3, (b) is Ag/α-Al_2O_3 after O_2 pretreatment and (c) is Ag/α-Al_2O_3 after ethylene epoxidation. Patterns offset for clarity.

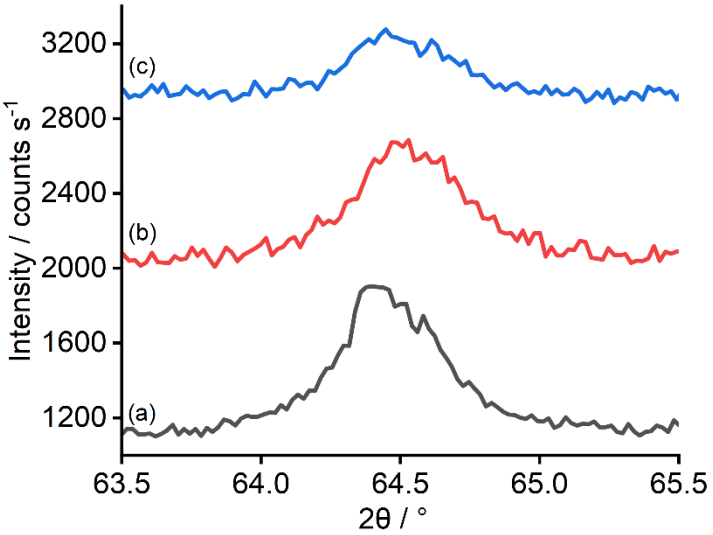

Figure 4.6: pXRD pattern where (a) is Ag/α-Al_2O_3, (b) is Ag/α-Al_2O_3 after O_2 pretreatment and (c) is Ag/α-Al_2O_3 after ethylene epoxidation. Patterns offset for clarity.

The size of the silver crystallite was investigated using the reflection at 64.5 ° with the Scherrer equation. The FWHM used for each catalyst and the resultant crystallite sizes are shown in *Table 4.5*. There is a slight decrease in average Ag crystallite size from 51 nm to 47 nm, during the O_2 pre-treatment, indicating that a part of the pre-treatment is to initiate the dispersal of silver crystallites, however, there increase in the average crystallite size after the ethylene epoxidation, owing to potential sintering of the particle during the reaction.

Table 4.5: Summary of FWHM and the particle size estimation from pXRD data using the Scherrer equation. Errors were calculated based on the error from fitting the Gaussian functions.

Catalyst	Reflection(s) used / °	FWHM / °	Estimated Crystallite Size / nm	Error in Gaussian fit of Crystallite Size / nm
Ag/α-Al_2O_3	64.5	0.36	51.2	±1.4
Ag/α-Al_2O_3 after O_2 pretreatment	64.5	0.39	47.2	±1.1
Ag/α-Al_2O_3 after ethylene epoxidation	64.5	0.32	57.6	±0.9

In the literature, it is thought that the selectivity towards EO is partially determined by the distribution of silver, where there are more Ag active sites and fewer hydroxyl groups (acid sites) on the surface of the Al_2O_3 with more distributed Ag.[3,21] Therefore, TEM (shown in *Figure 4.7*) was undertaken, to investigate the distribution of Ag on the Al_2O_3. Darker roughly spherical metal particles of silver are visible on the lighter alumina support, although they differ somewhat in size in the two images below, suggesting smaller and larger particles may both be present on the catalyst in different areas. From pXRD analysis as discussed earlier, the particle size was estimated using the Scherrer equation is around 51 nm – but this is obtained from a volume averaging technique and will be dominated by the large particles as seen in *Figure 4.7* left image. This suggests that the metal particles of Ag are sometimes well distributed and sometimes clumped together, which could correspond to the α-Al_2O_3 having a small surface area, so being less able to spatially separate the silver and inhibit agglomeration.

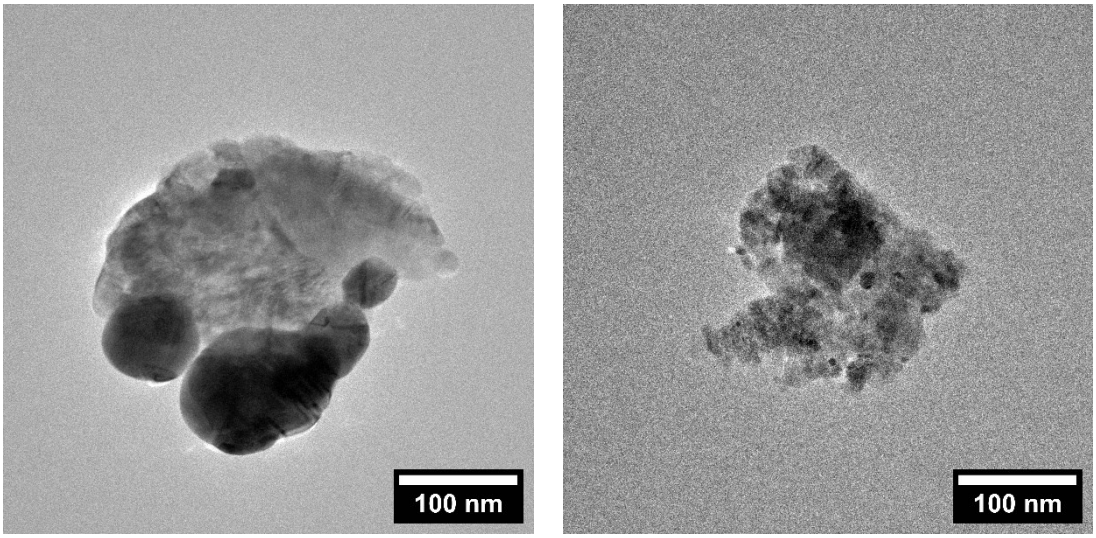

F*igure 4.7: Representative TEM images of Ag/α-Al_2O_3 catalyst*

For a comparison, Ag/γ-Al_2O_3 was investigated, as suggested in the TEM in *Figure 4.8*, the Ag metal particles are more distributed compared to the Ag/α-Al_2O_3 catalyst, which is likely to be a result of the γ-Al_2O_3 having a larger surface area compared to Ag/α-Al_2O_3. Although it seems like there is a larger distribution of the active Ag, there is also an increase in the hydroxyl groups on the support, explaining the lower EO and increased AA selectivity.

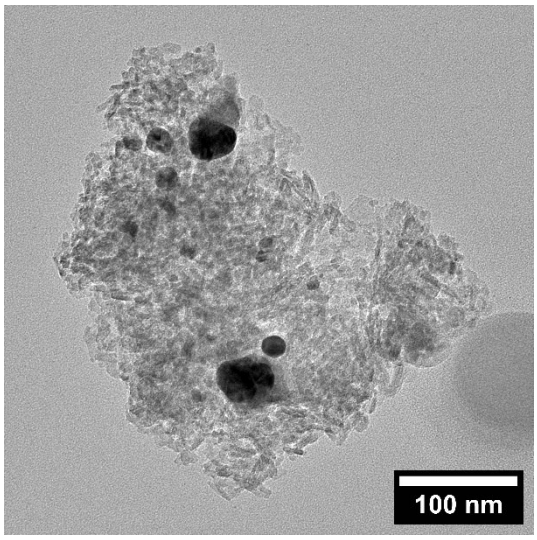

Figure 4.8: Representative TEM images of Ag/γ-Al_2O_3 catalyst

Due to the hidden reflections of Ag in the Ag/γ-Al_2O_3 pXRD, crystallite sizes were unable to be identified, therefore, the metal particle size distribution was investigated with Ag/γ-Al_2O_3 as shown in *Figure 4.9*. Here it was found that the average crystallite size is 31.3 ± 3.4 nm, this is much smaller compared to α-Al_2O_3, agreeing with the TEM and pXRD data that there is more distribution of Ag on γ-Al_2O_3.

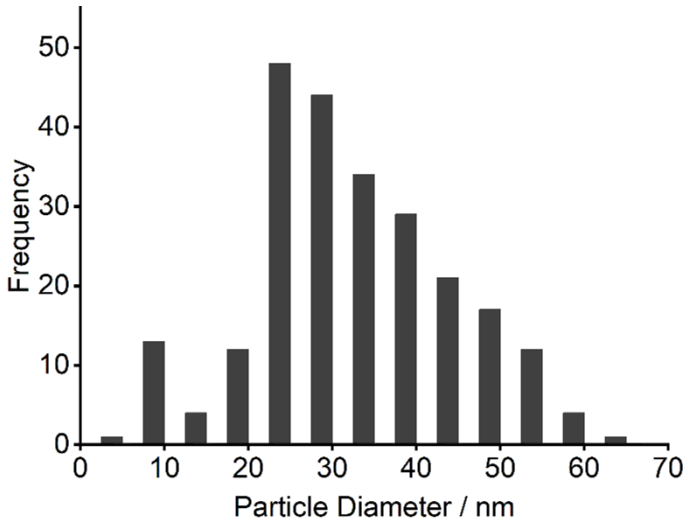

Figure 4.9: Metal particle size distribution for the Ag/γ-Al_2O_3 catalyst, looking at 240 silver particles.

Elemental analysis using STEM was undertaken on Ag/α-Al_2O_3 to investigate the locations of Ag. As shown in the STEM in *Figure 4.10*, there are large clusters of Ag towards the

edges of the catalyst, with distribution throughout. Whilst the TEM left image (*Figure 4.7*) showed little distribution with more clusters, the TEM right image, showed more distribution. This STEM image shows more clusters of Ag throughout the catalyst. The STEM images show areas where there appears to show a high intensity for Ag but a low intensity for Al, this gives indication that there is a large depth of the Ag surface layer, likely “hiding” the Al underneath.

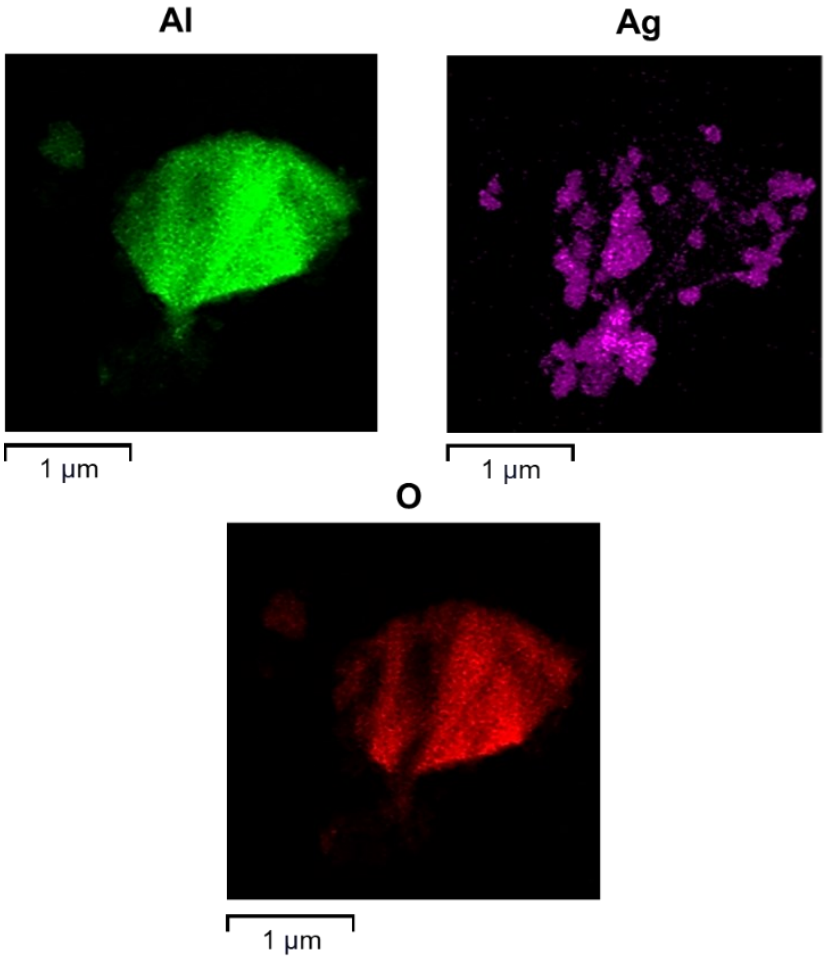

Figure 4.10: Elemental Mapping (using EDX), for the Ag/α-Al_2O_3, with aluminium shown in green, silver shown in purple, and oxygen shown in red.

The spent catalyst of Ag/α-Al_2O_3 was also investigated with STEM (shown in *Figure 4.11*), in agreement with the pXRD, there is sintering of the Ag particles and less distributed Ag.

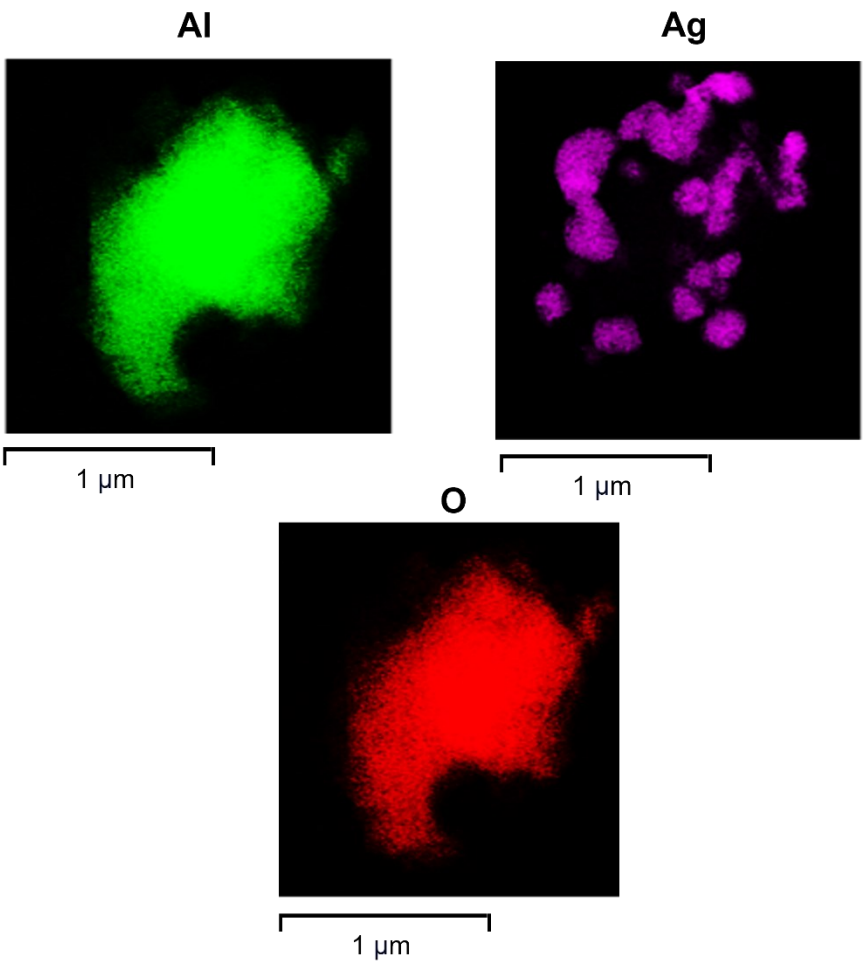

Figure 4.11: Elemental Mapping (using EDX), for the spent Ag/α-Al_2O_3, with aluminium shown in green, silver shown in purple, and oxygen shown in red.

4.1.2 Understanding the Role of Oxygen

As discussed in **Chapter 1.1.2.1**, there is still discussion over the type of oxygen species that are selective during ethylene epoxidation. Therefore, it was thought useful to investigate the oxygen species in the Ag/α-Al_2O_3 catalyst to compare this catalyst to the literature findings. Firstly, the O_2 TPD of α-Al_2O_3 was investigated (*Figure 4.12*), here as expected, there are no oxygen peaks.[22]

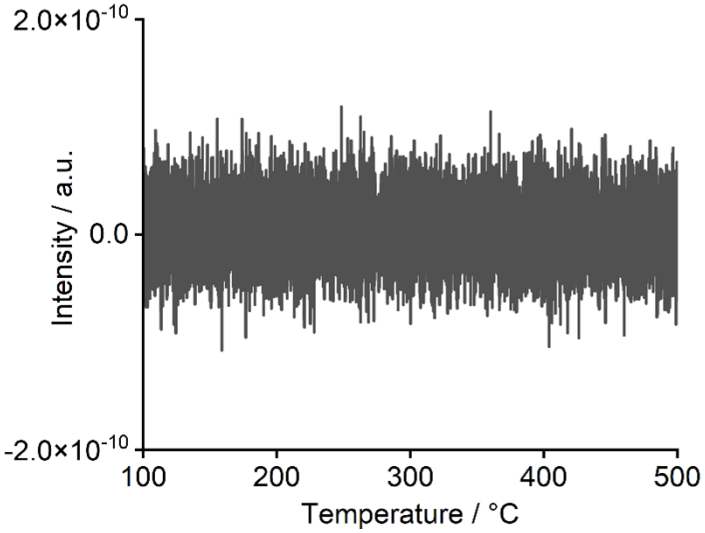

Figure 4.12: O_2-TPD profile of α-Al_2O_3 following O_2 adsorption at 225 °C (heating rate of 5 °C min^{-1}).

One peak was found in the Ag/α-Al_2O_3 O_2 TPD at 350 °C (shown in *Figure 4.13*), which is likely to correspond to surface-bound atomic oxygen desorbing.[2,23–25] Due to the γ-Al_2O_3 having a high surface area and porous structure, it is likely that it was plugging and blocking the reaction tubes leading to inaccurate results.[26,27] γ-Al_2O_3 makes an adsorbent leading to the accumulation of reaction by-products or impurities within its pores, causing blockages, the particles can also agglomerate under some reaction conditions leading to larger clusters that can obstruct the flow of reactants.[26,27] Therefore, due to inaccurate results no peaks were able to be distinguished in any of the Ag/γ-Al_2O_3-based catalysts.

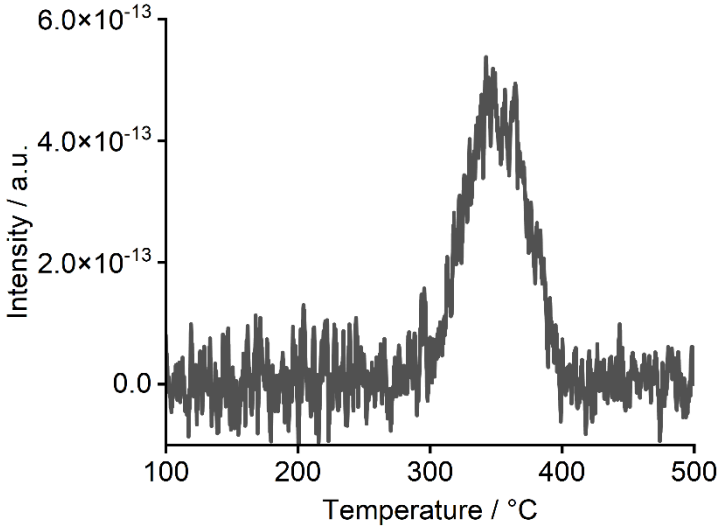

Figure 4.13: O_2-TPD profile of Ag/α-Al_2O_3 after O_2 pretreatment (heating rate of 5 °C min^{-1}).

H_2-TPR was undertaken, to investigate the Ag-O interactions. Whilst very little research has been undertaken on this, the hydrogen reduction of rhenium oxides ranges from between 300 – 600 °C where no literature can be found on the reduction of caesium oxides.[28–32] Therefore, due to the lack of literature and difficulty in peak deconvolution due to multiple

overlapping Ag-O interactions and promoter reductions, the total hydrogen consumption and therefore the amount of oxygen adsorbed was investigated where *Equation 4.1* applies.

$$H_2 + O_{ads} \longrightarrow H_2O$$

Equation 4.1: Forming water from hydrogen and the adsorbed oxygen at the silver sites.

H_2-TPR was undertaken on Ag/α-Al_2O_3 after argon pretreatment (shown in *Figure 4.14*) here the total corresponded to 0.56 ± 0.03 H_2 molecules per silver atom. There was an increase when the H_2-TPR was undertaken on Ag/α-Al_2O_3 after O_2 pretreatment (shown in *Figure 4.15*) to 0.79 ± 0.04 H_2 molecules per silver atom, indicating that there are more O_{ads}. Very little literature has been undertaken with looking at H_2-TPR on Ag/α-Al_2O_3 however there are some suggestions. It has been suggested that between 120 – 200 °C the peaks correspond to the reduction of surface oxygen on Ag. Between 135 – 367 °C the peaks are assigned to the reduction of large AgO clusters whilst between 290 – 500 °C the peaks correspond to the reduction of small and well-dispersed Ag_2O particles. At high reduction temperatures around 417 – 646 °C the isolated AgO clusters reduce whilst peaks between 460 – 680 °C were assigned to stable and well-dispersed Ag^+ (Ag_2O) ions.[33–35] As shown above there is large overlap between all different silver-oxygen species making it difficult to exactly identify and assigned different peaks.

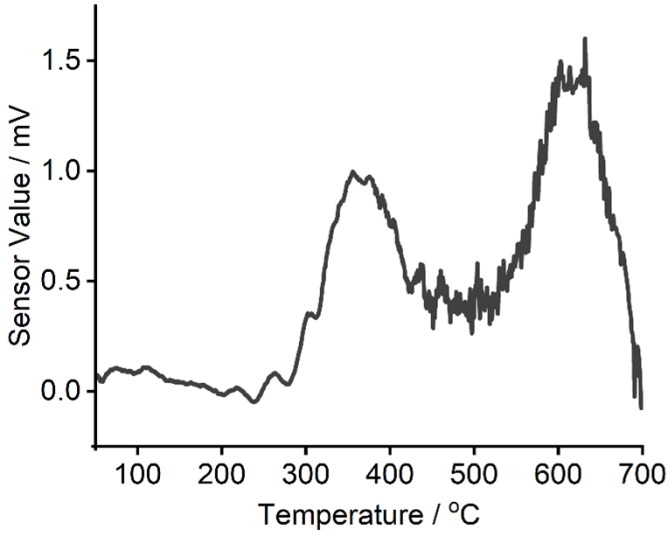

Figure 4.14: H_2-TPR of Ag/α-Al_2O_3 after argon pretreatment, (heating rate of 5 °C min^{-1}).

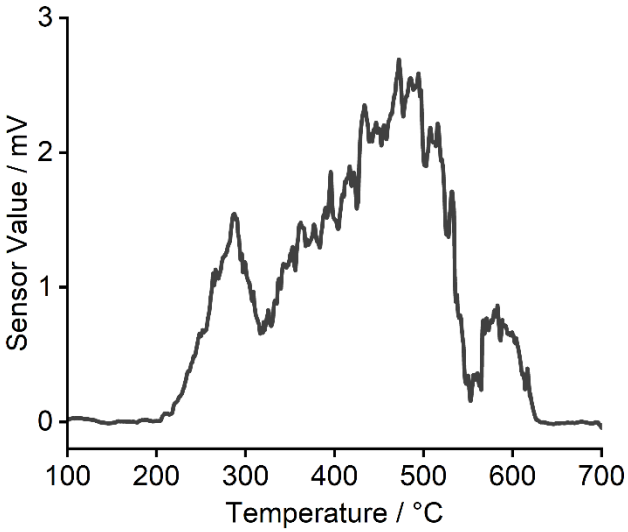

Figure 4.15: H_2-TPR of Ag/α-Al_2O_3 after O_2 pretreatment (heating rate of 5 °C min^{-1}).

Ex situ XPS was undertaken, as a starting point to give more evidence into the oxygen species present under atmospheric oxygen exposure. It is now commonly accepted that oxygen on silver can be classified as electrophilic (O_{elec}) or nucleophilic (O_{nuc}) where the O_{elec} is responsible for the selective reaction pathway to ethylene oxide.[2] Here O1s spectra were obtained, *Figure 4.16,* shows two species, there is a main peak at 530 eV, with a shoulder at 532 eV and no intensity below 529 eV (corresponding to O_{nuc}).[36,37] Due to the large ratio between oxygen and aluminium (shown in *Table 4.6*), this can be ascribed based on the literature as, atomic electrophilic oxygen and Ag_x-O_2 respectively.[36,37] As discussed in **Chapter 1.1.2.1**, It has been suggested that hybrid atomic-molecular oxygen structures form where one adsorbed O atom reacts with one lattice O atom on the surface or in the subsurface of Ag. Here one of the O atoms in the hybrid structure must be embedded into the Ag lattice, therefore there is a need for an oxidised Ag surface whilst the other is by the adsorbed O atom. This gives evidence of both Ag_x-O_2 and atomic electrophilic O being on the surface of the catalyst.

It should be noted that the low surface area support means the oxygen signal from α-Al_2O_3, while present is much smaller than on the γ-Al_2O_3 samples where it is overwhelmingly dominant (the α-Al_2O_3 is largely thought to be buried below a layer of Ag). There is a shift of γ-Al_2O_3 by 0.2 eV, which is likely to be within the calibration error due to the minute shift.

*Table 4.6: A table showing the ratios of oxygen: Al_2O_3 found by using the cross sections. This calculation is explained in **Appendix 3**.*

		Surface Metal Ratios	
		O1s	**Al2p**
Sample	**Ag/α-Al_2O_3**	12.5	1
	Ag/γ-Al_2O_3	13.7	1

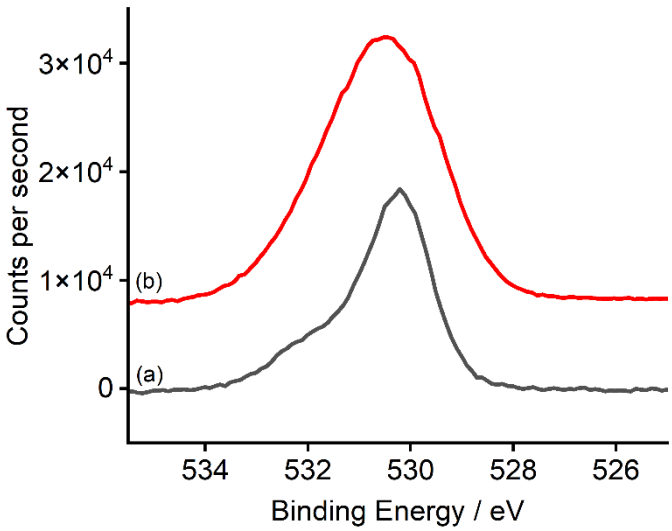

Figure 4.16: XPS spectra of all O1s data (after applying binding energy correction verified by the shift of the Al 2p peak and after subtraction of a Shirley background). Where (a) is Ag/α-Al_2O_3 and (b) is Ag/γ-Al_2O_3 both as prepared. All samples are as prepared. Spectra have been offset for clarity.

Peak deconvolution was undertaken on the *ex situ* O1s XPS of both Ag/α-Al_2O_3 and Ag/γ-Al_2O_3 to show the two species present in the catalysts shown in *Figure 4.17* and *Figure 4.18,* respectively. The determined peak areas of the two catalysts are also shown in *Table 4.7*.

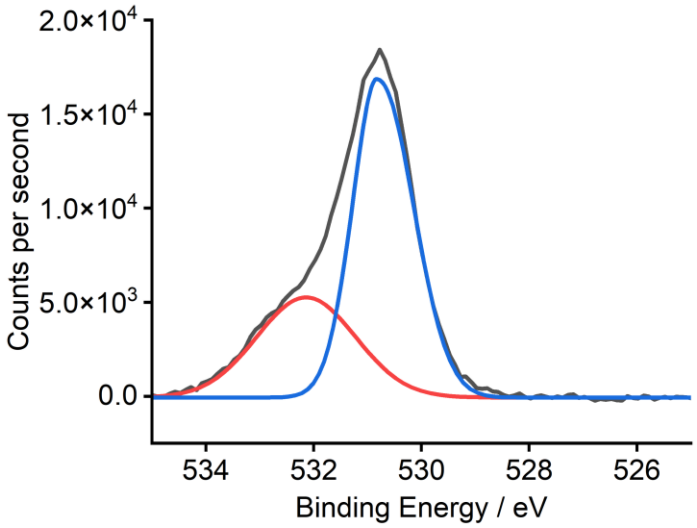

Figure 4.17: Peak deconvolution of the XPS spectra of the O1s looking at Ag/α-Al_2O_3. All samples are as prepared, after applying binding energy correction verified by the shift of the Al 2p peak and after subtraction of a Shirley background.

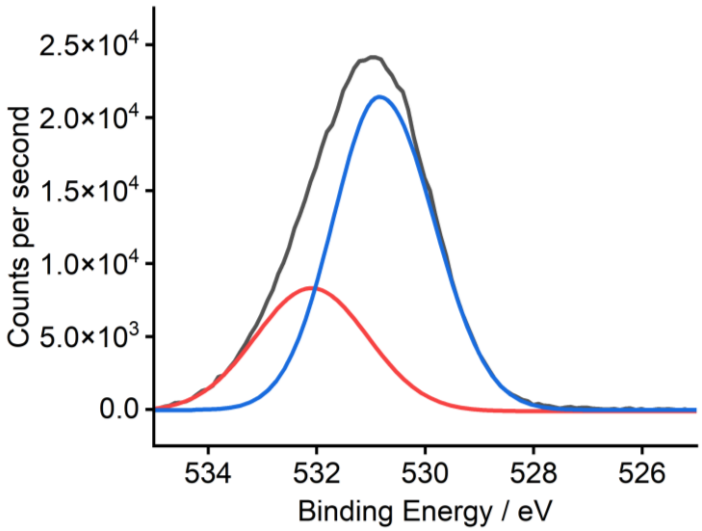

Figure 4.18: Peak deconvolution of the XPS spectra of the O1s looking at Ag/γ-Al_2O_3. All samples are as prepared, after applying binding energy correction verified by the shift of the Al 2p peak and after subtraction of a Shirley background.

Table 4.7: A table showing the peak areas for the peak deconvolution of the XPS spectra of the O1s looking at both Ag/α-Al_2O_3 and Ag/γ-Al_2O_3.

Catalyst	Peak Area of Blue Peak - atomic electrophilic oxygen / counts	Peak Area of Red Peak - Ag_x-O_2 / counts
Ag/α-Al_2O_3	25354.89	12227.33
Ag/γ-Al_2O_3	48935.63	21894.52

In situ XPS of Ag/α-Al_2O_3 was undertaken by looking at the oxygen species during both O_2 pretreatment and under ethylene epoxidation. As shown in *Figure 4.19*, at 225 °C under

argon, the peak is at 530.5 eV, which corresponds to atomic electrophilic oxygen.[38] There is an increase in the counts per second with the addition of O_2 pretreatment, indicating that there is more oxygen adsorbed agreeing with the H_2-TPR data. There is a small shift to 530.8 eV with the addition of O_2 pretreatment indicating that there is an increase in the electrophilicity of the oxygen, where there is a reduced electron density of the adsorbed oxygen. The addition of ethylene in a 5:1 ratio of oxygen: ethylene causes an increase of 0.5 eV. In literature, electrophilic oxygen has been shown to range between 530 to 531 eV, nucleophilic oxygen has been shown to range between 528 to 529 eV, whilst at 532 eV has been shown to correspond to surface Ag_x-O_2 dioxygen species, therefore indicating at the 5:1 ratio there is a mixture of both nucleophilic oxygen and the electrophilic oxygen.[36,39] When the conditions are under a 2:1 ratio of oxygen: ethylene at 225 °C the peak shifts to 531.8 eV. This corresponds to surface Ag_x-O_2 dioxygen species being present under reaction conditions. These O 1s peaks are all very broad indicating that there is a mixture of surface Ag_x-O_2 dioxygen species and atomic electrophilic oxygen present on the surface under reaction conditions. As shown in the peak deconvolutions there are two peaks corresponding to the Ag_x-O_2 dioxygen species and the atomic electrophilic oxygen. Finally, when the conditions are under a 1:1 ratio of oxygen: ethylene at 225 °C the peak shifts to 532 eV where the peak deconvolutions indicate there is only the Ag_x-O_2 dioxygen species present.

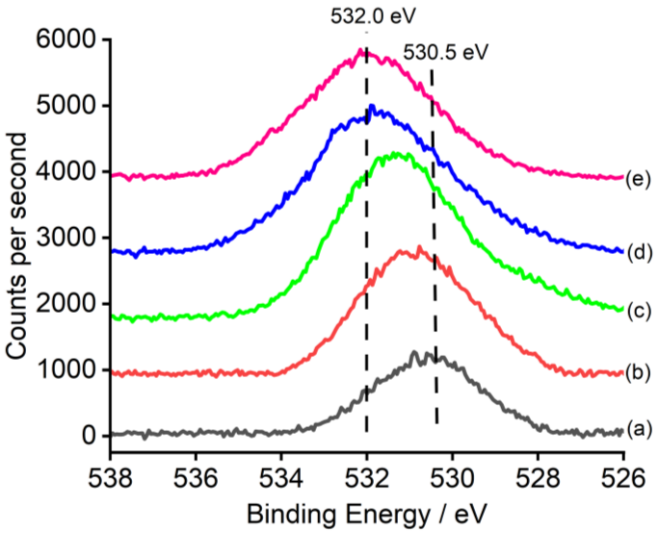

Figure 4.19: XPS spectra of all O1s data of Ag/α-Al_2O_3 at 225 °C (after applying binding energy correction verified by the shift of the Al 2p peak and after subtraction of a Shirley background). Where (a) is under argon, (b) is under O_2 pretreatment, (c) is a 5:1 ratio of oxygen: ethylene, (d) is a 2:1 ratio of oxygen: ethylene and (e) a 1:1 ratio of oxygen: ethylene.

Peak deconvolution was also undertaken on the *in situ* O1s XPS data with looking at Ag/α-Al_2O_3. Here *Figure 4.20, 4.21, 4.22, 4.23* and *4.24* shows the peak deconvolution of Ag/α-Al_2O_3 under argon, under O_2 pretreatment, under a 5:1 ratio of oxygen: ethylene, under

2:1 ratio of oxygen: ethylene and under 1:1 ratio of oxygen: ethylene, respectively. The determined peak areas of the catalyst under different reaction conditions are also shown in *Table 4.8*.

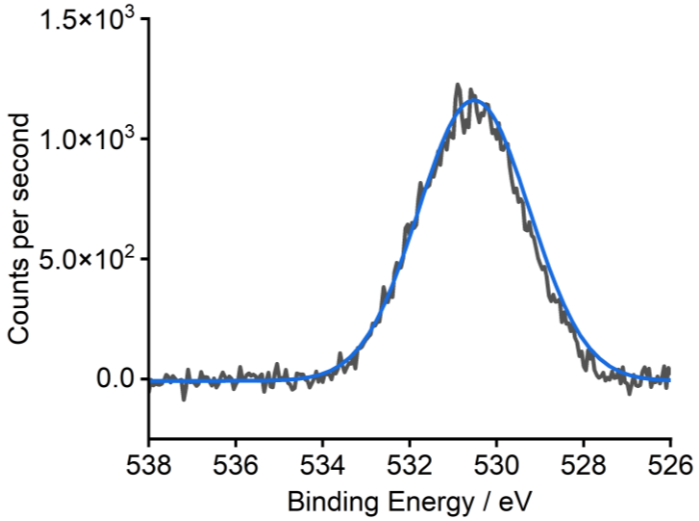

Figure 4.20: Peak deconvolution of the XPS spectra of the O1s looking at Ag/α-Al_2O_3 under argon. All samples are as prepared, after applying binding energy correction verified by the shift of the Al 2p peak and after subtraction of a Shirley background.

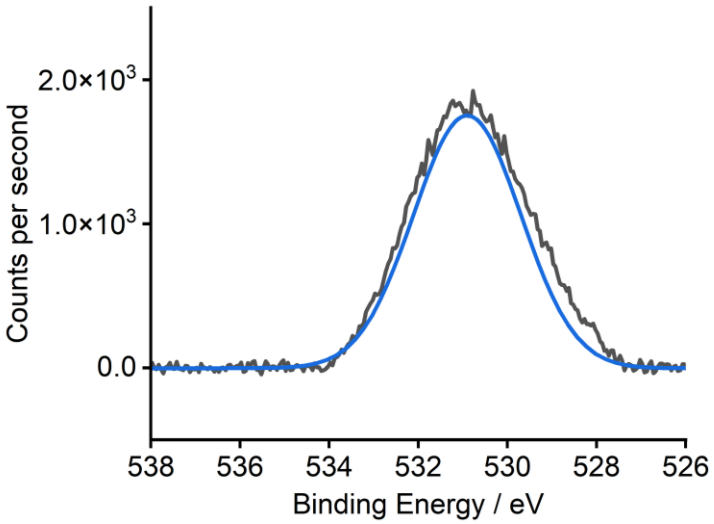

Figure 4.21: Peak deconvolution of the XPS spectra of the O1s looking at Ag/α-Al_2O_3 under O_2 pretreatment. All samples are as prepared, after applying binding energy correction verified by the shift of the Al 2p peak and after subtraction of a Shirley background.

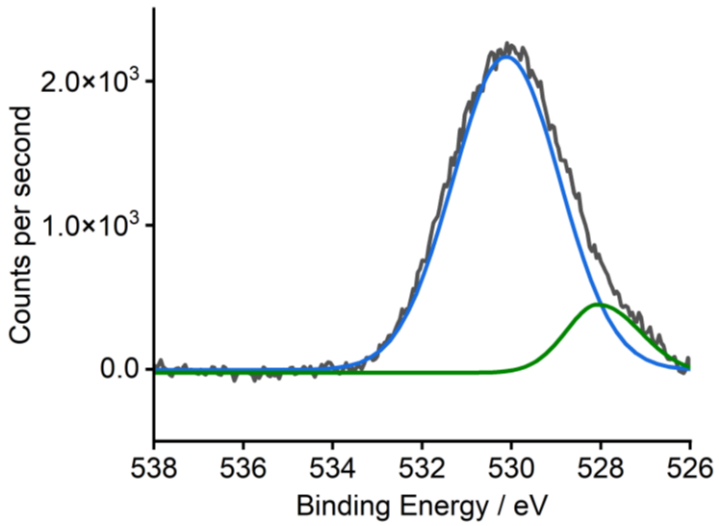

Figure 4.22: Peak deconvolution of the XPS spectra of the O1s looking at Ag/α-Al_2O_3 under a 5:1 ratio of oxygen: ethylene. All samples are as prepared, after applying binding energy correction verified by the shift of the Al 2p peak and after subtraction of a Shirley background.

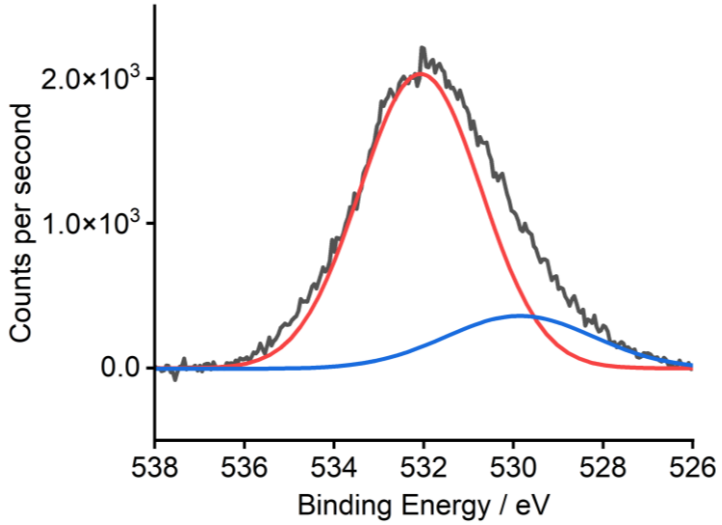

Figure 4.23: Peak deconvolution of the XPS spectra of the O1s looking at Ag/α-Al_2O_3 under a 2:1 ratio of oxygen: ethylene. All samples are as prepared, after applying binding energy correction verified by the shift of the Al 2p peak and after subtraction of a Shirley background.

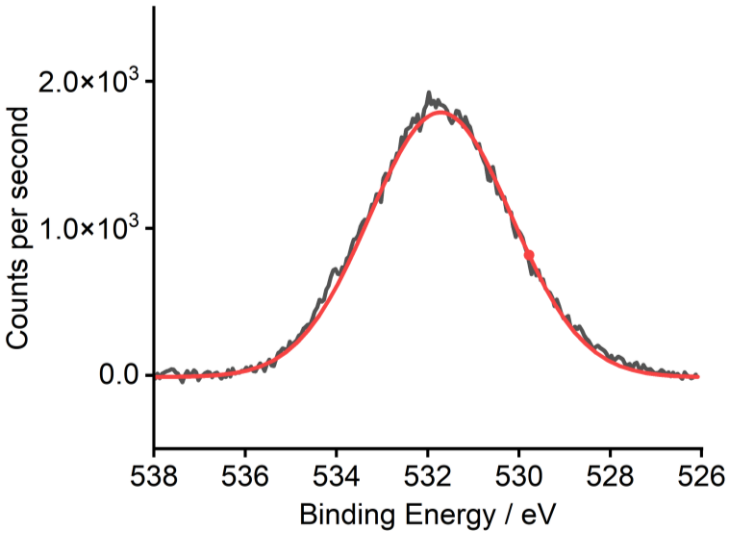

Figure 4.24: Peak deconvolution of the XPS spectra of the O1s looking at Ag/α-Al_2O_3 under a 1:1 ratio of oxygen: ethylene. All samples are as prepared, after applying binding energy correction verified by the shift of the Al 2p peak and after subtraction of a Shirley background.

Table 4.8: A table showing the peak areas for the peak deconvolution of the XPS spectra of the O1s looking at Ag/α-Al_2O_3 under different conditions.

Catalyst	Peak Area of Green Peak – nucleophilic oxygen / counts	Peak Area of Blue Peak - atomic electrophilic oxygen / counts	Peak Area of Red Peak - Ag_x-O_2 / counts
Ag/α-Al_2O_3 under argon	-	3423.02	-
Ag/α-Al_2O_3 under O_2 pretreatment	-	3751.61	-
Ag/α-Al_2O_3 under a 5:1 ratio of oxygen: ethylene	1704.35	8057.93	-
Ag/α-Al_2O_3 under a 2:1 ratio of oxygen: ethylene	-	1260.98	7664.27
Ag/α-Al_2O_3 under a 1:1 ratio of oxygen: ethylene	-	-	7035.17

4.1.3 Understanding the Structure of Silver

A large variety of different hypotheses are used to describe the nature of oxygen species on Ag and explain the drastic effects of oxygen coverage on EO formation rates and selectivity. To understand and gain information regarding the Ag species, Ag 3d XPS was undertaken (*Figure 4.25*).

The oxides of silver are of interest as in general they show an anomalous negative binding energy shift compared to the metal.[40] However, the overlaps of binding energy values for Ag 3d (shown in *Table 4.9*), makes species hard to distinguish.[41–43]

Table 4.9: Ag 3d bond energy values of interested Ag species.[41–44]

Species	Ag 3d 5/2 Bond Energy (eV)	Standard Deviation (eV)
Ag^0	368.2	0.1
AgO	367.9	0.4
Ag_2O	367.6	0.4

Table 4.9 shows that metallic Ag^0, Ag_2O and AgO are very difficult to distinguish at the surface with XPS, therefore it is difficult to distinguish in *Figure 4.25*. Due to the difficulty in distinguishing, the Ag 3d XPS will be investigated in terms of shifting binding energy. However, according to pXRD data discussed in **Chapter 4.1.1**, Ag^0 prevails in the bulk phase. There is a shift to 0.4 eV to a lower binding energy with Ag/γ-Al_2O_3, corresponding to an increase in silver oxide species.

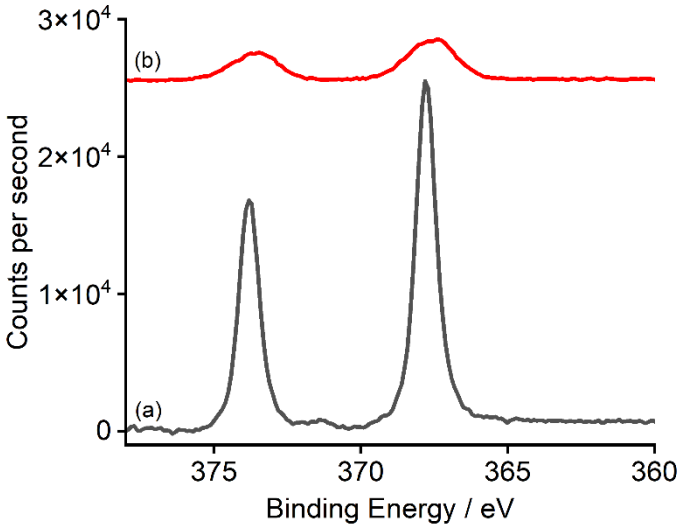

Figure 4.25: XPS spectra of all Ag3d data (after applying binding energy correction verified by the shift of the Al 2p peak and after subtraction of a Shirley background). Where (a) is Ag/α-Al_2O_3 and (b) is Ag/γ-Al_2O_3. All samples are as prepared. Spectra have been offset for clarity.

Table 4.10 shows that the ratios of Ag:Al have reduced, changing from Ag/α-Al_2O_3 to Ag/γ-Al_2O_3. Keijzer *et al*. found a clear trend of selectivity versus Ag:Al surface ratio, suggesting that there is an increased probability per ethylene oxide molecule to isomerise on support surface groups when the metal: support ratio is lower, leading to isomerisation of ethylene oxide to acetaldehyde.[45] This gives more indication into the large surface area of Ag/γ-Al_2O_3 having a large amount of hydroxyl groups leading to more isomerisation of EO to AA.

α-Al_2O_3 is primarily dominated by Lewis acid sites, but it does contain some Brønsted acid sites, whilst γ-Al_2O_3 is higher in both Lewis acid and Brønsted acid sites but more Brønsted acid sites due to the increase in hydroxyl groups. This large surface area of Ag/γ-Al_2O_3 leading to a larger amount of hydroxyl groups, therefore means that Ag/γ-Al_2O_3 contains more acid sites overall and more Brønsted acid sites compared to Ag/α-Al_2O_3.

Table 4.10: A table showing the ratios of metal: Al_2O_3 found by using the cross sections. This calculation is explained in ***Appendix 3****.*

		Surface Metal Ratios	
		Ag3d	**Al2p**
Sample	**Ag/α-Al_2O_3**	0.21	1
	Ag/γ-Al_2O_3	0.033	1

The depth of silver is theoretically present if the coverage is even across the surface. Therefore, this has been estimated from the XPS data using the electron escape depth or path length for both the Ag/α-Al_2O_3 and Ag/γ-Al_2O_3 catalysts (the calculations can be found in **Appendix 3**). The path length from the data which corresponds to being equivalent to a layer of Ag on Al_2O_3, for Ag/α-Al_2O_3, was found to be approximately 0.215 nm whilst for Ag/γ-Al_2O_3 it was found to be approximately 0.035 nm. This compares to the diameter of a silver atom of 0.144 nm and the diameter of an oxygen atom of 0.073 nm. This indicates that the Ag/α-Al_2O_3 surface is likely to be equivalent to a thin silver oxide layer on the surface. The layer of Ag on Ag/γ-Al_2O_3 is much less than an atom thick, meaning less of the oxide surface is covered by silver.

In situ Ag 3d XPS (shown in *Figure 4.26*) was undertaken on Ag/α-Al_2O_3 under four different conditions. These conditions included, at 225 °C under Ar, under the O_2 pretreatment, under a 5:1 ratio of oxygen: ethylene, a 2:1 ratio of oxygen: ethylene and a 1:1 ratio of oxygen to ethylene. There is a small decrease (0.4 eV) in the binding energy with the addition of O_2 pretreatment. This indicates that with the addition of O_2, the Ag becomes more oxidised. The addition of ethylene to the system indicates another small increase in binding energy,

indicating that under reaction conditions the Ag/α-Al_2O_3 becomes more oxidised. However, under the 5:1, 2:1 and 1:1 ratios of oxygen: ethylene, the binding energy of Ag did not change by a large amount, where they show very similar binding energies. Different signal-to-noise ratios are likely to be due to different gas attenuation/alignment reproducibility of the sample under different gas and heating conditions.

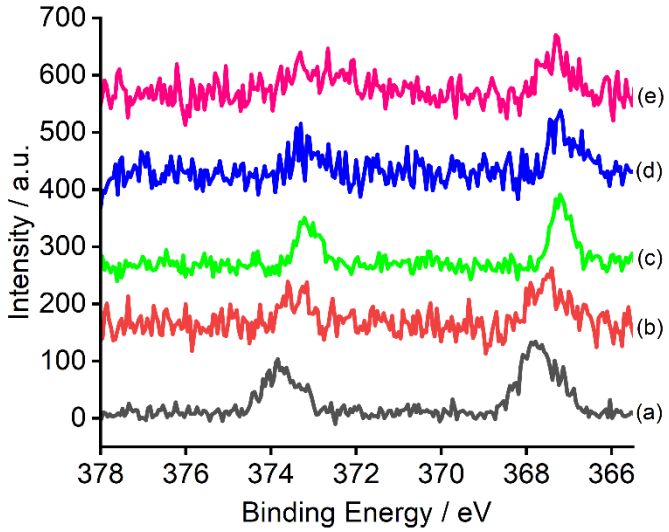

Figure 4.26: XPS spectra of all Ag3d data of Ag/α-Al_2O_3 at 225 °C (after applying binding energy correction verified by the shift of the Al 2p peak and after subtraction of a Shirley background). Where (a) is under argon, (b) is under O_2 pretreatment, (c) is a 5:1 ratio of oxygen: ethylene, (d) a 2:1 ratio of oxygen: ethylene and (e) a 1:1 ratio of oxygen: ethylene.

Raman spectroscopy can access the vibrational frequencies required to directly probe atomic oxygen and oxide layers on Ag surfaces and has been extensively used to examine these features.[46,47] Firstly as a reference, the Raman spectrum of α-Al_2O_3 was obtained, *Figure 4.27*. The two peaks that are at approximately 697 and 737 cm^{-1} are attributed to OH vibrations of weakly interacting hydroxyl groups on the Al_2O_3.[48]

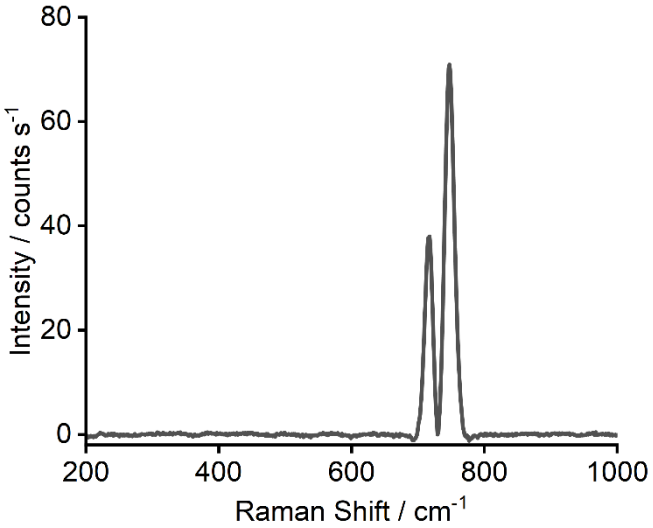

Figure 4.27: Raman spectrum of α-Al_2O_3 (after applying intensity response correction and subtraction of dark signal). Where the wavelength is 667-725 nm, slit width = 150 μm*, number of spectra = 10, and length of each spectrum = 10 s.*

A unique advantage of Raman with Ag surfaces is that it can give rise to surface-enhanced Raman spectroscopy (SERS), which can increase the intensity of the Raman vibrational signal by as much as a factor of 10^6.[49,50] The enhancement takes place at the metal surface, and it is where molecules which can undergo enhancement can be adsorbed onto the surface of a SERS particle or substrate material. SERS uses nanoscale roughened metal surfaces which are normally made from gold or silver however the exact mechanism of the enhancement effect of SERS is still a matter of debate in the literature.[51]

Although all Raman studies essentially detect the same oxygen species on Ag catalysts, there is no agreement as to the assignments for the different oxygen species on Ag.[2] Discussions of the molecular structures responsible for the high wavenumber (~600 – 1000 cm^{-1}) bands have not reached a consensus with researchers proposing that such features may reflect forms of atomic or diatomic oxygen present on surfaces and debating the roles (direct or indirect) these intermediates hold for ethylene epoxidation.[47]

Next, the Raman spectrum of Ag/α-Al_2O_3 was obtained, *Figure 4.29*. The broad peak between 200 – 400 cm^{-1}, is likely to correspond to atomic ν(Ag-O) on the Ag surface. The peak at around 620 cm^{-1} is likely to correspond to Ag-O_{bulk}.[2,36] The peaks that are at approximately 697 cm^{-1} and 737 cm^{-1} are attributed to OH vibrations of weakly interacting hydroxyl groups on α-Al_2O_3.[48]

As discussed in **Chapter 1.1.2.1**, It has been suggested that hybrid atomic-molecular oxygen structures form where one adsorbed O atom reacts with one lattice O atom on the surface or in the subsurface of Ag (shown in *Figure 4.28*). Here one of the O atoms in the hybrid structure must be embedded into the Ag lattice, therefore there is a need for an

oxidised Ag surface whilst the other is the adsorbed O atom. The small peak at 800 cm^{-1} is likely to correspond to the interaction of surface atomic O_{surf} with subsurface Ag-O on partially oxidised Ag O_{surf}=O_{sub}.[36] This is a hybrid species, where it is ν(O-O) in the surface atomic-molecular hybrid structure Ag_4-O-O.[36,39,46,52] This agrees with the data found in the O 1s XPS.

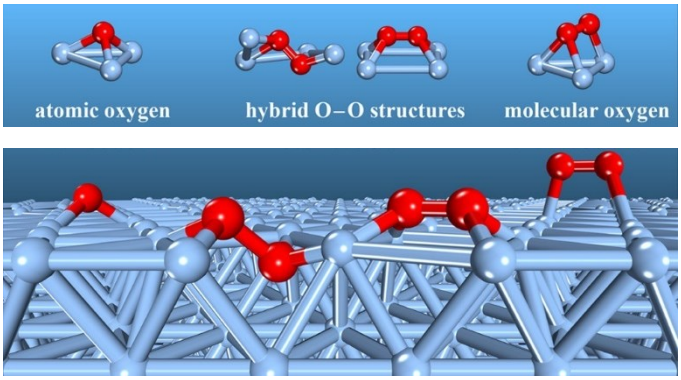

Figure 4.28: Showing the assignment of different oxygen species in Raman spectroscopy, where red shows the oxygen species, and grey shows the silver species. Reprinted with permission from Tang et al.[53] Copyright 2021 American Chemical Society.

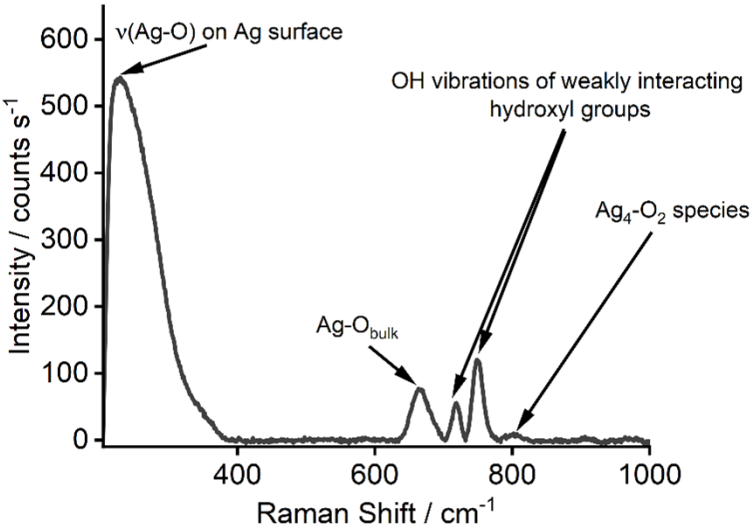

Figure 4.29: Raman spectrum of Ag/α-Al_2O_3 (after applying intensity response correction and subtraction of dark signal). Where the wavelength is 667-725 nm, slit width = 150 μm*, number of spectra = 10, and length of each spectrum = 10 s.*

Whilst recording the Ag/γ-Al_2O_3, the Raman spectrum was attempted (as shown in *Figure 4.30*), due to the large amount of fluorescence no peaks were able to be identified, even with the SERS improvement. SERS is also size dependent so this may be a weaker effect with smaller particles on the γ-Al_2O_3 and the enhancement is insufficient.[54] Due to γ-Al_2O_3 having a larger surface area it is thought that more impurities and defects lead to a large fluorescence signal with no peaks being able to be seen.

There are multiple ways to overcome these issues with fluorescence, these include Kerr Gated Raman, altering the wavelength of illumination and computational background removal.[55,56]

A way to eliminate fluorescence from swamping the weaker Raman signal in Raman spectroscopy is to have a Kerr-gated system. This takes advantage of the fact that after the interaction of light with a sample, Raman scattering happens instantaneously whilst the fluorescence happens picoseconds (ps) to nanoseconds (ns) later. Kerr-gating involves using a picosecond pulse length laser which is able to “gate out” the unwanted fluorescence after letting the Raman light come through.[57] Kerr-gating can be described as temporal gating, here the definition of temporal gating states that a pulsed laser produces a short pulsed Raman signal, the longer lived fluorescence is then rejected in the time domain. When the polarisers are parallel it is without a gate, the gating pulse is blocked and the experiment is dominated by fluorescence, whilst when they are crossed, there is a gate and the fluorescence is supressed.[57] Due to the two distinct time frames with only a small overlap, they are able to be easily split apart and be separated.

Another way to limit fluorescence from a Raman spectrum is altering the wavelength of illumination by selecting a different laser wavelength. For example, using a choice of a near infrared (NIR) or an ultraviolet (UV) laser wavelength may for some samples avoid exciting fluorescence. Using a near infrared laser wavelength, causes the laser photon to not have enough energy to be able to excite the molecular fluorescence, whilst with using a deep UV laser wavelength (< 300 nm), the fluorescence is excited, but the emission is separated in energy from the Raman signal therefore the Raman spectrum is able to be recorded without the fluorescence.[58]

As a result of the florescence causing the Raman spectrum to be “hidden”, another way to see the Raman spectrum is to remove the florescence background by computational methods. These have become quite a common way of correcting for the contributions from fluorescence background. They require no system modifications and show no limitations to the sample preparation.[59]

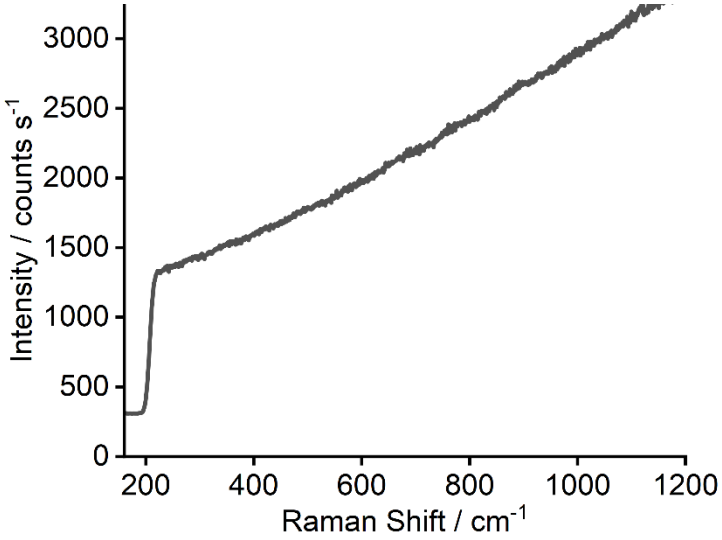

Figure 4.30: Raman spectrum of Ag/γ-Al_2O_3 (after applying intensity response correction and subtraction of dark signal). Where the is a wavelength of 667-725 nm, slit width = 150 μm*, number of spectra = 10, and length of each spectrum = 10 s.*

Investigations with Raman were undertaken with the comparison of the Ag catalysts after ethylene epoxidation (under a 2:1 ratio of oxygen: ethylene at 225 °C) transferred by cooling and preparing samples in air, shown in *Figure 4.31*. There is a change in peaks between 200 – 400 cm^{-1} which are known atomic Ag-O interactions, indicating a change in the surface Ag-O.[53] There is an increase in O-H hydroxyl groups on the α-Al_2O_3, this supports the evidence found with STEM, that sintering occurs after the ethylene epoxidation reaction as there is more α-Al_2O_3 exposed. There is a reduction in the peak at 800 cm^{-1}, corresponding to the hybrid O_{surf}=O_{sub} species. There are two new peaks at 900 cm^{-1} and 956 cm^{-1} which are likely to correspond to molecular oxygen, Ag-O_2.[53] This sample underwent ageing after ethylene epoxidation and before the Raman spectrum was undertaken.

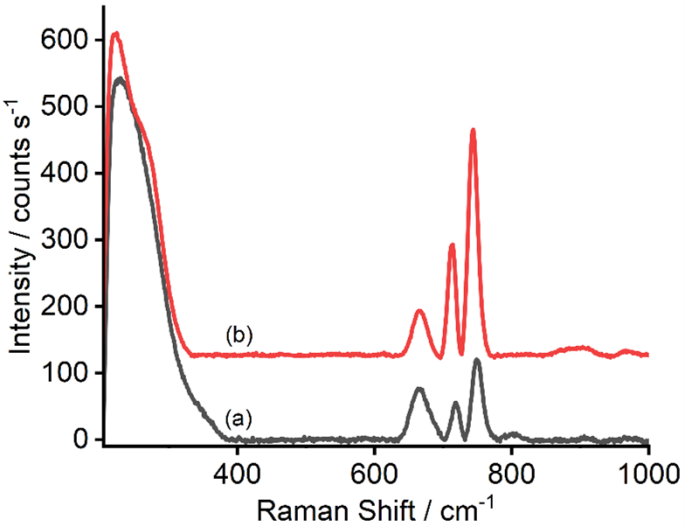

Figure 4.31: Raman spectra of Ag/α-Al_2O_3 zoomed in (after applying intensity response correction and subtraction of dark signal) where the wavelength of 667-725 nm, where (a) is Ag/α-Al_2O_3 before the reaction and (b) is Ag/α-Al_2O_3 after EE. Spectra have been offset for clarity.

4.1.4 Investigating Hydroxyl Groups and Acidity

As discussed previously, the hydroxyl groups cause the ethylene oxide to isomerise to acetaldehyde which is prone to rapid combustion on the silver surface.[21] Therefore, to investigate this *ex situ* DRIFTS was untaken on both α-Al_2O_3 as a reference (shown in *Figure 4.32*) and Ag/α-Al_2O_3 (shown in *Figure 4.33*) as a comparison. Most of the characteristic bands of α-Al_2O_3 were observed in the finger-print region of 400 – 1400 cm^{-1}. The bands at around 485 and 550, 627 and 668 cm^{-1} are assigned to the Al-O (Al-O-Al bending mode) stretching mode in the octahedral structure.[60,61] The band at 800 cm^{-1} is also likely to be due to the Al-O stretching mode in the tetrahedron.[61] The broad band between 1000 - 1150 cm^{-1}, is likely to indicate the symmetric bending of Al-O-H.[60] The weak absorption band at 1270 cm^{-1} indicates the presence of Al-O vibrations.[61] The broad bands between the range 3000 – 3500 cm^{-1} are due to hydroxyl (OH) vibrations, indicating the presence of Al-OH bonds in these samples.[62] When adding Ag, there are a few small bands between 1000 and 1400 cm^{-1} which could correspond to Ag-O, again indicating the presence of atomic oxygen.[60,61] The band at 3300 cm^{-1} is due to hydroxyl (OH) vibrations, indicating the presence of OH bonds in these samples.[62] There is a larger band here when Ag is added, indicating that the Ag affects the hydroxyl (OH) vibrations, indicating there are more surface hydroxyls.

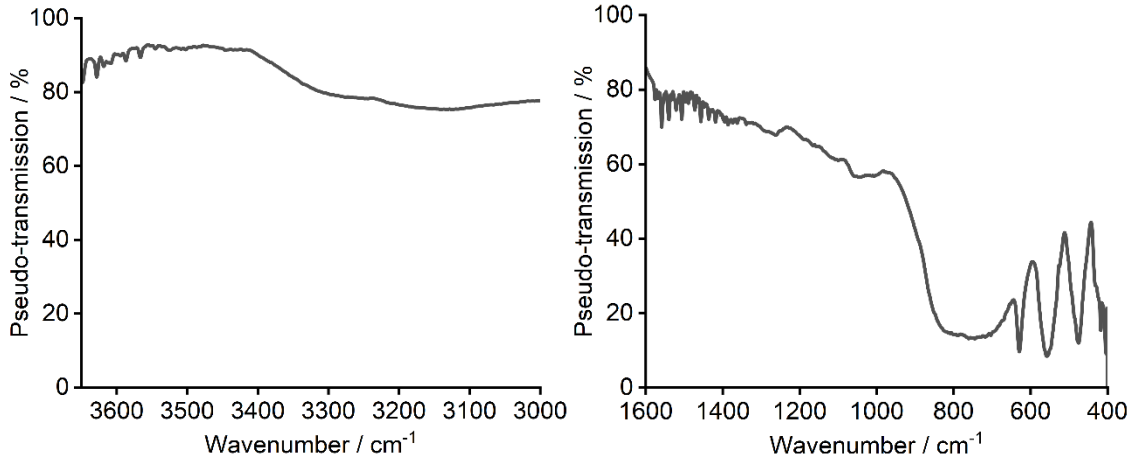

Figure 4.32: DRIFTS spectrum of α-Al_2O_3 showing the two key regions of interest, backgrounded against KBr.

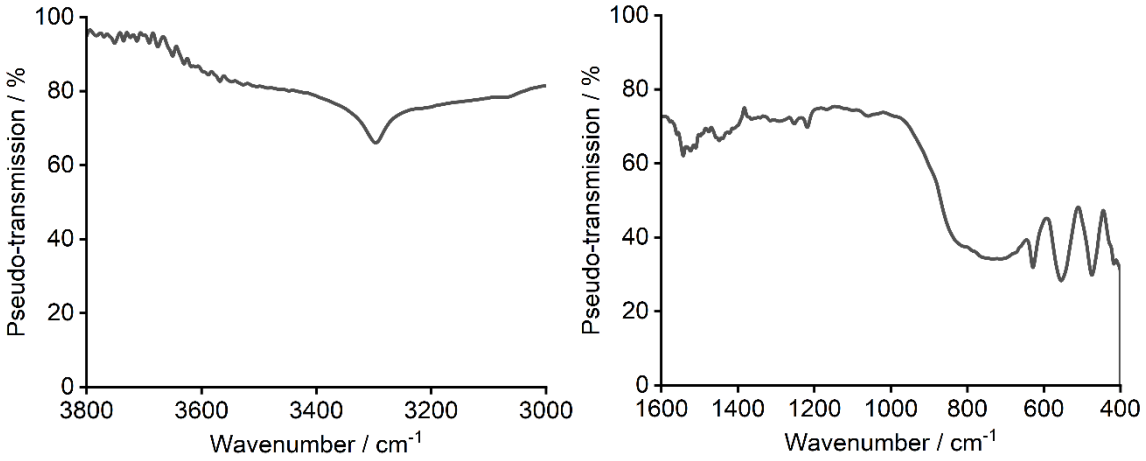

Figure 4.33: DRIFTS spectrum of Ag/α-Al_2O_3 showing the two key regions of interest, backgrounded against KBr.

Again, as a comparison γ-Al_2O_3 (shown in *Figure 4.34*) and Ag/γ-Al_2O_3 (shown in *Figure 4.35*) were undertaken using *ex situ* DRIFTS. The bands in the finger-print region of 400 – 1400 cm^{-1} normally gives the most characteristic peaks for crystalline Al_2O_3, however as shown in the pXRD the γ-Al_2O_3 is a very disordered material. The bands in the fingerprint region are complex and very sensitive to the crystallinity of the sample and have broadened so it is difficult to see individual bands.[60] The pXRD pattern shown in **Chapter 4.1.1** confirms that the sample is consistent with γ-Al_2O_3, however, it is difficult to decipher the broad bands in the DRIFTS spectrum. In the γ-Al_2O_3 there is a broad band between 1000 – 1200 cm^{-1}, which is likely to indicate the symmetric bending of Al-O-H.[60,61] There is a small band around 1300 cm^{-1}, which indicates the presence of Al-O vibrations.[61] The broad band in the range 3000 – 3600 cm^{-1} is due to hydroxyl (OH) vibrations, indicating the presence of Al-OH bonds

in these samples or the presence of water molecules.[60,62] For convenience, the key bands are shown in *Table 4.11*. With the additions of Ag, there are no observable changes between 400 – 1400 cm^{-1} due to peak broadening, indicating no change caused by the Ag in this catalyst. The band at around 3500 cm^{-1}, could correspond to O-H bending modes.[62] This band indicates that the Ag seems to affect the hydroxyl groups, potentially increasing the amount of hydroxyl groups on the surface of the catalyst. When comparing to Ag/α-Al_2O_3 there is a significant increase in hydroxyl groups, therefore indicating that the use of Ag/γ-Al_2O_3 would cause the ethylene oxide to isomerise to acetaldehyde.

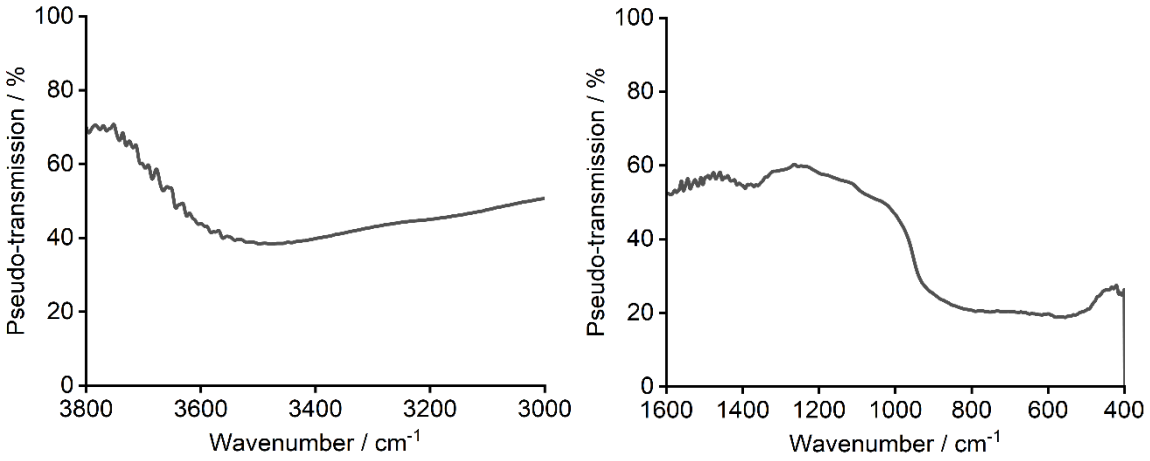

Figure 4.34: DRIFTS spectrum of γ-Al_2O_3 showing the two key regions of interest, backgrounded against KBr.

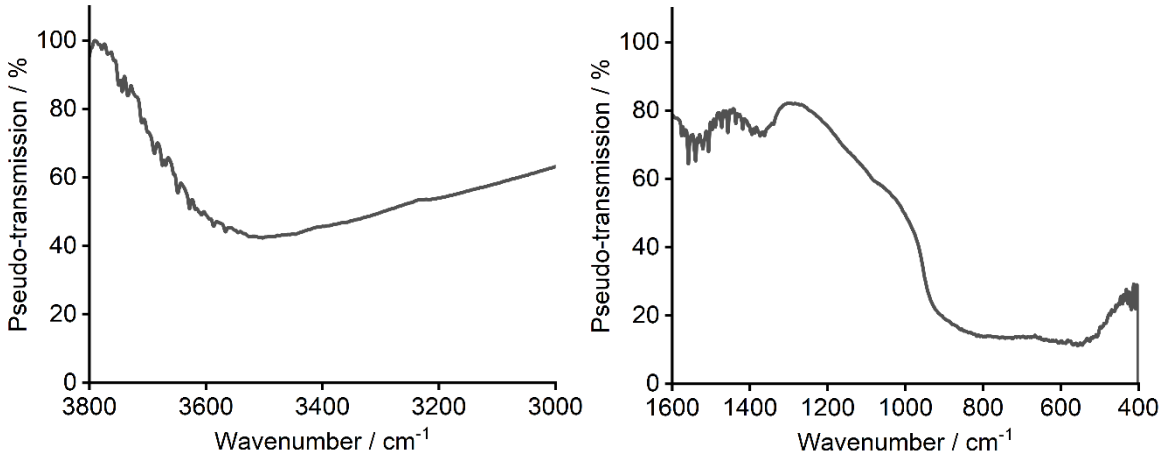

Figure 4.35: DRIFTS spectrum of Ag/γ-Al_2O_3 showing the two key regions of interest, backgrounded against KBr.

Table 4.11: Summary of the key bands identified in the DRIFTS spectra.

Assignment	α-Al_2O_3 / cm^{-1}	γ-Al_2O_3 / cm^{-1}
Al-O stretching mode in octahedral structure (Al-O-Al bending mode)	400 - 668	-
Al-O stretching mode in tetrahedron structure	800 - 1000	-
Symmetric bending of Al-O-H	1000 - 1200	1000 – 1200
Al-O vibrations	1200 - 1500	1200 - 1600
C-H stretching	2810 - 2990	2800 - 2950
Hydroxyl (OH) vibrations	3000 - 3600	3000 - 3600

In situ DRIFTS was undertaken to look at the role of the O_2 pretreatment on both Ag/α-Al_2O_3 (*Figure 4.36*) and the Ag/γ-Al_2O_3 (*Figure 4.37*) hydroxyl groups. As expected, Ag/γ-Al_2O_3 has a broad band corresponding to hydroxyl groups which is greater in intensity compared to Ag/α-Al_2O_3, which displays no change in intensity when heating between 30 and 256 °C. This indicates that the pre-treatments do not affect the hydroxyl groups on the support. At 275 °C there is a slight increase in hydroxyl groups, interpreted as Ag sintering having occurred at this temperature increasing the α-Al_2O_3 surface and therefore the number of hydroxyls. This therefore indicates that reaction conditions are preferable at temperatures below 275 °C. An additional peak appears at a higher wavenumber during the O_2 pretreatment Ag/γ-Al_2O_3 corresponding to an increase in O-H (hydroxyl) groups where this increases at 275 °C.

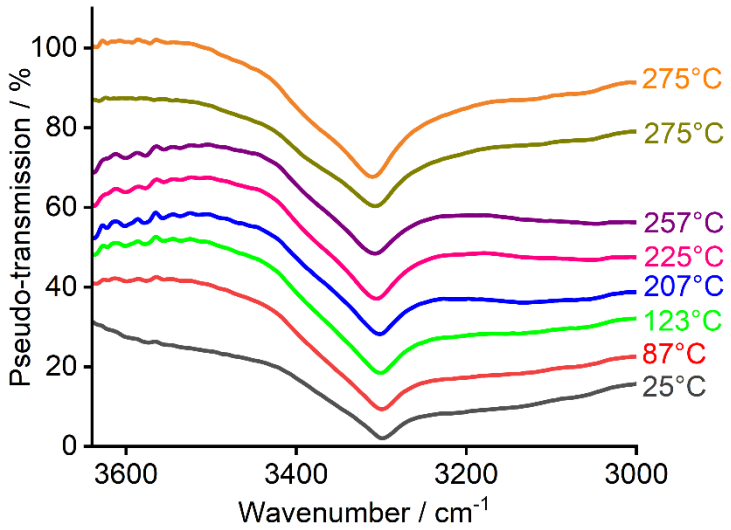

Figure 4.36: In situ DRIFTS on the O_2 pretreatment on Ag/α-Al_2O_3 backgrounded against KBr using the new DRIFTS cell. The second 275 °C shown is after 20 min of being held at 275 °C. Spectra have been offset for clarity.

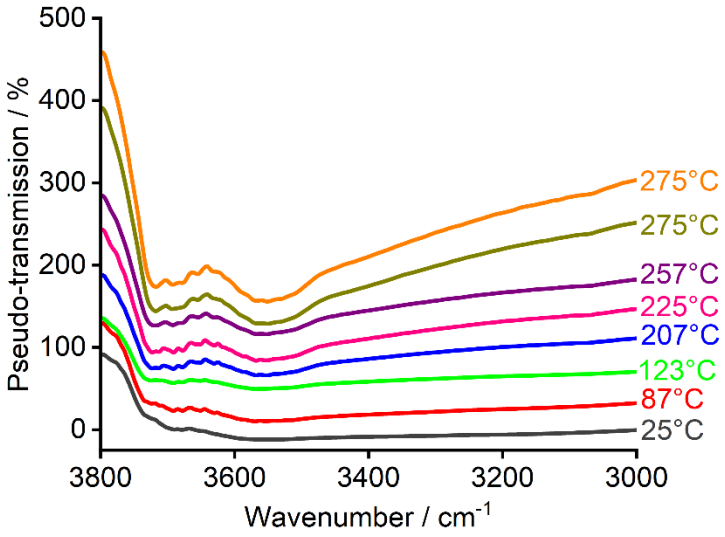

Figure 4.37: In situ DRIFTS on the O_2 pretreatment on Ag/γ-Al_2O_3 backgrounded against KBr using the new DRIFTS cell. The second 275 °C shown is after 20 min of being held at 275 °C. Spectra have been offset for clarity.

pXRD and Scherrer equation was used for the Ag/α-Al_2O_3 before and after heating to 275 °C to investigate sintering. As shown in *Table 4.12*, there is a large decrease in FWHM which therefore shows that there is a large increase in the average Ag crystallite particle sizes when heating to 275 °C indicating sintering occurring at this temperature. This increase in particle sizes means that they are less dispersed, and more support is exposed meaning there is a larger number of hydroxyl groups present in turn leading to slightly more sites for the isomerisation of ethylene oxide to acetaldehyde.[21]

Table 4.12: Summary of FWHM and particle size estimation from pXRD data using the Scherrer equation. Errors were calculated based on the error from fitting the Gaussian functions.

Catalyst	Reflection(s) used / °	FWHM / °	Estimated Crystallite Size / nm	Error in Gaussian fit of Crystallite Size / nm
Ag/α-Al_2O_3	64.5	0.36	51.2	±1.4
Ag/α-Al_2O_3 after heating to 275 °C	64.5	0.30	61.4	±0.5

Hammett indicators were used to determine the acid strength of the catalysts which arises from hydroxyl groups present on the surface. Firstly, methyl yellow was used for which all the solutions stayed yellow, as shown in *Figure 4.38*. Therefore, a higher pH indicator methyl red was chosen as shown in *Figure 4.39*. As shown the Ag/α-Al_2O_3 forms an orange/red solution, whilst the Ag/γ-Al_2O_3 forms a cloudy solution, with coloured catalyst layers. This indicates that Ag/γ-Al_2O_3 is more strongly acidic than Ag/α-Al_2O_3 and therefore is likely to have more strongly acidic hydroxyl groups on the surface.[63]

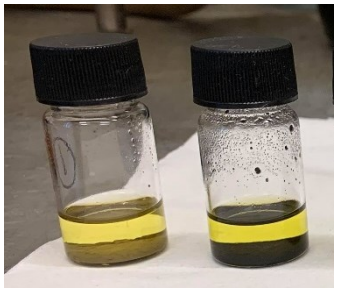

Figure 4.38: Methyl yellow with catalysts in toluene. Left is Ag/α-Al_2O_3 and right is Ag/γ-Al_2O_3.

Figure 4.39: Methyl red with catalysts in toluene. Left is Ag/α-Al_2O_3 and right is Ag/γ-Al_2O_3.

Temperature programmed ammonia desorption from Ag/α-Al_2O_3 (*Figure 4.41*) was undertaken to quantify the acidity of the catalysts. Ag/α-Al_2O_3 was compared to α-Al_2O_3 (*Figure 4.40*) showing a large increase in the peak at around 225 °C and a new peak at 350 °C, corresponding to weak acid sites and strongly acidic sites respectively.[64] This peak at 225 °C shows a very substantial increase, indicating that it is likely to be more than the change induced in hydroxyls. Ag is used as a NH_3 sensor therefore it is likely that the NH_3 is adsorbing on the silver.[65]

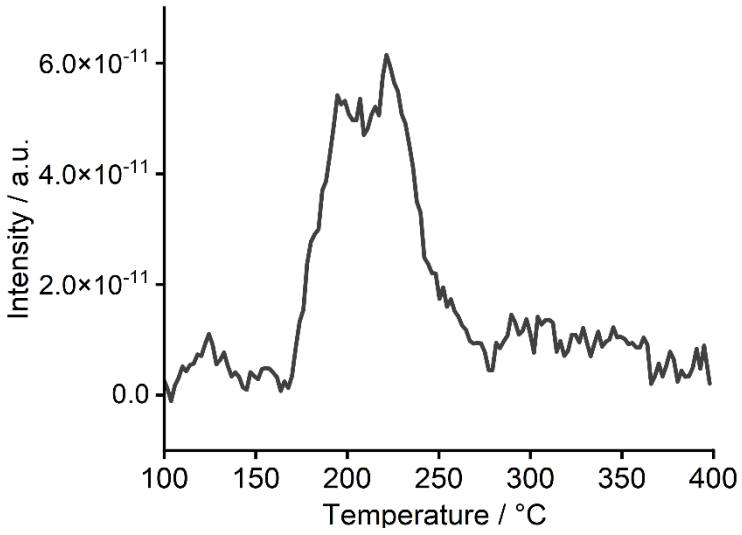

Figure 4.40: Ammonia Desorption of α-Al_2O_3 after O_2 pretreatment (heating rate of 5 °C min^{-1}).

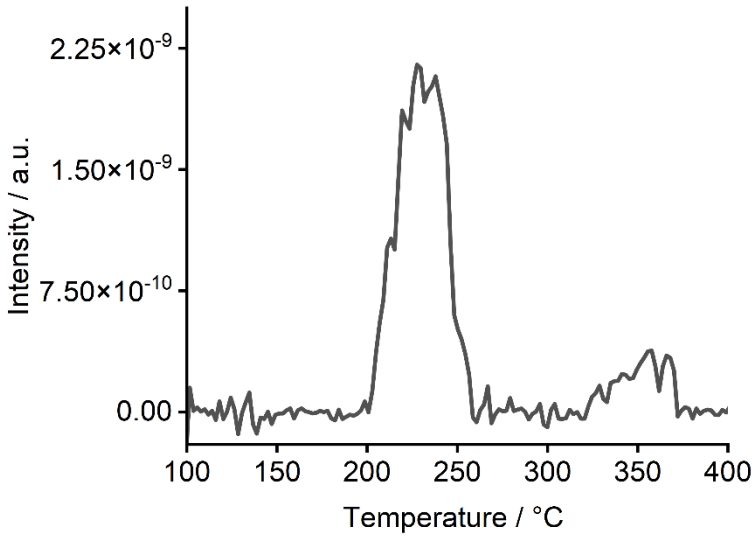

Figure 4.41: Ammonia Desorption of Ag/α-Al_2O_3 after O_2 pretreatment (heating rate of 5 °C min^{-1}).

4.1.5 Analysis Under Ethylene Conditions

As discussed in **Chapter 1.1.2**, there is a large number of arguments in the literature regarding the different conditions (temperature of the reaction and pressure of O_2) and how they lead to different selectivities of EO.[2] Whilst the pressure of O_2 was unable to be investigated, the reaction temperatures of 225 °C and 275 °C were tested.

In situ DRIFTS was undertaken on Ag/α-Al_2O_3 (shown in *Figure 4.42*) after 20 minutes of introducing ethylene (a), after 2 hours of introducing ethylene (b) and then when the reaction temperature was at 275 °C (c). Comparing Ag/α-Al_2O_3 of both 20 min and 2 h of introducing ethylene, there appears to be little differences in the intensity of the peaks. However, when the catalyst is at 275 °C there is change. There appears to be a slight decrease in the band at 1080 cm^{-1} corresponding to the C-O stretching mode of ethylene oxide.[66] This gives an indication of there being less ethylene oxide on the Ag/α-Al_2O_3 catalyst at 275 °C. The appears to be very little change in the band at 1245 cm^{-1} corresponding to the C-O-C stretching mode of ethylene oxide.[67–69] There appears to be a decrease in the peaks between 1400 and 1500 cm^{-1}, the peak at 1540 cm^{-1} and the peak at 1660 cm^{-1} which correspond to H-C-H scissoring and the C=C stretching in ethylene respectively.[67–69] There is a small increase in the peak at 1730 cm^{-1} corresponding to the stretching of the C=O bond in acetaldehyde indicating more acetaldehyde on the surface of the Ag/α-Al_2O_3 under reaction conditions at 275 °C.[67–69]

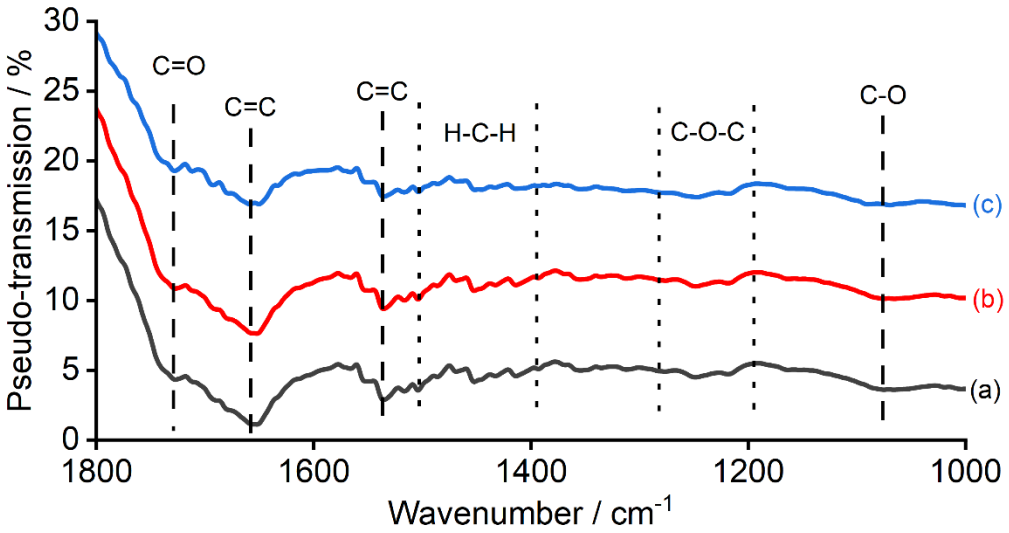

Figure 4.42: In situ, ethylene epoxidation reaction on Ag/α-Al_2O_3 where (a) shows the spectrum obtained following the addition of ethylene after 20 min at 225 °C, (b) shows the spectrum obtained following the addition of ethylene after 2 h at 225 °C and (c) shows the spectrum obtained following the addition of ethylene at 275 °C. All have been backgrounded again KBr where the new DRIFTS cell was used. Spectra have been offset for clarity.

Next, Ag/γ-Al_2O_3 was investigated using *in situ* DRIFTS and compared to Ag/α-Al_2O_3. The catalysts were both compared at 225 °C and under the flow of ethylene for 2 h. Bands before 1300 cm^{-1} are difficult to decipher as discussed earlier, due to the γ-Al_2O_3 being a very disordered material, therefore the bands between 1300 – 1800 cm^{-1} were investigated. Due to the high surface area of γ-Al_2O_3, no peaks other than noise could be identified between 1300 and 1800 cm^{-1}.

4.2 Understanding the Role of Re as a Promoter

As discussed in **Chapter 1.1.2.4**, the use of Re as a promoter is much less understood, although it causes a significant increase in EO selectivity when added.[2,9,70,71,71–73]

It was thought that the use of *in situ* and *ex situ* spectroscopic and characterisation techniques would be able to give more insight into both the role of Re and the oxidation state of Re. These results will be critically compared to the literature that helps with understanding the Re promoter.

Therefore, all Ag/α-Al_2O_3 and Ag/γ-Al_2O_3 based catalysts were made using incipient wetness impregnation with 10 wt. % Ag for a comparison. The optimum amount of Re required to improve the EO selectivity is widely debated in the literature, with ranges from 25 – 200 ppm being proposed.[9,71,72] However, when Cs and Re are together, it is thought that the optimum amount of Re required to improve the EO selectivity is between

400 – 600 ppm.[10] Whilst if the ppm increases to 800 ppm or 1600 ppm the selectivity of the EO decreases, rationalised by the suggestion that Re strengthens the binding of EO to the surface, which lengthens its residence time and therefore promotes its isomerisation to acetaldehyde.[9] Therefore, whilst the Re concentration of 500 ppm used here turned out to decrease EO selectivity, it was selected to act as a baseline to compare to the doubly promoted catalyst of Cs-Re-Ag/α-Al_2O_3 and to investigate why this 500 ppm of Re decreases the selectivity on its own but increases when Cs is added.

To confirm that the elemental composition of the catalysts was as expected, ICP-OES was conducted. The elemental composition of the catalysts is shown in *Table 4.13*. As shown, the silver and rhenium contents of the two catalysts were close to the expected values, with small fluctuations of value and low errors.

Table 4.13: Summary of ICP-OES results. The results reported are the average results of the duplicate samples where errors are one standard deviation calculated based on the duplicate samples for each material. Standards are run in the same batch to confirm no significant anomalies or deviations in the instrumental analysis of the samples.

Catalyst	Metal	Expected Metal Content / wt. %	Metal Content by ICP-OES / wt. %	Error in Metal Content by ICP-OES / wt. %
Ag/α-Al_2O_3	Ag	10	9.86	±0.69
Re-Ag/α-Al_2O_3	Ag	10	9.92	±0.35
	Re	0.05	0.05	±0.01
Ag/γ-Al_2O_3	Ag	10	10.12	±0.84
Re-Ag/γ-Al_2O_3	Ag	10	9.85	±0.15
	Re	0.05	0.05	±0.01

Both Re-Ag/α-Al_2O_3 and Re-Ag/γ-Al_2O_3 were evaluated for ethylene epoxidation, with the EO selectivity in *Figure 4.43* and *Figure 4.44,* respectively. There is a decrease between Ag/α-Al_2O_3 and Re-Ag/α-Al_2O_3 and also a decrease between Ag/γ-Al_2O_3 and Re-Ag/γ-Al_2O_3, with an increase in acetaldehyde selectivity.

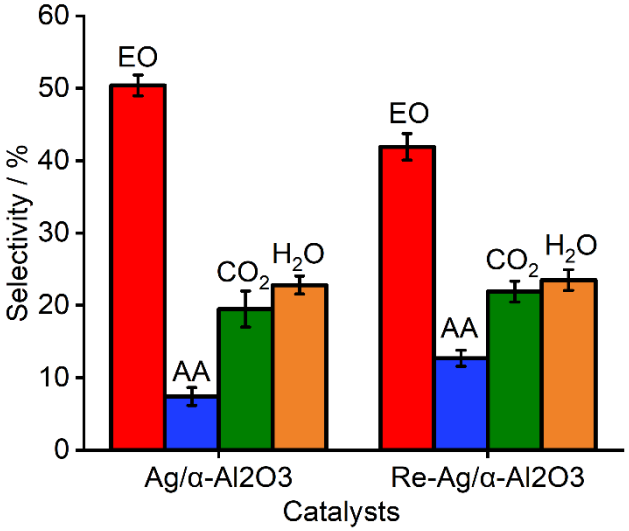

Figure 4.43: A comparison of selectivity between Ag/α-Al_2O_3 and Re-Ag/α-Al_2O_3. The errors shown are based on 3 repeat measurements.

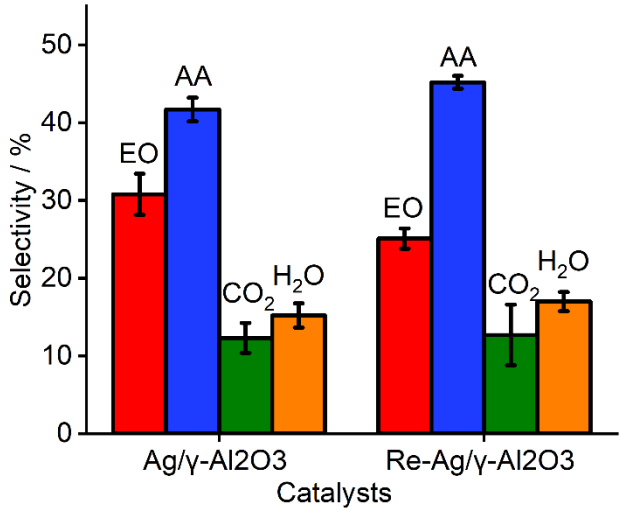

Figure 4.44: A comparison of selectivity between Ag/γ-Al_2O_3 and Re-Ag/γ-Al_2O_3. The errors shown are based on 3 repeat measurements.

Ethylene conversion was calculated and displayed in *Table 4.14*. As expected, (discussed in **Chapter 4.1**) there is a decrease in ethylene conversion between α-Al_2O_3 and γ-Al_2O_3.

Table 4.14: A table showing the ethylene conversion and percentage error based on 3 repeat measurements for both Ag/α-Al_2O_3 and Ag/γ-Al_2O_3.

Catalyst	Ethylene Conversion / %	% Error
Ag/α-Al_2O_3	7.7	0.4
Re-Ag/α-Al_2O_3	8.0	0.7
Ag/γ-Al_2O_3	3.7	0.1
Re-Ag/γ-Al_2O_3	3.6	0.1

Although there is a decrease in EO selectivity of the Re-Ag/α-Al_2O_3 catalyst compared to the Ag/α-Al_2O_3 catalyst, investigations were undertaken with comparison to the literature to

understand the effects of Re addition, in particular, to isolate the effect of Re from those of Cs in the dual promoted catalyst.

4.2.1 Particle Sizes and Morphology

Investigations into the particle sizes of Ag and the morphology of the catalyst were undertaken to find out why 500 ppm of Re-Ag/α-Al_2O_3 gives a lower EO selectivity, pXRD of Re-Ag/α-Al_2O_3 was compared to Ag/α-Al_2O_3. As shown in *Figure 4.45* there is minimal change between the two catalysts. The expanded figure shows the Ag (2 2 0) at 64.5 ° (*Figure 4.46*), which was used for particle size estimates using the Scherrer equation. The FWHM used for each catalyst and the resultant crystallite sizes are shown in *Table 4.15*. As shown the FWHM has changed by 0.02 °, therefore indicating that the average Ag particle size is essentially unchanged.

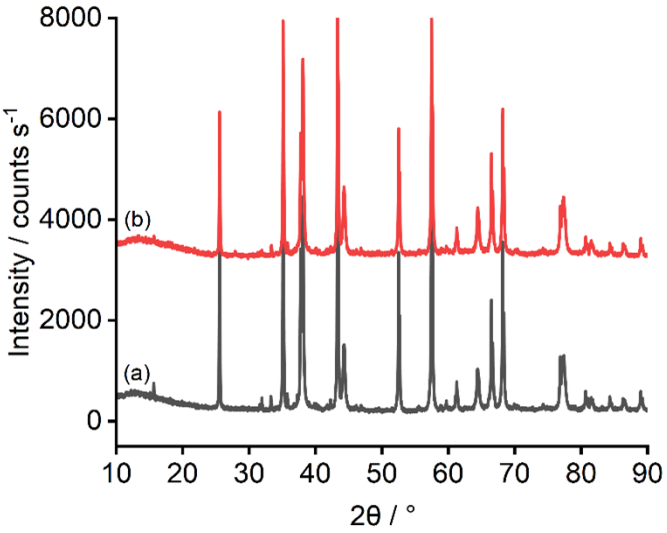

Figure 4.45: pXRD patterns for the α-alumina based *catalysts; (a) Ag/α-Al_2O_3 and (b) Re-Ag/α-Al_2O_3. Patterns offset vertically for clarity.*

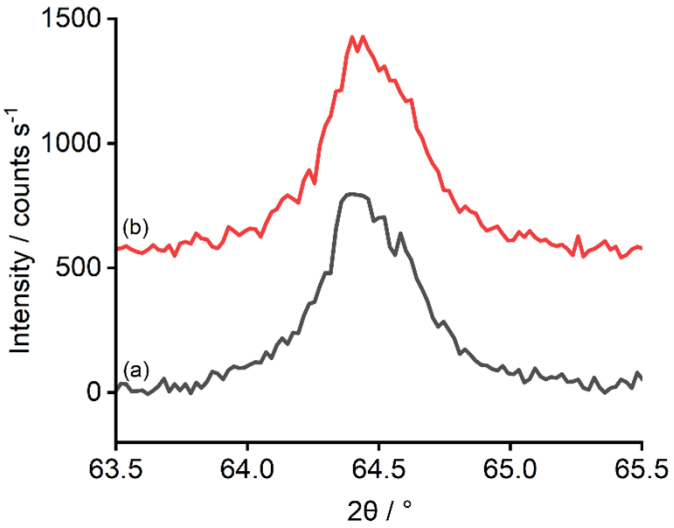

Figure 4.46: pXRD patterns for the α-Al_2O_3 based *catalysts; (a) Ag/α-Al_2O_3; (b) Re-Ag/α-Al_2O_3. Zoomed in on peak Ag (220). Patterns offset vertically for clarity.*

Table 4.15: Summary of FWHM and particle size estimation from pXRD data using the Scherrer equation. Errors were calculated based on the error from fitting the Gaussian functions.

Catalyst	Reflection(s) used / °	FWHM / °	Estimated Crystallite Size / nm	Error in Gaussian fit of Crystallite Size / nm
Ag/α-Al_2O_3	64.5	0.36	51.2	±1.4
Re-Ag/α-Al_2O_3	64.5	0.34	49.8	±1.5

The addition of Re to Ag/γ-Al_2O_3 was also monitored by pXRD, as shown in *Figure 4.47*. There is again extremely limited change to the pXRD pattern also. Given the findings on α-Al_2O_3, this is unsurprising as the larger γ-Al_2O_3 surface area would mean there would be less Ag-Re interaction.

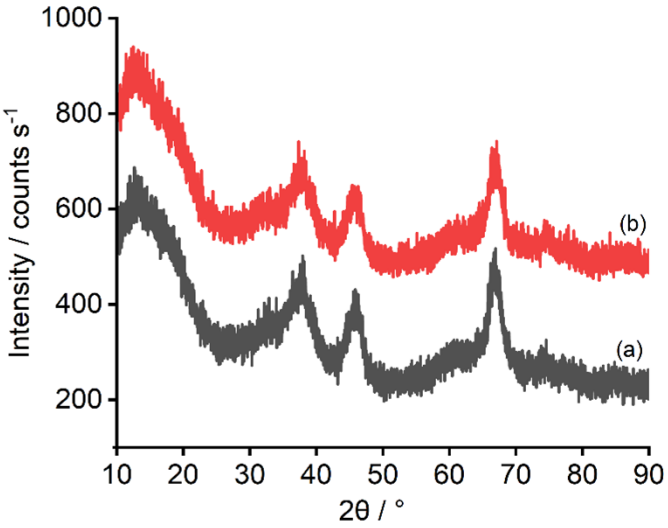

Figure 4.47: pXRD patterns for the γ-alumina-based catalysts; (a) Ag/γ-Al_2O_3; (b) Re-Ag/γ-Al_2O_3. Patterns offset vertically for clarity.

In the literature, it is thought that the selectivity towards EO is partially determined by the distribution of silver, where more selective catalysts have more active sites and fewer hydroxyl groups (acid sites) on the surface of the α-Al_2O_3 with more distributed Ag.[3,21] Dellamorte *et al*. suggested that the Re causes an increase in Ag dispersion on the surface of the Al_2O_3.[71] Therefore, TEM and STEM were undertaken on both catalysts to test this hypothesis with this concentration of Re as it is possible that pXRD crystallite size is not fully reflective of morphology changes and/or being a bulk technique is too strongly dominated by larger crystallites.[71] Comparing the TEM in *Figure 4.7* and *4.48*, there seems to be very little change between the two, although this is only one example image and it is challenging to obtain useful data on samples with inherent size inhomogeneity.

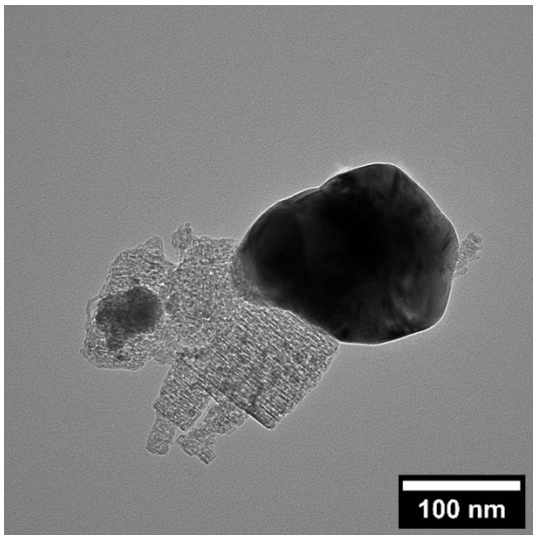

Figure 4.48: Representative TEM images of Re-Ag/α-Al_2O_3 catalyst

Elemental analysis using STEM was undertaken on Ag/α-Al_2O_3 (shown in *Figure 4.10*) and Re-Ag/α-Al_2O_3 (shown in *Figure 4.49*) to investigate the locations of the Ag and Re in the catalysts. As suggested in the TEM and pXRD, the STEM indicates no increase in the distribution of Ag with this concentration of Re added. When looking at the location of Re, it appears that Re is denser in the same locations as the larger densities of Ag, therefore indicating that the location of Re is clustered around the Ag.

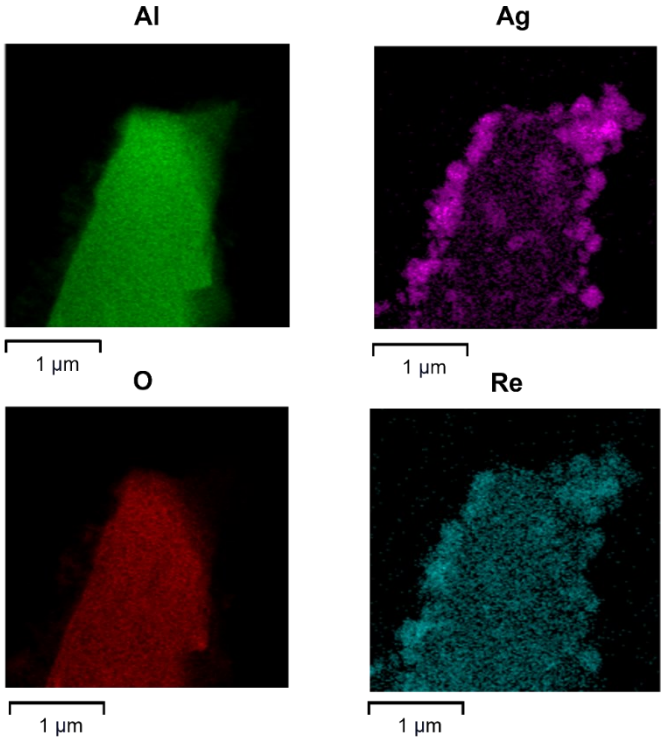

Figure 4.49: Elemental Mapping (using EDX), for the Re-Ag/α-Al_2O_3, with aluminium shown in green, silver shown in purple, oxygen shown in red, and rhenium shown in blue.

4.2.2 Understanding the Structure of Silver in the Presence of Re

As discussed in **Chapter 1.1.2.4**, Diao *et al*. believe that the Re makes the Ag sites more electron-deficient and the resulting O adsorbed on Ag more electrophilic.[9] Therefore the structure of silver was investigated with the addition of the Re promoter. Firstly, the XPS of Ag 3d was investigated, as shown in *Figure 4.50*, the addition of 500 ppm Re causes a shift of no more than 0.1 eV which is likely to be within the calibration error.

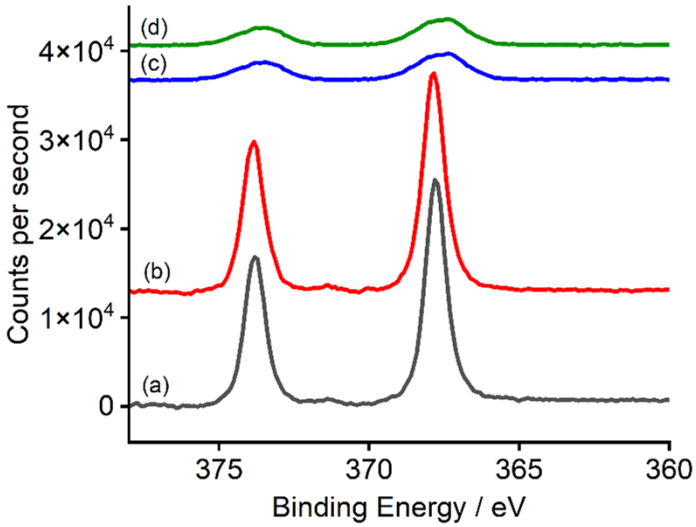

Figure 4.50: XPS spectra of all Ag 3d data (after applying binding energy correction verified by the shift of the Al 2p peak and after subtraction of a Shirley background). Where (a) is Ag/α-Al_2O_3, (b) is Re-Ag/α-Al_2O_3, (c) is Ag/γ-Al_2O_3 and (d) is Re-Ag/γ-Al_2O_3. All samples are as prepared. Spectra have been offset for clarity.

Table 4.16 shows that the ratios of Ag:Al have no change from Ag/α-Al_2O_3 to Re-Ag/α-Al_2O_3. This is again consistent with little change in Ag particle size with the addition of Re. Calculations repeated as with Ag/α-Al_2O_3 where the calculations are shown in **Appendix 3**.

*Table 4.16: A table showing the ratios of metal: Al_2O_3 found by calculations shown in **Appendix 3**.*

		Surface Metal Ratios		
		Ag3d	**Al2p**	**Re4f**
Sample	**Ag/α-Al_2O_3**	0.21	1	-
	Re-Ag/α-Al_2O_3	0.20	1	0.017

Figure 4.51 shows the Raman spectrum of Re-Ag/α-Al_2O_3 catalyst before and after ethylene epoxidation. One main difference between the Ag/α-Al_2O_3 and Re-Ag/α-Al_2O_3 is there is now a peak at 532 cm^{-1}, this is likely to be an Ag-oxide-like surface represented by O-Ag-O motifs that can be a combination of subsurface and surface oxygens.[47,74] This feature has decreased after ethylene epoxidation indicating the use or depletion of subsurface and surface oxygens.

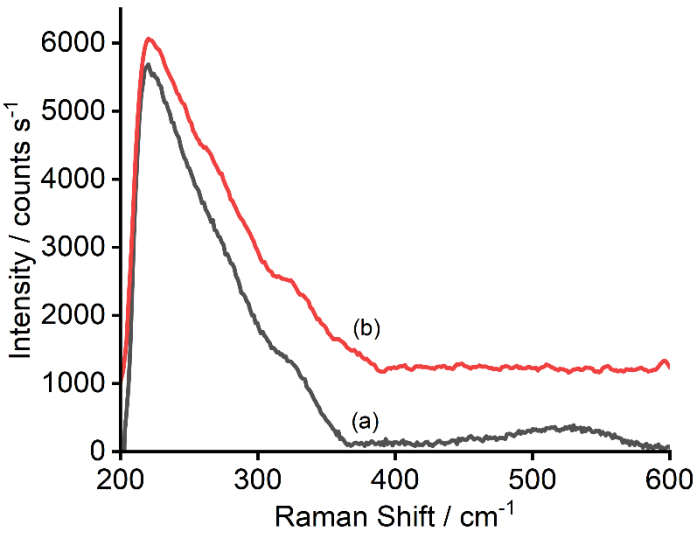

Figure 4.51: Raman spectra of Re-Ag/α-Al_2O_3 (a) before ethylene epoxidation and (b) after ethylene epoxidation zoomed in (after applying intensity response correction and subtraction of dark signal) where the wavelength of 667-725 nm. Spectra have been offset for clarity.

4.2.3 Understanding the Role of Oxygen in the Presence of Re

Jun *et al*. suggested that the Re competes with the adsorbed oxygen for the silver outer electrons, reducing the electron density of the adsorbed oxygen, it was thought understanding the effect of Re on oxygen was very important.[70] Therefore, the oxygen species on the Re-Ag/α-Al_2O_3 were compared to the oxygen species on the Ag/α-Al_2O_3 catalyst using O_2-TPD (shown in *Figure 4.52*). Re-Ag/α-Al_2O_3 shows a peak at 320 °C indicating a weaker Ag-O bond compared to Ag/α-Al_2O_3 which has a peak at 350 °C. In the literature, reports have indicated that a weaker Ag-O bond results in increased EO selectivity.[75,76]

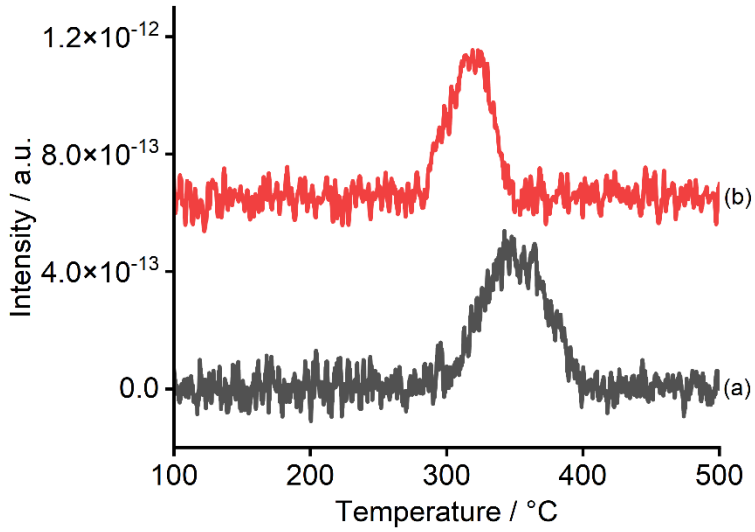

Figure 4.52: O_2-TPD profile of (a) Ag/α-Al_2O_3 and (b) Re-Ag/α-Al_2O_3 after O_2 pretreatment (heating rate of 5 °C min^{-1}). Spectra have been offset for clarity.

H_2-TPR was undertaken on Re-Ag/α-Al_2O_3 (shown in *Figure 4.53*) and compared to Ag/α-Al_2O_3 here there are 0.74 ± 0.02 H_2 molecules per silver atom, indicating that there is very little change in the total O_{ads} with the addition of 500 ppm of Re.

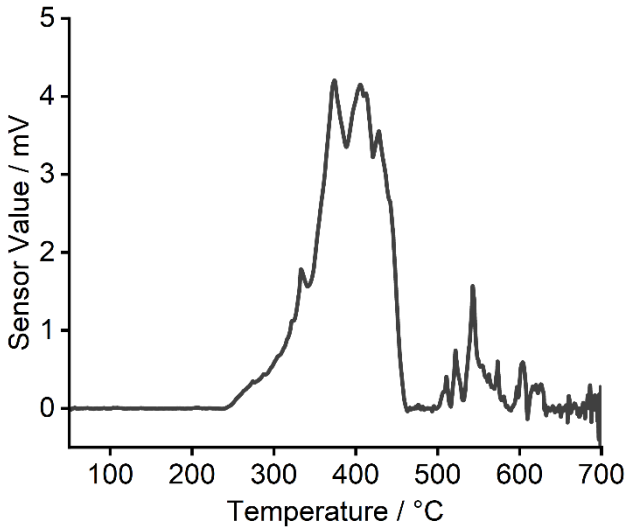

Figure 4.53: H_2-TPR of Re-Ag/α-Al_2O_3 after O_2 pretreatment (heating rate of 5 °C min^{-1}).

Ex situ XPS of the as-prepared sample was also undertaken to give more insight into the oxygen species. It is now commonly accepted that the O_{elec} is responsible for the selective reaction pathway to ethylene oxide. Here the O 1s spectra were investigated shown in *Figure 4.54.* Where the ratio of oxygen to aluminium is shown in *Table 4.17*. These show two species, there is a main peak at 530 eV, with a shoulder at 532 eV and no intensity below 529 eV (corresponding to O_{nuc}).[36,37] This can be ascribed based on the literature as, atomic electrophilic oxygen and Ag_x-O_2 respectively.[36,37] This gives evidence of both Ag_x-O_2 and atomic electrophilic O being on the surface of the catalyst.[36,37] There is a shift

from Ag/α-Al_2O_3 to Re-Ag/α-Al_2O_3 of 0.1 eV, indicating this is likely to be within the calibration error.

Table 4.17: A table showing the ratios of oxygen: Al_2O_3 found by using the cross sections. This calculation is explained in Appendix 4.

		Surface Metal Ratios	
		O1s	**Al2p**
Sample	**Ag/α-Al_2O_3**	12.5	1
	Re-Ag/α-Al_2O_3	13.9	1

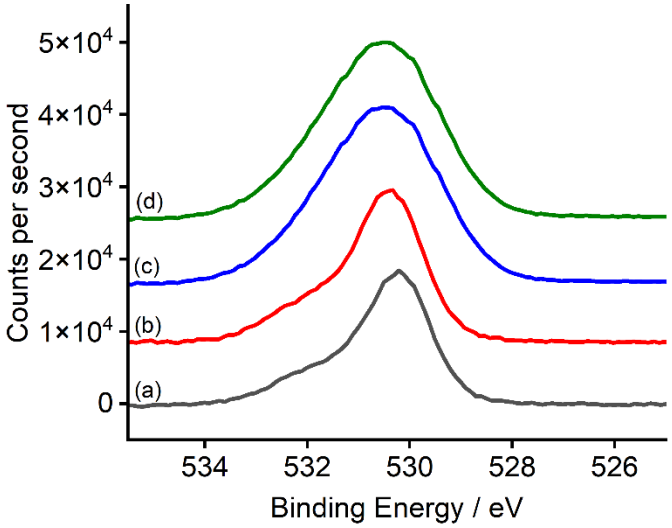

Figure 4.54: XPS spectra of all O1s data (after applying binding energy correction verified by the shift of the Al 2p peak and after subtraction of a Shirley background). Where (a) is Ag/α-Al_2O_3, (b) is Re-Ag/α-Al_2O_3, (c) is Ag/γ-Al_2O_3 and (d) is Re-Ag/γ-Al_2O_3. All samples are as prepared. Spectra have been offset for clarity.

Peak deconvolution was undertaken on the *ex situ* O1s XPS of Ag/α-Al_2O_3, Ag/γ-Al_2O_3, Re-Ag/α-Al_2O_3 and Re-Ag/γ-Al_2O_3 to show the two species present in the catalysts. Whilst the peak deconvolutions of Ag/α-Al_2O_3 and Ag/γ-Al_2O_3 are shown in *Figure 4.17* and *Figure 4.18* respectively, the peak deconvolutions of Re-Ag/α-Al_2O_3 and Re-Ag/γ-Al_2O_3 are shown in *Figure 4.55* and *Figure 4.56,* respectively. The determined peak areas of the four catalysts are shown in *Table 4.18*.

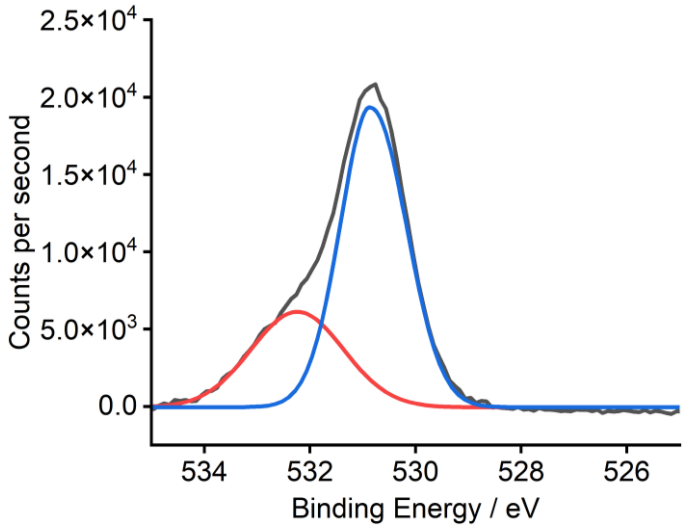

Figure 4.55: Peak deconvolution of the XPS spectra of the O1s looking at Re-Ag/α-Al_2O_3. All samples are as prepared, after applying binding energy correction verified by the shift of the Al 2p peak and after subtraction of a Shirley background.

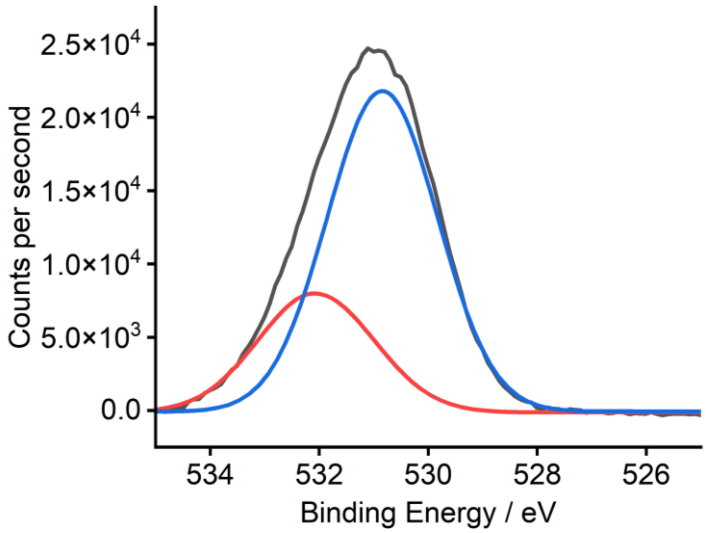

Figure 4.56: Peak deconvolution of the XPS spectra of the O1s looking at Re-Ag/γ-Al_2O_3. All samples are as prepared, after applying binding energy correction verified by the shift of the Al 2p peak and after subtraction of a Shirley background.

Table 4.18: A table showing the peak areas for the peak deconvolution of the XPS spectra of the O1s looking at Ag/α-Al_2O_3, Ag/γ-Al_2O_3, Re-Ag/α-Al_2O_3 and Re-Ag/γ-Al_2O_3.

Catalyst	Peak Area of Blue Peak - atomic electrophilic oxygen / counts	Peak Area of Red Peak - Ag_x-O_2 / counts
Ag/α-Al_2O_3	25354.89	12227.33
Ag/γ-Al_2O_3	48935.63	21894.52
Re-Ag/α-Al_2O_3	30391.52	13536.35
Re-Ag/γ-Al_2O_3	55785.29	16672.04

4.2.4 Investigating Hydroxyl Groups and Acidity

Hydroxyl sites were investigated with the use of *ex situ* DRIFTS and Hammett indicators. When looking at *Figure 4.57*, which compares Ag/α-Al_2O_3 with Re-Ag/α-Al_2O_3, there is shown to be an increase in the peak at 3300 cm^{-1}, which corresponds to O-H stretching in the hydroxyl groups, indicating that Re at this concentration increases the hydroxyl groups on the support.[21,62]

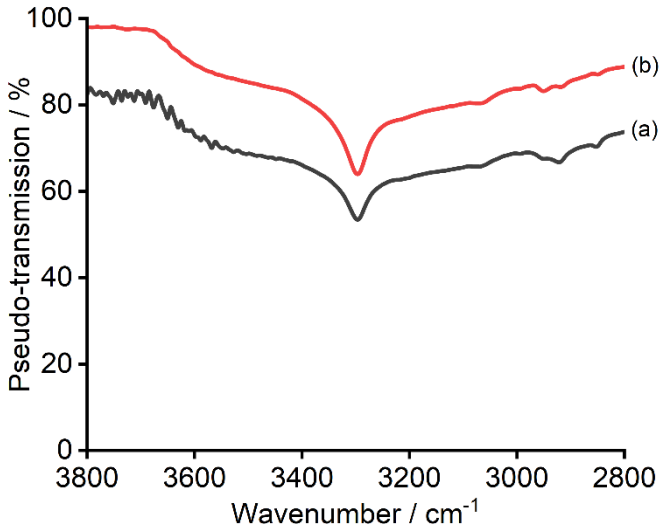

Figure 4.57: DRIFTS spectra of (a) Re-Ag/α-Al_2O_3 and (b) Ag/α-Al_2O_3 on the right showing the region of interest, backgrounded against KBr. Spectra have been offset for clarity.

Hammett indicators were used to investigate the acidity of the catalysts. Here methyl red was chosen, shown in *Figure 4.58*. As shown the Ag/α-Al_2O_3 forms an orange solution, whilst the Re-Ag/α-Al_2O_3 forms a red solution and therefore is likely to have more strongly acidic hydroxyl groups.[63]

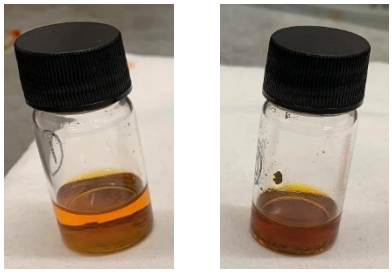

Figure 4.58: Hammett Indicators of Ag/α-Al_2O_3 on the left and Re-Ag/α-Al_2O_3 on the right.

4.2.5 Understanding the Structure of Re

As discussed in **Chapter 4.2**, there is a large discussion regarding the oxidation state and the structure of Re.[9,10,72,77–79] Therefore, the oxidation state and structure were investigated with the use of *ex situ* XPS, *ex situ* Raman and *in situ* XAFS.

Ex situ XPS on Re 4f was investigated, as shown in *Figure 4.59* although ICP-OES confirms the correct concentration of Re in the Re-Ag/γ-Al_2O_3, no Re 4f peaks were able to be identified, it is thought that this was due to the Re surface concentration being much lower due to the large surface area of γ-Al_2O_3. However, for Re-Ag/α-Al_2O_3 a peak at 46.1 eV corresponds to Re^{+7}, indicating that the Re at the surface is in the +7 oxidation state.[10] This assignment agrees with Hardcastle *et al*., Dellamorte *et al*. and Diao *et al*. who have all suggested that the surface Re oxidation state is +7.[9,72,77]

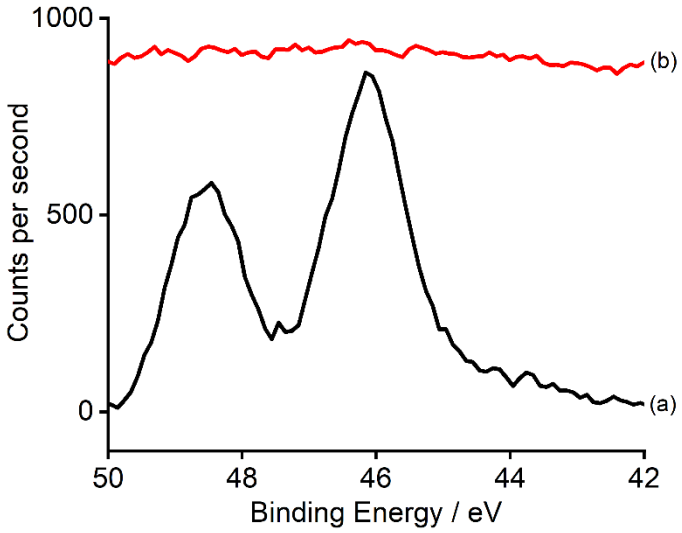

Figure 4.59: XPS spectra of all Re4f data (after applying binding energy correction verified by the shift of the Al 2p peak and after subtraction of a Shirley background). Where (a) is Re-Ag/α-Al_2O_3 and (b) is Re-Ag/γ-Al_2O_3. All samples are as prepared. Spectra have been offset for clarity.

It was thought that *ex situ* Raman spectroscopy would also give information regarding the oxidation state and the structure of Re (shown in *Figure 4.60*). There are three new peaks

compared to the non-Re case, one at 330 cm^{-1}, which is likely to correspond to two bending modes or deformations which are degenerate in ReO_4^-, and two at 890 cm^{-1} and 970 cm^{-1} which are likely to correspond to both the antisymmetric stretch and the symmetric stretch of the rhenium-oxygen vibrations, from ReO_4^-, giving more indication that the oxidation state of the Re is in the +7.[77] The peaks correspond to a tetrahedral ReO_4^-, where the peak at 330 cm^{-1} corresponds to Re-O, and the two bands at 890 cm^{-1} and 970 cm^{-1} correspond to Re=O.[77,80]

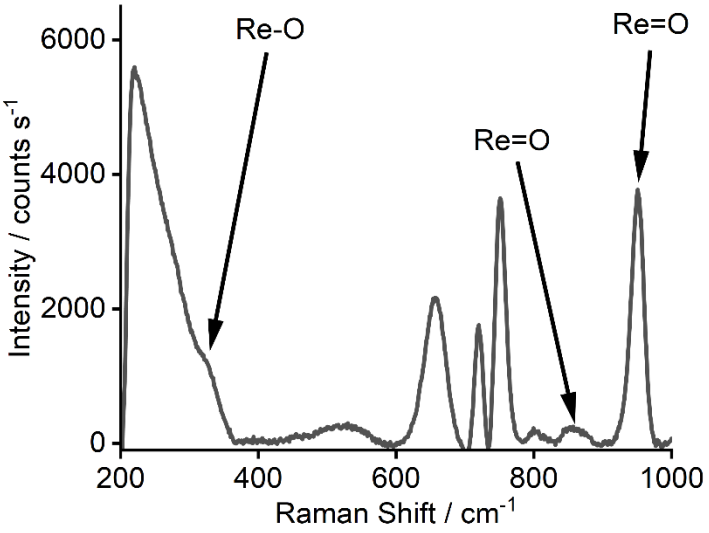

Figure 4.60: Re-Ag/α-Al_2O_3 (after applying intensity response correction and subtraction of dark signal). Where the wavelength is 667-725 nm, slit width = 150 μm*, number of spectra = 10, and length of each spectrum = 10 s. Laser power was increased to 800 mW.*

As a comparison, *ex situ* Raman spectroscopy (*Figure 4.61*) was undertaken before and after ethylene epoxidation, whilst the peak for Re-O did not change, the antisymmetric stretch of the rhenium-oxygen vibration increased, and the symmetric stretch of the rhenium-oxygen vibration decreased. This indicates that it is unlikely there is a change in the oxidation state, however, the bonding appears to have changed during ethylene epoxidation.

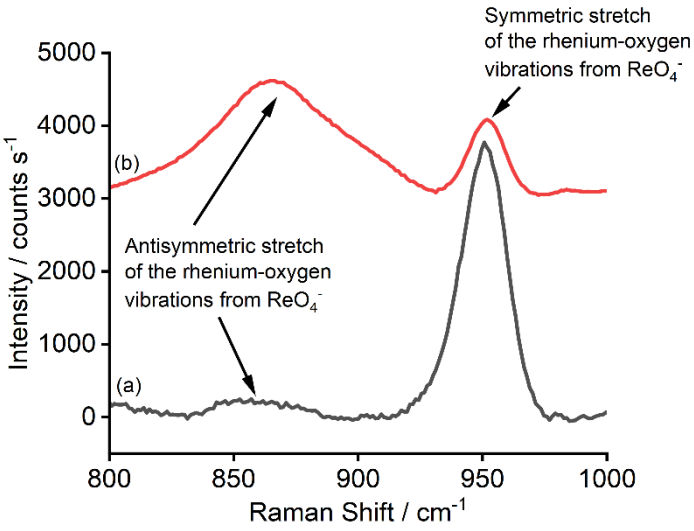

Figure 4.61: Raman spectra of Re-Ag/α-Al_2O_3 zoomed in (after applying intensity response correction and subtraction of dark signal) where the wavelength of 667-725 nm, slit width = 150 µm*, number of spectra = 10, and length of each spectrum = 10 s. Where (a) is Re-Ag/α-Al_2O_3 before EE and (b) is Re-Ag/α-Al_2O_3 after EE. Laser power was increased to 800 mW. Spectra have been offset for clarity.*

To give an improved understanding of the structure of the Re species during O_2 pretreatment and ethylene epoxidation the *in situ* XAS of the Re L3 edge were obtained. Re is well known to be mobile and the knowledge of dispersion versus cluster formation from EXAFS is essential to map out the extent of Re-Ag interactions and underpin ideas about the structure of the Re promoter.[81] Due to the low wt. % of Re used in these catalysts, a high enough signal-to-noise could not be achieved using transmission mode, therefore the spectra were collected in fluorescence. Both Re-Ag/α-Al_2O_3 and Re-Ag/γ-Al_2O_3 were investigated under 4 different conditions, under Ar at room temperature, under O_2 pretreatment at 225 °C, under ethylene and oxygen at 225 °C and under ethylene and oxygen at 275 °C.

Whilst there is no change between the XANES of the Re-Ag/γ-Al_2O_3 under O_2 at 225 °C, O_2 and C_2H_4 under 225 °C or O_2 and C_2H_4 under 275 °C (shown in *Figure 4.62*), there is a small intensity decrease in peaks at the edge compared to under Ar at RT. This decrease is likely to be due to the drop in surface coverage of the ReO_4 with increased temperature as the surface rhenium oxide can be recombined at elevated temperatures to give gaseous Re_2O_7.

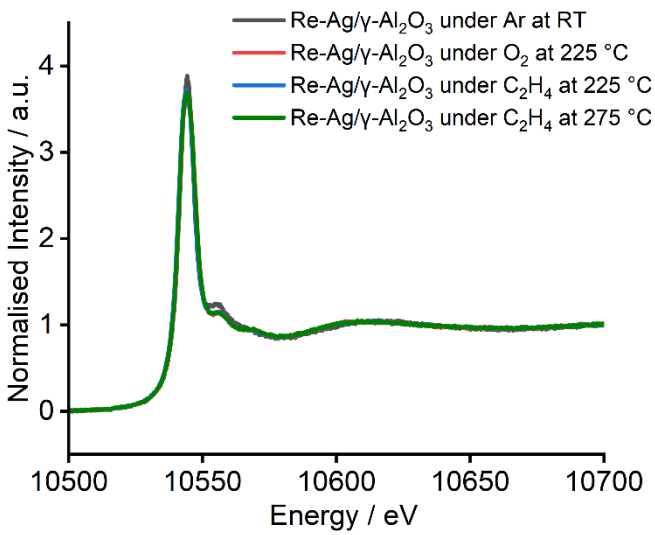

Figure 4.62: Re L3-edge XANES region for the Re-Ag/γ-Al_2O_3 catalyst under argon at room temperature, under O_2 pretreatment at 225 °C, under C_2H_4 at 225 °C and under C_2H_4 under 275 °C. Spectra have been offset for clarity.

Fitting using FEFF in Artemis was carried out for the EXAFS spectrum of Re-Ag/γ-Al_2O_3 to determine the average bond lengths around the rhenium, giving insight into the potential position and bonding of the rhenium atoms. The Re-O (1) path used was at 1.73 Å from Re_2O_7 and the Re-Re path used was at 2.81 Å from ReO_2 (due to less distortion of the Re-Re bond in an oxide species).

As shown in *Figures 4.63 – 4.66* and *Table 4.19*, there is a reasonable coordination of 3-4 oxygen atoms when the coordination number is allowed as a fitting parameter. As shown in *Table 4.20* there are no Re-O-Re therefore no Re-Re scattering paths indicating that there are Re oxide clusters on the surface of the catalyst. Hardcastle *et al.* investigated the interaction of rhenium oxide with an alumina support, where they found that supported rhenium oxide on alumina is present as an atomically dispersed surface $[ReO_4]_{ads}$ species coordinated to the alumina support.[77] They found that the $[ReO_4]_{ads}$ species possessed the presence of three equivalent terminal Re=O bonds and one inequivalent Re-O bond as part of the Re-O-Al linkage to the alumina support. They found that there was a drop in the surface coverage of the $[ReO_4]_{ads}$ with increasing calcination temperature as the surface rhenium oxide species can recombine at elevated temperatures to give gaseous dimeric Re_2O_7.[77] Whilst Okal also found that the rhenium particle as a Re^{7+} species, forms some kind of surface complex with an Al-O-ReO_3 or Al-(O-ReO_3)$_3$ structure.[80] The ReO_4 cluster is found to contain three Re=O bonds, with an elongated Re-O$^{\bullet}$ oxyl bond with oxygen radical character.

This extra Re-O bond is likely to be coordinated with Al due to the large surface area of γ-Al_2O_3 with only small amounts of Ag, however, a structural model needs to be used to fit

this. Attempts to fit a Re-O or a Re-Al path to the EXAFS features at 2.05 and 3.01 Å, respectively.

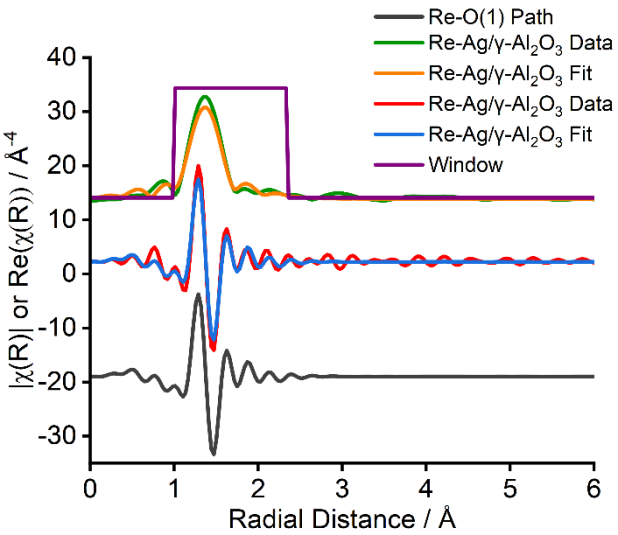

Figure 4.63: Magnitude and real part of the k^3-weighted, FT of the Re L3-edge EXAFS data for the Re-Ag/γ-Al_2O_3 catalyst under Ar at RT, with the fitted Re-O path shown. Spectra have been offset for clarity.

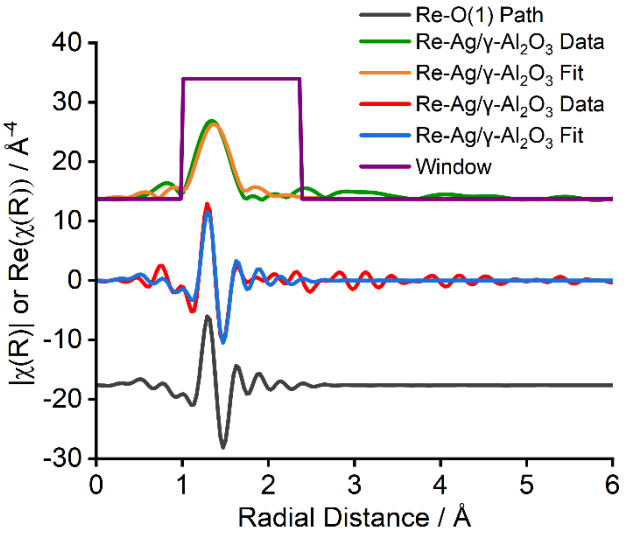

Figure 4.64: Magnitude and real part of the k^3-weighted, FT of the Re L3-edge EXAFS data and fits for the Re-Ag/γ-Al_2O_3 catalyst under O_2 pretreatment at 225 °C, with the fitted Re-O path shown. Spectra have been offset for clarity.

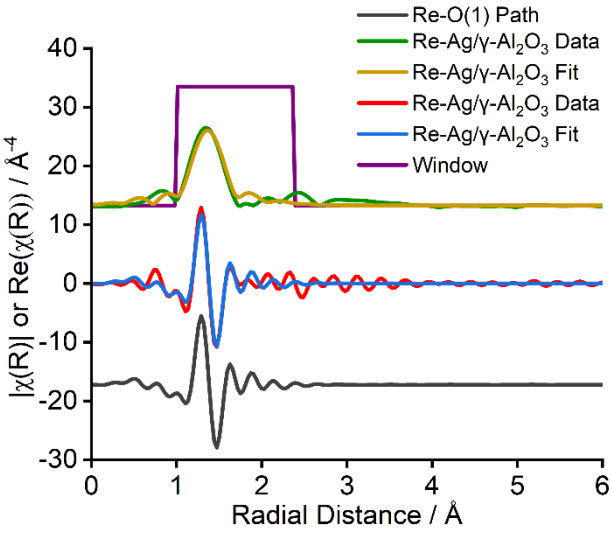

Figure 4.65: Magnitude and real part of the k^3-weighted, FT of the Re L3-edge EXAFS data and fits for the Re-Ag/γ-Al_2O_3 catalyst under C_2H_4 at 225 °C, with the fitted Re-O path shown. Spectra have been offset for clarity.

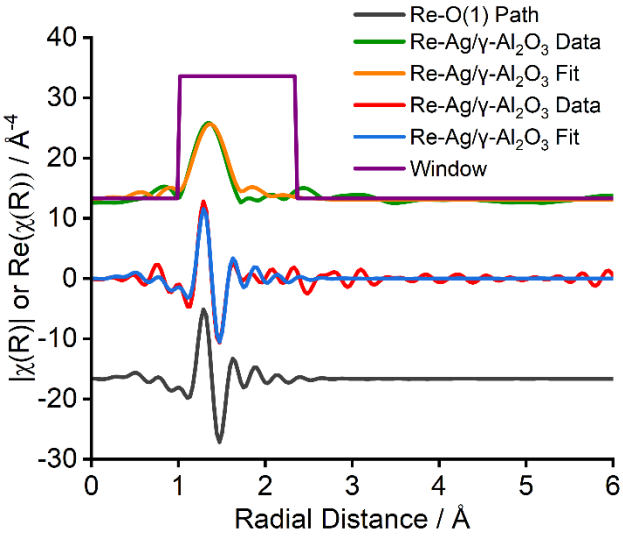

Figure 4.66: Magnitude and real part of the k^3-weighted, FT of the Re L3-edge EXAFS data and fits for the Re-Ag/γ-Al_2O_3 catalyst under C_2H_4 at 275 °C, with the fitted Re-O path shown. Spectra have been offset for clarity.

Table 4.19: Re L3-edge EXAFS fitting parameters of Re-O(1) for the Re-Ag/γ-Al_2O_3

Conditions	Abs-Scatterer	∆ E0 /eV	Coordination Number	Radial Distance /Å	σ ^{2} /Å^2	R_{factor}
RT Argon	Re-O (1)	11 ± 2	4.16 ± 0.24	1.73 ± 0.002	0.001	0.03
225 °C under O_2 pretreatment	Re-O (1)	9 ± 3	3.21 ± 0.32	1.73 ± 0.005	0.001	0.05
225 °C under ethylene	Re-O (1)	10 ± 2	3.18 ± 0.31	1.73 ± 0.002	0.001	0.05
275 °C under ethylene	Re-O (1)	9 ± 3	3.15 ± 0.33	1.73 ± 0.003	0.001	0.05

Fitting Parameters: S_0^2 determined from W foil = 0.78, 1 < R < 3.0 Å. k-range 6.0 – 14.8, no. of independent points 10.9.

Table 4.20: Re L3-edge EXAFS fitting parameters of Re-O(1) and Re-Re for the Re-Ag/γ-Al_2O_3

Conditions	Abs-Scatterer	∆ E0 /eV	Coordination Number	Radial Distance /Å	σ ^{2} /Å^2	R_{factor}
RT Argon	Re-O (1)	10 ± 1	4.03 ± 1.86	1.73 ± -0.0005	-0.0004	0.05
	Re-Re (in ReO_2)		-0.005 ± 0.41	2.60 ± -0.07	-0.01	
225 °C under O_2 pretreatment	Re-O (1)	8 ± 3	3.12 ± 0.58	1.73 ± 0.002	0.002	0.03
	Re-Re (in ReO_2)		357.14 ± 1358.20	3.06 ± 0.09	0.15	
225 °C under ethylene	Re-O (1)	10 ± 3	3.07 ± 0.27	1.73 ± 0.0004	-0.00002	0.03
	Re-Re (in ReO_2)		76.13 ± 194.40	3.02 ± 0.07	0.09	
275 °C under ethylene	Re-O (1)	10 ± 3	3.04 ± 0.55	1.73 ± 0.02	0.00002	0.03
	Re-Re (in ReO_2)		27.63 ± 50.90	3.00 ± 0.07	0.085	

Fitting Parameters: S_0^2 determined from W foil = 0.78, 1 < R < 3.0 Å. k-range 6.0 – 14.8, no. of independent points 10.9.

Compared to Re-Ag/γ-Al_2O_3 for Re-Ag/α-Al_2O_3 (shown in *Figure 4.67*) there are changes in the Re structure, there appears to be an addition of a second longer Re-O bond, potentially indicating that Re-O is on the Ag, rather than the Al. Whilst there is a slight change from Re-Ag/α-Al_2O_3 to Re-Ag/α-Al_2O_3 at 225 °C likely to do with the increase in temperature, there is no change in the Re structure with the addition of ethylene. There is a shift in the Re structure at 275 °C, where it appears more like Re-Ag/γ-Al_2O_3. As shown above, at 275 °C sintering occurs, potentially indicating that more Re-O species are on the aluminium rather than the silver surface.

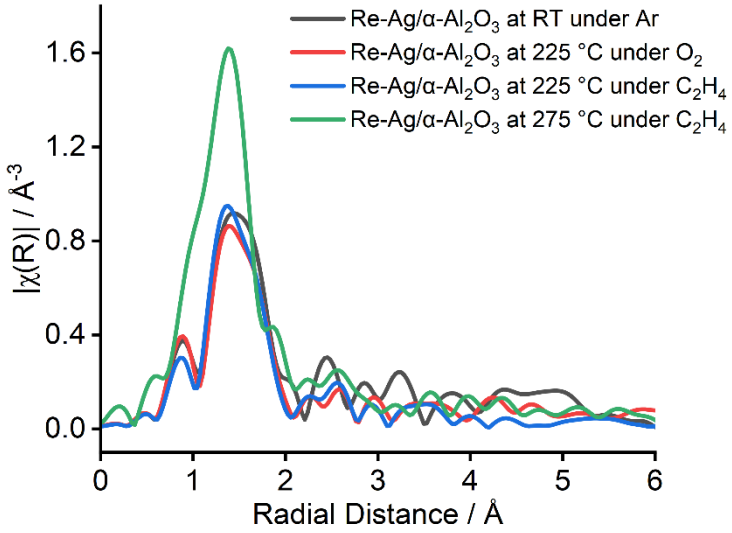

Figure 4.67: Re L3-edge XANES R value for the Re-Ag/α-Al_2O_3 catalyst under argon at room temperature, under O_2 pretreatment at 225 °C, under C_2H_4 at 225 °C and under C_2H_4 under 275 °C.

Due to a lack of structural models for the Re-O species on Ag/Al_2O_3, there was difficulty in fitting the Re-Ag/α-Al_2O_3. As shown in *Table 4.21*, *4.22* and *4.23*, (due to the similarity of the Re-Ag/α-Al_2O_3 at the conditions of O_2 pretreatment at 225 °C and C_2H_4 at 225 °C, only the C_2H_4 at 225 °C condition is shown) Re-Ag/α-Al_2O_3 did not fit the above fits used for Re-Ag/γ-Al_2O_3 or two different oxygen species of Re-O(1) and Re-O(2). However, this does indicate that more than one species of oxygen is needed to fit this data and that there are no Re-Re bonds again indicating a Re oxide cluster. Due to the smaller surface area of α-Al_2O_3, it is thought that it is more likely that the Re oxide clusters are on the Ag (STEM indicates that the Re clusters around the Ag), therefore there are likely to be more interactions between the Re-O and Ag particles. A structural model is needed to identify these interactions.

Table 4.21: Re L3-edge EXAFS different fitting parameters for the Re-Ag/α-Al_2O_3

Conditions	Abs-Scatterer	∆ E0 /eV	Coordination Number	Radial Distance /Å	σ^2 /Å^2	R_{factor}
RT Argon	Re-O (1)	14 ± 1	0.25 ± 0.23	1.71 ± -0.007	-0.007	0.4
RT Argon	Re-O (1)	17 ± 3	0.68 ± 0.18	1.73 ± 0.0006	-0.002	0.06
	Re-O (2)		2.71 ± 0.82	2.10 ± 0.02	0.005	
RT Argon	Re-O (1)	2 ± 8	0.33 ± 0.32	1.69 ± -0.02	-0.005	0.40
	Re-Re (in ReO_2)		23.1 ± 63.6	2.94 ± 0.05	0.048	
RT Argon	Re-O (2)	-49 ± 16	1.84 ± 1.53	1.91 ± -0.07	-0.003	0.25

Fitting Parameters: S_0^2 determined from W foil = 0.78, 1 < R < 3.0 Å. k-range 6.0 – 14.8, no. of independent points 10.9.

Table 4.22: Re L3-edge EXAFS different fitting parameters for the Re-Ag/α-Al_2O_3

Conditions	Abs-Scatterer	∆ E0 /eV	Coordination Number	Radial Distance /Å	σ^2 /Å^2	R_{factor}
225 °C under C_2H_4	Re-O (1)	9 ± 11	0.30 ± 0.21	1.70 ± -0.01	-0.006	0.33
225 °C under C_2H_4	Re-O (1)	15 ± 5	0.67 ± 0.22	1.73 ± -0.001	-0.002	0.02
	Re-O (2)		2.32 ± 0.97	2.08 ± 0.01	0.005	
225 °C under C_2H_4	Re-O (1)	4 ± 9	0.35 ± 0.37	1.69 ± -0.02	-0.02	0.3
	Re-Re (in ReO_2)		32.91 ± 159.0	2.99 ± 0.07	0.06	
225 °C under C_2H_4	Re-O (2)	-54 ± 12	2.02 ± 1.25	1.90 ± -0.077	-0.003	0.2

Fitting Parameters: S_0^2 determined from W foil = 0.78, 1 < R < 3.0 Å. k-range 6.0 – 14.8, no. of independent points 10.9.

Table 4.23: Re L3-edge EXAFS different fitting parameters for the Re-Ag/α-Al_2O_3

Conditions	Abs-Scatterer	∆ E0 /eV	Coordination Number	Radial Distance /Å	σ^2 /Å^2	R_{factor}
275 °C under C_2H_4	Re-O (1)	10 ± 4	2.77 ± 0.22	1.73 ± 0.003	0.001	0.15
275 °C under C_2H_4	Re-O (1)	6 ± 3	2.67 ± 0.33	1.71 ± 0.02	-0.0005	0.02
	Re-O (2)		0.31 ± 0.32	2.07 ± 0.006	-0.01	
275 °C under C_2H_4	Re-O (1)	11 ± 5	2.33 ± 0.35	1.73 ± 0.004	-0.001	0.11
	Re-Re (in ReO_2)		-0.02 ± 0.20	2.74 ± -0.02	-0.01	
275 °C under C_2H_4	Re-O (2)	-47 ± 3	7.53 ± 1.23	1.94 ± -0.05	0.001	0.04

Fitting Parameters: S_0^2 determined from W foil = 0.78, 1 < R < 3.0 Å. k-range 6.0 – 14.8, no. of independent points 10.9.

Whilst a structural model is needed to understand more of the Re-O, Re-O-Ag and Re-O-Al bonds, some conclusions can be drawn from this Re XAFS data:

1. For Re-Ag/γ-Al_2O_3 the Re structure remains stable under different conditions studied
2. For Re-Ag/α-Al_2O_3 the Re structure changes under different conditions studied
3. The Re oxide species appear to be a distorted tetrahedral structure
4. For the Re-Ag/γ-Al_2O_3 catalyst the Re species is likely to be bonded to the γ-Al_2O_3 due to the large surface area
5. For the Re-Ag/α-Al_2O_3 the structure is more distorted on Ag – assumed 2 different oxygen species however could not fit
6. No Re-Re bonds fit indicating Re oxide clusters are on the surface

4.3 Conclusions

As discussed in Chapter **1.1.2.1**, the role of the oxygen species, promoters and mechanism is still debated in the literature.[2] In this chapter, the role of the support, the O_2 pre-treatment, the role of the oxygen species and the role of the Re promoter have been discussed and provide information into improving the understanding of the catalysts used in ethylene epoxidation. Four catalysts Ag/α-Al_2O_3, Re-Ag/α-Al_2O_3, Ag/γ-Al_2O_3 and Re-Ag/γ-Al_2O_3 were characterised and analysed using a variety of *in situ* and *ex situ* techniques. The conclusions given below have been separated into different sections for clarity.

It should be stated that whilst the Re concentration is more than the optimal for Re alone to compare with the Cs-Re case (**Chapter 5**), so there is no guarantee that these affects are maintained with lower Re concentrations that are more selective for EO.

New Information Concluded:

- O_2 pretreatment causes a decrease in average Ag crystallite sizes causing a redispersion of Ag and an increase in O_{ads}.
- A reaction temperature of 275 °C causes sintering meaning a reaction at temperatures lower than this is optimal.
- γ-Al_2O_3 compared to α-Al_2O_3 causes more distribution with smaller Ag crystallites and shows more adsorbed oxygen.
- The addition of 500 ppm of Re caused a decrease in EO selectivity.
- Re appeared to weaken the Ag-O bond however there was an increase in acidity and hydroxyl groups, which is likely to be due to the cause of a reduced EO selectivity.
- Both *ex situ* Raman and *in situ* XAFS indicate to changes occurring with the Re-O bonds throughout ethylene epoxidation on the Re-Ag/α-Al_2O_3.
- For the Re-Ag/γ-Al_2O_3 catalyst the Re species is likely to be bonded to the γ-Al_2O_3 due to the large surface area, whilst for the Re-Ag/α-Al_2O_3 the structure is more distorted on Ag – assumed 2 different oxygen species.

Contradictions to the Literature:

- *Ex situ* XPS indicates that the Ag/α-Al_2O_3 surface is equivalent to a thin silver oxide layer. This conclusion disagrees with Linic and Barteau who proposed the oxametallacycle mechanism on metallic Ag where the observed increase in selectivity with increasing oxygen coverage cannot be explained by the OMC mechanism.[82]

- Re does not cause a change in the distribution of Ag. This disagrees with Dellamorte *et al.,* who states that Re causes a redistribution of the Ag into a trimodal particle size distribution.[71]
- Re does not affect the binding energy of Ag. This disagrees with Diao *et al*., who stated that Re is connected with making the Ag sites more electron-deficient.[9]
- In agreement with the above bullet point, the Re was not found to affect the binding energy of oxygen, which disagrees with Jun *et al*., who stated that Re competes with the adsorbed oxygen for the silver outer electrons which therefore reduces the electron density of the adsorbed oxygen and enhances the EO selectivity.[70]
- The oxidation state of Re was found to be +7. This disagrees with Ren *et al*. who stated that the Re oxidation state is between +4 to +7.[10]

Agreements with Previous Arguments in the Literature:

- Ag/γ-Al_2O_3 has lower EO selectivity and conversion compared to Ag/α-Al_2O_3. This agrees with the literature where commonly the catalyst support used for this is α-Al_2O_3 mainly due to the high selectivity due to small surface area leading to a reduction in the hydroxyl groups, whereas γ-Al_2O_3 has a higher surface area leading to more hydroxyl groups.[11,45,83,84]
- γ-Al_2O_3 compared to α-Al_2O_3 has more hydroxyl groups on the surface leading to the unselective isomerisation of EO to AA. It is common knowledge that γ-Al_2O_3 generally has more hydroxyl groups on its surface compared to α-Al_2O_3 due to the its higher surface area and more disordered structure, therefore this conclusion also agrees.[85,86]
- *Ex situ* XPS indicates that the Ag/α-Al_2O_3 surface is equivalent to a thin silver oxide layer. This agrees with the more recent literature that ethylene epoxidation occurs on an oxidised silver surface.[2,87,88]
- Both *ex situ* XPS and Raman spectroscopy identified a hybrid atomic molecular oxygen structure of Ag_4-O_2. This agrees with new literature of this hybrid species being present on the surface of ethylene epoxidation catalysts.[38,39,47,53,74]
- Result from *in situ* XPS indicates that there is a mixture of Ag_x–O_2 dioxygen and atomic electrophilic oxygen under reaction conditions. This agrees with Wachs and Alzahrani *et al.* who have both stated that a mixture of oxygen species including both atomic and hybrid electrophilic oxygen species are active under ethylene epoxidation conditions.[53,74]
- There is a shift of the Ag 3d XPS which indicates that the surface becomes slightly more oxidised during the O_2 pretreatment and under reaction conditions. This agrees with

literature from both Artiglia and Carbonio *et al.* who stated that under oxidation and ethylene epoxidation condition, there is an increase in the oxidation of silver.[89,90]

- The Re was found to cluster around the Ag in a +7 oxidation state, where they are likely to be as Re-O clusters with no Re-Re interaction. This agrees with Dellamorte and Diao *et al.* who stated that the Re is in a +7 oxidation state.[9,72] This also agrees with Hardcastle and Okal et al. who stated that on Al_2O_3 there are three equivalent terminal Re-O bonds and one inequivalent Re-O bond.[77,80]
- Using TEM, STEM and pXRD Re was found to not change the Ag particle sizes or morphology which agrees with Diao *et al.*[9]

4.4 References

1 US Pat., US1998878A, 1935.
2 T. Pu, H. Tian, M. E. Ford, S. Rangarajan and I. E. Wachs, *ACS Catal.*, 2019, **9**, 10727–10750.
3 D. M. Minahan, G. B. Hoflund, W. S. Epling and D. W. Schoenfeld, *J. Catal.*, 1997, **168**, 393–399.
4 H. Kestenbaum, A. Lange de Oliveira, W. Schmidt, F. Schüth, W. Ehrfeld, K. Gebauer, H. Löwe, T. Richter, D. Lebiedz, I. Untiedt and H. Züchner, *Ind. Eng. Chem. Res.*, 2002, **41**, 710–719.
5 S. Linic and M. A. Barteau, *J. Am. Chem. Soc.*, 2003, **125**, 4034–4035.
6 D. Jingfa, Y. Jun, Z. Shi and Y. Xiaohong, *J. Catal.*, 1992, **138**, 395–399.
7 S. N. Goncharova, E. A. Paukshtis and B. S. Bal'zhinimaev, *Appl. Catal. A: Gen.*, 1995, **126**, 67–84.
8 J. T. Jankowiak and M. A. Barteau, *J. Catal.*, 2005, **236**, 366–378.
9 W. Diao, C. D. DiGiulio, M. T. Schaal, S. Ma and J. R. Monnier, *J. Catal.*, 2015, **322**, 14–23.
10 D. Ren, G. Cheng, J. Li, J. Li, W. Dai, X. Sun and D. Cheng, *Catal. Letters.*, 2017, **147**, 2920–2928.
11 S. Rojluechai, S. Chavadej, J. W. Schwank and V. Meeyoo, *Catal. Commun.*, 2007, **1**, 57–64.
12 J. T. Jankowiak and M. A. Barteau, *J. Catal.*, 2005, **236**, 366–378.
13 K. Y. Paranjpe, *J. Pharm. Innov.*, 2017, **6**, 236–238.
14 S. Lamouri, M. Hamidouche, N. Bouaouadja, H. Belhouchet, V. Garnier, G. Fantozzi and J. F. Trelkat, *Bol. Soc. Esp. Ceram. V.*, 2017, **56**, 47–54.
15 L. Ding, M. Li, Y. Zhao, H. Zhang, J. Shang, J. Zhong, H. Sheng, C. Chen and J. Zhao, *Appl. Catal. B: Environ.*, 2020, **266**, 118634.
16 X. Liu, *J. Phys. Chem. C.*, 2008, **112**, 5066–5073.
17 P. Mulpur, S. Patnaik, A. Chunduri, T. M. Rattan, A. M. Rao and V. Kamisetti, *Soft Nanoscience Letters.*, 2013, **2013**, 27–31.
18 H. Ayoola, University of Pittsburgh, 2021.
19 C. F. Holder and R. E. Schaak, *ACS Nano.*, 2019, **13**, 7359–7365.
20 Powder X-ray Diffraction, https://chem.libretexts.org/Bookshelves/Analytical_Chemistry/Supplemental_Modules_(Analytical_Chemistry)/Instrumentation_and_Analysis/Diffraction_Scattering_Techniques/Powder_X-ray_Diffraction, (accessed 14 October 2024).
21 A. J. F. van Hoof, E. A. R. Hermans, A. P. van Bavel, H. Friedrich and E. J. M. Hensen, *ACS Catal.*, 2019, **9**, 9829–9839.
22 K. Suematsu, N. Ma, M. Yuasa, T. Kida and K. Shimanoe, *RSC Adv.*, 2015, **5**, 86347–86354.
23 C. Backx, C. P. M. De Groot and P. Biloen, *Surf. Sci.*, 1981, **104**, 300–317.
24 G. I. N. Waterhouse, G. A. Bowmaker and J. B. Metson, *Appl. Surf. Sci.*, 2003, **214**, 36–51.
25 X. Jing, H. Wang, H. Chen, J. Huang, Q. Li and D. Sun, *RSC Adv.*, 2014, **4**, 27597–27603.
26 T. E. Bell, J. M. González-Carballo, R. P. Tooze and L. Torrente-Murciano, *J. Mater. Chem. A.*, 2015, **3**, 6196–6201.
27 N. M. Stuart and K. Sohlberg, *Energies.*, 2021, **14**, 6472.
28 M. F. L. Johnson and V. M. LeRoy, *J. Catal.*, 1974, **35**, 434–440.
29 J. Tang, Y. Sun, C. Zhang, L. Wang, Y. Zhou, D. Fang and Y. Liu, *Metals.*, 2020, **10**, 640.
30 W. T. Tysoe, F. Zaera and G. A. Somorjai, *Surf. Sci.*, 1988, **200**, 1–14.
31 A. Moen, D. G. Nicholson, M. Rønning and H. Emerich, *J. Mater. Chem.*, 1998, **8**, 2533–2539.
32 J. Räty and T. A. Pakkanen, *J. Mol. Catal. A Chem.*, 2001, **166**, 275–281.

33 R. Chanerika, M. L. Shozi and H. B. Friedrich, *ACS Omega.*, 2022, **7**, 4026–4040.
34 T. Furusawa, K. Seshan, J. A. Lercher, L. Lefferts and K. Aika, *Appl. Catal. B: Environ.*, 2002, **37**, 205–216.
35 F. Wang, J. Ma, G. He, M. Chen, C. Zhang and H. He, *ACS Catal.*, 2018, **8**, 2670–2682.
36 T. Pu, A. Setiawan, B. Mosevitzky Lis, M. Zhu, M. E. Ford, S. Rangarajan and I. E. Wachs, *ACS Catal.*, 2022, **12**, 4375–4381.
37 T. J. Frankcombe and Y. Liu, *Chem. Mater.*, 2023, **35**, 5468–5474.
38 T. Pu, A. Setiawan, B. Mosevitzky Lis, M. Zhu, M. E. Ford, S. Rangarajan and I. E. Wachs, *ACS Catal.*, 2022, **12**, 4375–4381.
39 T. Pu, A. Setiawan, A. C. Foucher, M. Guo, J.-M. Jehng, M. Zhu, M. E. Ford, E. A. Stach, S. Rangarajan and I. E. Wachs, *ACS Catal.*, 2024, **14**, 406–417.
40 S. W. Gaarenstroom and N. Winograd, *J. Chem. Phys.*, 1977, **67**, 3500–3506.
41 Silver, http://www.xpsfitting.com/2013/04/silver.html, (accessed 13 April 2024).
42 NIST Chemistry WebBook, https://webbook.nist.gov/chemistry/, (accessed 22 October 2023).
43 Silver – HarwellXPS Guru, https://www.harwellxps.guru/knowledgebase/silver/, (accessed 13 April 2024).
44 R. B. Grant and R. M. Lambert, *J. Catal.*, 1985, **92**, 364–375.
45 C. J. Keijzer, L. C. J. Smulders, D. Wezendonk, J. W. de Rijk and P. E. de Jongh, *Catal. Today.*, 2024, **428**, 114447.
46 T. Pu, J.-M. Jehng, A. Setiawan, B. Mosevitzky Lis, M. E. Ford, S. Rangarajan and I. E. Wachs, *J. Phys. Chem. C.*, 2022, **126**, 21568–21575.
47 C. Liu, D. P. Wijewardena, A. Sviripa, A. Sampath, D. W. Flaherty and C. Paolucci, *J. Catal.*, 2022, **405**, 445–461.
48 H. D. Ruan, R. L. Frost and J. T. Kloprogge, *J. Raman Spectrosc.*, 2001, **32**, 745–750.
49 T. Hartman, C. S. Wondergem, N. Kumar, A. van den Berg and B. M. Weckhuysen, *J. Phys. Chem. Lett.*, 2016, **7**, 1570–1584.
50 S. Schlücker, *Angew. Chem., Int. Ed. Engl.*, 2014, **53**, 4756–4795.
51 G. Demirel, H. Usta, M. Yilmaz, M. Celik, H. A. Alidagi and F. Buyukserin, *J. Mater. Chem. C.*, 2018, **6**, 5314–5335.
52 C.-B. Wang, G. Deo and I. E. Wachs, *J. Phys. Chem. B.*, 1999, **103**, 5645–5656.
53 Z. Tang, T. Chen, K. Liu, H. Du and S. G. Podkolzin, *Langmuir.*, 2021, **37**, 11603–11610.
54 K.-K. Liu, S. Tadepalli, L. Tian and S. Singamaneni, *Chem. Mater.*, 2015, **27**, 5261–5270.
55 RTN, https://www.edinst.com/resource/technical-note-how-to-reduce-fluorescence-in-raman-spectroscopy/, (accessed 6 October 2024).
56 D. Wei, S. Chen and Q. Liu, *Appl. Spectrosc. Rev.*, 2015, **50**, 387–406.
57 L. Cabo-Fernandez, A. R. Neale, F. Braga, I. V. Sazanovich, R. Kostecki and L. J. Hardwick, *Phys. Chem. Chem. Phys.*, 2019, **21**, 23833–23842.
58 O. Abbas, A. Pissard and V. Baeten, in *Chemical Analysis of Food (Second Edition)*, ed. Y. Pico, Academic Press, 2020, pp. 77–134.
59 P. J. Cadusch, M. M. Hlaing, S. A. Wade, S. L. McArthur and P. R. Stoddart, *J. Raman Spectrosc.*, 2013, **44**, 1587–1595.
60 K. Djebaili, Z. Mekhalif, A. Boumaza and A. Djelloul, *J. Spectrosc.*, 2015, **2015**, 868109.
61 T. P. Mokoena, E. C. Linganiso, H. C. Swart, V. Kumar and O. M. Ntwaeaborwa, *Ceram. Int.*, 2017, **43**, 174–181.
62 IR Spectrum Table & Chart, https://www.sigmaaldrich.com/technical-documents/articles/biology/ir-spectrum-table.html, (accessed 24 May 2021).
63 M. V. Zakharova, F. Kleitz and F.-G. Fontaine, *Dalton Trans.*, 2017, **46**, 3864–3876.
64 M. Armenta, V. Maytorena and D. Buentello Montoya, *Fuel.*, 2023, **358**, 130268.
65 Anusha, A. Ani, P. Poornesh, A. Antony, Bhaghyesh, I. V. Shchetinin, K. K. Nagaraja, S. Chattopadhyay and K. B. Vinayakumar, *Sensors.*, 2022, **22**, 2033.

66 IR Spectrum Table, https://www.sigmaaldrich.com/GB/en/technical-documents/technical-article/analytical-chemistry/photometry-and-reflectometry/ir-spectrum-table, (accessed 12 January 2024).
67 M. R. D'Oliveira, J. Rabelo, A. G. Veiga, C. A. Chagas and M. Schmal, *Catal Lett.*, 2020, **150**, 3036–3048.
68 M. C. N. Amorim de Carvalho, F. B. Passos and M. Schmal, *J. Catal.*, 2007, **248**, 124–129.
69 D. A. Bulushev, E. A. Paukshtis, Y. N. Nogin and B. S. Bal'zhinimaev, *Appl. Catal. A: Gen.*, 1995, **123**, 301–322.
70 Y. Jun, D. Jingfa, Y. Xiaohong and Z. Shi, *Appl. Catal. A: Gen.*, 1992, **92**, 73–80.
71 J. C. Dellamorte, J. Lauterbach and M. A. Barteau, *Ind. Eng. Chem. Res.*, 2009, **48**, 5943–5953.
72 J. C. Dellamorte, J. Lauterbach and M. A. Barteau, *Catal. Today.*, 2007, **120**, 182–185.
73 M. A. Salaev, A. A. Salaeva, O. Kh. Poleschuk and O. V. Vodyankina, *J Struct Chem.*, 2019, **60**, 1713–1724.
74 H. A. Alzahrani and J. J. Bravo-Suárez, *J. Catal.*, 2023, **418**, 225–236.
75 M. Atkins, J. Couves, M. Hague, B. H. Sakakini and K. C. Waugh, *J. Catal.*, 2005, **235**, 103–113.
76 D. Ren, H. Xu, J. Li, J. Li and D. Cheng, *Mol. Catal.*, 2017, **441**, 92–99.
77 F. D. Hardcastle, I. E. Wachs, J. A. Horsley and G. H. Via, *Mol. Catal.*, 1988, **46**, 15–36.
78 M. T. Greiner, T. C. R. Rocha, B. Johnson, A. Klyushin, A. Knop-Gericke and R. Schlögl, *Z. Phys. Chem.*, 2014, **228**, 521–541.
79 J. Okal, L. Kępiński, L. Krajczyk and W. Tylus, *J. Catal.*, 2003, **219**, 362–371.
80 J. Okal, *Appl. Catal. A: Gen.*, 2005, **287**, 214–220.
81 D. A. Simonetti, E. L. Kunkes and J. A. Dumesic, *J. Catal.*, 2007, **247**, 298–306.
82 S. Linic and M. A. Barteau, *J. Am. Chem. Soc.*, 2002, **124**, 310–317.
83 J. E. van den Reijen, S. Kanungo, T. A. J. Welling, M. Versluijs-Helder, T. A. Nijhuis, K. P. de Jong and P. E. de Jongh, *J. Catal.*, 2017, **356**, 65–74.
84 A. Ayame, Y. Uchida, H. Ono, M. Miyamoto, T. Sato and H. Hayasaka, *Appl. Catal. A Gen.*, 2003, **244**, 59–70.
85 J. Lv, D. Wang, L. Peng, X. Guo, W. Ding and W. Yang, *Catalysts.*, 2023, **13**, 994.
86 V. Sanchez Escribano, G. Garbarino, E. Finocchio and G. Busca, *Top Catal.*, 2017, **60**, 1554–1564.
87 G. Rovida, F. Pratesi and E. Ferroni, *Appl. Surf. Sci.*, 1980, **5**, 121–132.
88 M. O. Özbek and R. A. van Santen, *Catal Lett.*, 2013, **143**, 131–141.
89 E. A. Carbonio, T. C. R. Rocha, A. Y. Klyushin, I. Píš, E. Magnano, S. Nappini, S. Piccinin, A. Knop-Gericke, R. Schlögl and T. E. Jones, *Chem. Sci.*, 2017, **9**, 990.
90 M. Guo, N. Dongfang, M. Iannuzzi, J. A. van Bokhoven and L. Artiglia, *ACS Catal.*, 2024, **14**, 10234–10244.

Chapter 5: Understanding the Role of Cs and Cs & Re as Promoters for Ethylene Epoxidation

As discussed in **Chapter 1.1.2**, the role of the promoters is still debated in the literature.[1] In this chapter Cs-Ag/α-Al_2O_3 has been investigated to give more information regarding both the role and the structure. As discussed, the combined role of the promoters Cs and Re when used together has been minimally investigated, therefore in the second part of this chapter, Cs-Re-Ag/α-Al_2O_3 has been investigated to give more information regarding its role of both promoters when used together. These catalysts have been characterised by both *in situ* and *ex situ* techniques and the activity and selectivity profiles of these catalysts have been determined with comparison to the literature. The role of the Cs promoter and the Cs-Re promoters together have been discussed in detail and provide information to improve the understanding of the catalysts used in ethylene epoxidation. Throughout the chapter relevant Ag/α-Al_2O_3 data from **Chapter 4** is included as a benchmark.

5.1 Understanding the Role of Cs as a Promoter

As discussed in **Section 1.1.2.3**, whilst the use of Cs as a promoter has been discussed, its specific role in the selective oxidation of ethylene is still a subject of much debate although it causes a significant increase in EO selectivity when added.[2–11]

It was thought that the use of *in situ* and *ex situ* spectroscopic and characterisation techniques would be able to give more insight into both the role of Cs and the electronic properties of Cs. These results will be critically compared to the literature to help with understanding the Cs promoter.

Both Cs-Ag/α-Al_2O_3 and Cs-Ag/γ-Al_2O_3 catalysts were made using incipient wetness impregnation with 10 wt. % Ag to be able to compare to the previous catalysts. It is thought that the optimum amount of Cs required to improve the EO selectivity is between 200 - 600 ppm, therefore approximately 600 ppm was added.[1,5,10,12] To confirm that the elemental composition of the catalysts was as expected, ICP-OES was conducted on both. The elemental composition of the catalysts is shown in *Table 5.1*. The silver and caesium contents of the two catalysts were close to the expected values, with small fluctuations of value and with low errors.

Table 5.1: Summary of ICP-OES results. The results reported are the average results of the duplicate samples where errors are one standard deviation calculated based on the duplicate samples for each material. Standards are run in the same batch to confirm no significant anomalies or deviations in the instrumental analysis of the samples.

Catalyst	Metal	Expected Metal Content / wt. %	Metal Content by ICP-OES / wt. %	Error in Metal Content by ICP-OES / wt. %
Ag/α-Al_2O_3 (from Chapter 4)	Ag	10	9.86	±0.35
Ag/γ-Al_2O_3 (from Chapter 4)	Ag	10	10.12	±0.84
Cs-Ag/α-Al_2O_3	Cs	0.06	0.06	±0.01
	Ag	10	10.41	±0.57
Cs-Ag/γ-Al_2O_3	Cs	0.06	0.06	±0.01
	Ag	10	9.16	±0.84

Both Cs-Ag/α-Al_2O_3 and Cs-Ag/γ-Al_2O_3 were evaluated for ethylene epoxidation and compared to Ag/α-Al_2O_3 and Ag/γ-Al_2O_3 (both from Chapter 4) with the results displayed in *Figure 5.1* and *Figure 5.2,* respectively. As expected, there is an increase in the selectivity when adding in Cs, to the unpromoted catalysts.[2–11] There is also a reduction in acetaldehyde, carbon dioxide and water, corresponding to a more selective catalyst.

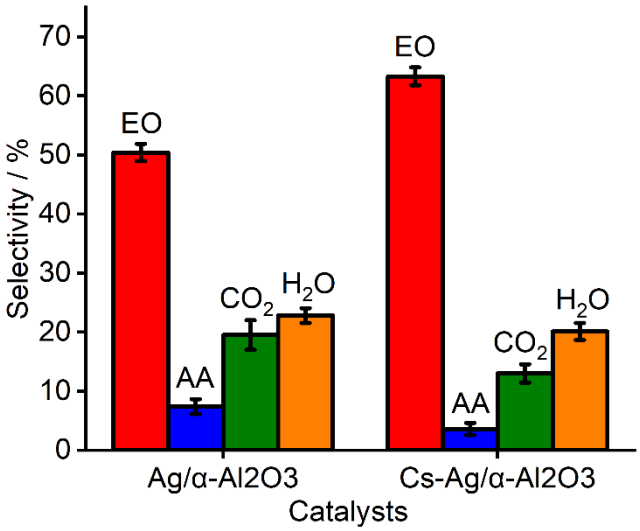

Figure 5.1: A comparison of selectivity between Ag/α-Al_2O_3 (from Chapter 4) and Cs-Ag/α-Al_2O_3. Errors shown are based on 3 repeat measurements.

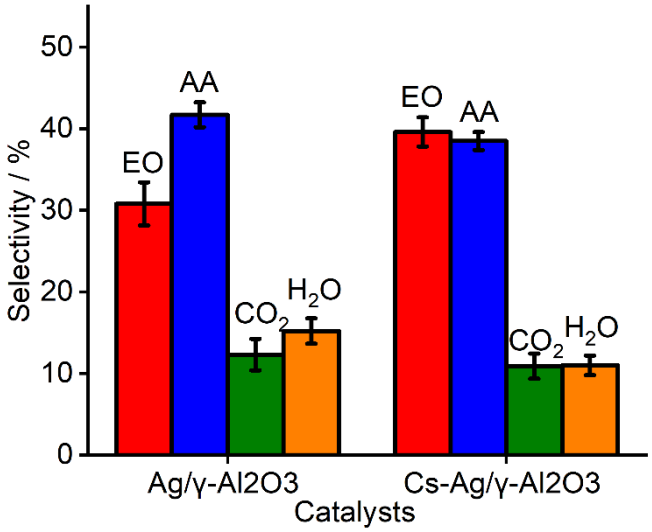

Figure 5.2: A comparison of selectivity between Ag/γ-Al_2O_3 (from Chapter 4) and Cs-Ag/γ-Al_2O_3. Errors shown are based on 3 repeat measurements.

Ethylene conversion was calculated and displayed in *Table 5.2*. There is a decrease in ethylene conversion between Cs-Ag/α-Al_2O_3 and Cs-Ag/γ-Al_2O_3, which is likely due to the γ-Al_2O_3 (as discussed in **Chapter 4**). There is no change in conversion when adding Cs.

Table 5.2: A table showing the ethylene conversion and percentage error based on 3 repeat measurements for both Ag/α-Al_2O_3 and Ag/γ-Al_2O_3.

Catalyst	Ethylene Conversion / %	% Error
Ag/α-Al_2O_3 (from Chapter 4)	7.7	0.4
Cs-Ag/α-Al_2O_3	8.8	0.3
Ag/γ-Al_2O_3 (from Chapter 4)	3.7	0.1
Cs-Ag/γ-Al_2O_3	3.7	0.2

5.1.1 Particle Sizes and Morphology

One suggestion of the role of Cs is that it can distribute the silver particles more uniformly on the support, therefore showing a more uniform distribution of sites for oxygen adsorption and reducing the amount of hydroxyl groups on the support.[5,13] As shown in *Figure 5.3,* which shows the pXRD of Cs-Ag/α-Al_2O_3 and Ag/α-Al_2O_3, there is a minor change between the two therefore, the figure was expanded to show the Ag (2 2 0) at 64.5 ° (shown in *Figure 5.4*). Ren *et al*. showed that with the use of XRD analysis, the composition of the catalyst can slightly influence the degree of Ag crystallisation.[10]

The Ag (2 2 0) reflection in the pXRD pattern suggests that Cs influences the degree of Ag crystallisation, based on the broadening of the reflection widths, indicating that Cs can affect the distribution of Ag.

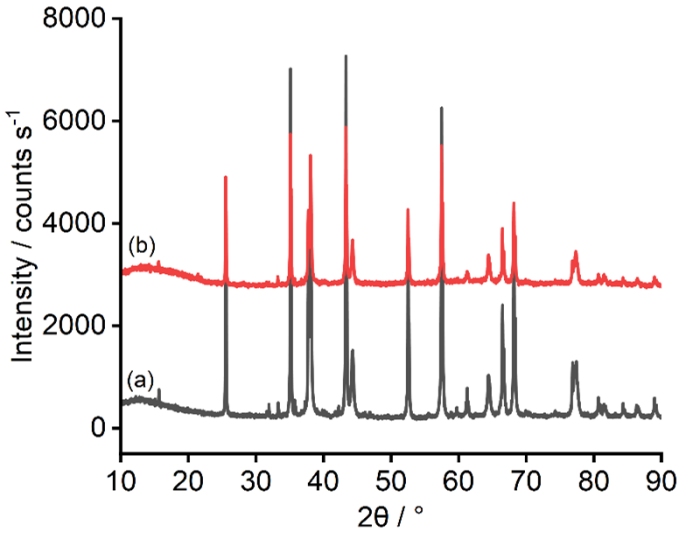

Figure 5.3: pXRD patterns for the α-alumina-based *catalysts; (a) Ag/α-Al_2O_3 (from Chapter 4); (b) Cs-Ag/α-Al_2O_3. Patterns offset vertically for clarity.*

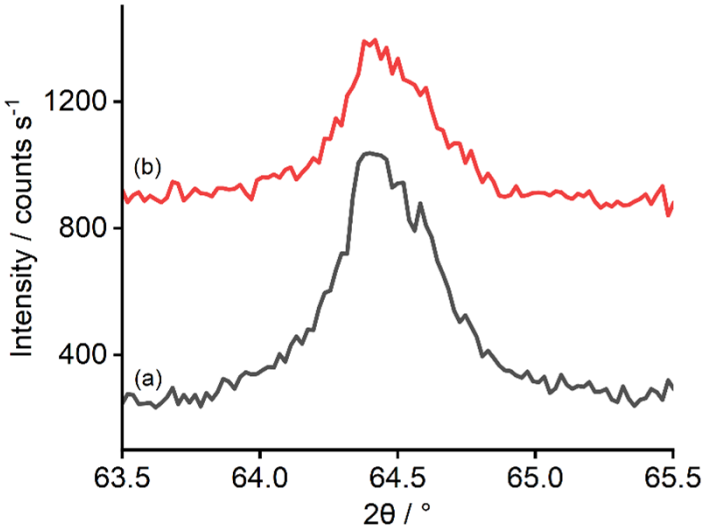

Figure 5.4: pXRD patterns for the α-Al_2O_3 based *catalysts; (a) Ag/α-Al_2O_3 (from Chapter 4); (b) Cs-Ag/α-Al_2O_3. Zoomed in on peak Ag (111). Patterns offset vertically for clarity.*

It has been suggested that Cs promotes the formation of very small particles over silver patches which increase the selectivity of ethylene oxide by increasing the contact with the reactants.[13] However, as discussed in **Chapter 1.1.2.1** there are several arguments for how the Ag crystallite affects ethylene epoxidation.[1,14–16] Therefore the size of the silver crystallite was investigated using the reflection at 64.5 ° with the Scherrer equation. The FWHM used for each catalyst and the resultant crystallite sizes are shown in *Table 5.3*. There is an increase of 0.5 ° of the FWHM, which is indicative of a decrease in the average Ag crystallite size of 6 nm therefore causing a dispersion of Ag.

Table 5.3: Summary of the FWHM and the particle size estimation from pXRD data using the Scherrer equation. Errors were calculated based on the error from fitting the Gaussian functions.

Catalyst	FWHM / °	Reflection(s) used / °	Estimated Crystallite Size / nm	Error in Gaussian fit of Crystallite Size / nm
Ag/α-Al_2O_3 (from Chapter 4)	0.36	64.5	51.2	± 1.4
Cs-Ag/α-Al_2O_3	0.41	64.5	44.9	± 2.5

To give more evidence regarding the suggestion that Cs distributes the silver particles more uniformly on the support, TEM and STEM were undertaken on the catalysts to test this hypothesis.[5,13] *Figure 5.5* showing the TEM results suggests that some of the metal particles have had morphology changes by the addition of Cs, however, STEM is needed to confirm this.

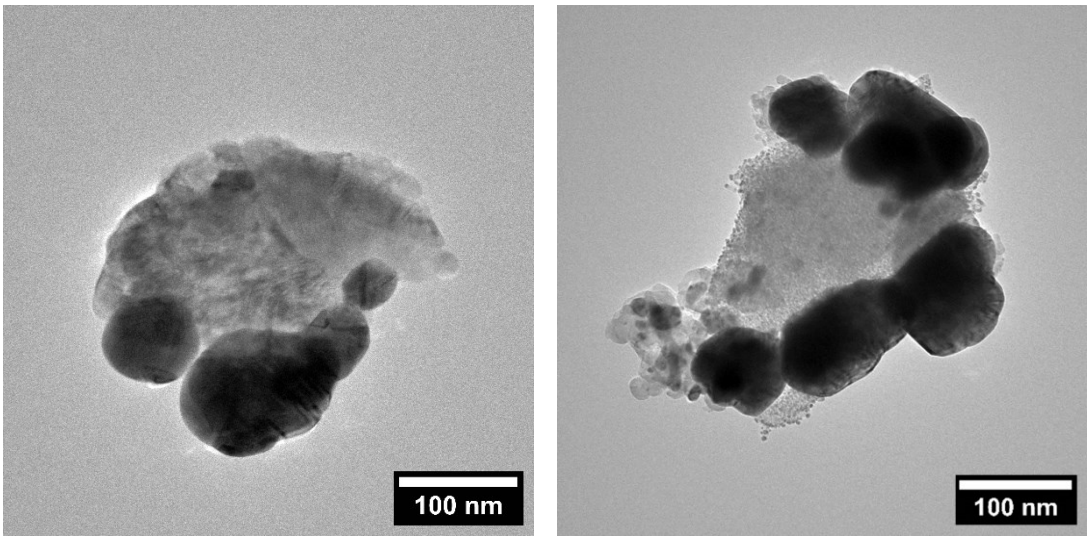

Figure 5.5: Representative TEM images of Ag/α-Al_2O_3 (from Chapter 4) on the left and Cs-Ag/α-Al_2O_3 on the right.

Elemental analysis using STEM was undertaken on Cs-Ag/α-Al_2O_3 (shown in *Figure 5.6*) to investigate the locations and the distribution of the Ag and Cs within the catalysts and to compare to Ag/α-Al_2O_3 (shown in **Chapter 4**). As suggested in the TEM and pXRD, STEM confirms the greater distribution of Ag with the addition of Cs. The caesium appears all over the surface of the catalyst rather than just at the Ag sites, indicating that the caesium is present as a thin layer rather than clusters.

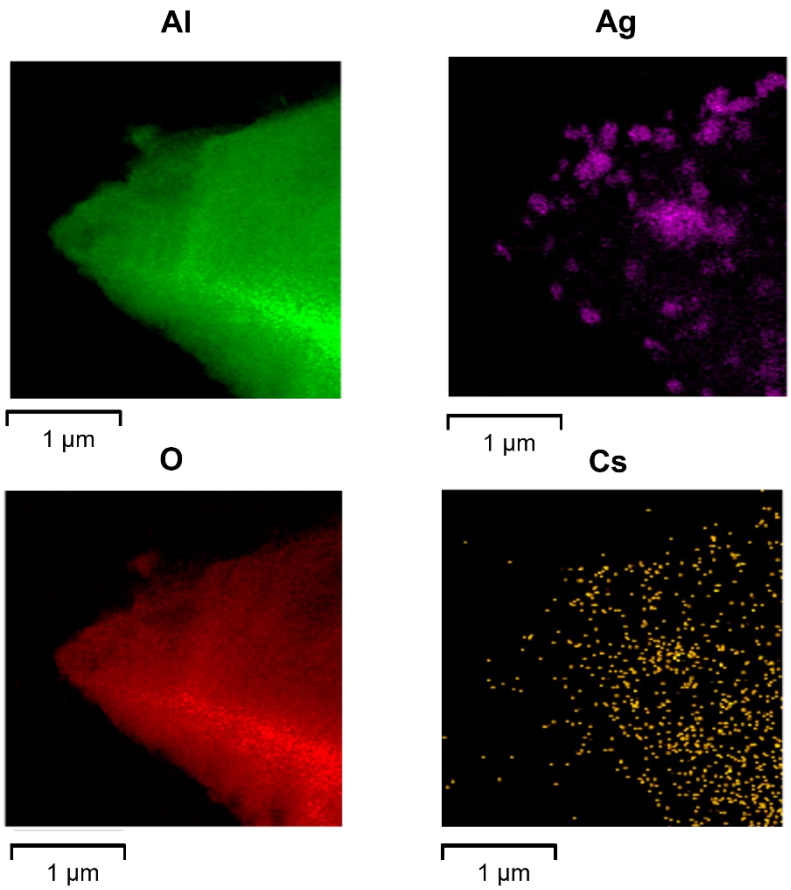

Figure 5.6: Elemental Mapping (using EDX), for the Cs-Ag/α-Al_2O_3, with aluminium shown in green, silver shown in purple, oxygen shown in red, and caesium shown in orange.

5.1.2 Understanding the Role of Oxygen and the Interaction with Silver with the Addition of Cs

There are suggestions that Cs plays a role in the oxygen species, therefore this was investigated.[17,18] The oxygen species on the Cs-Ag/α-Al_2O_3 were compared to the oxygen species on the Ag/α-Al_2O_3 catalyst (from Chapter 4). As shown in *Figure 5.7*, Cs-Ag/α-Al_2O_3 shows a peak at ~ 300 °C on the O_2-TPD indicating a weaker Ag-O bond compared to Ag/α-Al_2O_3 which has a peak at 350 °C.[1,19–21] This agrees with reports in the literature indicating that a weaker Ag-O bond results in increased EO selectivity.[8,18] Very little research has been undertaken on the desorption temperature of different Cs oxide species. However, the desorption of Cs_2O_2 (Cs peroxide) is reported to occur between 270 – 310 °C, the desorption of Cs_2O_4 (Cs superoxide) is reported to occur between 240 - 275 °C, the desorption of $Cs_{2+x}O$ (Cs suboxides) are reported to occur between 500 - 550 °C and the desorption of Cs_2O (Cs monoxide) is reported to occur between 440 - 480 °C.[22,23] This therefore gives indication that this peak could be a mixture of both the desorption of atomic oxygen and the desorption of a Cs oxide species if these form, individual peaks here are unable to be deconvoluted due to the likelihood of multiple species.[23] There is also an

increase in the amount of oxygen adsorbed on Cs-Ag/α-Al_2O_3 compared to Ag/α-Al_2O_3 due to the increase in the intensity of the O_2-TPD.

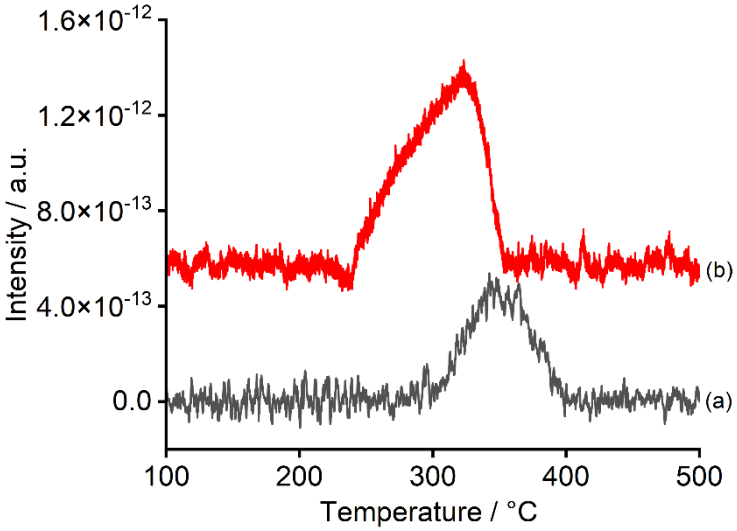

Figure 5.7: O_2-TPD profile of (a) Ag/α-Al_2O_3 (from Chapter 4) and (b) Cs-Ag/α-Al_2O_3 after O_2 pretreatment (heating rate of 5 °C min^{-1}). Spectra have been offset for clarity.

XPS of Ag 3d was investigated to understand whether Cs affects the Ag binding energy. *Figure 5.8*, shows the addition of Cs, causes a very small shift (0.1 eV) in the electron density of Ag, however, due to the low change in binding energy, this change is likely to be within the calibration error.

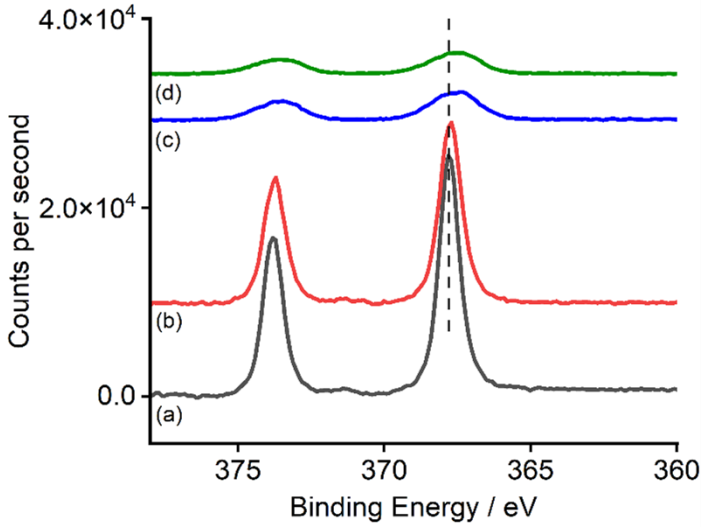

Figure 5.8: XPS spectra of all Ag3d data (after applying binding energy correction verified by the shift of the Al 2p peak and after subtraction of a Shirley background). Where (a) is Ag/α-Al_2O_3 (from Chapter 4), (b) is Cs-Ag/α-Al_2O_3, (c) is Ag/γ-Al_2O_3 (from Chapter 4) and (d) is Cs-Ag/γ-Al_2O_3. All samples are as prepared. Spectra have been offset for clarity.

O1s XPS of Ag/α-Al_2O_3 (from Chapter 4) and Cs-Ag/α-Al_2O_3 (shown in *Figure 5.9*) confirmed this result, there is no shift in binding energy of oxygen with the addition of Cs. *Table 5.4* shows a small increase in the O:Al ratio with the addition of Cs. This agrees with the

O_2-TPD data indicating an increased amount of O_{ads}. Due to the large ratio between oxygen and aluminium (i.e. the oxygen on the silver surface dominates over any signal from Al_2O_3), the main peak at 530 eV can be ascribed based on the literature as atomic electrophilic oxygen.[24,25] Whilst the shoulder at 532 eV can be ascribed Ag_x-O_2.[24,25]

Table 5.4: A table showing the ratios of oxygen: Al_2O_3 found by using the cross sections. This calculation is explained in ***Appendix 4****.*

		Surface Metal Ratios	
		O1s	**Al2p**
Sample	**Ag/α-Al_2O_3**	12.5	1
	Cs-Ag/α-Al_2O_3	13.6	1

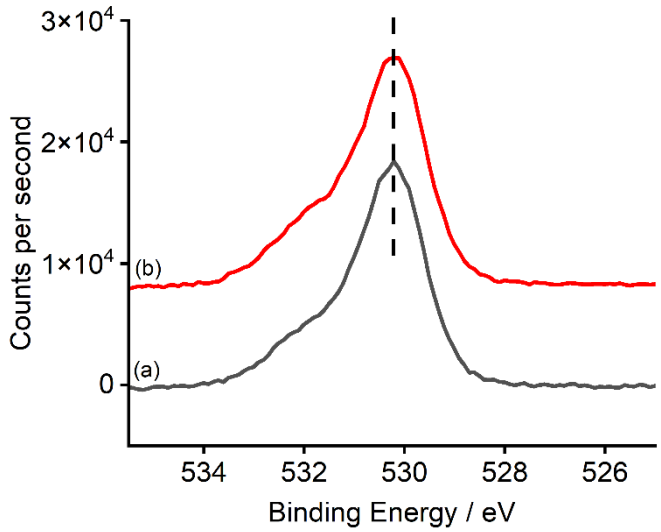

Figure 5.9: XPS spectra of all O1s data (after applying binding energy correction verified by the shift of the Al 2p peak and after subtraction of a Shirley background). Where (a) is Ag/α-Al_2O_3 and (b) is Cs-Ag/α-Al_2O_3. All samples are as prepared. Spectra have been offset for clarity.

Peak deconvolution was undertaken on the *ex situ* O1s XPS of Ag/α-Al_2O_3 and Cs-Ag/α-Al_2O_3 to show the two species present in the catalysts. Whilst the peak deconvolution of Ag/α-Al_2O_3 is shown in *Figure 4.17* the peak deconvolution of Cs-Ag/α-Al_2O_3 is shown in *Figure 5.10*. The determined peak areas of the two catalysts are shown in *Table 5.5.*

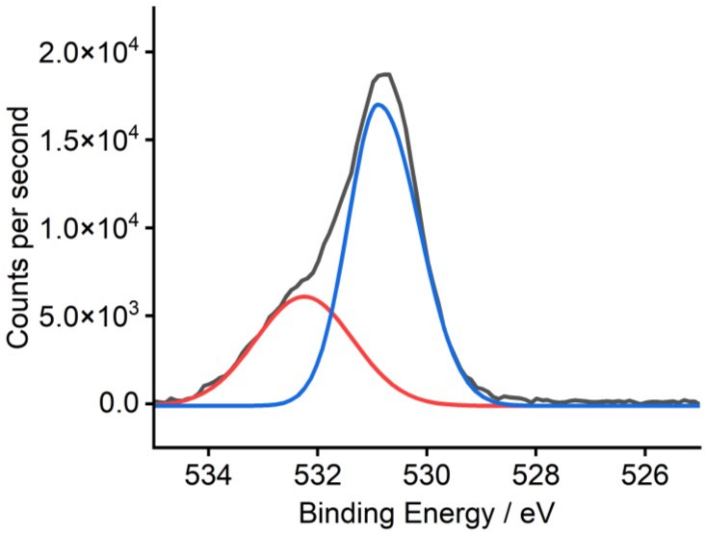

Figure 5.10: Peak deconvolution of the XPS spectra of the O1s looking at Cs-Ag/α-Al_2O_3. All samples are as prepared, after applying binding energy correction verified by the shift of the Al 2p peak and after subtraction of a Shirley background.

Table 5.5: A table showing the peak areas for the peak deconvolution of the XPS spectra of the O1s looking at both Ag/α-Al_2O_3 and Cs-Ag/α-Al_2O_3.

Catalyst	Peak Area of Blue Peak - atomic electrophilic oxygen / counts	Peak Area of Red Peak - Ag_x-O_2 / counts
Ag/α-Al_2O_3	25354.89	12227.33
Cs-Ag/α-Al_2O_3	26608.38	13879.29

H_2-TPR was undertaken on Cs-Ag/α-Al_2O_3 after O_2 pretreatment (shown in *Figure 5.11*), here there is a large increase to 0.83 ± 0.05 H_2 molecules per silver atom compared to Ag/α-Al_2O_3, agreeing with the O_2-TPD and XPS data that there are more O_{ads} on Cs-Ag/α-Al_2O_3 compared to Ag/α-Al_2O_3. The H_2-TPR is quite broad and featureless, making it hard to assign further.

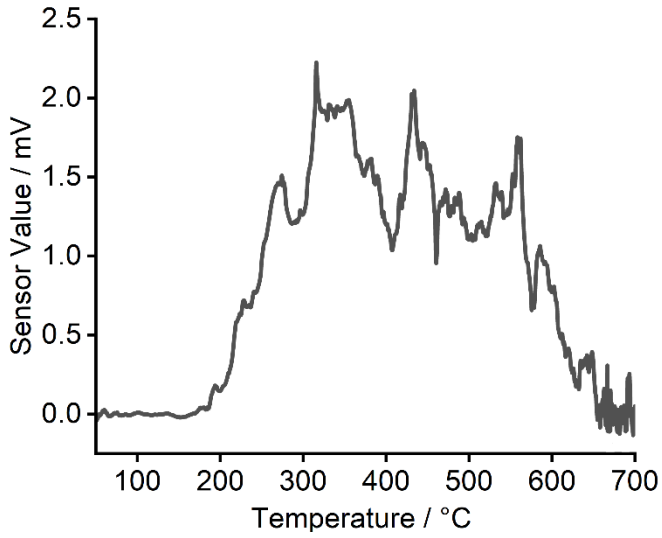

Figure 5.11: H_2-TPR of Cs-Ag/α-Al_2O_3 after O_2 pretreatment (heating rate of 5 °C min^{-1}).

The main difference between the Raman spectrum of Cs-Ag/α-Al_2O_3 and Ag/α-Al_2O_3 (shown in *Figure 5.12*) is a broad peak at 500 cm^{-1}, this is likely to be an Ag-oxide-like surface represented by O-Ag-O motifs that can be attributed to a combination of subsurface and surface oxygens.[15,26] There has also been a change in the peak at 280 cm^{-1}, which corresponds to atomic Ag-O interactions, indicating that there is a change in the surface Ag-O when Cs is added.[27]

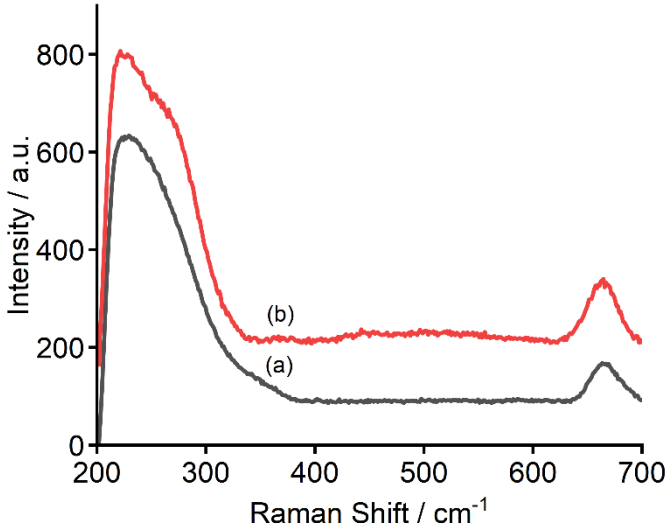

Figure 5.12: Raman spectra of (a) Ag/α-Al_2O_3 and (b) Cs-Ag/α-Al_2O_3 (after applying intensity response correction and subtraction of dark signal). Slit width = 150 µm*, number of spectra = 10, length of each spectrum = 10 s. Spectra have been offset for clarity.*

5.1.3 Investigating Hydroxyl Groups and Acidity

As suggested by Lambert *et al*. and Minahan *et al*. a proposed role of Cs is that it neutralises acid sites on the oxide support which are responsible for the isomerisation of the epoxide

to acetaldehyde.[5,28] The use of DRIFTS and Hammett indicator tests was used to investigate this. When looking at *Figure 5.13* (which shows the whole spectra) and *Figure 5.14* which shows the zoomed in area, comparing Ag/α-Al_2O_3 with Cs-Ag/α-Al_2O_3 there is shown to be a reduction in the band at 3300 cm^{-1} which corresponds to O-H hydroxyl groups.[29] This decrease in hydroxyl groups and acidity indicates that Cs neutralises the hydroxyl groups on the support.

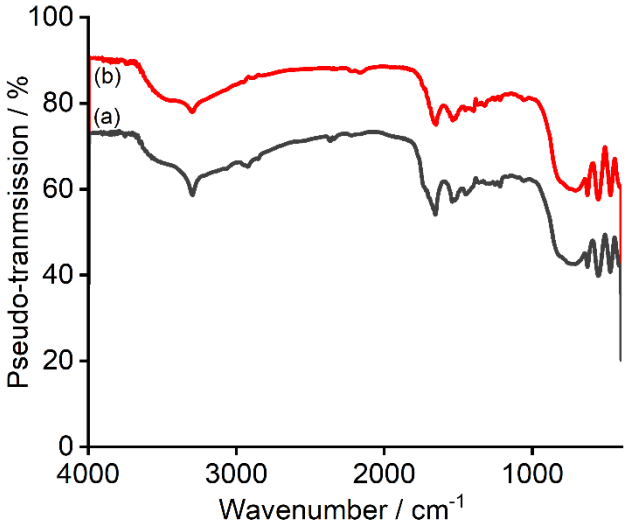

Figure 5.13: DRIFTS spectra of (a) Ag/α-Al_2O_3 (from Chapter 4) and (b) Cs-Ag/α-Al_2O_3, backgrounded against KBr. Spectra have been offset for clarity.

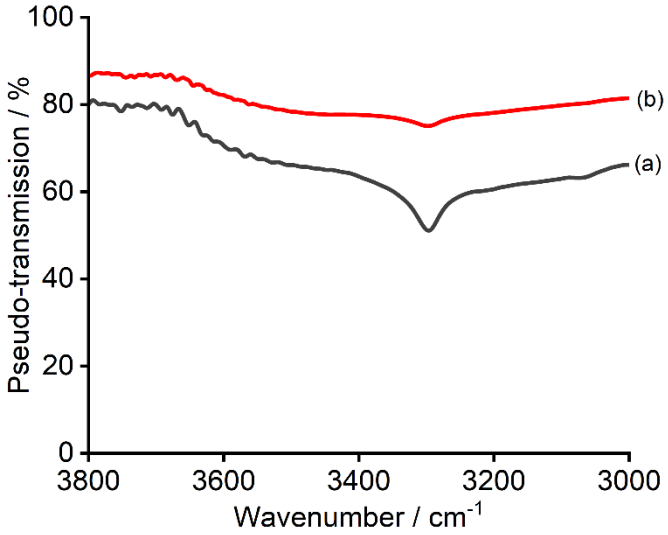

Figure 5.14: DRIFTS spectra of (a) Ag/α-Al_2O_3 (from Chapter 4) and (b) Cs-Ag/α-Al_2O_3 showing the region of interest, backgrounded against KBr. Spectra have been offset for clarity. Zoomed in between 3000 – 3800 cm^{-1}.

As discussed in **Section 4.1.4**, methyl red was used as the Hammett indicator. *Figure 5.15* shows that the two catalysts without caesium showed a lighter orange colour compared to the darker orange colour of the catalysts with caesium. Therefore, indicating that the catalysts with caesium are less acidic, indicating that Cs does neutralise the acid sites.

Figure 5.15: Methyl red with catalysts in toluene. From left to right: Ag/α-Al_2O_3 (from Chapter 4), Ag/γ-Al_2O_3 (from Chapter 4), Cs-Ag/α-Al_2O_3, Cs-Ag/γ-Al_2O_3.

5.1.4 Analysis Under Ethylene Conditions

In situ DRIFTS of ethylene epoxidation was undertaken on Ag/α-Al_2O_3 and Cs-Ag/α-Al_2O_3, both compared at 225 °C and under the flow of ethylene for 2 h. Comparing Cs-Ag/α-Al_2O_3 to Ag/α-Al_2O_3 (shown in *Figure 5.16*) there appears to be no change in the band at 1080 cm^{-1} corresponding to the C-O stretching mode of ethylene oxide.[30] There is an increase in the band at 1245 cm^{-1} corresponding to the C-O-C stretching mode of ethylene oxide.[31–33] This indicates that there is more ethylene oxide on the surface of the Cs-Ag/α-Al_2O_3 catalyst under reaction conditions. The peaks between 1400 and 1500 cm^{-1} correspond to the ethylene gas phase, where there is H-C-H scissoring, and there is very little change when comparing Ag/α-Al_2O_3 to Cs-Ag/α-Al_2O_3.[31–33] The broad peaks at both 1540 cm^{-1} and 1660 cm^{-1} corresponds to C=C stretching in ethylene, there is again very little change when comparing Ag/α-Al_2O_3 to Cs-Ag/α-Al_2O_3.[31–33] The peak at 1730 cm^{-1} corresponds to the stretching of the C=O bond in acetaldehyde, here it is difficult to infer if there is any change at this peak.[31–33]

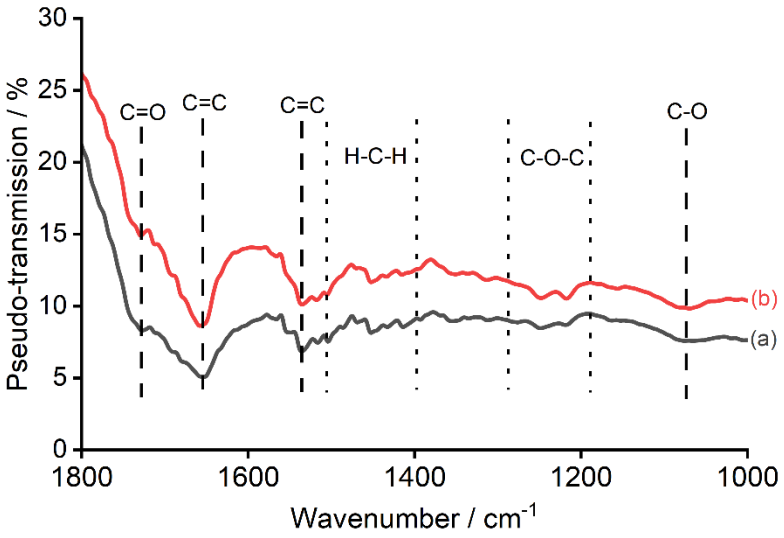

Figure 5.16: In situ DRIFTS of ethylene epoxidation reaction on (a) Ag/α-Al_2O_3 (from Chapter 4) and (b) Cs-Ag/α-Al_2O_3 after 2 hr of exposure to ethylene at 225 °C backgrounded against KBr. The O_2:C_2H_4 ratio in all cases is 2:1 where the new DRIFTS cell was used. Spectra have been offset for clarity.

5.1.5 Understanding the Structure of Cs

As discussed in **Section 1.1.2.3**, whilst the oxidation state is commonly confirmed at +1, there is a large discussion regarding the speciation/location of Cs.[2,10,11,23] There appears to be evidence for caesium both on the support and on the silver from the above results, therefore understanding the structure of caesium is challenging as it is likely to comprise of two or more different types of species. It should be noted here that the catalyst is likely to have an oxide surface, either the oxide surface of the support or the oxygen on silver, therefore it is possible that caesium is part of a surface oxide structure rather than an adsorbed molecular species, however, it is difficult to assign to anything other than molecular species. This assignment of molecular Cs is likely to have a similar surface structure. The likely possibilities of the +1 oxidation state structures are caesium suboxides (Cs_7O, Cs_4O and $Cs_{11}O_3$), caesium monoxide (Cs_2O), caesium peroxide (Cs_2O_2) and caesium superoxide (CsO_2 and Cs_2O_4). Whilst caesium ozonide (CsO_3) is also in a +1 oxidation state, it appears to decompose into caesium superoxide at room temperature therefore indicating that it is unlikely to be this. Caesium sesquioxide (Cs_2O_3) is also in a +1 oxidation state; however, it is only formed at the thermal decomposition of caesium superoxide at 290 °C, this catalyst does not reach that temperature therefore indicating this will not be formed. *Table 5.6* shows the reported binding energies of O 1s and Cs 3d for the different Cs oxides to be able to distinguish between the Cs species.[23] Therefore, looking at Cs-Ag/α-Al_2O_3 in *Figure 5.17* and *Table 5.6*, the Cs oxide is indistinguishable between the different oxide species with a peak at 724.5 eV. The O 1s XPS (shown in *Figure 5.18)*

shows no peak at 532.9 or <528.0 eV, with a peak at approximately 530.2 eV, therefore indicating that the Cs species is likely to be a mixture of suboxides and peroxides. When looking at Cs-Ag/γ-Al_2O_3, there is a decrease in binding energy in the Cs 3d spectra to 724.0 eV, and an increase in the O 1s spectra to 530.4 eV indicating that in the Cs oxide structure, the Cs becomes more electron-rich likely being a mixture of species.

Table 5.6: Binding energies for O1s and Cs3d for different Cs oxides.[23]

	Cs Oxides			
Element Investigating	Suboxides - $Cs_{2+x}O$	Monoxide - Cs_2O	Peroxide - Cs_2O_2	Superoxide – Cs_2O_4 / CsO_2
O1s	530.6	<528.0	530.2	532.9
Cs3d	724.9	724.2	724.2	724.2

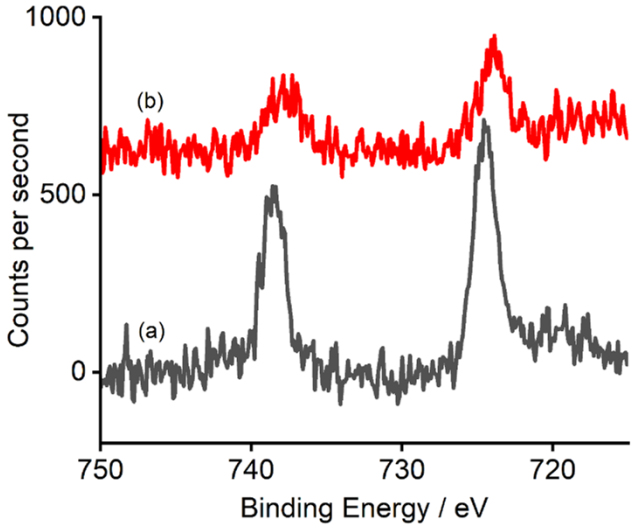

Figure 5.17: XPS spectra of all Cs3d data (after applying binding energy correction verified by the shift of the Al 2p peak and after subtraction of a Shirley background). All samples are as prepared. Where (a) is Cs-Ag/α-Al_2O_3.and (b) is Cs-Ag/γ-Al_2O_3. Spectra have been offset for clarity.

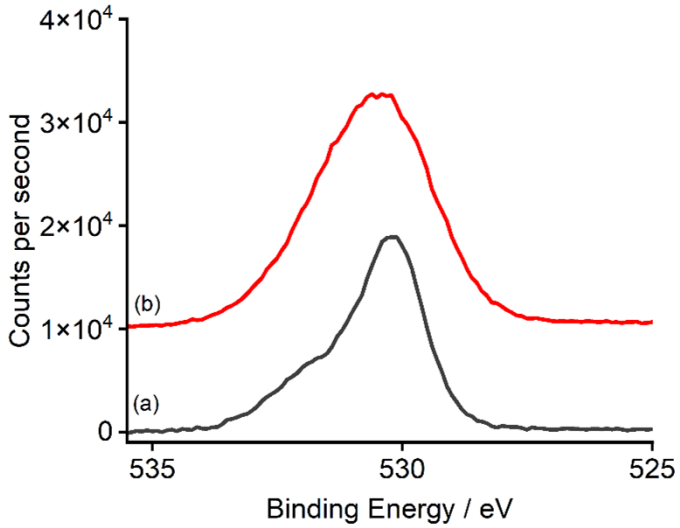

Figure 5.18: XPS spectra of all O1s data (after applying binding energy correction verified by the shift of the Al 2p peak and after subtraction of a Shirley background). Where (a) is Cs-Ag/α-Al_2O_3.and (b) is Cs-Ag/γ-Al_2O_3. All samples are as prepared. Spectra have been offset for clarity.

Peak deconvolution was undertaken on the *ex situ* O1s XPS of Cs-Ag/α-Al_2O_3 and Cs-Ag/γ-Al_2O_3 to show the two oxygen species present in the catalysts. Whilst the peak deconvolution of Cs-Ag/α-Al_2O_3 is shown in *Figure 5.10* the peak deconvolution of Cs-Ag/γ-Al_2O_3 is shown in *Figure 5.19*. The determined peak areas of the two catalysts are shown in *Table 5.7*.

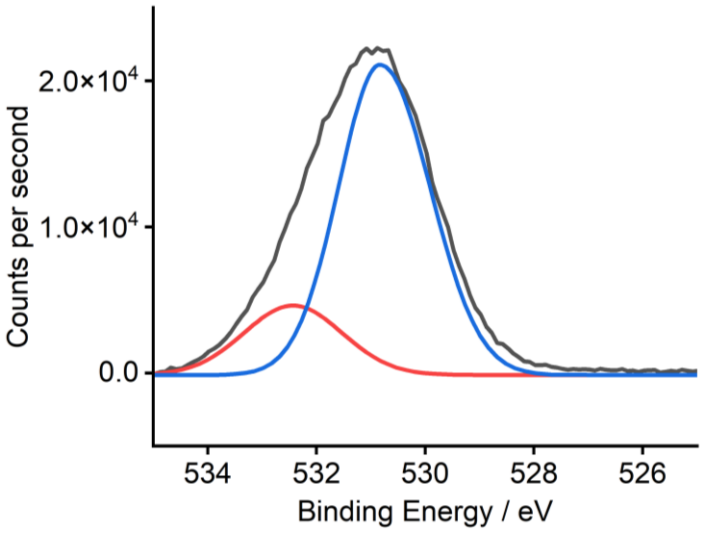

Figure 5.19: Peak deconvolution of the XPS spectra of the O1s looking at Cs-Ag/γ-Al_2O_3. All samples are as prepared, after applying binding energy correction verified by the shift of the Al 2p peak and after subtraction of a Shirley background.

Table 5.7: A table showing the peak areas for the peak deconvolution of the XPS spectra of the O1s looking at both Cs-Ag/α-Al_2O_3 and Cs-Ag/γ-Al_2O_3.

Catalyst	Peak Area of Blue Peak - atomic electrophilic oxygen / counts	Peak Area of Red Peak - Ag_x-O_2 / counts
Cs-Ag/α-Al_2O_3	26608.38	13879.29
Cs-Ag/γ-Al_2O_3	54515.25	10729.68

The local chemical environment of caesium was investigated by cross polarisation (CP) ^{133}Cs NMR spectroscopy. Caesium-133 has 100% natural abundance, I = 7/2 and a small quadrupole moment. Caesium spectral referencing is relative to 1 M $CsNO_3$, shown in **Appendix 4**. Cs-Ag/α-Al_2O_3 was undertaken as shown in *Figure 5.20*, the chemical shift observed at -5.1 ppm is due to caesium in interaction with silver particles.[34] Whilst the shoulder at -7.0 ppm is likely the quadrupolar interaction.[34]

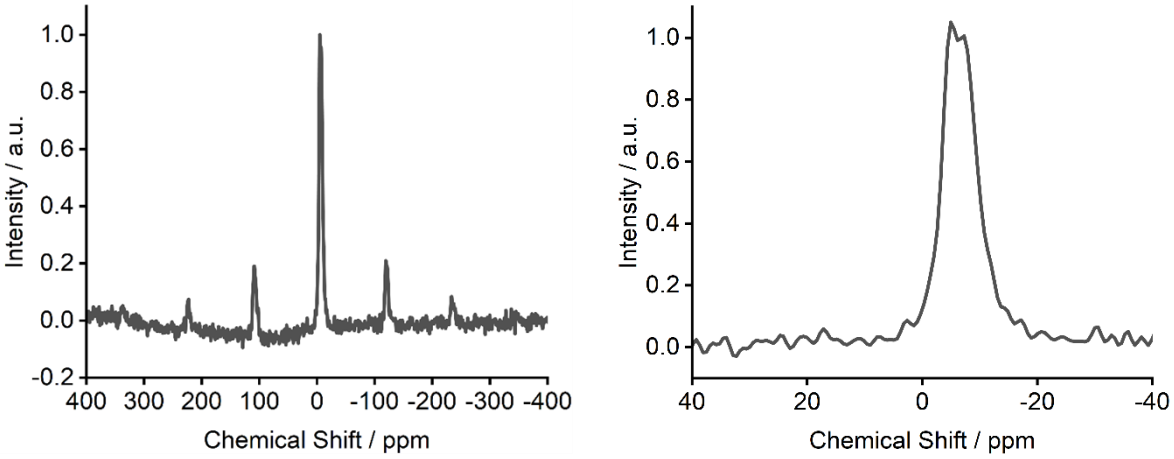

Figure 5.20: Solid State CP ^{133}Cs NMR spectrum of Cs-Ag/α-Al_2O_3.

Whilst there was an interaction of caesium with the silver particles, there was no interaction of caesium observed with the α-Al_2O_3 therefore, SS CP ^{133}Cs NMR spectroscopy was undertaken on Cs/α-Al_2O_3, as shown in *Figure 5.21,* no chemical shifts were observed. It has been suggested that the Cs is located between the Ag and the α-Al_2O_3 support however the chemical shift interaction of Cs and Al may be too broad to be viewed or may not be present in the catalyst.

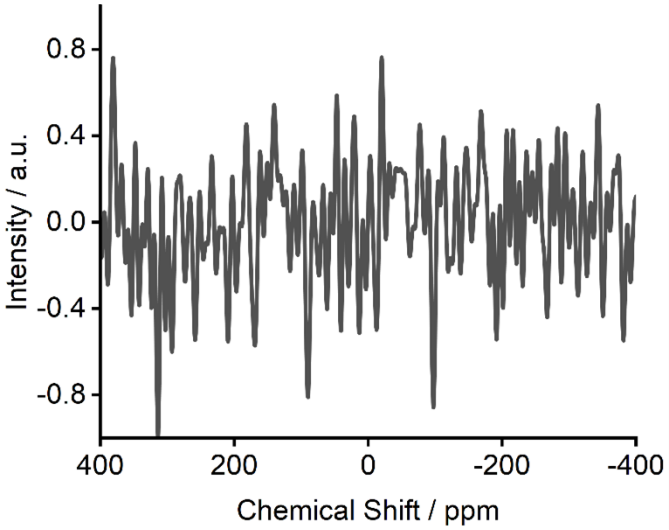

Figure 5.21: Solid State CP ^{133}Cs NMR spectrum of Cs/α-Al_2O_3.

^{27}Al SS NMR spectroscopy was undertaken to see if the interaction between Cs and Al_2O_3 could be shown. As shown in *Figure 5.22*, there are two main chemical shifts, one at 15.5 ppm and the second at 70.3 ppm, these correspond to octahedral and tetrahedral Al respectively.[35] This indicates that the majority of Al is octahedral. On the other hand, the Cs-Ag/α-Al_2O_3 and the Cs-Ag/γ-Al_2O_3 (*Figure 5.23*) indicate that there is more tetrahedral aluminium in Cs-Ag/γ-Al_2O_3 compared to Cs-Ag/α-Al_2O_3.

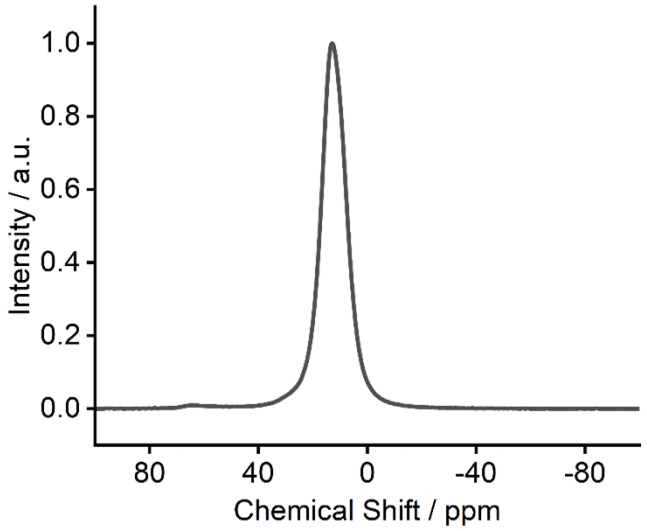

Figure 5.22: Solid State ^{27}Al NMR spectrum of Cs-Ag/α-Al_2O_3.

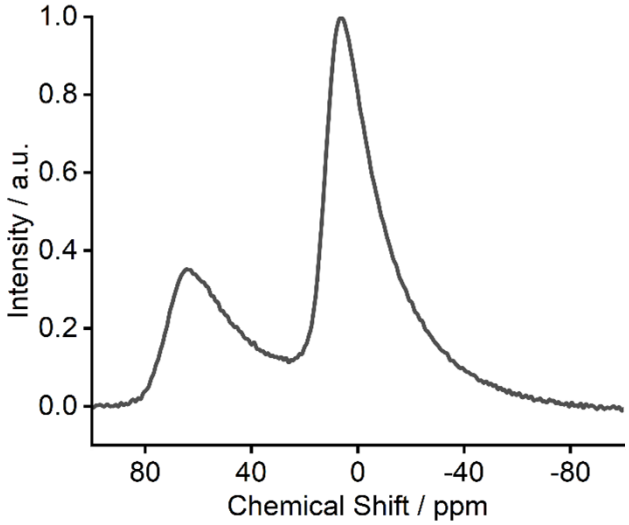

Figure 5.23: Solid State ^{27}Al NMR spectrum of Cs-Ag/γ-Al_2O_3.

As shown in *Table 5.8*, there is a shift upfield from Cs-Ag/α-Al_2O_3 to Cs-Ag/γ-Al_2O_3 at site 1, indicating that octahedral aluminium is less deshielded on Cs-Ag/α-Al_2O_3, whilst it is difficult to find the exact ppm from such a broad peak, Quadfit was used to identify the δ_{Iso}. The addition of Cs to Ag/α-Al_2O_3 has led to a reduction in chemical shift at site 1, indicating that the Cs causes the octahedral alumina to be more shielded. This indicates that the Cs interacts with the Al_2O_3.

Table 5.8: A table showing the two different catalysts with the main details and assignments taken from the ^{27}Al NMR spectra.

Catalyst	Site	δ_{Iso} (ppm)	Assignment
Cs-Ag/γ-Al_2O_3	1	12.7	Octahedral Al
	2	74.2	Tetrahedral Al
Cs-Ag/α-Al_2O_3	1	15.5	Octahedral Al
	2	70.3	Tetrahedral Al
Ag/α-Al_2O_3	1	16.3	Octahedral Al
	2	76.6	Tetrahedral Al

The ^{133}Cs and ^{27}Al show a clear interaction between Cs and Ag, indicating that the Cs interact with the Ag. No chemical shifts were observed for the ^{133}Cs NMR, however shifting occurring in the ^{27}Al and results from the STEM have indicated Cs interacting with both Ag and Al_2O_3.

5.2 Understanding the Role of Cs and Re Together as Promoters

As discussed in **Section 1.1.2.5**, the use of Cs and Re together as promoters is much less understood, although it causes a significant increase in EO selectivity when added.

Therefore, it was thought that the use of *in situ* and *ex situ* spectroscopic and characterisation techniques alongside reaction data would be able to give more insight into both the role and the structure of Cs and Re. These results will be critically compared to the literature that helps with understanding the properties of the Cs and Re promoters.

Both Cs-Re-Ag/α-Al_2O_3 and Cs-Re-Ag/γ-Al_2O_3 catalysts were made using incipient wetness impregnation with 10 wt. % Ag to be able to compare to the previous catalysts synthesised. It is thought that the optimum amount of Re required in a Cs-Re-Ag catalyst to improve the EO selectivity is between 400 – 600 ppm.[10] Whilst if the ppm increases to 800 ppm and 1600 ppm the selectivity of the EO decreases, suggestions being that it strengthens the binding of EO to the surface, which lengthens its residence time and therefore promotes its isomerisation to acetaldehyde.[36] Therefore 500 ppm of Re was used for these catalysts. It is thought that the optimum amount of Cs required to improve the EO selectivity is between 200 - 600 ppm, therefore approximately 600 ppm was added.[1,5,10,12]

To confirm that the elemental composition of the catalysts was as expected, ICP-OES was conducted on both. The elemental composition of the catalysts is shown in *Table 5.9*. The silver, caesium and rhenium contents of the two catalysts were close to the expected values, with small fluctuations of value and with low errors.

Table 5.9: Summary of ICP-OES results. The results reported are the average results of the duplicate samples where errors are one standard deviation calculated based on the duplicate samples for each material. Standards are run in the same batch to confirm no significant anomalies or deviations in the instrumental analysis of the samples.

Catalyst	Metal	Expected Metal Content / wt. %	Metal Content by ICP-OES / wt. %	Error in Metal Content by ICP-OES/ wt. %
Ag/α-Al_2O_3 (from Chapter 4)	Ag	10	9.86	±0.35
Ag/γ-Al_2O_3 (from Chapter 4)	Ag	10	10.12	±0.84
Cs-Re-Ag/α-Al_2O_3	Cs	0.06	0.06	±0.01
	Re	0.05	0.05	±0.00
	Ag	10	10.31	±0.15
Cs-Re-Ag/γ-Al_2O_3	Ag	10	9.13	±0.05
	Cs	0.06	0.06	±0.00
	Re	0.05	0.05	±0.01

Both Cs-Re-Ag/α-Al_2O_3 and Cs-Re-Ag/γ-Al_2O_3 were evaluated for ethylene epoxidation, with the EO selectivity in *Figure 5.24* and *Figure 5.25,* respectively. As expected, there is a substantial increase in EO selectivity when adding Cs and Re as promoters in these quantities on the α-Al_2O_3 support.[18,36–39] There is also a large decrease in acetaldehyde,

carbon dioxide and water which also causes a more selective catalyst with adding Cs and Re. When comparing to Cs-Ag/α-Al_2O_3 there is an increase in EO selectivity with the addition of both Cs and Re together, with a decrease of acetaldehyde, carbon dioxide and water. Whilst there is an increase in the addition of Cs and Re compared to Ag/γ-Al_2O_3, when comparing to Cs-Ag/γ-Al_2O_3 the EO selectivity is very similar, with a decrease in AA but an increase in CO_2 and H_2O.

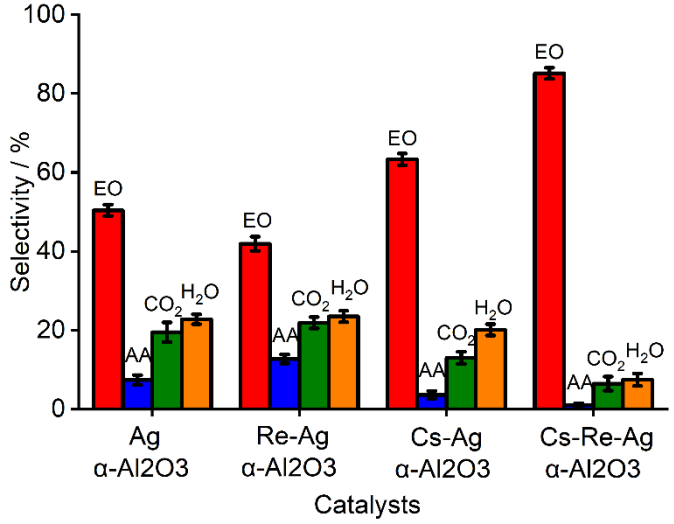

Figure 5.24: A comparison of selectivity between Ag/α-Al_2O_3, Cs-Ag/α-Al_2O_3, Re-Ag/α-Al_2O_3 and Cs-Re-Ag/α-Al_2O_3. Errors shown are based on 3 repeat measurements.

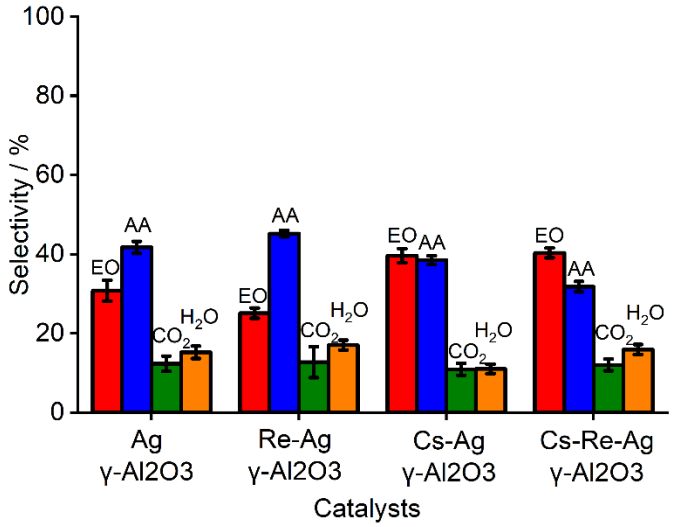

Figure 5.25: A comparison of selectivity between Ag/γ-Al_2O_3, Cs-Ag/γ-Al_2O_3, Re-Ag/γ-Al_2O_3 and Cs-Re-Ag/γ-Al_2O_3. Errors shown are based on 3 repeat measurements.

Ethylene conversion was calculated and displayed in *Table 5.10.* As expected, there is a decrease in ethylene conversion between Ag/α-Al_2O_3 and Ag/γ-Al_2O_3 which is likely the surface area of γ-Al_2O_3 as discussed in **Chapter 4**. When taking in the percentage error, there is very little change in the ethylene conversion with the addition of Cs and Re both separately and together.

Table 5.10: A table showing the ethylene conversion and percentage error based on 3 repeat measurements for both Ag/α-Al_2O_3 and Ag/γ-Al_2O_3 based catalysts.

Catalyst	Ethylene Conversion / %	% Error
Ag/α-Al_2O_3	7.7	0.4
Re-Ag/α-Al_2O_3	8.0	0.7
Cs-Ag/α-Al_2O_3	8.8	0.3
Cs-Re-Ag/α-Al_2O_3	8.6	0.5
Ag/γ-Al_2O_3	3.7	0.1
Re-Ag/γ-Al_2O_3	3.6	0.1
Cs-Ag/γ-Al_2O_3	3.7	0.2
Cs-Re-Ag/γ-Al_2O_3	4.1	0.0

5.2.1 Particle Sizes and Morphology

Chapter 4.2 found that Re does not affect the Ag particle sizes or the distribution. However, **Chapter 5.1**, found that Cs causes the Ag particles to be more distributed and the Ag particles to decrease in size, therefore reducing the amount of hydroxyl groups on the support and making it more selective to EO. It was thought to be useful to investigate the properties of the Cs and Re promoters together on the particle sizes and morphology of Ag. pXRD of Cs-Re-Ag/α-Al_2O_3 was undertaken and compared to Ag/α-Al_2O_3 from Chapter 4. *Figure 5.26* was expanded (*Figure 5.27*) to show the Ag (2 2 0) at 64.5 °. Looking at the Ag (2 2 0) reflection in the pXRD pattern, suggests that the Re and Cs together influence the degree of Ag crystallisation due to the broadening of the reflection widths. This therefore indicates that the Cs and Re together can slightly affect the distribution of Ag. This gives evidence that Cs plays the same role with and without Re by causing the slightly increased distribution of Ag across the α-Al_2O_3.

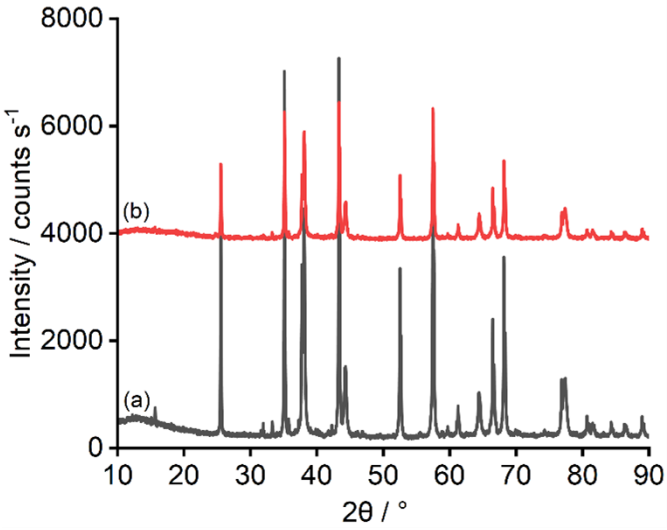

Figure 5.26: pXRD patterns for the α-alumina based *catalysts; (a) Ag/α-Al_2O_3; (b) Cs-Re-Ag/α-Al_2O_3. Patterns offset vertically for clarity.*

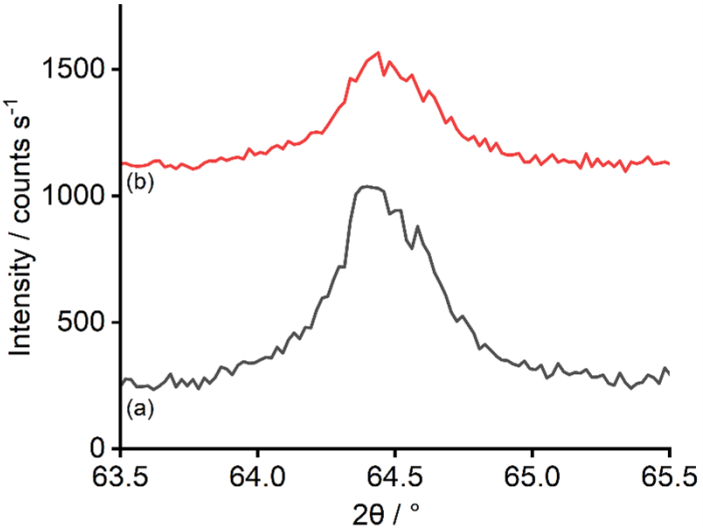

Figure 5.27: pXRD patterns for the α-Al_2O_3 based *catalysts; (a) Ag/α-Al_2O_3 and (b) Cs-Re-Ag/α-Al_2O_3. Zoomed in on peak Ag (2 0 0). Patterns offset vertically for clarity.*

The size of the silver crystallite was investigated using the reflection at 64.5 ° with the Scherrer equation. The FWHM used for each catalyst and the resultant crystallite sizes are shown in *Table 5.11*. As shown the FWHM has changed by 0.04 ° which therefore means there is a small decrease in the Ag crystallite size of 5 nm. Therefore, this shows that Cs is likely to cause a decrease in the Ag crystallite sizes. This indicates that with or without Re, Cs causes a decrease in Ag crystallite sizes. The FWHM is very similar for both Cs-Ag/α-Al_2O_3 and Re-Cs-Ag/α-Al_2O_3 indicates that Re does not have a role in the size of the Ag crystallites in both Re-Ag/α-Al_2O_3 and Re-Cs-Ag/α-Al_2O_3.

Table 5.11: Summary of FWHM and particle size estimation from pXRD data using the Scherrer equation. Errors were calculated based on the error from fitting the Gaussian functions.

Catalyst	Reflection(s) used / °	FWHM / °	Estimated Crystallite Size / nm	Error in Gaussian fit of Crystallite Size / nm
Ag/α-Al_2O_3	64.5	0.36	51.2	±1.4
Re-Ag/α-Al_2O_3	64.5	0.34	49.8	±1.5
Cs-Ag/α-Al_2O_3	64.5	0.41	44.9	±2.5
Cs-Re-Ag/α-Al_2O_3	64.5	0.40	46.1	±2.7

Figure 5.28 compares the TEM of Re-Cs-Ag/α-Al_2O_3 with Ag/α-Al_2O_3, Cs-Ag/α-Al_2O_3 and Re-Ag/α-Al_2O_3, from Chapter 4, some of the metal particles have had huge morphology changes and distribution by the addition of Cs and Re, however, STEM is needed to confirm this.

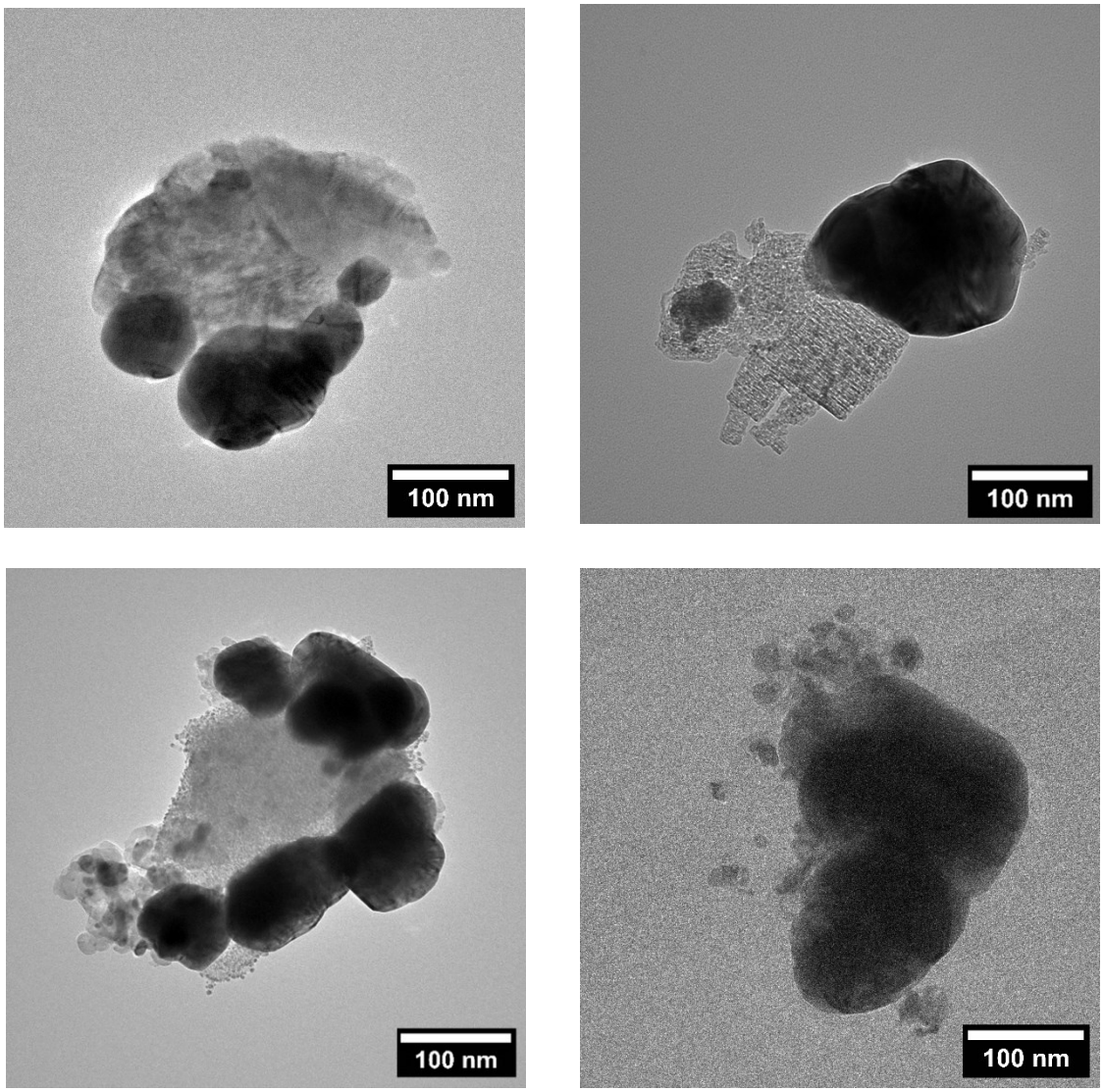

Figure 5.28: Representative TEM images of Ag/α-Al_2O_3 on the top left, Re-Ag/α-Al_2O_3 on the top right, Cs-Ag/α-Al_2O_3 on the bottom left and Cs-Re-Ag/α-Al_2O_3 on the bottom right.

Elemental analysis using STEM was undertaken on Cs-Re-Ag/α-Al_2O_3 (shown in *Figure 5.29*) to investigate the locations and the distribution of the Ag, Cs and Re in the catalysts. As suggested in the TEM and pXRD, the STEM is consistent with the slightly increased distribution of Ag with the addition of Cs and Re, therefore giving more active sites for ethylene epoxidation, whilst reducing the amount of "free" α-Al_2O_3, allowing less unselective reactions of EO to acetaldehyde.[5,13] When looking at the location of Re, it appears that Re is denser in the same locations as the larger densities of Ag, therefore indicating that the location of Re is clustered around the Ag. The caesium seems to appear all over the surface of the catalyst rather than at the Ag sites like the rhenium, indicating that the caesium is a thin layer rather than clusters. These locations of Cs and Re do not appear to change from Cs-Ag/α-Al_2O_3 and Re-Ag/α-Al_2O_3 where there is an overlap of sites between the two promoters. One suggestion by Chen *et al*. is that ReO_4^- acts as molecular spacers that evenly disperse Cs^+ across the surface, thereby maximizing the promotional effects of Cs.[37]

Comparing the STEM of Cs-Re-Ag/α-Al_2O_3 to Cs-Ag/α-Al_2O_3 shows no change in the distribution of Cs, indicating that this is not a role of the two promoters, although it must be noted the Cs appears dispersed on this scale this effect, it could still be contributing at a more local level, as the EDX Cs signal is weak here.

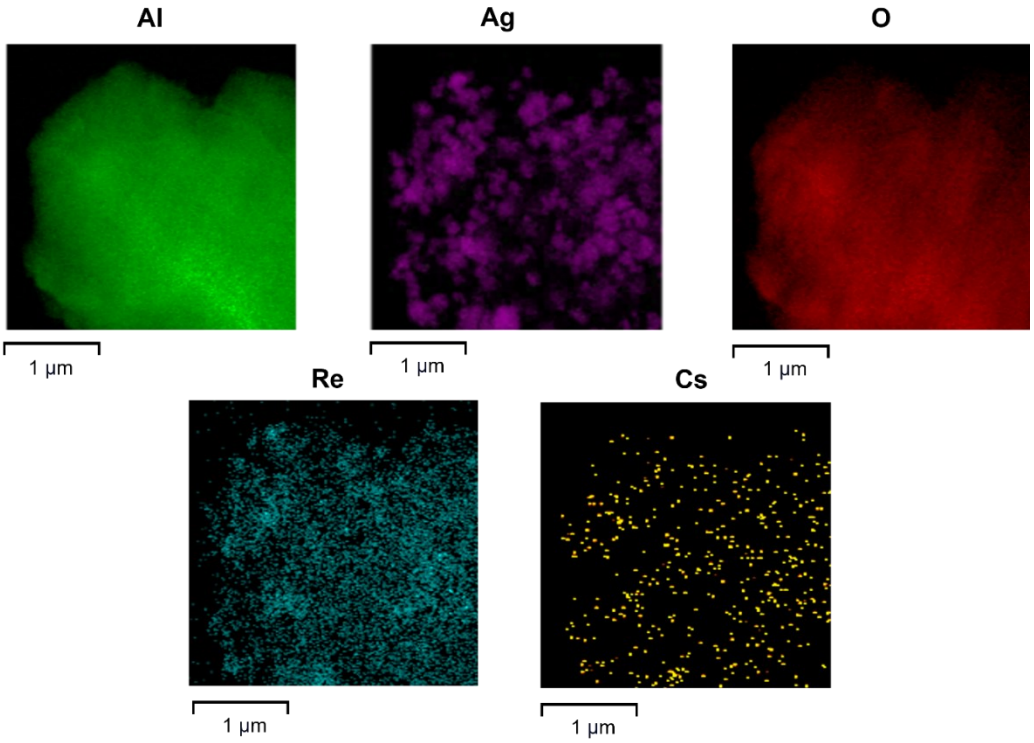

Figure 5.29: Elemental Mapping (using EDX), for the Cs-Re-Ag/α-Al_2O_3, with aluminium shown in green, silver shown in purple, oxygen shown in red, rhenium shown in blue, and caesium shown in orange.

Looking at the spent catalyst of Cs-Re-Ag/α-Al_2O_3 STEM shown in *Figure 5.30*, the Cs has distributed the Ag more evenly, however, there is again another clear indication that ethylene epoxidation causes a sintering effect of the Ag. Once these larger more sintered particles are formed, there does now seem to be evidence for caesium clustering. This potentially indicates to the caesium migrating with the silver to form the larger particles.

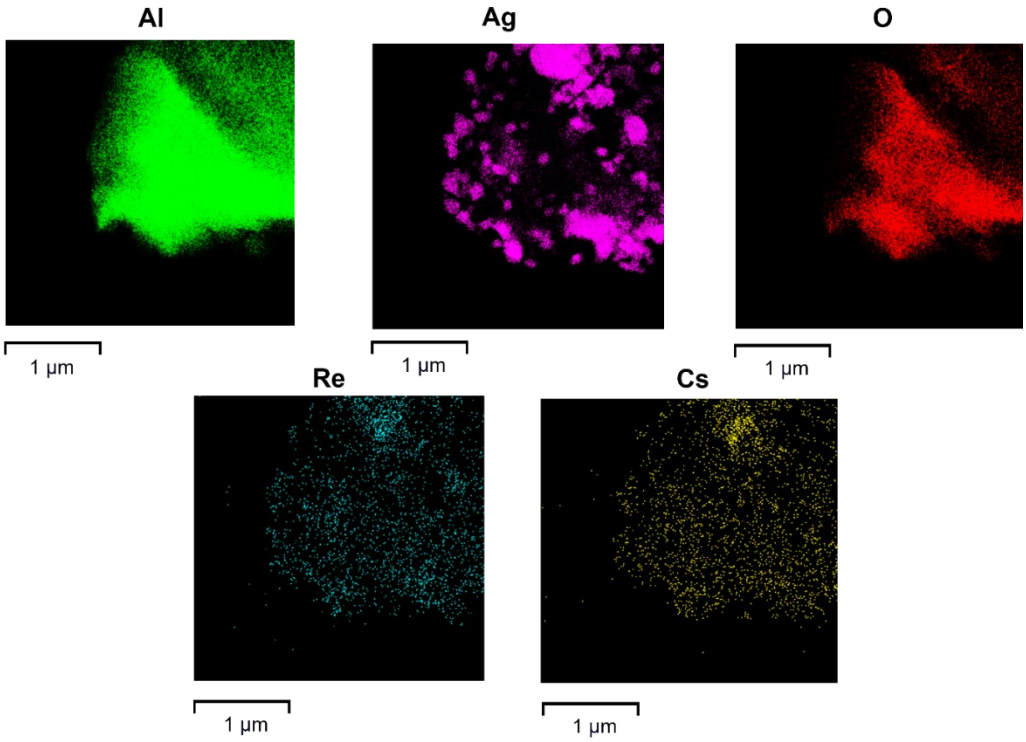

Figure 5.30: Elemental Mapping (using EDX), for the spent Cs-Re-Ag/α-Al_2O_3, with aluminium shown in green, silver shown in purple, oxygen shown in red, rhenium shown in blue, caesium shown in orange.

5.2.2 Understanding the Structure of Silver in the Presence of Re and Cs

XPS of Ag 3d was investigated, *Figure 5.31* shows that the addition of Cs and Re, causes the Ag to shift to a slightly higher binding energy by 0.1 eV, this is likely to be within the calibration error.

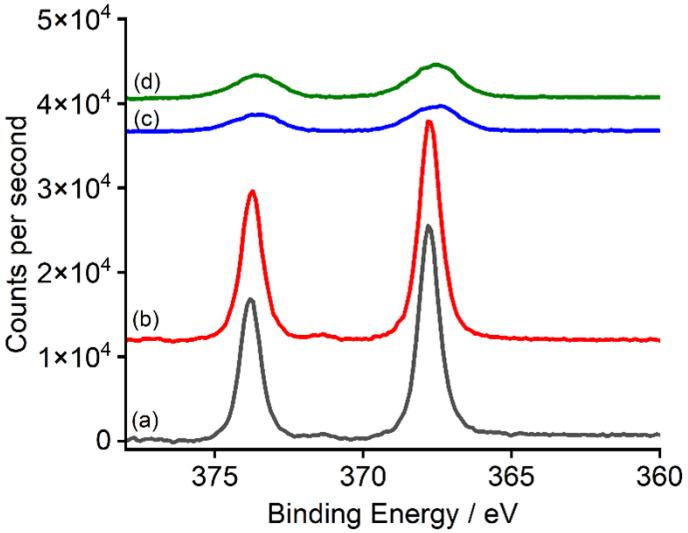

Figure 5.31: XPS spectra of all Ag3d data (after applying binding energy correction verified by the shift of the Al 2p peak and after subtraction of a Shirley background). Where (a) is Ag/α-Al_2O_3, (b) is Cs-Re-Ag/α-Al_2O_3, (c) is Ag/γ-Al_2O_3 and (d) is Cs-Re-Ag/γ-Al_2O_3. All samples are as prepared. Spectra have been offset for clarity.

Table 5.12 shows the ratio of Ag:Al has increased from Ag/α-Al_2O_3 and Re-Ag/α-Al_2O_3 to Cs-Re-Ag/α-Al_2O_3. This gives more indication that the role of Cs with and without Re is to distribute Ag. As discussed in **Chapter 4** the Ag/α-Al_2O_3 surface is likely to be a thin silver oxide layer on the surface, which agrees with the literature.[40] When Cs and Re are added, there is an increase in oxygen coverage here of 0.056 nm to 0.271 nm, this therefore indicates more of the surface is oxygenated. Calculations repeated as with Ag/α-Al_2O_3 where the calculations are shown in **Appendix 4**. There is however a large difference between the ratios of Re between Re-Ag/α-Al_2O_3 to Cs-Re-Ag/α-Al_2O_3.

*Table 5.12: A table showing the ratios of metal: Al_2O_3 found by using cross-section and calculations shown in **Appendix 4**.*

		Surface Metal Ratios			
		Ag3d	**Al2p**	**Cs3d**	**Re4f**
Sample	**Ag/α-Al_2O_3**	0.21	1	-	-
	Re-Ag/α-Al_2O_3	0.20	1	-	0.017
	Cs-Re-Ag/α-Al_2O_3	0.27	1	0.012	0.004

One main difference between the Raman spectrum of Ag/α-Al_2O_3 and Cs-Re-Ag/α-Al_2O_3 (shown in *Figure 5.32*) is there is now a broad peak at 500 cm^{-1}, this is likely to be an Ag-oxide-like surface represented by O-Ag-O motifs that can be a combination of subsurface and surface oxygens.[15,26]

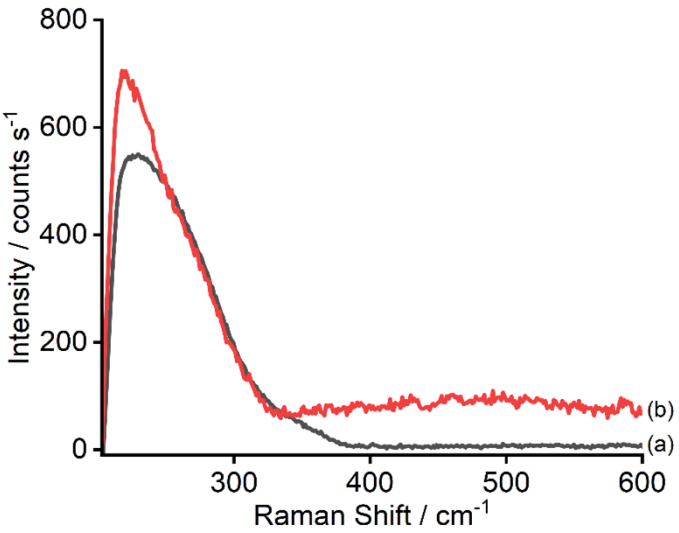

Figure 5.32: Raman spectra zoomed in (after applying intensity response correction and subtraction of dark signal) where the wavelength of 667-725 nm. Where (a) is Ag/α-Al_2O_3 and (b) is Cs-Re-Ag/α-Al_2O_3. Spectra have been offset for clarity.

5.2.3 Understanding the Role of Oxygen

As discussed in both **Section 4.2** and **5.1**, both Cs and Re separately caused the Ag-O bond to weaken, whilst 600 ppm of Cs causes the amount of O_{ads} to increase and 500 ppm of Re shows no change in the amount of O_{ads} compared to the unpromoted Ag/α-Al_2O_3. *Figure 5.33* shows the O_2-TPD comparing Cs-Re-Ag/α-Al_2O_3 to Ag/α-Al_2O_3. As shown, there is a decrease in the temperature, indicating a weakening of the Ag-O bond, leading to weaker oxygen species that have shown to be more electrophilic and an increase in the intensity, indicating an increase in the O_{ads}.[18] This agrees with reports in the literature indicating that a weaker Ag-O bond results in increased EO selectivity.[8,18] Looking at *Figure 5.33* when comparing Cs-Re-Ag/α-Al_2O_3 to both Cs-Ag/α-Al_2O_3 and Re-Ag/α-Al_2O_3 there is a slight decrease in the temperature and an increase in the intensity of the adsorbed oxygen. This gives evidence to Cs and Re together increasing the O_{ads} and weakening the Ag-O bond.

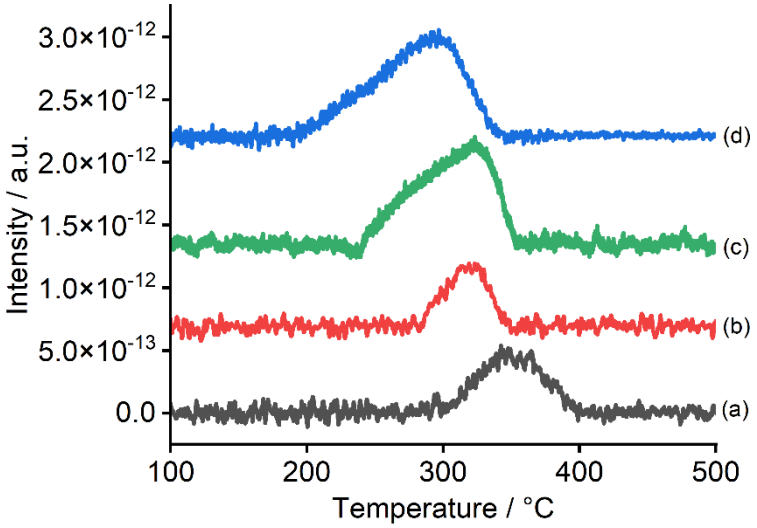

Figure 5.33: O_2-TPD profile of (a) Ag/α-Al_2O_3 (b) Re-Ag/α-Al_2O_3, (c) Cs-Ag/α-Al_2O_3 and (d) Cs-Re-Ag/α-Al_2O_3 after O_2 pretreatment (heating rate of 5 °C min^{-1}). Spectra have been offset for clarity.

H_2-TPR was undertaken on Cs-Re-Ag/α-Al_2O_3 (shown in *Figure 5.34*) here there are 0.99 ± 0.01 H_2 molecules per silver atom. *Table 5.13* indicates that there is an increase in the total O_{ads} compared to Ag/α-Al_2O_3, Re-Ag/α-Al_2O_3 and Cs-Ag/α-Al_2O_3 agreeing with the O_2-TPD data.

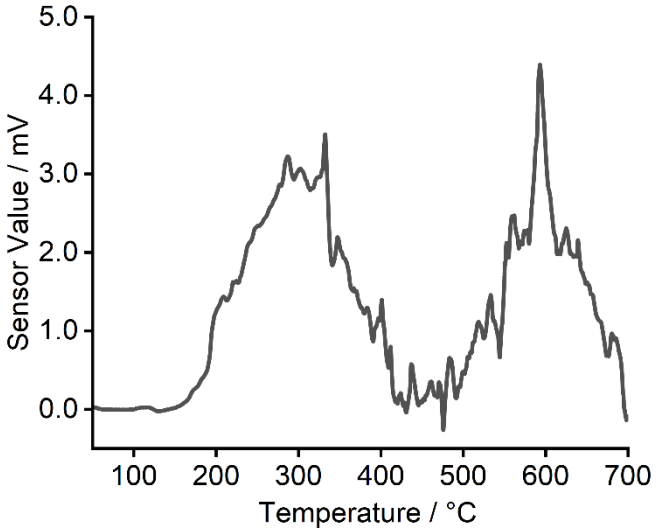

Figure 5.34: H_2-TPR of Cs-Re-Ag/α-Al_2O_3 after O_2 pretreatment (heating rate of 5 °C min^{-1}).

Table 5.13: A table comparing the number of H_2 molecules per silver atom of the different catalysts.

Catalyst	H_2 Molecules Per Silver Atom	Error
Ag/α-Al_2O_3	0.79	± 0.04
Cs-Ag/α-Al_2O_3	0.83	± 0.05
Re-Ag/α-Al_2O_3	0.74	± 0.02
Cs-Re-Ag/α-Al_2O_3	0.99	± 0.01

O1s XPS of Ag/α-Al_2O_3 (from Chapter 4) and Cs-Re-Ag/α-Al_2O_3 (shown in *Figure 5.35*) showed no shift in binding energy of oxygen with the addition of Cs and Re, as might be expected from what was seen with the data from Cs-Ag/α-Al_2O_3 and Re-Ag/α-Al_2O_3. *Table 5.14* shows an increase in the O:Al ratio with the addition of Cs and Re. This agrees with the O_2-TPD data indicating an increased amount of O_{ads}. Whilst there is an increase in the ratio with the addition of Cs and Re separately, there is a much larger increase with the addition of Cs and Re together. Due to the large ratio between oxygen and aluminium, the main peak at 530.2 eV can be ascribed based on the literature as being electrophilic oxygen.[24,25] Whilst the small shoulder at 532 eV can be ascribed to Ag_x-O_2.[24,25]

Table 5.14: A table showing the ratios of oxygen: Al_2O_3 found by using the cross sections. This calculation is explained in Appendix 3.

		Surface Metal Ratios	
		O1s	**Al2p**
Sample	**Ag/α-Al_2O_3**	12.5	1
	Cs-Ag/α-Al_2O_3	13.6	1
	Re-Ag/α-Al_2O_3	13.9	1
	Cs-Re-Ag/α-Al_2O_3	16.3	1

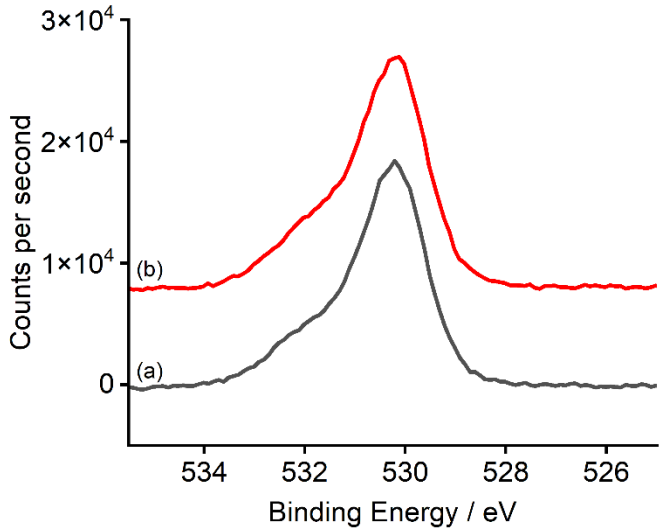

Figure 5.35: XPS spectra of all O1s data (after applying binding energy correction verified by the shift of the Al 2p peak and after subtraction of a Shirley background). Where (a) is Ag/α-Al_2O_3 and (b) is Cs-Re-Ag/α-Al_2O_3. All samples are as prepared. Spectra have been offset for clarity.

Peak deconvolution was undertaken on the *ex situ* O1s XPS of Ag/α-Al_2O_3 and Cs-Re-Ag/α-Al_2O_3 to show the two species present in the catalysts. Whilst the peak

deconvolution of Ag/α-Al_2O_3 is shown in *Figure 4.17* the peak deconvolution of Cs-Re-Ag/α-Al_2O_3 is shown in *Figure 5.36*. The determined peak areas of the two catalysts are shown in *Table 5.15.*

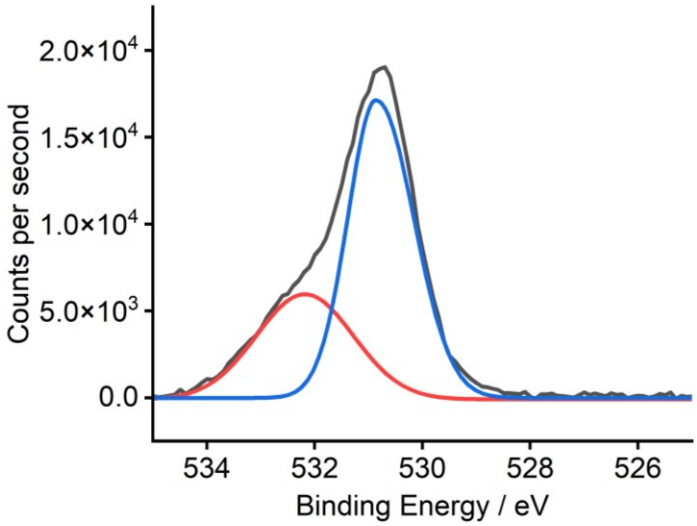

Figure 5.36: Peak deconvolution of the XPS spectra of the O1s looking at Cs-Re-Ag/α-Al_2O_3. All samples are as prepared, after applying binding energy correction verified by the shift of the Al 2p peak and after subtraction of a Shirley background.

Table 5.15: A table showing the peak areas for the peak deconvolution of the XPS spectra of the O1s looking at both Ag/α-Al_2O_3 and Cs-Re-Ag/α-Al_2O_3.

Catalyst	Peak Area of Blue Peak - atomic electrophilic oxygen / counts	Peak Area of Red Peak - Ag_x-O_2 / counts
Ag/α-Al_2O_3	25354.89	12227.33
Cs-Re-Ag/α-Al_2O_3	26512.20	13634.74

5.2.4 Investigating Hydroxyl Groups and Acidity

In **Section 4.2** it was found that 500 ppm of Re increased the amount of hydroxyl groups on the surface whilst in **Section 5.1**, it was found that 600 ppm of Cs decreased the amount of hydroxyl groups on the surface. Therefore, it was thought that with the use of DRIFTS to investigate the effect these promoters have on the hydroxyl groups. When looking at *Figure 5.37*, which compares Ag/α-Al_2O_3, Re-Ag/α-Al_2O_3 and Cs-Ag/α-Al_2O_3 with Cs-Re-Ag/α-Al_2O_3, there is a decrease in the band at 3300 cm^{-1}, which corresponds to O-H stretching in the hydroxyl groups, indicating that with Cs and Re together there is a decrease in the hydroxyl groups on the support, this indicates that Cs reduced the hydroxyl groups with/without Re.[14,41]

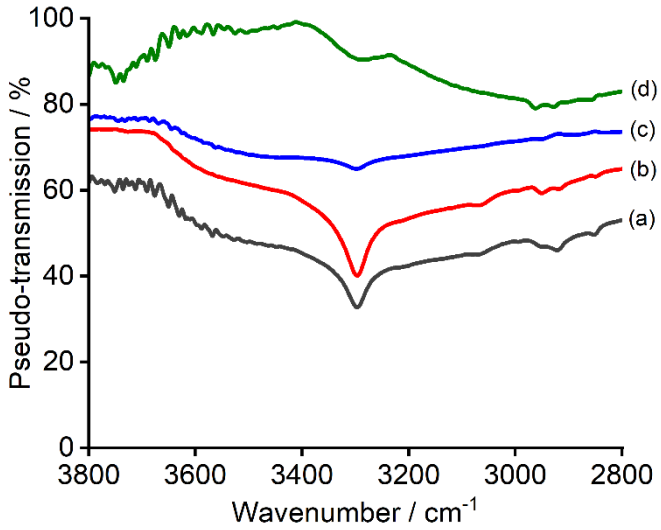

Figure 5.37: DRIFTS spectra of (a) Ag/α-Al_2O_3, (b) Re-Ag/α-Al_2O_3, (c) Cs-Ag/α-Al_2O_3 and (d) Cs-Re-Ag/α-Al_2O_3 showing the region of interest, backgrounded against KBr. Spectra have been offset for clarity.

5.2.5 Understanding the Interaction Between Cs and Re

As discussed in **Chapter 1.1.2.5**, there is thought to be a large amount of interaction between Cs and Re in the catalysts, therefore this was investigated.[10,36–39] *Ex situ* XPS on Re 4f was investigated, as shown in *Figure 5.38.* The peak at 46.1 eV on the Re-Ag/α-Al_2O_3 corresponds to Re^{+7} indicating that the Re at the surface is in the +7 oxidation state.[10] There is a slight shift to higher binding energies of 0.3 eV to 46.4 eV when Cs is added, indicating that Re is present in a higher valence state on the Cs-Re-Ag/α-Al_2O_3 catalyst because of the addition of Cs. This change in binding energy indicates that the presence of Re with high valence around Ag will cause the electrons to shift towards the Re atom, facilitating the formation of weakly adsorbed oxygen. There is a reduction in binding energy when looking at Cs-Re-Ag/γ-Al_2O_3 compared to Cs-Re-Ag/α-Al_2O_3 to 45.3 eV, which corresponds to a mixture of both Re^{6+} and Re^{7+} species.[36,42,43]

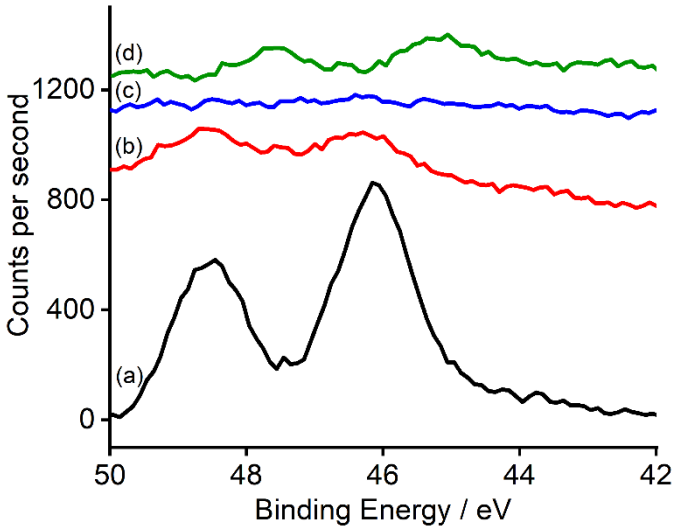

Figure 5.38: XPS spectra of all Re4f data (after applying binding energy correction verified by the shift of the Al 2p peak and after subtraction of a Shirley background). Where (a) is Re-Ag/α-Al_2O_3, (b) is Cs-Re-Ag/α-Al_2O_3, (c) is Re-Ag/γ-Al_2O_3 and (d) is Cs-Re-Ag/γ-Al_2O_3. All samples are as prepared. Spectra have been offset for clarity.

It was thought that *ex situ* Raman spectroscopy would also give information regarding the oxidation state and the structure of Re (shown in *Figure 5.39*). There are three new peaks compared to the non-Re case, one at 330 cm^{-1}, which is likely to correspond to two bending modes or deformations which are degenerate in ReO_4^-, and two at 890 cm^{-1} and 970 cm^{-1} which are likely to correspond to both the antisymmetric stretch and the symmetric stretch of the rhenium-oxygen vibrations, from ReO_4^-, giving more indication that the oxidation state of the Re is in the +7.[44] The peaks correspond to a tetrahedral ReO_4^-, where the peak at 330 cm^{-1} corresponds to Re-O, and the two bands 890 cm^{-1} and 970 cm^{-1} correspond to Re=O.[43,44] Before and after ethylene epoxidation the peak for Re-O did not change, however, the antisymmetric stretch of the rhenium-oxygen vibration increased, whilst the symmetric stretch of the rhenium-oxygen vibration decreased. This indicates that it is unlikely there is a change in the oxidation state, however, the bonding appears to have changed during ethylene epoxidation. When compared to Re-Ag/α-Al_2O_3 there appears to be a shoulder on both peaks, indicating that Cs causes a change in the Re-O bonding.

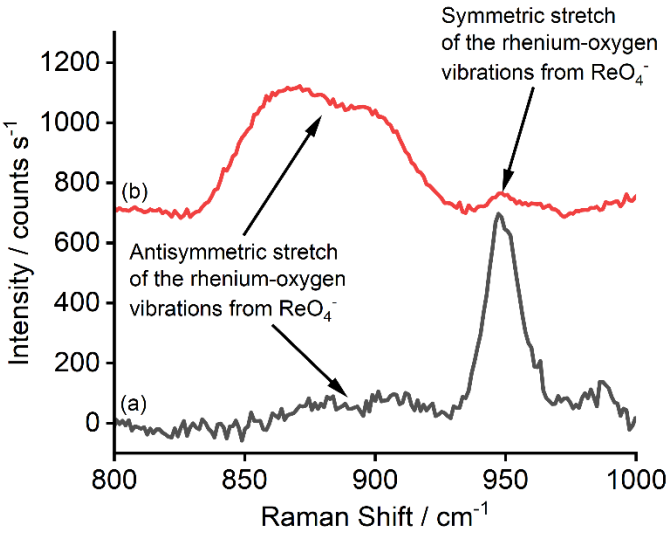

Figure 5.39: Raman spectra of Cs-Re-Ag/α-Al_2O_3 zoomed in (after applying intensity response correction and subtraction of dark signal) where the wavelength of 667-725 nm. Where (a) is Cs-Re-Ag/α-Al_2O_3 before EE and (b) is Cs-Re-Ag/α-Al_2O_3 after EE. Spectra have been offset for clarity.

As discussed in **Section 1.1.2.3**, whilst the oxidation state is commonly confirmed at +1, there is a large discussion regarding the speciation/location of Cs.[2,10,11] The likely possibilities of the +1 oxidation state structures are caesium suboxides (Cs_7O, Cs_4O and $Cs_{11}O_3$), caesium monoxide (Cs_2O), caesium peroxide (Cs_2O_2) and caesium superoxide (CsO_2 and Cs_2O_4). *Table 5.16*, shows the reported binding energies of O 1s and Cs 3d XPS for the different Cs oxides to be able to distinguish between the two.[23] It was suggested in **Section 5.1**, that the Cs species in Cs-Ag/α-Al_2O_3 are a mixture of suboxides and peroxides. As shown in *Figure 5.40*, there appears to be a slight decrease in the binding energy of 0.3 eV (not enough to change the oxide) when Re is added, suggesting the transfer of e^- from the highly polarisable Re to the Cs. This is consistent with the increased binding energy seen in Re 4f XPS on the addition of Cs.

Table 5.16: Binding energies for O1s and Cs3d for different Cs oxides.[23]

	Cs Oxides			
Element Investigating	Suboxides - $Cs_{2+x}O$	Monoxide - Cs_2O	Peroxide - Cs_2O_2	Superoxide – Cs_2O_4 / CsO_2
O1s	530.6	<528.0	530.2	532.9
Cs3d	724.9	724.2	724.2	724.2

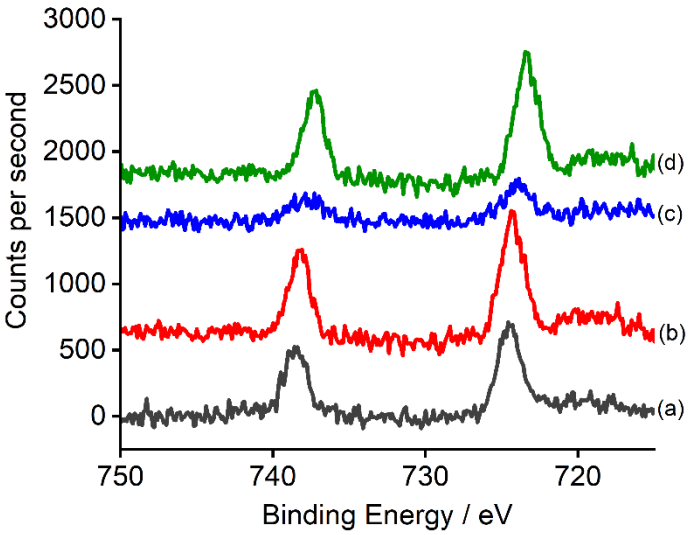

Figure 5.40: XPS spectra of all Cs3d data (after applying binding energy correction verified by the shift of the Al 2p peak and after subtraction of a Shirley background). Where (a) is Cs-Ag/α-Al_2O_3, (b) is Cs-Re-Ag/α-Al_2O_3, (c) is Cs-Ag/γ-Al_2O_3 and (d) is Cs-Re-Ag/γ-Al_2O_3. All samples are as prepared. Spectra have been offset for clarity.

In situ Cs 3d XPS was undertaken under ethylene epoxidation conditions (shown in *Figure 5.41*). This indicates that Cs does not change oxidation state through the reaction as the Cs XPS has not changed with 2:1 of oxygen: ethylene compared to O_2 pretreatment. However, under *in situ* ethylene epoxidation reaction conditions the Cs 3d XPS has shifted to 724.8 eV compared to when measured before exposure to oxygen or reaction conditions, indicating that the suboxide-type species are predominantly present as the only species during ethylene epoxidation.

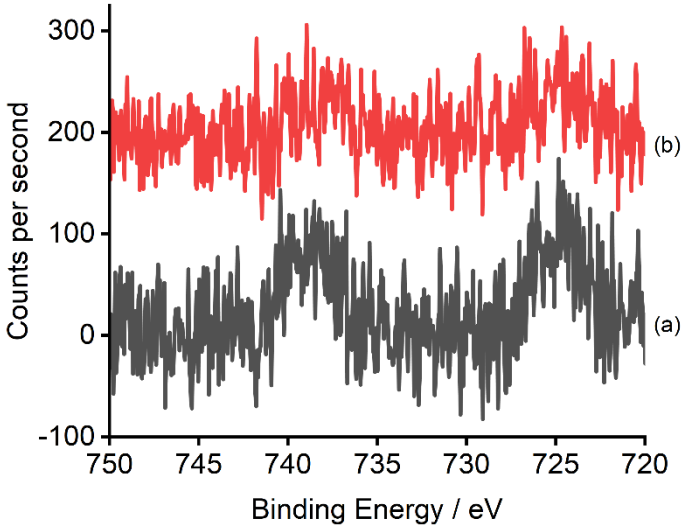

Figure 5.41: XPS spectra of Cs3d data (after applying binding energy correction verified by the shift of the Al 2p peak and after subtraction of a Shirley background), at 225 °C under (a) O_2 pretreatment and (b) 2:1 of oxygen: ethylene. Spectra have been offset for clarity.

The local chemical environment of caesium was investigated by cross polarisation (CP) ^{133}Cs NMR spectroscopy. The spectrum for Cs-Re-Ag/α-Al_2O_3 is shown in *Figure 5.42*,

where the two chemical shifts observed at -4.8 and -7.4 ppm are likely to be due to caesium interacting with silver particles and the quadrupolar shoulder which is similar to Cs-Ag/α-Al_2O_3.[45] A third chemical shift is present at -107.7 ppm when Re is added which is likely to be an interaction of Cs with Re. It has been suggested that there is a complex formed with the addition of Cs and Re, suggestions indicate that it could be $CsReO_x$, therefore some form of complex could be forming here.[36,39] This has a significant amount of broadening and there is a large sideband pattern. There is a significant electron distortion around this environment. This indicates that Re interacts with the Cs and causes electron distortion of the Cs, agreeing with the *ex situ* XPS data. It should also be noted here that CP-MAS NMR may or may not enhance the intensity of some peaks over others due to multiple reasons. These include the fact that it relies on the transfer of polarisation from abundant nuclei to less abundant nuclei and the efficiency of this transfer can vary depending on the proximity and interaction between these nuclei.[46] Another reason is that in heterogeneous samples, the local environment around each nucleus can very, leading to differences in how effectively polarisation is transferred. Lastly, the strength of the dipolar couplings between the nuclei affects the efficiency of polarisation transfer, where stronger couplings generally lead to better enhancement.[46]

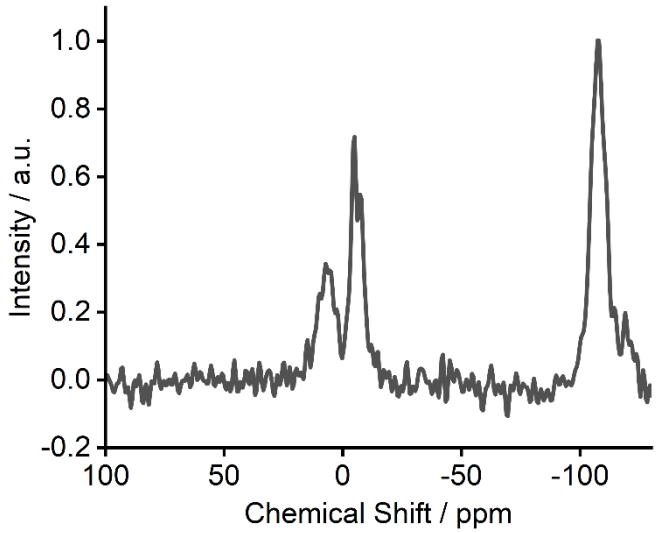

Figure 5.42: Solid State CP ^{133}Cs NMR spectrum of Cs-Re-Ag/α-Al_2O_3.

Again, as before there was no interaction showing Cs with Al_2O_3, therefore, ^{27}Al SS NMR spectroscopy was undertaken to see Cs interacts with the Al_2O_3. As shown in *Figure 5.43* there are two main chemical shifts, the first one is at 15.5 ppm and the second one is at 70.3 ppm, these are likely to correspond to octahedral and tetrahedral Al respectively.

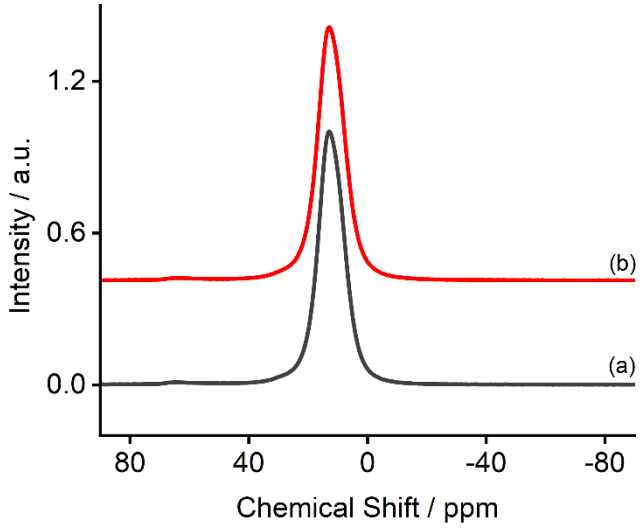

Figure 5.43: Solid State ^{27}Al NMR spectra of Cs/α-Al_2O_3, where (a) is Cs-Ag/α-Al_2O_3 and (b) is Cs-Re-Ag/α-Al_2O_3. Spectra have been offset for clarity.

When Re is added there is only a small shift in site 2 (*Table 5.17*), here it is electronically more deshielded. It could indicate a higher loading however ICP-OES and XRF have confirmed the wt. % are similar, therefore it is likely to be a small distortion to the species.[47] This potentially indicates that the addition of Re to the Cs-Ag/α-Al_2O_3 slightly distorts the Al species.

Table 5.17: A table showing the two different catalysts with the main details and assignments taken from the ^{27}Al NMR spectra.

Catalyst	Site	δ_{iso} (ppm)	Assignment
Cs-Ag/α-Al_2O_3	1	15.5	Octahedral Al
	2	70.3	Tetrahedral Al
Cs-Re-Ag/α-Al_2O_3	1	15.5	Octahedral Al
	2	70.6	Tetrahedral Al

To give an improved understanding of the structure of the Re species during O_2 pretreatment and ethylene epoxidation the *in situ* XAS of the Re L3 edge were obtained. Both Cs-Re-Ag/α-Al_2O_3 and Cs-Re-Ag/γ-Al_2O_3 were investigated under 4 different conditions, under Ar at room temperature, under O_2 pretreatment at 225 °C, under ethylene at 225 °C and under ethylene at 275 °C.

Compared to Re-Ag/α-Al_2O_3, for Cs-Re-Ag/α-Al_2O_3 there are changes in the Re structure (shown in *Figure 5.44*), and there is a decrease in the Re-O bond length with the addition of Cs. This agrees with the Raman data, where there is a change in the Re-O bonds.

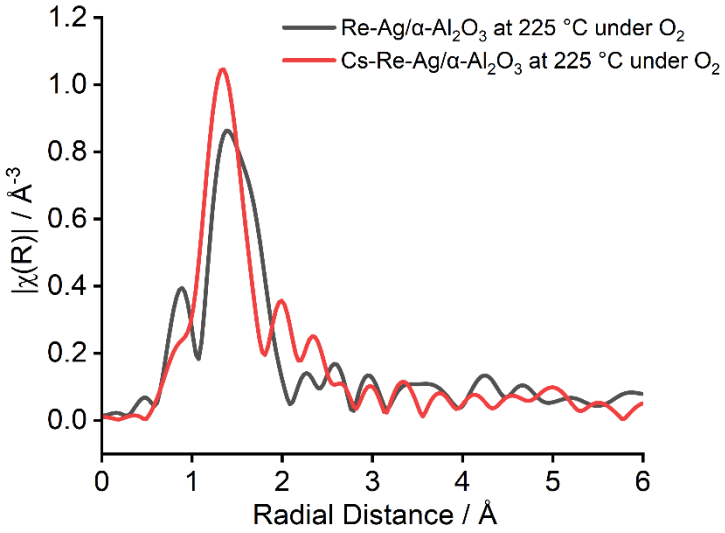

Figure 5.44: Re L3-edge XANES R value for the Re-Ag/α-Al_2O_3 and the Cs-Re-Ag/α-Al_2O_3 catalyst under O_2 pretreatment at 225 °C.

Following the sequence of conditions to which the sample was exposed, shown in *Figure 5.45*, there appears to be a slight change in bonds comparing RT to 225 °C indicating the change in temperature. The structure appears to not change at 225 °C between under O_2 and under C_2H_4. However, at 275 °C there is a large change indicating the Re oxide species changes substantially at 275 °C under ethylene epoxidation conditions. Due to the smaller surface area of α-Al_2O_3, it is thought that it is more likely that the Re oxide clusters are on the Ag (STEM indicates that the Re clusters around the Ag), therefore there are likely to be more interactions between the Re-O and Ag particles. As shown in *Table 5.18* at 275 °C sintering occurs, which increases the amount of α-Al_2O_3 surface available potentially changing the bonding of Re-O-Ag to Re-O-Al, which is a plausible hypothesis for the substantial change at 275 °C.

Table 5.18: Summary of FWHM and particle size estimation from pXRD data using the Scherrer equation. Errors were calculated based on the error from fitting the Gaussian functions.

Catalyst	Reflection(s) used / °	FWHM / °	Estimated Crystallite Size / nm	Error in Gaussian fit of Crystallite Size / nm
Cs-Re-Ag/α-Al_2O_3	64.5	0.40	46.1	±2.7
Cs-Re-Ag/α-Al_2O_3 after heating to 275 °C	64.5	0.25	73.8	±1.9

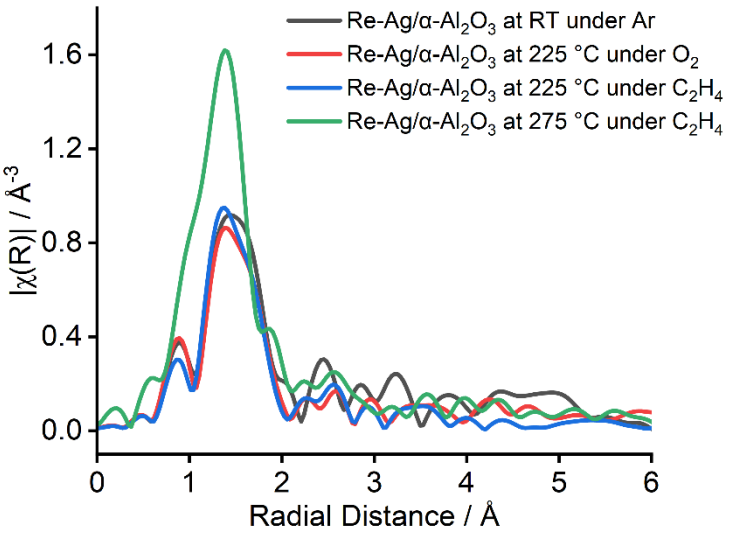

Figure 5.45: Re L3-edge XANES R value for the Cs-Re-Ag/α-Al_2O_3 catalyst under argon at room temperature, under O_2 pretreatment at 225 °C, under C_2H_4 at 225 °C and under C_2H_4 under 275 °C.

Due to a lack of structural models for the Re-O species on Ag/Al_2O_3, there was difficulty in fitting the Cs-Re-Ag/α-Al_2O_3. As shown in *Table 5.19*, (due to the similarity of the Cs-Re-Ag/α-Al_2O_3 at the conditions of O_2 pretreatment and C_2H_4 at 225 °C, only the C_2H_4 at 225 °C condition is shown) Cs-Re-Ag/α-Al_2O_3 did not fit the models used for Re-Ag/γ-Al_2O_3 or to two different oxygen species of Re-O(1) and Re-O(2) (shown in *Tables 5.20* and *5.21*). However, this does indicate that more than one species of oxygen is needed to fit this data and that there are no Re-Re scattering paths again indicating a single Re atom, Re oxide cluster. As discussed above, it is thought that for α-Al_2O_3 is more likely that the Re oxide clusters are on the Ag (STEM indicates that the Re clusters around the Ag), therefore there are likely to be more interactions between the Re-O and Ag particles. A structural model is needed to identify these interactions.

Table 5.19: Re L3-edge EXAFS different fitting parameters for the Cs-Re-Ag/α-Al_2O_3

Conditions	Abs-Scatterer	∆ E0 /eV	Coordination Number	Radial Distance /Å	σ^2 /Å^2	R_{factor}
RT Argon	Re-O (1)	6 ± 15	0.28 ± 0.25	1.67 ± -0.02	-0.007	0.42
RT Argon	Re-O (1)	16 ± 11	0.64 ± 0.52	1.72 ± -0.006	-0.003	0.17
	Re-O		3.02 ± 3.33	2.09 ± 0.02	0.009	
RT Argon	Re-O (1)	3 ± 10	0.64 ± 0.76	1.68 ± -0.027	-0.006	0.32
	Re-Re (in ReO_2)		37.45 ± 189.4	2.98 ± 0.06	0.06	
RT Argon	Re-O (2)	6 ± 15	0.28 ± 0.25	1.69 ± -0.023	-0.007	0.42

Fitting Parameters: S_0^2 determined from W foil = 0.78, 1 < R < 3.0 Å. k-range 6.0 – 14.8, no. of independent points 10.9.

Table 5.20: Re L3-edge EXAFS different fitting parameters for the Cs-Re-Ag/α-Al_2O_3

Conditions	Abs-Scatterer	∆ E0 /eV	Coordination Number	Radial Distance /Å	σ^2 /Å^2	R_{factor}
225 °C under C_2H_4	Re-O (1)	9 ± 7	0.55 ± 0.26	1.70 ± -0.016	-0.005	0.16
225 °C under C_2H_4	Re-O (1)	16 ± 7	2.12 ± 1.10	1.73 ± 0.001	-0.001	0.04
	Re-O (2)		3.91 ± 3.90	2.09 ± 0.01	0.015	
225 °C under C_2H_4	Re-O (1)	6 ± 9	1.20 ± 1.00	1.69 ±	-0.004	0.14
	Re-Re (in ReO_2)		49.22 ± 336.5	3.08 ±	0.07	
225 °C under C_2H_4	Re-O (2)	-51 ± 8	3.88 ± 1.78	1.91 ±	-0.0006	0.10

Fitting Parameters: S_0^2 determined from W foil = 0.78, 1 < R < 3.0 Å. k-range 6.0 – 14.8, no. of independent points 10.9.

Table 5.21: Re L3-edge EXAFS different fitting parameters for the Cs-Re-Ag/α-Al_2O_3

Conditions	Abs-Scatterer	∆ E0 /eV	Coordination Number	Radial Distance /Å	σ^2 /Å^2	R_{factor}
275 °C under C_2H_4	Re-O (1)	8 ± 7	0.97 ± 0.41	1.69 ± -0.023	-0.004	0.19
275 °C under C_2H_4	Re-O (1)	17 ± 5	1.80 ± 0.32	1.72 ± -0.005	-0.001	0.05
	Re-O (2)		3.72 ± 2.73	2.08 ± 0.01	0.016	
275 °C under C_2H_4	Re-O (1)	6 ± 6	1.06 ± 0.60	1.68 ± -0.004	-0.004	0.14
	Re-Re (in ReO_2)		26.42 ± 111.4	3.00 ± 0.06	0.06	
275 °C under C_2H_4	Re-O (2)	-56 ± 9	3.41 ± 1.56	1.88 ± -0.08	-0.0006	0.14

Fitting Parameters: S_0^2 determined from W foil = 0.78, 1 < R < 3.0 Å. k-range 6.0 – 14.8, no. of independent points 10.9.

Fitting using FEFF in Artemis was carried out for the EXAFS spectrum of Cs-Re-Ag/γ-Al_2O_3 to determine the average bond lengths around the rhenium, giving insight into the potential position and bonding of the rhenium atoms. The Re-O (1) path used was at 1.73 Å from Re_2O_7 and the Re-Re path used was at 2.81 Å from ReO_2 (due to less distortion of the Re-Re bond in an oxide species). As shown in *Figures 5.46 – 5.49* and *Table 5.22*, there is a reasonable coordination of 3-4 oxygen atoms when the coordination number is allowed as a fitting parameter. As shown in *Table 5.23* no Re-O-Re therefore no Re-Re interaction of the kind seen in bulk oxide implies single Re atom species, indicating that there are Re oxide clusters on the surface of the catalyst. Cs does not seem to affect the Re-O bond in the Cs-Re-Ag/γ-Al_2O_3 catalyst.

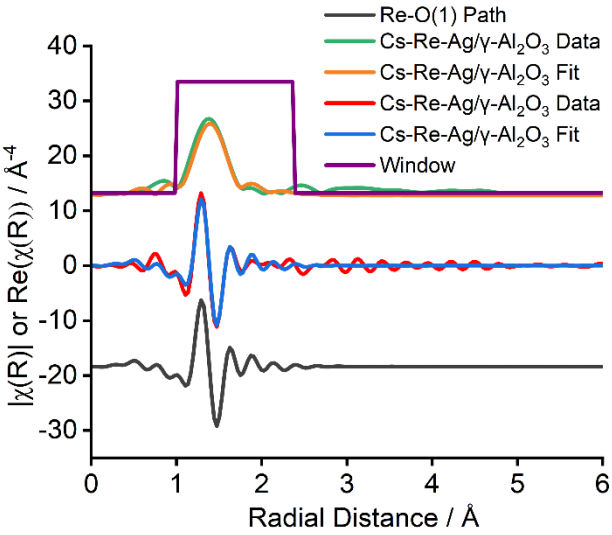

Figure 5.46: Magnitude and real part of the k^3-weighted, FT of the Re L3-edge EXAFS data and fits for the Re-Ag/γ-Al_2O_3 catalyst under Ar at RT, with the fitted Re-O(1) path shown. Spectra have been offset for clarity.

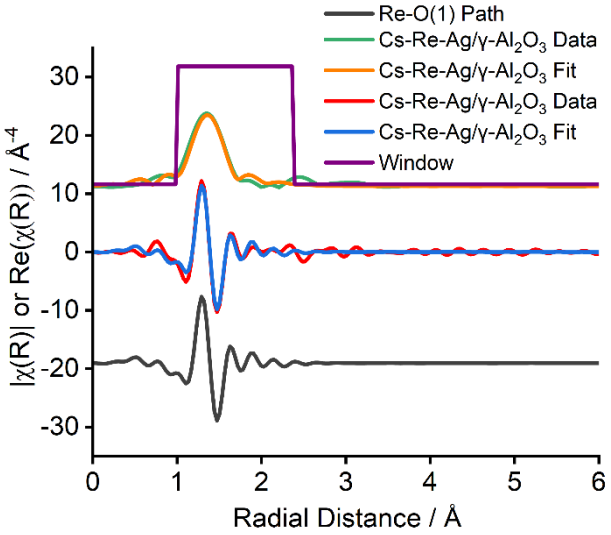

Figure 5.47: Magnitude and real part of the k^3-weighted, FT of the Re L3-edge EXAFS data and fits for the Cs-Re-Ag/γ-Al_2O_3 catalyst under O_2 pretreatment at 225 °C, with the fitted Re-O(1) path shown. Spectra have been offset for clarity.

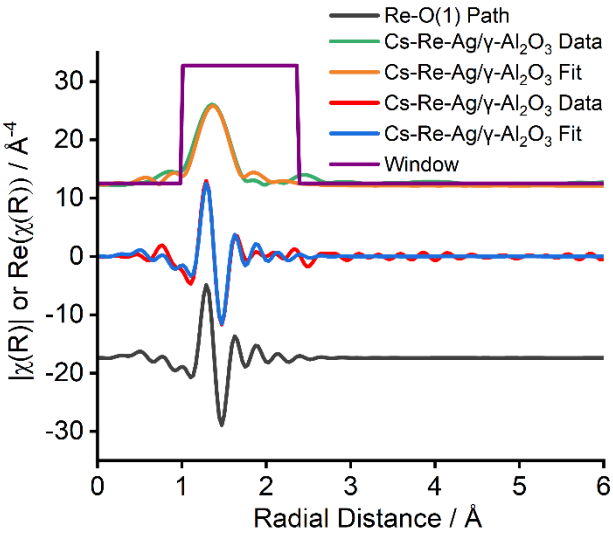

Figure 5.48: Magnitude and real part of the k^3-weighted, FT of the Re L3-edge EXAFS data and fits for the Cs-Re-Ag/γ-Al_2O_3 catalyst under C_2H_4 at 225 °C, with the fitted Re-O(1) path shown. Spectra have been offset for clarity.

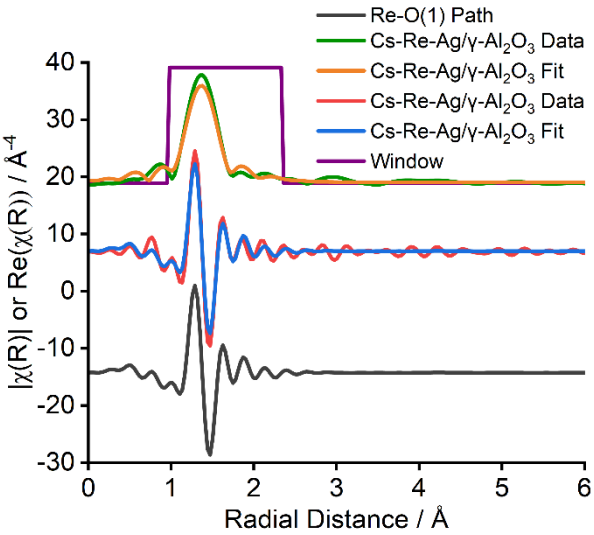

Figure 5.49: Magnitude and real part of the k^3-weighted, FT of the Re L3-edge EXAFS data and fits for the Cs-Re-Ag/γ-Al_2O_3 catalyst under C_2H_4 at 275 °C, with the fitted Re-O(1) path shown. Spectra have been offset for clarity.

Table 5.22: Re L3-edge EXAFS parameters of Re-O(1) for the Cs-Re-Ag/γ-Al_2O_3

Conditions	Abs-Scatterer	Δ E0 /eV	Coordination Number	Radial Distance /Å	σ ^{2} /Å^2	R_{factor}
RT Argon	Re-O (1)	11 ± 2	3.93 ± 0.12	1.73 ± 0.002	0.001	0.02
225 °C under O_2 pretreatment	Re-O (1)	8 ± 3	3.33 ± 0.30	1.73 ± 0.004	0.001	0.04
225 °C under ethylene	Re-O (1)	10 ± 2	3.42 ± 0.25	1.73 ± 0.003	0.001	0.03
275 °C under ethylene	Re-O (1)	9 ± 2	3.29 ± 0.28	1.73 ± 0.003	0.001	0.04

Fitting Parameters: S_0^2 determined from W foil = 0.78, 1 < R < 3.0 Å. k-range 6.0 – 14.8, no. of independent points 10.9.

Table 5.23: Re L3-edge EXAFS fitting parameters of Re-O(1) and Re-Re for the Re-Ag/γ-Al_2O_3

Conditions	Abs-Scatterer	Δ E0 /eV	Coordination Number	Radial Distance /Å	σ ^{2} /Å^2	R_{factor}
RT Argon	Re-O (1)	11 ± 2	3.49 ± 0.20	1.73 ± 0.002	-0.0009	0.009
	Re-Re (in ReO_2)		37.64 ± 136.24	3.09 ± 0.005	0.099	
225 °C under O_2 pretreatment	Re-O (1)	9 ± 3	3.09 ± 0.23	1.73 ± 0.003	0.0001	0.02
	Re-Re (in ReO_2)		64.27 ± 158.31	3.00 ± 0.07	0.086	
225 °C under ethylene	Re-O (1)	11 ± 2	3.38 ± 0.26	1.73 ± 0.004	0.0003	0.02
	Re-Re (in ReO_2)		36.73 ± 99.08	3.02 ± 0.08	0.07	
275 °C under ethylene	Re-O (1)	8 ± 3	3.10 ± 0.25	1.73 ± -0.0002	-0.0002	0.02
	Re-Re (in ReO_2)		369.98 ± 1602.37	3.10 ± 0.10	0.16	

Fitting Parameters: S_0^2 determined from W foil = 0.78, 1 < R < 3.0 Å. k-range 6.0 – 14.8, no. of independent points 10.9.

5.2.6 *In Situ* Ethylene Reactions

Due to this catalyst being the least studied, *in situ* ethylene epoxidation was undertaken of the catalyst using DRIFTS and XPS. *In situ* DRIFTS at 225 °C after 2 h of addition of ethylene was undertaken on both Ag/α-Al_2O_3 and Cs-Re-Ag/α-Al_2O_3 (shown in *Figure 5.50*). Comparing Cs-Re-Ag/α-Al_2O_3 to Ag/α-Al_2O_3 (from Chapter 4) there appears to be a slight increase in the band at 1080 cm^{-1} corresponding to the C-O stretching mode of ethylene oxide.[30] There is an increase in the band at 1245 cm^{-1} corresponding to the C-O-C stretching mode of ethylene oxide.[31–33] This indicates that there is more ethylene oxide on the surface of the Cs-Re-Ag/α-Al_2O_3 catalyst under reaction conditions. The peaks between 1400 and 1500 cm^{-1} correspond to the ethylene gas phase where there is H-C-H scissoring, this shows very little change when comparing Ag/α-Al_2O_3 to Cs-Re-Ag/α-Al_2O_3.[31–33] The broad peaks at both 1540 cm^{-1} and 1660 cm^{-1} correspond to C=C stretching in ethylene, there is an increase in this peak when comparing Ag/α-Al_2O_3 to Cs-Re-Ag/α-Al_2O_3.[31–33] The peak at 1730 cm^{-1} corresponds to the stretching of the C=O bond in acetaldehyde, whilst it is difficult to see, there appears to be very little change in this peak.[31–33]

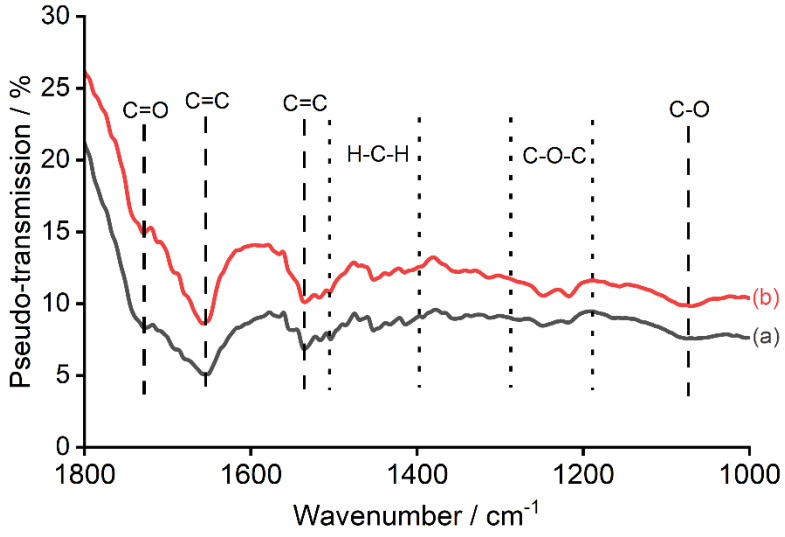

Figure 5.50: In situ ethylene epoxidation reaction on (a) Ag/α-Al_2O_3 and (b) Cs-Re-Ag/α-Al_2O_3 after 2 hr of exposure to ethylene at 225 °C backgrounded against KBr. The O_2:C_2H_4 ratio in all cases is 2:1 where the new DRIFTS cell was used. Spectra have been offset for clarity.

Next *in situ* XPS was undertaken to compare Ag/α-Al_2O_3 to Cs-Re-Ag/α-Al_2O_3 at 225 °C under different conditions including Ar, O_2 pretreatment, 5:1 ratio of oxygen to ethylene (oxygen rich), 2:1 ratio of ethylene to oxygen (practical) and a 1:1 ratio of ethylene to oxygen (fuel rich). Both 0.25 mbar and 10 mbar were investigated, however whilst peaks were able to be seen at 0.25 mbar no peaks were seen at 10 mbar therefore all experiments shown below were taken at 0.25 mbar.

Firstly, Ag 3d was investigated, when looking at Cs-Re-Ag/α-Al_2O_3 (*Figure 5.51*) there is no change in binding energy under argon at 225 °C compared to Ag/α-Al_2O_3. As with Ag/α-Al_2O_3, there is a decrease in binding energy 0.5 eV which corresponds to the surface being more oxidised with the addition of the O_2 pretreatment. There is a small decrease with the addition of a 2:1 ratio of oxygen: ethylene again indicating the Ag surface becoming more oxidised.[48] Unfortunately, due to time constraints, Cs-Re-Ag/α-Al_2O_3 was only undertaken at 225 °C at three different conditions including Ar, O_2 pretreatment and a 2:1 ratio of ethylene to oxygen.

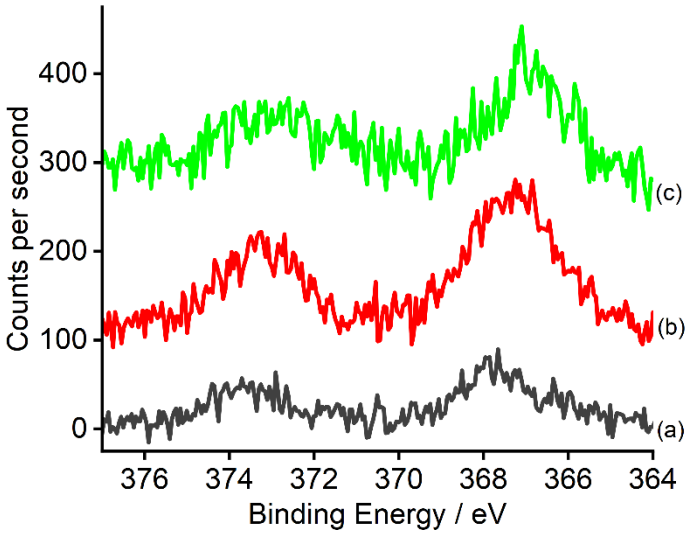

Figure 5.51: Ag 3d XPS data (after applying binding energy correction verified by the shift of the Al 2p peak and after subtraction of a Shirley background) of in situ ethylene epoxidation reaction on Cs-Re-Ag/α-Al_2O_3 at 225 °C under (a) argon, (b) O_2 pretreatment, and (c) practical conditions. Spectra have been offset for clarity.

When looking at Cs-Re-Ag/α-Al_2O_3 at 225 °C under C_2H_4 (*Figure 5.52*), there is a very small shift in binding energy when comparing Ag/α-Al_2O_3 to Cs-Re-Ag/α-Al_2O where it is likely to be mostly silver oxide on the surface.

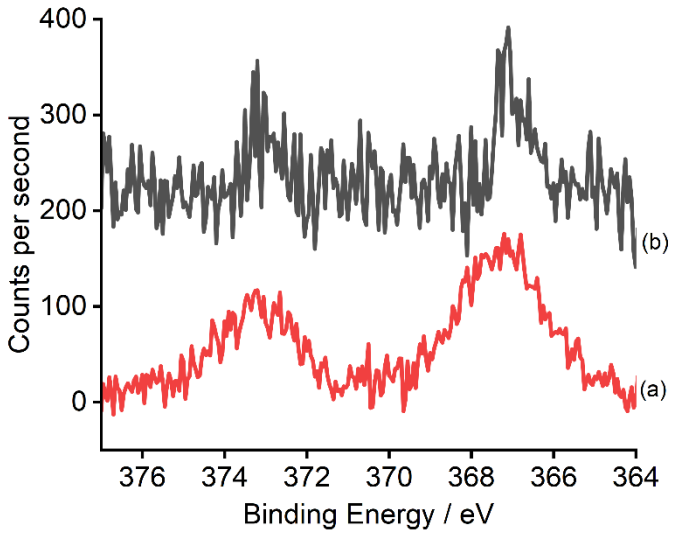

Figure 5.52: Ag3d XPS data (after applying binding energy correction verified by the shift of the Al 2p peak and after subtraction of a Shirley background) showing in situ ethylene epoxidation reaction on (a) Ag/α-Al_2O_3 and (b) Cs-Re-Ag/α-Al_2O_3 at 225 °C under C_2H_4. Spectra have been offset for clarity.

In situ XPS of Cs-Re-Ag/α-Al_2O_3 was undertaken by looking at the oxygen species during both O_2 pretreatment and under ethylene epoxidation. As shown in *Figure 5.53*, at 225 °C under argon, the peak is at 531.0 eV, corresponding to atomic electrophilic oxygen with a smaller peak at 529 eV corresponding to atomic nucleophilic oxygen.[24] There is an increase in the binding energy of this peak during O_2 pretreatment versus in argon of 0.6 eV indicating an increase in the electrophilicity of the oxygen, there is a reduced electron density of the adsorbed oxygen. The addition of O_2 causes an increase in the counts per second, indicating that there is more oxygen adsorbed. The peak deconvolutions show two peaks corresponding to both surface Ag_x-O_2 dioxygen species and atomic electrophilic oxygen. The addition of ethylene in a 2:1 ratio of oxygen: ethylene causes a further increase of 0.4 eV. In literature, electrophilic oxygen has been shown to range between 530 to 531 eV, whilst at 532 eV has been shown to correspond to surface Ag_x-O_2 dioxygen species, this very broad peak indicates at the 2:1 ratio there is a mixture of Ag_x-O_2 dioxygen species and atomic electrophilic oxygen being present under reaction conditions, this agrees with the data collected from Ag/α-Al_2O_3.[24,40]

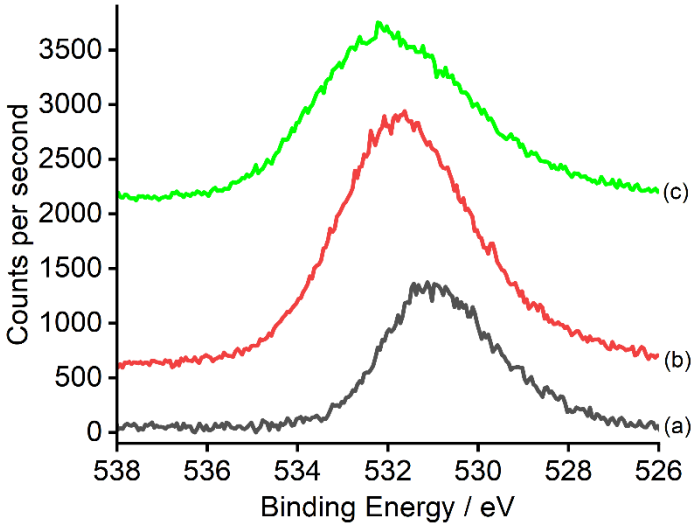

Figure 5.53: O 1s XPS data (after applying binding energy correction verified by the shift of the Al 2p peak and after subtraction of a Shirley background) of in situ ethylene epoxidation reaction on Cs-Re-Ag/α-Al_2O_3 at 225 °C under (a) argon, (b) O_2 pretreatment, (c) practical conditions. Spectra have been offset for clarity.

Peak deconvolution was also undertaken on the *in situ* O1s XPS data with looking at Cs-Re-Ag/α-Al_2O_3. Here *Figure 5.54, 5.55* and *5.56* shows the peak deconvolution of Cs-Re-Ag/α-Al_2O_3 under argon, under O_2 pretreatment and under 2:1 ratio of oxygen: ethylene, respectively. The determined peak areas of the catalyst under different reaction conditions are also shown in *Table 5.24*.

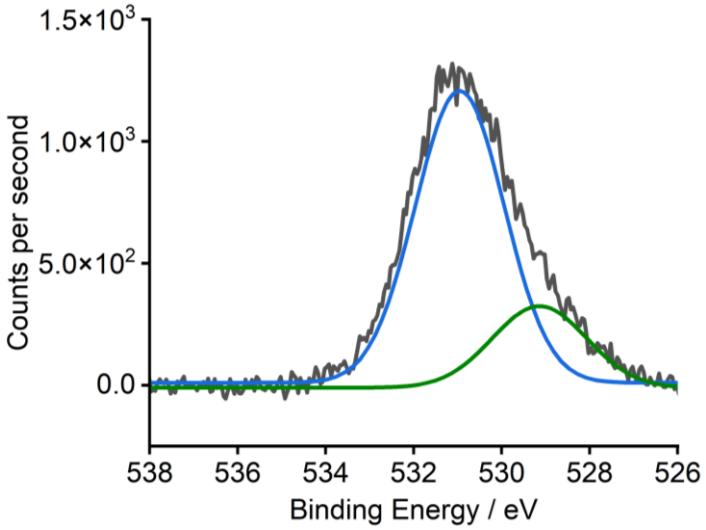

Figure 5.54: Peak deconvolution of the XPS spectra of the O1s looking at Cs-Re-Ag/α-Al_2O_3 under argon. All samples are as prepared, after applying binding energy correction verified by the shift of the Al 2p peak and after subtraction of a Shirley background.

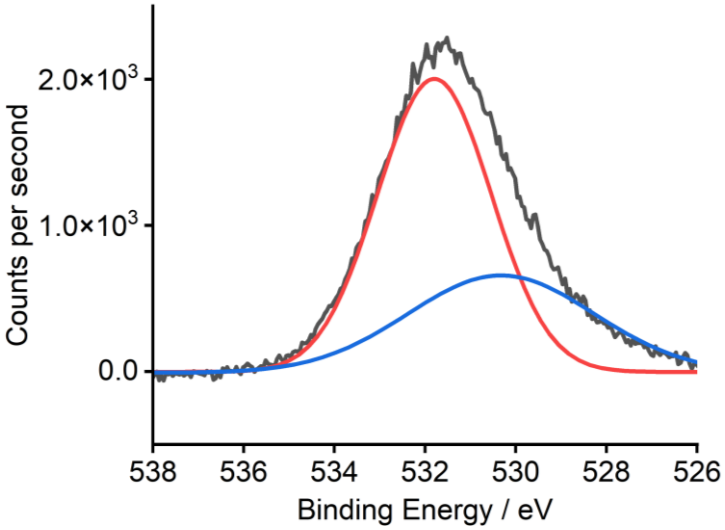

Figure 5.55: Peak deconvolution of the XPS spectra of the O1s looking at Cs-Re-Ag/α-Al_2O_3 under O_2 pretreatment. All samples are as prepared, after applying binding energy correction verified by the shift of the Al 2p peak and after subtraction of a Shirley background.

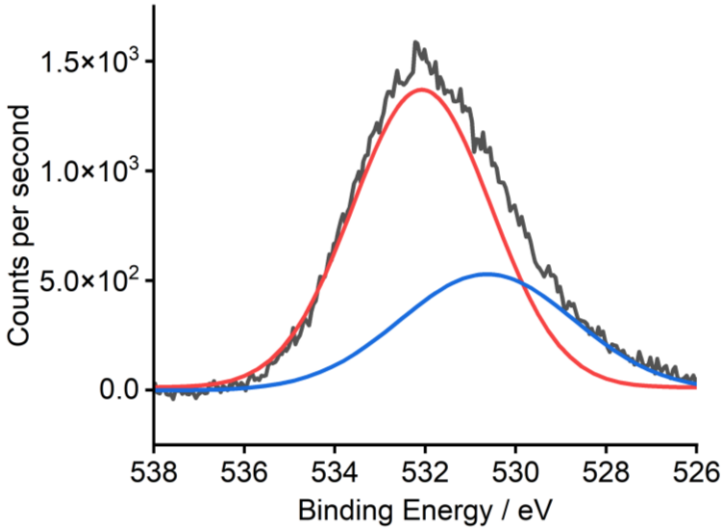

Figure 5.56: Peak deconvolution of the XPS spectra of the O1s looking at Cs-Re-Ag/α-Al_2O_3 under a 2:1 ratio of oxygen: ethylene. All samples are as prepared, after applying binding energy correction verified by the shift of the Al 2p peak and after subtraction of a Shirley background.

Table 5.24: A table showing the peak areas for the peak deconvolution of the XPS spectra of the O1s looking at Ag/α-Al_2O_3 under different conditions.

Catalyst	Peak Area of Green Peak – nucleophilic oxygen / counts	Peak Area of Blue Peak - atomic electrophilic oxygen / counts	Peak Area of Red Peak - Ag_x-O_2 / counts
Ag/α-Al_2O_3 under argon	899.82	3028.18	-
Ag/α-Al_2O_3 under O_2 pretreatment	-	3430.15	5174.06
Ag/α-Al_2O_3 under a 2:1 ratio of oxygen: ethylene	-	2559.77	3955.11

When comparing Ag/α-Al_2O_3 and Cs-Re-Ag/α-Al_2O_3 at 225 °C under O_2 pretreatment (*Figure 5.57*), there is an increase in binding energy of 0.5 eV when adding Cs & Re, therefore causing the oxygen to be more electrophilic in nature indicating that the Cs and Re cause an increase in the electrophilicity of the oxygen. Whilst Ag/α-Al_2O_3 shows one peak corresponding to atomic electrophilic oxygen, the Cs-Re-Ag/α-Al_2O_3 catalyst shows two peaks corresponding to both atomic electrophilic oxygen and Ag_x-O_2.

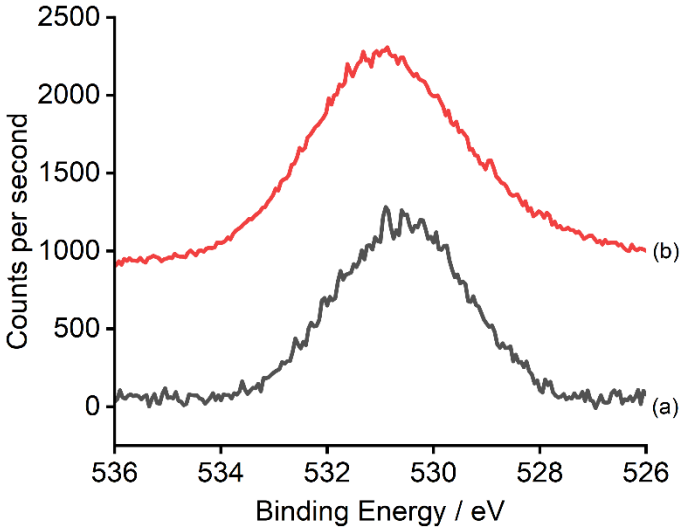

Figure 5.57: O 1s XPS data (after applying binding energy correction verified by the shift of the Al 2p peak and after subtraction of a Shirley background) showing in situ ethylene epoxidation reaction on (a) Ag/α-Al_2O_3 and (b) Cs-Re-Ag/α-Al_2O_3 at 225 °C under O_2 pretreatment. Spectra have been offset for clarity.

The peak deconvolutions of both Ag/α-Al_2O_3 and Cs-Re-Ag/α-Al_2O_3 at 225 °C under O_2 pretreatment are shown in *Figures 4.21* and *5.55,* respectively. A table of comparison of the determined peak areas of the two catalysts is shown in *Table 5.25*.

Table 5.25: A table showing the peak areas for the peak deconvolution of the XPS spectra of the O1s looking at both Ag/α-Al_2O_3 and Cs-Re-Ag/α-Al_2O_3 under O_2 pretreatment.

Catalyst – both under O_2 pretreatment	Peak Area of Blue Peak - atomic electrophilic oxygen / counts	Peak Area of Red Peak - Ag_x-O_2 / counts
Ag/α-Al_2O_3	3751.61	-
Cs-Re-Ag/α-Al_2O_3	2430.15	5174.06

5.3 Conclusions

In this chapter, Cs-Ag/α-Al_2O_3 has been investigated to give more information regarding both the role and the structure giving a detailed study on the Cs promoter. As discussed, the role of the promoters Cs and Re together has minimal information, therefore in the second part of this chapter, Cs-Re-Ag/α-Al_2O_3 was investigated to give more information regarding the role of both promoters. These catalysts have been characterised with both *in situ* and *ex situ* techniques and the activity and selectivity profiles of these catalysts have been determined with comparison to the literature. The conclusions given below have been separated into different sections for clarity.

New Information Concluded:

- The addition of 600 ppm of Cs caused an increase in EO selectivity and a decrease in acetaldehyde selectivity.
- O_2-TPD and H_2-TPR indicate an increase in O_{ads} with the addition of Cs.
- The addition of 600 ppm of Cs and 500 ppm of Re caused a large increase in EO selectivity and a decrease in acetaldehyde selectivity.
- O_2-TPD, H_2-TPR and *ex situ* O1s XPS all indicate an increase in the amount of O_{ads} with the addition of Cs and Re compared to all other combinations of Ag/α-Al_2O_3 catalysts studied.
- The addition of Cs and Re together causes a change in the Re-O bonding and a significant amount of electron distortion of the Cs.
- The structure of the Cs species during the reaction was found to be suboxide-like.
- The Re species was found to be a single Re atom oxide species coordinated to 3-4 oxygen atoms around the Ag. Both ex situ Raman and *in situ* XAFS indicate to changes occurring with the Re-O bonds throughout ethylene epoxidation on the Cs-Re-Ag/α-Al_2O_3.
- Cs does not seem to affect the Re-O bond in the Cs-Re-Ag/γ-Al_2O_3 catalyst.

- pXRD and STEM confirm that Cs and Re added together slightly decrease the Ag crystallite sizes and cause more Ag dispersion, giving more sites for oxygen adsorption.
- For samples containing Cs and Re together, the hydroxyl acidic groups on the support are still titrated, reducing the isomerisation of EO to form acetaldehyde.
- Whilst Ag/α-Al_2O_3 has been investigated with looking at the oxygen species, Cs-Re-Ag/α-Al_2O_3 has not. However, this data agrees with the Ag/α-Al_2O_3 that there is a mixture of Ag_x-O_2 dioxygen species and atomic electrophilic oxygen under reaction conditions on the Cs-Re-Ag/α-Al_2O_3 catalyst.

Contradictions to the Literature:

- There is no change in the Ag or O binding energy in *ex situ* XPS of Cs-Ag/α-Al_2O_3. This conclusion disagrees with Diao *et al.* who stated that Cs lowers the Ag binding energy to facilitate the desorption of the EO precursor to form gas phase EO.[36]
- Zhang *et al.* stated that Re increases the dispersion of Cs which maximises the promotional effects of Cs. However, STEM evidence suggests that the dispersion of Cs does not change between Cs-Ag/α-Al_2O_3 and Cs-Re-Ag/α-Al_2O_3.[37]

Agreements with Previous Arguments in the Literature:

- Cs titrates the hydroxyl acidic groups on the support, expected to reduce the isomerisation of EO to form acetaldehyde. This agrees with Grant, Lambert and Schoenfeld *et al.* who stated that Cs neutralises the acid sites on the support that are active for the isomerisation of EO to form acetaldehyde.[4,5]
- Cs decreased the Ag crystallite sizes and caused more distribution of Ag. This agrees with Schoenfeld and Bal'zhinimaev *et al.* who stated that Cs is able to distribute the silver particles more uniformly on the support.[5,9] Whilst also agreeing with Schmal *et al.* who stated that Cs promoted the formation of very small silver particles which increased the selectivity of ethylene oxide by increasing the contact with the reactants.[13]
- O_2-TPD after O_2 pretreatment indicates that Cs weakens the Ag-O bond, which agrees with Ren *et al.* who stated that Cs decreases the adsorption strength of oxygen on Ag/weakens the adsorption of atomic oxygen.[18]
- The structure of the Cs species is a mixture of peroxide and suboxide-like species, which supports the evidence given by Bukhtiyarov *et al.* who stated that there was a mixture of Cs peroxide and Cs suboxide species present.[23]

- Cs was found to interact with both Ag and Al_2O_3, this agrees with Minahan *et al.* who stated that Cs acts as a binder between the Ag and alumina support in ethylene epoxidation catalysts.[5]
- There is no change in the binding energy of Ag with the addition of Cs and Re under reaction conditions or in *ex situ* XPS. However, in the O 1s, there is an increase in the electrophilicity of the oxygen with the addition of Cs and Re under Ar and O_2 pretreatment. This agrees with Diao *et al.* who stated that Re causes the Ag binding energy to increase which means that Ag sites are more electron deficient and therefore the resulting O adsorbed on Ag more electrophilic, whilst Cs lowers the desorption energy of the EO precursor which is strongly bound.[36]
- O_2-TPD after O_2 pretreatment indicates that Cs and Re together weaken the Ag-O bond. This agrees with Ren *et al.* who stated that Re and Cs together cause a higher concentration of weakly adsorbed oxygen and lower concentrations of strongly adsorbed oxygen.[10]
- Vodyankina *et al.* found the formation of a $CsReO_x$ species on the surface of a Cs-Re-Ag/α-Al_2O_3, whilst this was not found, the ss NMR found a new interaction between Cs and Re which indicates that some form of complex is present on the surface.[39]

5.4 References

1 T. Pu, H. Tian, M. E. Ford, S. Rangarajan and I. E. Wachs, *ACS Catal.*, 2019, **9**, 10727–10750.
2 R. B. Grant, C. A. J. Harbach, R. M. Lambert and S. A. Tan, *J. Chem. Soc., Faraday Trans.*, 1987, **83**, 2035–2046.
3 R. B. Grant and R. M. Lambert, *J. Catal.*, 1985, **92**, 364–375.
4 R. B. Grant and R. M. Lambert, *Langmuir.*, 1985, **1**, 29–33.
5 D. M. Minahan, G. B. Hoflund, W. S. Epling and D. W. Schoenfeld, *J. Catal.*, 1997, **168**, 393–399.
6 S. T. Oyama, *Mechanisms in Homogeneous and Heterogeneous Epoxidation Catalysis*, Elsevier, Amsterdam, 1st edn., 2008.
7 J. Couves, M. Atkins, M. Hague, B. H. Sakakini and K. C. Waugh, *Catal Lett.*, 2005, **99**, 45–53.
8 M. Atkins, J. Couves, M. Hague, B. H. Sakakini and K. C. Waugh, *J. Catal.*, 2005, **235**, 103–113.
9 S. N. Goncharova, E. A. Paukshtis and B. S. Bal'zhinimaev, *Appl. Catal. A: Gen.*, 1995, **126**, 67–84.
10 D. Ren, G. Cheng, J. Li, J. Li, W. Dai, X. Sun and D. Cheng, *Catal. Letters.*, 2017, **147**, 2920–2928.
11 S. Linic and M. A. Barteau, *J. Am. Chem. Soc.*, 2004, **126**, 8086–8087.
12 D. Lafarga, M. A. Al-Juaied, C. M. Bondy and A. Varma, *Ind. Eng. Chem. Res.*, 2000, **39**, 2148–2156.
13 M. C. N. A. Carvalho, C. A. Perez, R. A. Simão, F. B. Passos and M. Schmal, *An. Acad. Bras. Ciênc.*, 2004, **76**, 19–27.
14 A. J. F. van Hoof, E. A. R. Hermans, A. P. van Bavel, H. Friedrich and E. J. M. Hensen, *ACS Catal.*, 2019, **9**, 9829–9839.
15 H. A. Alzahrani and J. J. Bravo-Suárez, *J. Catal.*, 2023, **418**, 225–236.
16 M. Lamoth, T. Jones, M. Plodinec, A. Machoke, S. Wrabetz, M. Krämer, A. Karpov, F. Rosowski, S. Piccinin, R. Schlögl and E. Frei, *ChemCatChem.*, 2020, **12**, 2977–2988.
17 M. Huš and A. Hellman, *J. Catal.*, 2018, **363**, 18–25.
18 D. Ren, H. Xu, J. Li, J. Li and D. Cheng, *Mol. Catal.*, 2017, **441**, 92–99.
19 C. Backx, C. P. M. De Groot and P. Biloen, *Surf. Sci.*, 1981, **104**, 300–317.
20 G. I. N. Waterhouse, G. A. Bowmaker and J. B. Metson, *Appl. Surf. Sci.*, 2003, **214**, 36–51.
21 X. Jing, H. Wang, H. Chen, J. Huang, Q. Li and D. Sun, *RSC Adv.*, 2014, **4**, 27597–27603.
22 G. Ebbinghaus and A. Simon, *Chem. Phys.*, 1970, **43**, 117.
23 E. A. Podgornov, I. P. Prosvirin and V. I. Bukhtiyarov, *J. Mol. Catal. A Chem.*, 2000, **158**, 337–343.
24 T. Pu, A. Setiawan, B. Mosevitzky Lis, M. Zhu, M. E. Ford, S. Rangarajan and I. E. Wachs, *ACS Catal.*, 2022, **12**, 4375–4381.
25 T. J. Frankcombe and Y. Liu, *Chem. Mater.*, 2023, **35**, 5468–5474.
26 C. Liu, D. P. Wijewardena, A. Sviripa, A. Sampath, D. W. Flaherty and C. Paolucci, *J. Catal.*, 2022, **405**, 445–461.
27 Z. Tang, T. Chen, K. Liu, H. Du and S. G. Podkolzin, *Langmuir.*, 2021, **37**, 11603–11610.
28 F. J. Williams, D. P. C. Bird, A. Palermo, A. K. Santra and R. M. Lambert, *J. Am. Chem. Soc.*, 2004, **126**, 8509–8514.
29 Infrared Spectroscopy Absorption Table, https://chem.libretexts.org/Ancillary_Materials/Reference/Reference_Tables/Spectroscopic_Reference_Tables/Infrared_Spectroscopy_Absorption_Table, (accessed 8 February 2024).

30 IR Spectrum Table, https://www.sigmaaldrich.com/GB/en/technical-documents/technical-article/analytical-chemistry/photometry-and-reflectometry/ir-spectrum-table, (accessed 12 January 2024).
31 M. R. D'Oliveira, J. Rabelo, A. G. Veiga, C. A. Chagas and M. Schmal, *Catal Lett.*, 2020, **150**, 3036–3048.
32 M. C. N. Amorim de Carvalho, F. B. Passos and M. Schmal, *J. Catal.*, 2007, **248**, 124–129.
33 D. A. Bulushev, E. A. Paukshtis, Y. N. Nogin and B. S. Bal'zhinimaev, *Appl. Catal. A: Gen.*, 1995, **123**, 301–322.
34 A. J. F. van Hoof, Technische Universiteit Eindhoven, 2019.
35 M. Ravi, V. L. Sushkevich and J. A. van Bokhoven, *Chem. Sci.*, 2021, **12**, 4094–4103.
36 W. Diao, C. D. DiGiulio, M. T. Schaal, S. Ma and J. R. Monnier, *J. Catal.*, 2015, **322**, 14–23.
37 B. W. J. Chen, B. Wang, M. B. Sullivan, A. Borgna and J. Zhang, *ACS Catal.*, 2022, **12**, 2540–2551.
38 D. Jingfa, Y. Jun, Z. Shi and Y. Xiaohong, *J. Catal.*, 1992, **138**, 395–399.
39 M. A. Salaev, A. A. Salaeva and O. V. Vodyankina, *Catal. Today.*, 2021, **375**, 585–590.
40 T. Pu, A. Setiawan, A. C. Foucher, M. Guo, J.-M. Jehng, M. Zhu, M. E. Ford, E. A. Stach, S. Rangarajan and I. E. Wachs, *ACS Catal.*, 2024, **14**, 406–417.
41 IR Spectrum Table & Chart, https://www.sigmaaldrich.com/technical-documents/articles/biology/ir-spectrum-table.html, (accessed 24 May 2021).
42 J. Okal, L. Kępiński, L. Krajczyk and W. Tylus, *J. Catal.*, 2003, **219**, 362–371.
43 J. Okal, *Appl. Catal. A: Gen.*, 2005, **287**, 214–220.
44 F. D. Hardcastle, I. E. Wachs, J. A. Horsley and G. H. Via, *Mol. Catal.*, 1988, **46**, 15–36.
45 A. J. F. van Hoof, I. A. W. Filot, H. Friedrich and E. J. M. Hensen, *ACS Catal.*, 2018, **8**, 11794–11800.
46 T. Wolf, S. Jayanthi, A. Lupulescu and L. Frydman, *J. Chem. Phys.*, 2023, **159**, 224304.
47 T. F. Kemp and M. E. Smith, *Solid State Nucl. Magn. Reson.*, 2009, **35**, 243–252.
48 NIST Chemistry WebBook, https://webbook.nist.gov/chemistry/, (accessed 22 October 2023).

Chapter 6: Investigating the Use of Cu and Au for Ethylene Epoxidation

As discussed in **Section 1.1.3**, the use of Cu and Au-based catalysts for propylene epoxidation has been widely investigated however very little experimental data on using these metals for the catalysis of ethylene epoxidation has been reported. Therefore, the purpose of this chapter is to investigate the use of these metals for EO catalysts, the extent to which Cu and Au catalysts are selective towards ethylene epoxidation and possible reasons for this. These catalysts have been characterised with both *in situ* and *ex situ* techniques and the activity and selectivity profiles of these catalysts have been determined and compared to the literature. The role of Au and Cu both separately and together are discussed with the overarching goal of improving the understanding of the catalysts used in ethylene epoxidation. Throughout the chapter relevant Ag/α-Al_2O_3 data from earlier chapters is included as a benchmark. Although comparisons are to Ag/α-Al_2O_3 it should be noted that the catalyst has 10 wt. % of Ag and the pretreatment occurred at 225 °C, therefore these catalysts are synthesised differently. However, pretreatment above 275 °C of silver catalysts can lead to sintering (as discussed in **Chapter 4.1.4**) and as discussed by Minahan *et al*. the Ag metal loadings are typically high commonly around 10 wt. %, where lower wt. % and higher pretreatment can lead to unselective catalysts.[1] Therefore, these catalysts have been compared to the "standard" Ag/α-Al_2O_3 to see the changes in EO selectivity. All catalytic reactions were undertaken at laboratory scale using 150 mg of catalyst where the online gas analysis was carried out with a mass spectrometer and a least squares fitting approach was used to fit the data to concentrations of each species.

6.1 Investigating Au/α-Al_2O_3 as a Catalyst for Ethylene Epoxidation

Firstly, the catalyst Au/α-Al_2O_3 was investigated. No experimental information regarding the Au/α-Al_2O_3 catalyst was found within the literature for direct ethylene epoxidation.

Therefore, it was thought that the use of *in situ* and *ex situ* spectroscopic and characterisation techniques, alongside reaction data would be able to give more insight into whether an Au/α-Al_2O_3 catalyst is selective towards EO and why this is the case.

Whilst no catalysts of Au/α-Al_2O_3 have been synthesised for ethylene epoxidation, they have been extensively used for propylene epoxidation. Therefore this catalyst was synthesised by the method adapted from Xuan who prepared Cu, Au, Cu-Ag and Cu-Au supported on ZnO catalysts for propylene epoxidation.[2] 2 wt. % of every metal was used, therefore this was also used for the synthesis on α-Al_2O_3. To confirm that the elemental composition of

the catalyst was as expected, ICP-OES was conducted. The elemental composition of the catalyst is shown in *Table 6.1*. As shown, the gold content of the catalyst was close to the expected value, with small fluctuations of value and low errors.

Table 6.1: Summary of ICP-OES results. The results reported are the average results of the duplicate samples where errors are one standard deviation calculated based on the duplicate samples for each material. Standards are run in the same batch to confirm no significant anomalies or deviations in the instrumental analysis of the samples.

Catalyst	Metal	Expected Metal Content / wt. %	Metal Content by ICP-OES / wt. %	Error in Metal Content by ICP-OES / wt. %
Au/α-Al_2O_3	Au	2	1.9	± 0.1

Au/α-Al_2O_3 was evaluated for ethylene epoxidation, with the EO selectivity in *Figure 6.1*. As shown with the comparison to Ag/α-Al_2O_3, the EO selectivity is very similar compared to Au/α-Al_2O_3 with a small increase in acetaldehyde and similar values for CO_2 and H_2O. This gives evidence of the potential use of an Au/α-Al_2O_3 catalyst for ethylene epoxidation.

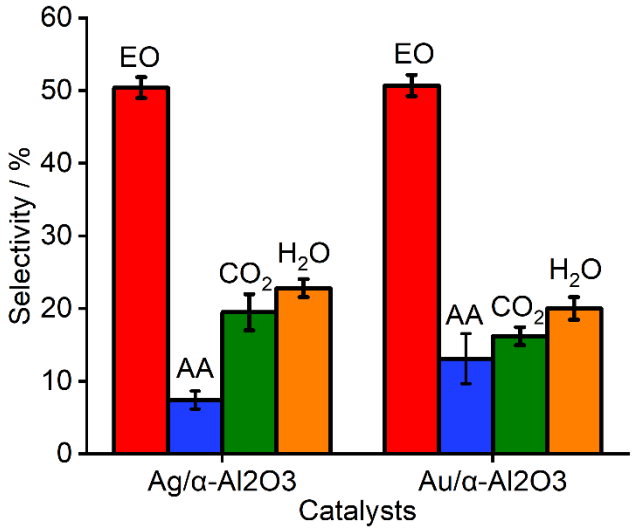

Figure 6.1: A comparison of selectivity between Ag/α-Al_2O_3 (from Chapter 4) and Au/α-Al_2O_3. Errors are based on 3 repeat measurements.

Ethylene conversion was calculated and displayed in *Table 6.2*. There is a slight decrease in the conversion between Ag/α-Al_2O_3 and Au/α-Al_2O_3.

Table 6.2: A table showing the ethylene conversion and percentage error based on 3 repeat measurements for both Ag/α-Al_2O_3 and Au/α-Al_2O_3.

Catalyst	Ethylene Conversion / %	% Error
Ag/α-Al_2O_3 (from Chapter 4)	7.7	0.4
Au/α-Al_2O_3	5.4	0.2

Therefore, this catalyst was characterised and analysed to give more information into why this catalyst is selective towards EO.

6.1.1 Particle Sizes and Morphology

XRD analysis was conducted to be able to confirm the crystallinity of the material and give an insight into the form of Au present. *Figure 6.2* shows the pXRD pattern of Au/α-Al_2O_3 before and after ethylene epoxidation. When comparing to α-Al_2O_3 there are new reflections corresponding to the metallic gold. Many of the reflections from gold are hidden by the α-Al_2O_3 as they overlap. The metallic gold reflections are at 38.1 ° (1 1 1), 44.3 ° (2 0 0), 64.5 ° (2 2 0) and 77.7 (3 1 1).[3,4] Tetrachloroauric (III) acid trihydrate is thermally decomposed at 75 °C and is known to take place in three steps in the temperature range of 75 to 320 °C where after 320 °C, it is metallic Au.[5] The pre-treatment in this study reaches 450 °C, therefore metallic Au is expected to be present on the surface of the α-Al_2O_3.

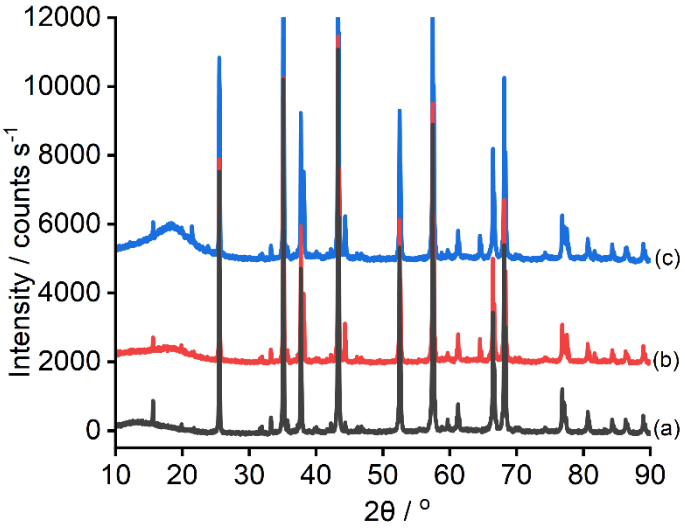

Figure 6.2: pXRD pattern for (a) α-Al_2O_3, (b) Au/α-Al_2O_3 before ethylene epoxidation and (c) Au/α-Al_2O_3 after ethylene epoxidation. Patterns offset for clarity.

The reflection at 64.5 ° corresponding to the 2 2 0 plane is used to identify the size of the Au crystallite with the Scherrer equation (shown in *Figure 6.3*).

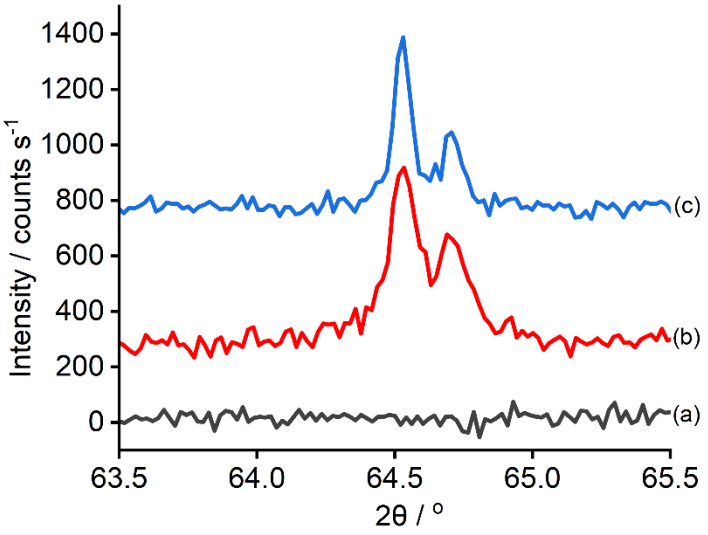

Figure 6.3: pXRD pattern for zoomed-in between 63.5 and 65.5 ° where (a) α-Al_2O_3, (b) Au/α-Al_2O_3 before ethylene epoxidation and (c) Au/α-Al_2O_3 after ethylene epoxidation. Patterns offset for clarity.

The FWHM used for each catalyst with the resultant crystallite sizes is shown in *Table 6.3*. As shown, there is a large decrease in the FWHM and an increase in average crystallite sizes compared to Ag/α-Al_2O_3, indicating that Ag is more dispersed than Au. After ethylene epoxidation, there is an increase in average crystallite size indicating the ethylene epoxidation reaction causes sintering of the average Au crystallites. This agrees with the EO selectivity changing from 50.7% at 2 h to 47.5% at 10 h.

Table 6.3: Summary of full width at half maximum (FWHM) and the particle size estimation from pXRD data using the Scherrer equation. Errors were calculated based on the error from fitting the Gaussian functions.

Catalyst	Reflection(s) used / °	FWHM / °	Estimated Crystallite Size / nm	Error in Gaussian fit of Crystallite Size / nm
Ag/α-Al_2O_3 (from Chapter 4)	64.5	0.36	51.2	± 1.4
Au/α-Al_2O_3 before EE	64.5	0.26	70.9	± 3.7
Au/α-Al_2O_3 after EE	64.5	0.21	87.8	± 5.6

In the literature, it is thought that the selectivity towards EO is partially determined by the distribution of silver, where there are more Ag active sites and fewer hydroxyl groups (acid sites) on the surface of the Al_2O_3 with more distributed Ag.[1,6] Therefore, TEM was undertaken (shown in *Figure 6.4*), to investigate the distribution of Au on the Al_2O_3 to see if this could be a reason as to why the Au/α-Al_2O_3 is selective to EO. Darker roughly spherical

metal particles of gold are visible on the lighter alumina support. As shown, when comparing Au/α-Al_2O_3 to Ag/α-Al_2O_3 (from Chapter 4), there is very little change in the structure however the darker spheric gold agrees with the pXRD indicating larger crystallites.

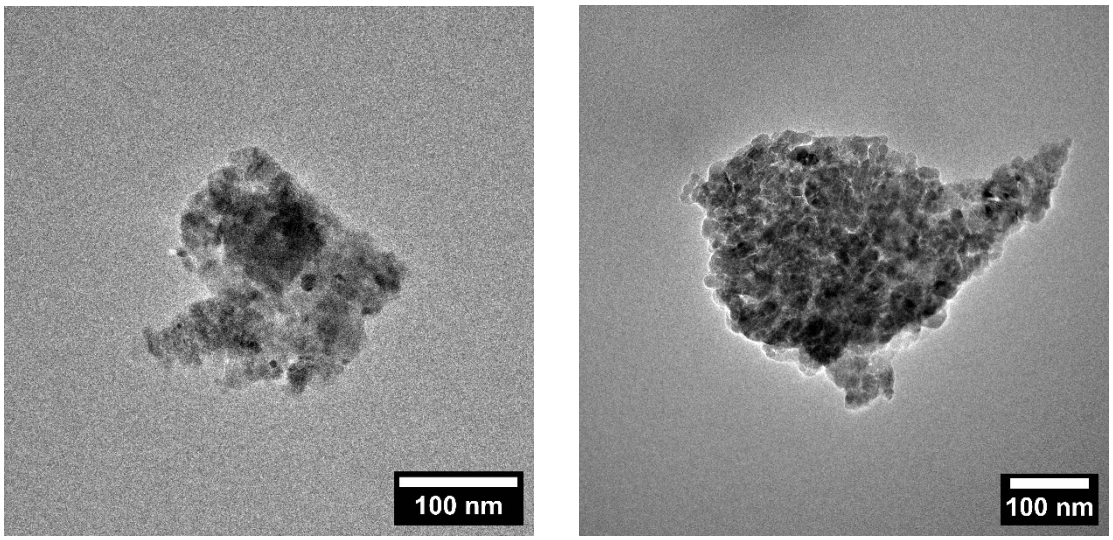

Figure 6.4: Representative TEM of Ag/α-Al_2O_3 (from Chapter 4) on the left-hand side and Au/α-Al_2O_3 on the right-hand side.

6.1.2 Investigating Hydroxyl Groups and Acidity

The hydroxyl groups were investigated with the use of DRIFTS. *Figure 6.5* compares Ag/α-Al_2O_3 (from Chapter 4) with Au/α-Al_2O_3, there is a clear decrease in O-H stretching in the hydroxyl groups. Ag/α-Al_2O_3 shows a band at 3300 cm^{-1} corresponding to non-H bonding hydroxyls whilst the broad band on Au/α-Al_2O_3 corresponds to H bonding hydroxyls.[7] The hydrogen-bonded hydroxyls are less acidic than the non-hydrogen bonded hydroxyls.[8] This decrease in hydroxyl groups and acidity, is likely to be due to the higher pretreatment temperature of 450 °C used for Au/α-Al_2O_3 compared to 225 °C used for Ag/α-Al_2O_3.

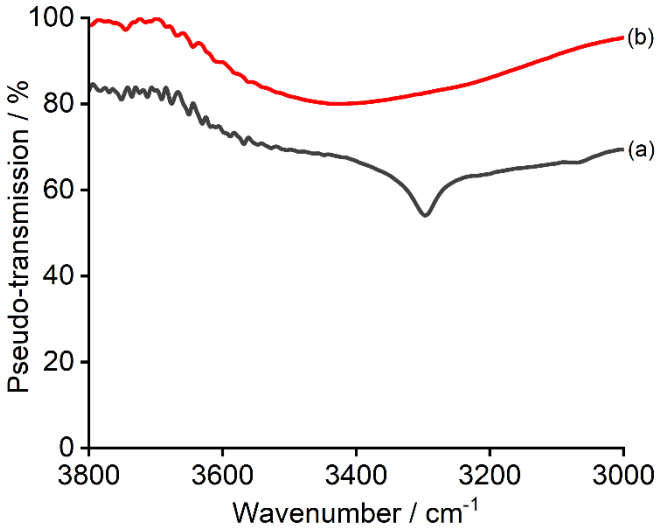

Figure 6.5: DRIFTS spectra of (a) Ag/α-Al_2O_3 (from Chapter 4) and (b) Au/α-Al_2O_3 showing the region of interest, backgrounded against KBr. Spectra have been offset for clarity.

In situ DRIFTS was undertaken during O_2 pretreatment, as shown in *Figure 6.6* there is a clear decrease in hydroxyl groups from Au/α-Al_2O_3 versus Ag/α-Al_2O_3 as suggested by the *ex situ* DRIFTS. Au/α-Al_2O_3 shows a decrease in the hydroxyl groups as the temperature of the reaction increases, whilst for Ag/α-Al_2O_3 this stays very similar. This therefore means at reaction temperature (225 °C) there are very few hydroxyl groups.

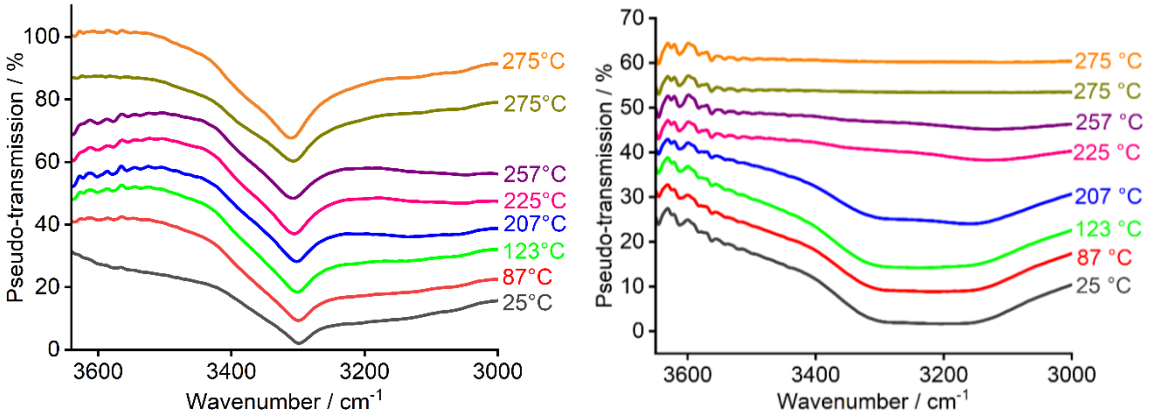

Figure 6.6: In situ O_2 pretreatment DRIFTS on (a) Ag/α-Al_2O_3 (from Chapter 4) and (b) Au/α-Al_2O_3 backgrounded against KBr using the new DRIFTS cell. The second 275 °C shown is after 20 min of being held at 275 °C. Spectra have been offset for clarity.

In situ DRIFTS under ethylene epoxidation conditions was undertaken on Au/α-Al_2O_3 using the new DRIFTS cell however a large broad band between 880 and 1400 cm^{-1} was found to obscure bands making band assignment difficult, this result is shown in **Appendix 5**.

6.1.3 Understanding the Structure of Au

As discussed in **Chapter 1.1.3**, no experimental work has been undertaken on the Au catalyst for direct ethylene epoxidation, therefore it was thought to be useful to investigate the structure of the Au on the α-Al_2O_3. H_2-TPR was undertaken on the Au/α-Al_2O_3 (*Figure 6.7*), as expected there are no peaks, corresponding to Au reducing, therefore agreeing with the pXRD, where the gold is in its metallic form on this catalyst.

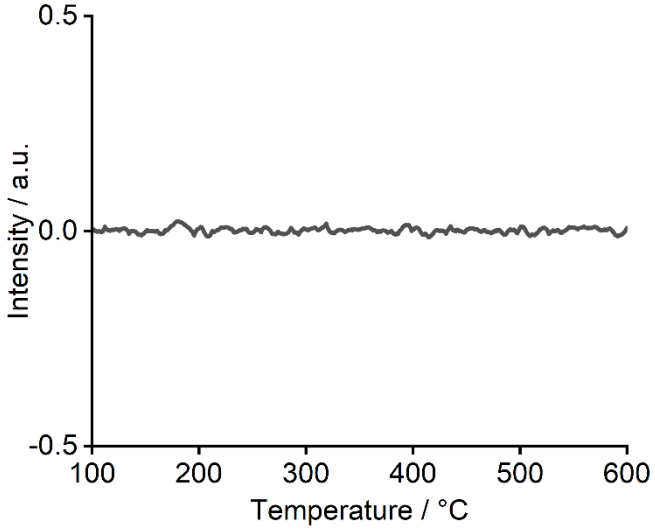

Figure 6.7: H_2-TPR profile of Au/α-Al_2O_3 after O_2 pretreatment (ramp rate 5 °C min^{-1}).

The O_2-TPD (*Figure 6.8*) shows no peak. This is to be expected as normally hot filaments or O_3 are needed to study O_{ads} as gold does not dissociate oxygen.[9,10]

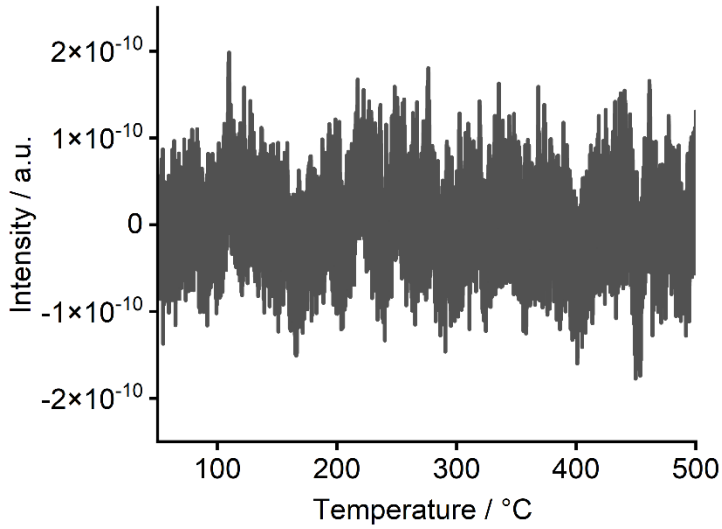

Figure 6.8: O_2-TPD profile of Au/α-Al_2O_3 after O_2 pretreatment (ramp rate 5 °C min^{-1}).

Ex situ XANES was undertaken of Au/α-Al_2O_3 before and after ethylene epoxidation to give more indication into the structure of Au throughout the reaction. A reference for $Au(OH)_3$ was found on BENTEN, the database for SPring-8.[11] As shown in *Figure 6.9,* the fresh

Au/Al_2O_3 matches the Au foil and therefore shows metallic Au. The catalysts have not been oxidised as no similarities to $Au(OH)_3$ are shown. This indicates that the spent $Au/\alpha\text{-}Al_2O_3$ catalyst is also metallic Au.

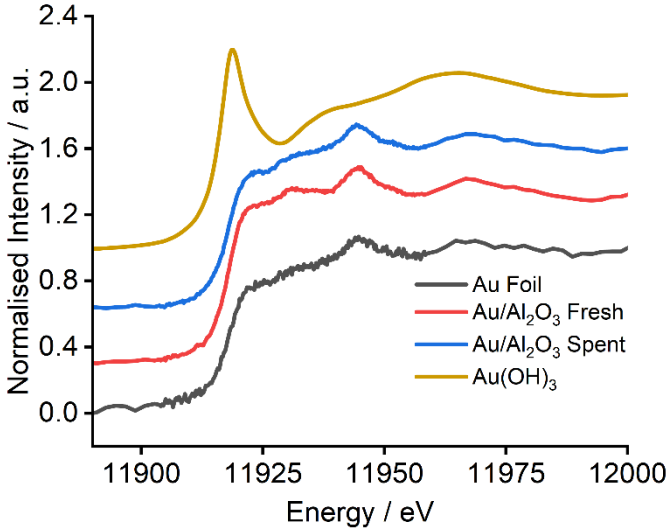

Figure 6.9: XANES at the Au L3 edge of $Au/\alpha\text{-}Al_2O_3$ before and after ethylene epoxidation with references of Au foil and $Au(OH)_3$. Spectra have been offset for clarity.

6.2 Investigating $Cu/\alpha\text{-}Al_2O_3$ as a Catalyst for Ethylene Epoxidation

Next, $Cu/\alpha\text{-}Al_2O_3$ was investigated. Compared to $Au/\alpha\text{-}Al_2O_3$ there are a large number of suggestions on the role and structure of $Cu/\alpha\text{-}Al_2O_3$ used for ethylene epoxidation, here copper catalysts were investigated to give more evidence compared to the literature.[12–15]

It was thought that the use of *in situ* and *ex situ* spectroscopic and characterisation techniques and catalytic testing would be able to give more insight into whether a $Cu/\alpha\text{-}Al_2O_3$ catalyst is selective towards EO and why this is the case.

To correspond to the $Au/\alpha\text{-}Al_2O_3$ catalyst this catalyst was also prepared using 2 wt. % of Cu. To confirm that the elemental composition of the catalyst was as expected, ICP-OES was conducted, as shown in *Table 6.4*. As shown, the copper contents of the catalyst were close to the expected value, with small fluctuations of value and low errors.

Table 6.4: Summary of ICP-OES results. The results reported are the average results of the duplicate samples where errors are one standard deviation calculated based on the duplicate samples for each material. Standards are run in the same batch to confirm no significant anomalies or deviations in the instrumental analysis of the samples.

Catalyst	Metal	Expected Metal Content / wt. %	Metal Content by ICP-OES / wt. %	Error in Metal Content by ICP-OES / wt. %
Cu/α-Al_2O_3	Cu	2	1.6	± 0.1

Cu/α-Al_2O_3 was evaluated for ethylene epoxidation, with the EO selectivity shown in *Figure 6.10*. As shown with the comparison to Ag/α-Al_2O_3 (from Chapter 4), there is a substantial decrease in EO selectivity with Cu/α-Al_2O_3 with an increase in CO_2 and H_2O. However, whilst there is a decrease in EO selectivity there is also a slight increase in acetaldehyde selectivity. Copper supported on α-Al_2O_3 was shown in the literature to epoxidise ethylene with selectivity of around 28%, similar to the values obtained here.[15] There was a decrease in EO selectivity from 25.3% at 2 h to 15.5% at 10 h.

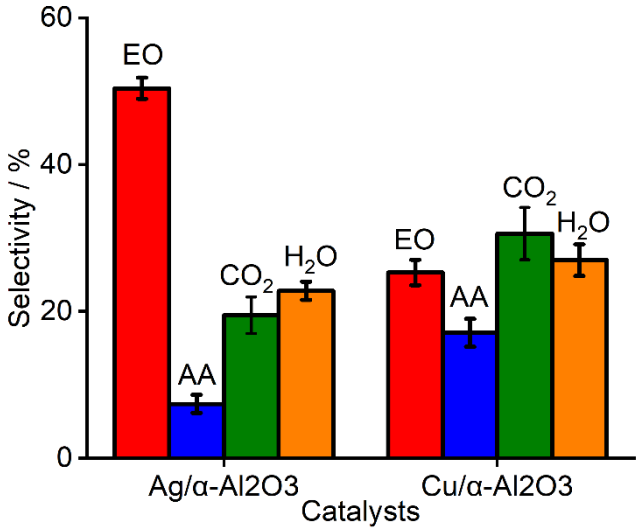

Figure 6.10: A comparison of EO selectivity between Ag/α-Al_2O_3 and Cu/α-Al_2O_3. Errors shown are based on 3 repeat measurements

Ethylene conversion was calculated and displayed in *Table 6.5* and is lower than for both the Ag/α-Al_2O_3 and the Au/α-Al_2O_3 catalyst.

Table 6.5: A table showing the ethylene conversion and percentage error based on 3 repeat measurements for Ag/α-Al_2O_3 (from Chapter 4), Au/α-Al_2O_3 and Cu/α-Al_2O_3.

Catalyst	Ethylene Conversion / %	% Error
Ag/α-Al_2O_3 (from Chapter 4)	7.7	0.4
Au/α-Al_2O_3	5.4	0.2
Cu/α-Al_2O_3	3.1	0.7

6.2.1 Particle Sizes and Morphology

XRD analysis was conducted to be able to confirm the crystallinity of the material and form of present Cu. *Figure 6.11* shows the pXRD pattern of Cu/α-Al_2O_3 before and after ethylene epoxidation. The reflections from copper are either hidden by the α-Al_2O_3 as they overlap or are so broad, they are difficult to identify. Therefore, it is difficult to see if the crystallinity or phase of the catalyst changes before and after ethylene epoxidation. Due to the overlap between the Cu and the α-Al_2O_3, the particle sizes were unable to be identified by the Scherrer equation. However, the absence of any distinctive reflections above the α-Al_2O_3 signal points to small particles or low crystallinity of the copper within the sample.

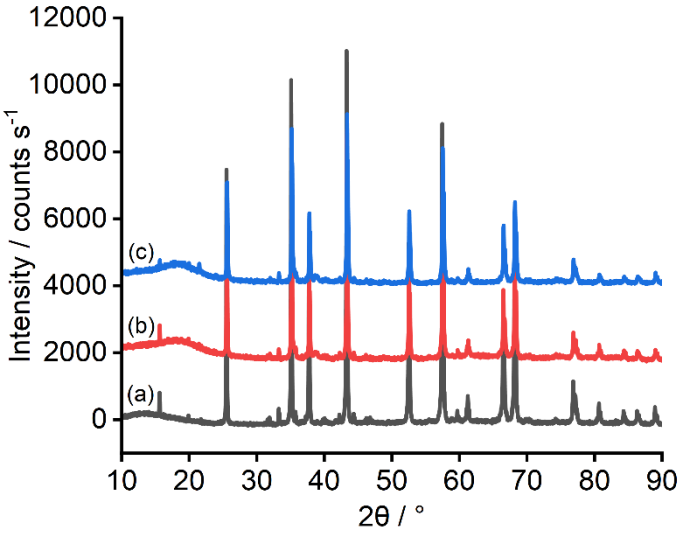

Figure 6.11: pXRD pattern for Cu/α-Al_2O_3 where (a) is α-Al_2O_3, (b) is Cu/α-Al_2O_3 before ethylene epoxidation and (c) is Cu/α-Al_2O_3 after ethylene epoxidation. Patterns have been offset for clarity.

TEM was used (*Figure 6.12*), to investigate the distribution of Cu on the Al_2O_3, here there appears to be a large amount of Cu on the surface of Al_2O_3 indicating that the Cu is dispersed over the surface of the Al_2O_3. There is very little difference between the catalysts Ag/α-Al_2O_3 (from Chapter 4) where the distribution of metal on α-Al_2O_3 is very similar.

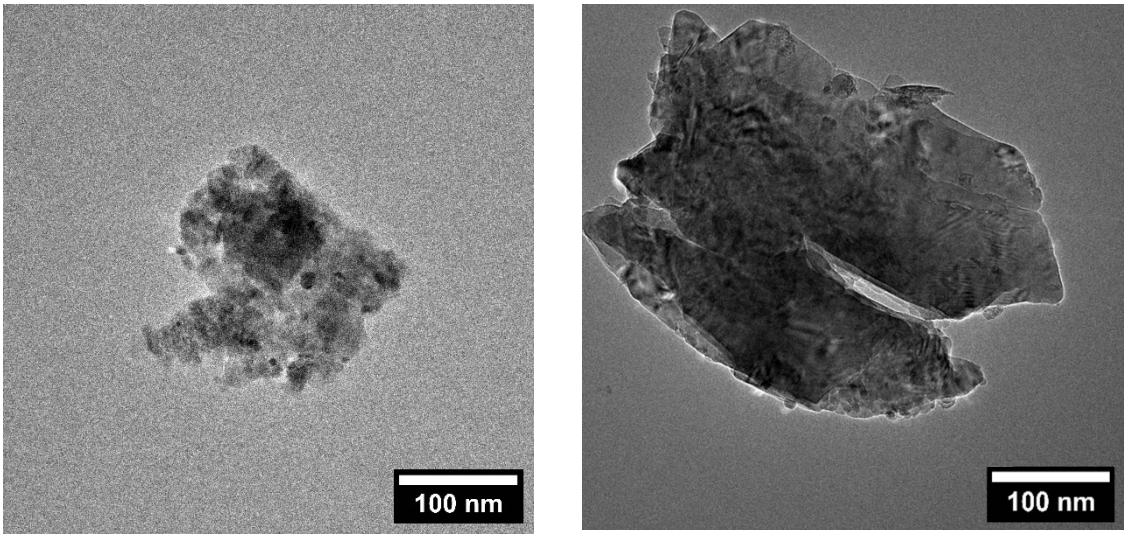

Figure 6.12: Representative TEM of Ag/α-Al_2O_3 (from Chapter 4) on the left-hand side and Cu/α-Al_2O_3 on the right-hand side.

6.2.2 Investigating Hydroxyl Groups and Acidity

The hydroxyl groups were investigated with the use of DRIFTS. When looking at *Figure 6.13,* the DRIFTS spectra of Cu/α-Al_2O_3 and Au/α-Al_2O_3 do not change, this gives an indication that the higher pretreatment temperature of 450 °C used for Au/α-Al_2O_3 compared to 225 °C used for Ag/α-Al_2O_3 is likely to have a substantial effect on the decrease in hydroxyl groups and acidity. There is a clear decrease in O-H stretching in the hydroxyl groups. Ag/α-Al_2O_3 shows a band at 3300 cm^{-1} corresponding to non-H bonding hydroxyls whilst the broad band on Cu/α-Al_2O_3 corresponds to H bonding hydroxyls.[7] The hydrogen-bonded hydroxyls are less acidic than the non-hydrogen-bonded hydroxyls.[8]

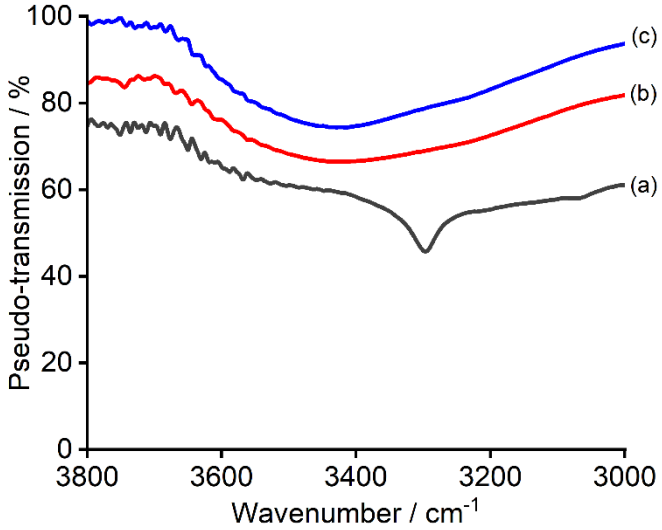

Figure 6.13: DRIFTS spectra of (a) Ag/α-Al_2O_3 (from Chapter 4), (b) Au/α-Al_2O_3 and (c) Cu/α-Al_2O_3 showing the region of interest, backgrounded against KBr. Spectra have been offset for clarity.

In situ DRIFTS was undertaken by looking at the O_2 pretreatment (shown in *Figure 6.14*), as expected with Cu/α-Al_2O_3 there appears to be a decrease in the hydroxyl groups as the temperature of the reaction increases. Therefore, under pre-treatment reaction conditions, there is a reduction in the hydroxyl groups on the surface of the α-Al_2O_3.

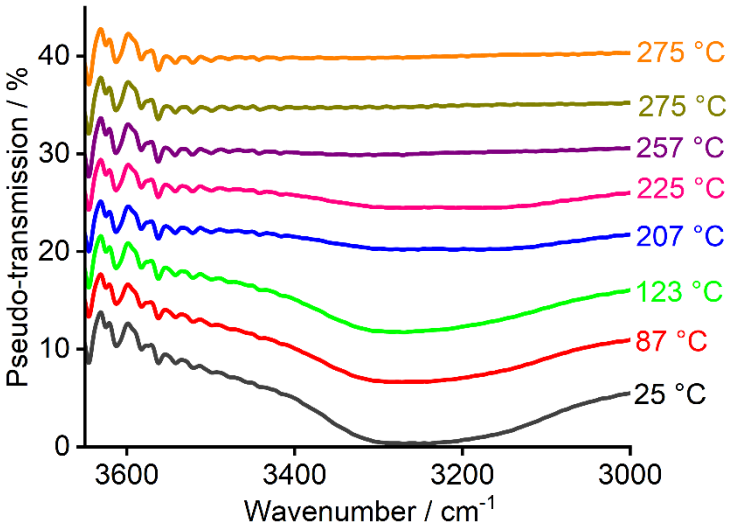

Figure 6.14: In situ O_2 pretreatment DRIFTS on Cu/α-Al_2O_3, backgrounded against KBr using the new DRIFTS cell. The second 275 °C shown is after 20 min of being held at 275 °C. Spectra have been offset for clarity.

In situ DRIFTS under ethylene epoxidation conditions was undertaken on Cu/α-Al_2O_3 as with Au/α-Al_2O_3 using the new DRIFTS cell however a large broad band between 880 and 1400 cm^{-1} was found to obscure bands making band assignment difficult, this result is shown in **Appendix 5**.

6.2.3 Understanding the Structure of Cu

Due to the large arguments into which structure/oxide of Cu is active for ethylene epoxidation and for acetaldehyde, it was thought to be useful to investigate the structure of Cu. H_2-TPR was undertaken on the Cu/α-Al_2O_3 (*Figure 6.15*), as shown in the figure, there are 2 overlapping but visible peaks, one is at 235 °C whilst the other is at 270 °C, which likely corresponds to Cu^{2+} to Cu^{+} and Cu^{+} to Cu^{0} respectively.[16] This therefore indicates the catalyst is in a +2 oxidation state. The total hydrogen consumption was found to be 0.64 ± 0.03 H_2 molecules per copper atom.

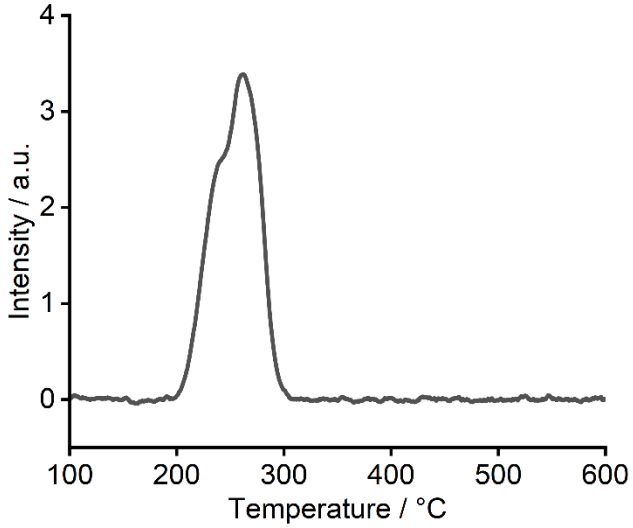

Figure 6.15: H_2-TPR profile of Cu/α-Al_2O_3 after O_2 pretreatment (ramp rate 5 °C min^{-1}).

The O_2-TPD (*Figure 6.16*) of Cu/α-Al_2O_3 shows a peak at 348 °C, which is likely to correspond to surface-bound atomic oxygen species.[17–19]

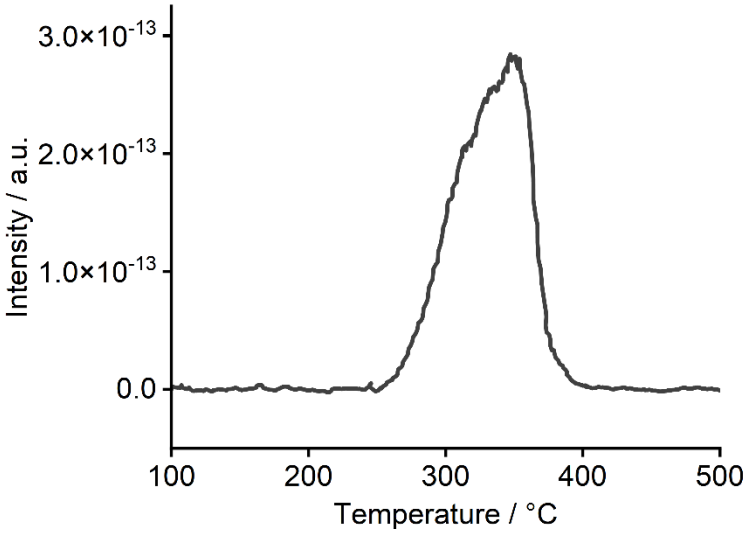

Figure 6.16: O_2-TPD profile of Cu/α-Al_2O_3 after O_2 pretreatment (ramp rate 5 °C min^{-1}).

Ex situ XANES was undertaken of Cu/α-Al_2O_3 before and after ethylene epoxidation to give more indication into the speciation of Cu throughout the reaction. As shown in *Figure 6.17,* the Cu oxidation state does not change before and after the reaction, and it appears to be Cu^{2+}, agreeing with the H_2-TPR data.

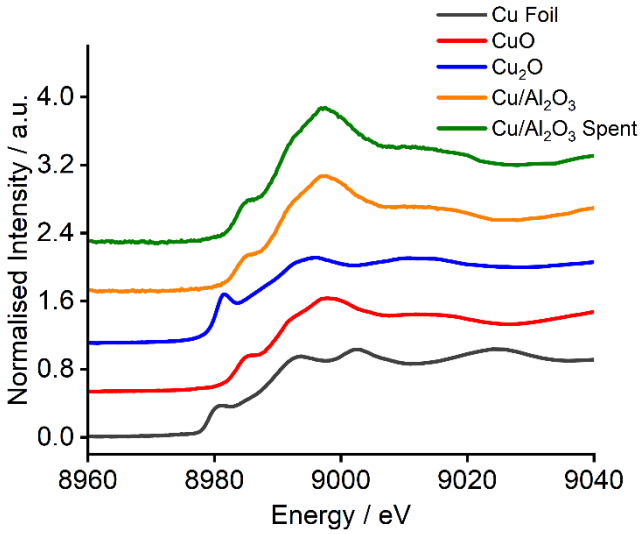

Figure 6.17: XAFS at the Cu K edge of Cu/α-Al_2O_3 before and after ethylene epoxidation alongside references of CuO, Cu_2O and Cu foil. Spectra have been offset for clarity.

6.3 Investigating Cu-Au/α-Al_2O_3 as a Catalyst for Ethylene Epoxidation

Next, the catalyst Cu-Au/α-Al_2O_3 was investigated. No experimental information regarding the Cu-Au/α-Al_2O_3 catalyst was found with only one DFT study identified trying to understand Cu and Au together.[20]

Therefore, it was thought that the use of *in situ* and *ex situ* spectroscopic, characterisation techniques and reaction data would be able to give more insight into the Cu-Au/α-Al_2O_3 catalyst system applied to EO synthesis.

Whilst no catalysts of Cu-Au/α-Al_2O_3 have been synthesised for ethylene epoxidation, they have for propylene epoxidation. Therefore a Cu-Au catalyst was synthesised by the method adapted from Xuan.[2] They used 2 wt. % of every metal, therefore this was used for the synthesis on α-Al_2O_3. It should be noted that due to their different atomic weights, this represents a ~3:1 atomic loading Cu:Au. To confirm that the elemental composition of the catalyst was as expected, ICP-OES was conducted, as shown in *Table 6.6*. As shown, the copper and gold contents of the catalyst were close to the expected value, with small fluctuations in value and low errors.

Table 6.6: Summary of ICP-OES results. The results reported are the average results of the duplicate samples where errors are one standard deviation calculated based on the duplicate samples for each material. Standards are run in the same batch to confirm no significant anomalies or deviations in the instrumental analysis of the samples.

Catalyst	Metal	Expected Metal Content / wt. %	Metal Content by ICP-OES / wt. %	Error in Metal Content by ICP-OES / wt. %
Cu-Au/α-Al_2O_3	Cu	2	1.8	± 0.1
	Au	2	1.8	± 0.2

Cu-Au/α-Al_2O_3 was evaluated for ethylene epoxidation, with the EO selectivity in *Figure 6.18*. As shown with the comparison to Ag/α-Al_2O_3 (from Chapter 4), there is an increase in EO selectivity with Cu-Au/α-Al_2O_3 with a decrease in acetaldehyde, CO2, and H_2O. There is an increase in EO selectivity compared to Au/α-Al_2O_3 (51% versus 59%) indicating that the Cu causes a slight increase in the EO selectivity.

Xuan found that using 2% Cu and 2% Au on a ZnO support gave a larger PO selectivity compared to 2% Cu/ZnO and 2% Au/ZnO individually, therefore showing a similar trend, albeit for a different reaction.[2]

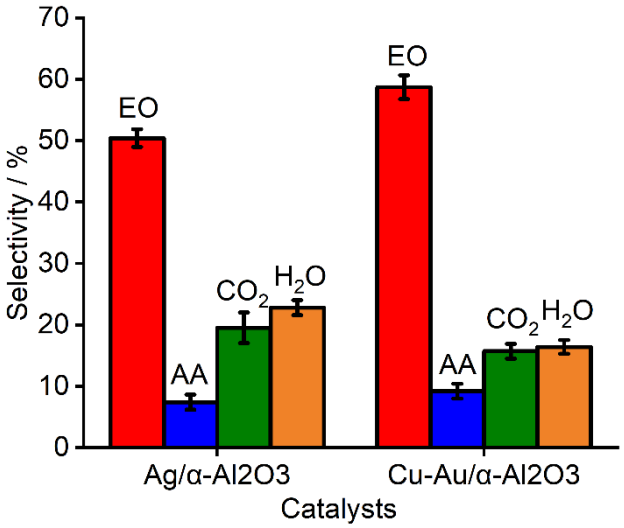

Figure 6.18: A comparison of selectivity between Ag/α-Al_2O_3 (from Chapter 4) and Cu-Au/α-Al_2O_3. The errors shown are based on 3 repeat measurements.

As shown in *Table 6.7*, there is an increase in EO selectivity between Au/α-Al_2O_3 and Cu-Au/α-Al_2O_3, and a slight decrease in AA, CO_2 and H_2O selectivity with the addition of Cu. Therefore, this needs to be investigated further.

Table 6.7: A table showing the comparison of selectivity between Au/α-Al_2O_3 and Cu-Au/α-Al_2O_3

Selectivity	Au/α-Al_2O_3	Cu-Au/α-Al_2O_3
EO / %	50.7	58.7
AA / %	13.1	9.2
CO_2 / %	19.2	15.7
H_2O / %	20.0	16.4

Ethylene conversion was calculated and displayed in *Table 6.8*. There is a slight decrease in the conversion between Ag/α-Al_2O_3 and Cu-Au/α-Al_2O_3. Compared to Cu/α-Al_2O_3 and Au/α-Al_2O_3 there is an increase in ethylene conversion, which could be due to the increase in metal wt. % or having more disperse Au on the surface of the catalyst.

Table 6.8: A table showing the ethylene conversion and percentage error based on 3 repeat measurements for both Ag/α-Al_2O_3, Cu/α-Al_2O_3, Au/α-Al_2O_3 and Cu-Au/α-Al_2O_3.

Catalyst	Ethylene Conversion / %	% Error
Ag/α-Al_2O_3 (from Chapter 4)	7.7	0.4
Cu/α-Al_2O_3	3.1	0.7
Au/α-Al_2O_3	5.4	0.2
Cu-Au/α-Al_2O_3	6.1	0.3

Therefore, this catalyst was characterised and analysed to give more information into why this catalyst is more selective towards EO compared to Ag/α-Al_2O_3 (from Chapter 4) and why it has changed selectivity compared to Au/α-Al_2O_3.

6.3.1 Particle Sizes and Morphology

XRD analysis was conducted to be able to confirm the crystallinity of the material and give an insight into the Cu and Au structure. *Figure 6.19* shows the pXRD pattern of Cu-Au/α-Al_2O_3 before and after ethylene epoxidation. When comparing to α-Al_2O_3 there are new reflections corresponding to Au, however, as discussed earlier the Cu reflections are likely to be either hidden by the α-Al_2O_3 or are too broad to be able to be identified. The metallic gold reflections are at 38.1 ° (1 1 1), 44.3 ° (2 0 0), 64.5 ° (2 2 0) and 77.7 (3 1 1), the latter two being distinctively visible when compared to the α-Al_2O_3 only pattern.[3] It is therefore expected that metallic Au is on the surface of the α-Al_2O_3, and is not substantially alloyed to the copper, which would change the 2θ value.

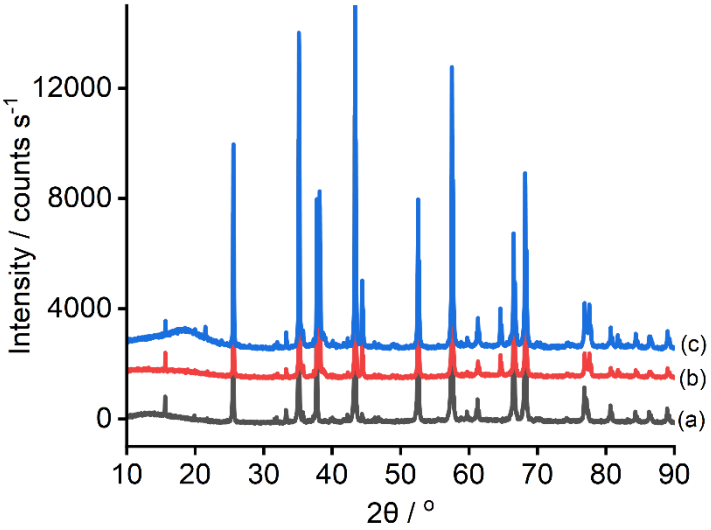

Figure 6.19: pXRD pattern for where (a) α-Al_2O_3, (b) Cu-Au/α-Al_2O_3 before ethylene epoxidation and (c) Cu-Au/α-Al_2O_3 after ethylene epoxidation. Patterns have been offset for clarity.

The reflection at 64.5 ° corresponding to the 2 2 0 plane is used to estimate the size of the Au crystallite with the Scherrer equation, this expansion is shown in *Figure 6.20*.

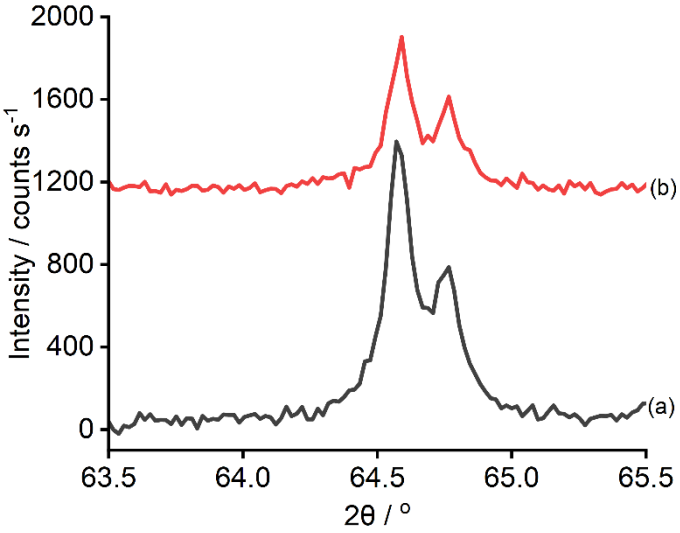

Figure 6.20: pXRD pattern for zoomed-in between 63.5 and 65.5 ° where (a) Cu-Au/α-Al_2O_3 before ethylene epoxidation and (b) Cu-Au/α-Al_2O_3 after ethylene epoxidation. Patterns offset for clarity.

The FWHM used for each catalyst with the resultant Au crystallite sizes are shown in *Table 6.9*. There is a large increase in the average crystallite sizes when compared to Ag, indicating that the Au in Au-Cu is less dispersed on the α-Al_2O_3. There appears to be a decrease in average Au crystallite size with the addition of Cu indicating there is more dispersion of Au reducing the available support for the isomerisation of EE to AA. There is a small increase in average crystallite size after EE, again indicating sintering occurring after ethylene epoxidation. This agrees with the reaction data, where under ethylene

epoxidation conditions for 2 h the EO selectivity is at 58.7% and after 10 h it decreases slightly to 54.2%.

Table 6.9: Summary of FWHM and the particle size estimation from pXRD data using the Scherrer equation. Errors were calculated based on the error from fitting the Gaussian functions.

Catalyst	Reflection(s) used / °	FWHM / °	Estimated Crystallite Size / nm	Error in Gaussian fit of Crystallite Size / nm
Ag/α-Al_2O_3 (from Chapter 4)	64.5	0.36	51.2	± 1.4
Au/α-Al_2O_3 before EE	64.5	0.26	70.9	± 3.7
Au/α-Al_2O_3 after EE	64.5	0.21	87.8	± 5.6
Cu-Au/α-Al_2O_3 before EE	64.5	0.28	65.9	± 2.4
Cu-Au/α-Al_2O_3 after EE	64.5	0.25	73.8	± 3.2

TEM was undertaken (shown in *Figure 6.21*), to further investigate the distribution of Au and Cu on the Al_2O_3 to see if this could be a reason why the Cu-Au/α-Al_2O_3 is more selective to EO than Ag/α-Al_2O_3. Whilst it is difficult to identify, there does appear to be larger particles covering more of the Al_2O_3.

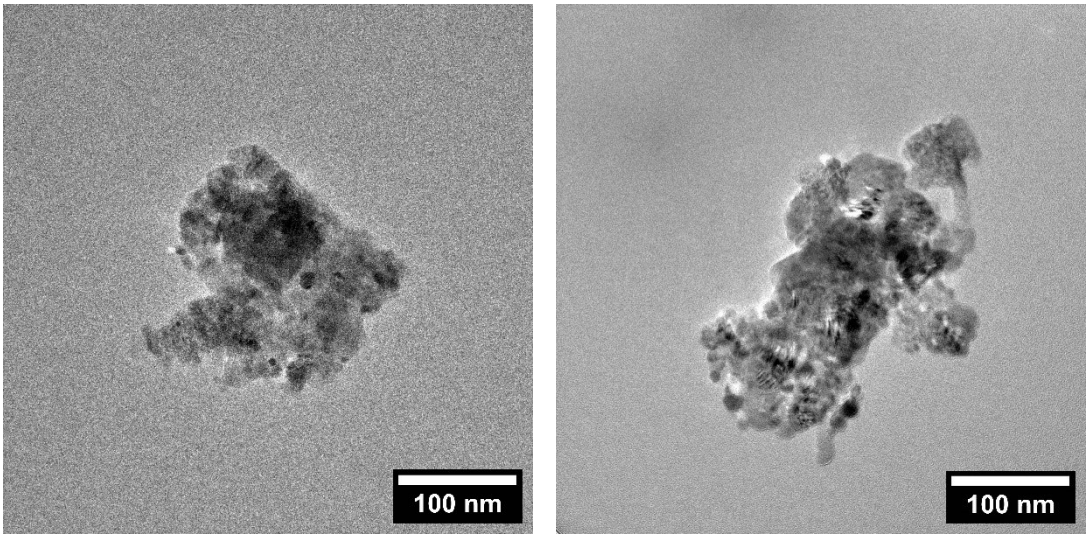

Figure 6.21: Representative TEM of Ag/α-Al_2O_3 (from Chapter 4) on the left-hand side and Cu-Au/α-Al_2O_3 on the right-hand side.

6.3.2 Investigating Hydroxyl Groups and Acidity

The hydroxyl groups were investigated with the use of DRIFTS. As shown in *Figure 6.22*, there is a clear decrease in O-H stretching in the hydroxyl groups. Ag/α-Al_2O_3 shows a band

at 3300 cm^{-1} corresponding to non-H bonding hydroxyls whilst the broad band on Cu-Au/α-Al_2O_3 corresponds to H bonding hydroxyls, which are less acidic.[7] There is also a decrease in the number of hydroxyl groups compared to Au/α-Al_2O_3; this could be due to the smaller average Au crystallites leading to a more dispersed Au surface and therefore fewer hydroxyl groups.

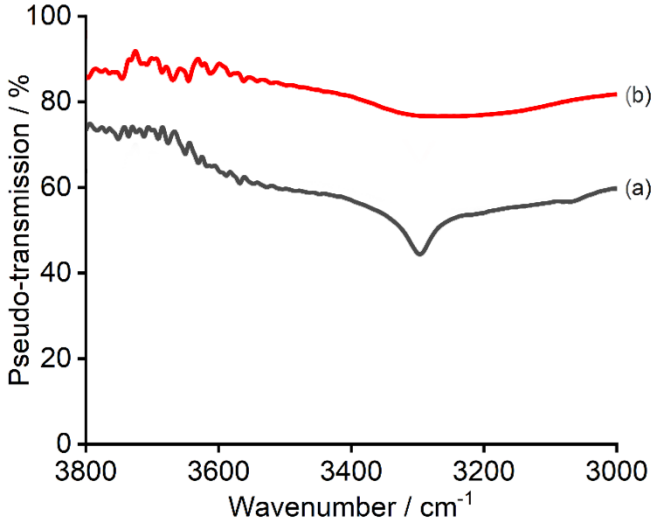

Figure 6.22: DRIFTS spectra of (a) Ag/α-Al_2O_3 (from Chapter 4) and (c) Cu-Au/α-Al_2O_3 showing the region of interest, backgrounded against KBr. Spectra have been offset for clarity.

In situ DRIFTS was undertaken during the O_2 pretreatment (shown in *Figure 6.23*) as expected from the *ex situ* DRIFTS, there is a decrease in the hydroxyl groups compared to Au/α-Al_2O_3. However, this does match the data from Au/α-Al_2O_3 and Cu/α-Al_2O_3 where there is a decrease in hydroxyl groups as the temperature of the pretreatment is increased.

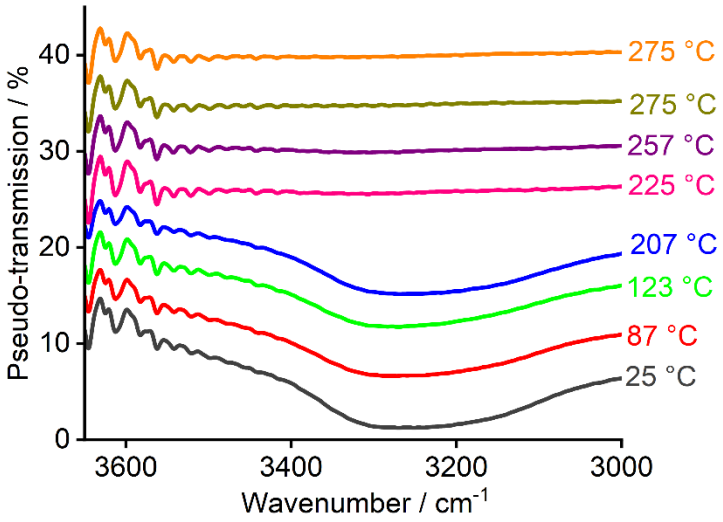

Figure 6.23: In situ O_2 pretreatment DRIFTS on Cu-Au/α-Al_2O_3 backgrounded against KBr using the new DRIFTS cell. The second 275 °C shown is after 20 min of being held at 275 °C. Spectra have been offset for clarity.

In situ DRIFTS under ethylene epoxidation conditions was undertaken on Cu-Au/α-Al_2O_3 as with Au/α-Al_2O_3 and Cu/α-Al_2O_3 using the new DRIFTS cell however a large broad band between 880 and 1400 cm^{-1} was found to obscure bands making band assignment difficult, this result is shown in **Appendix 5**.

6.3.3 Understanding the Structure of Cu and Au Together

H_2-TPR was undertaken on the Cu-Au/α-Al_2O_3 (*Figure 6.24*), as shown in the figure, there are two overlapping peaks corresponding to Cu^{2+} to Cu^{+} and Cu^{+} to Cu^{0} respectively.[16] This indicates the Cu species is in the Cu^{2+} state. As discussed earlier, the Au is metallic gold, therefore there are no peaks corresponding to Au. When compared to Cu/α-Al_2O_3 (shown in *Figure 6.17*), the total hydrogen consumption remained the same, where Cu-Au/α-Al_2O_3 was found to correspond to 0.65 ± 0.03 H_2 molecules per copper atom. When looking at Cu/α-Al_2O_3 the peak corresponding to Cu^{2+} to Cu^{+} is larger compared to Cu^{+} to Cu^{0}, however on the Cu-Au/α-Al_2O_3 catalyst this has reversed. More work needs to be undertaken to investigate this however it could be due to an alloy of Cu-Au however there was no shift in pXRD or due to the Cu-Au interaction versus isolated Cu particles.

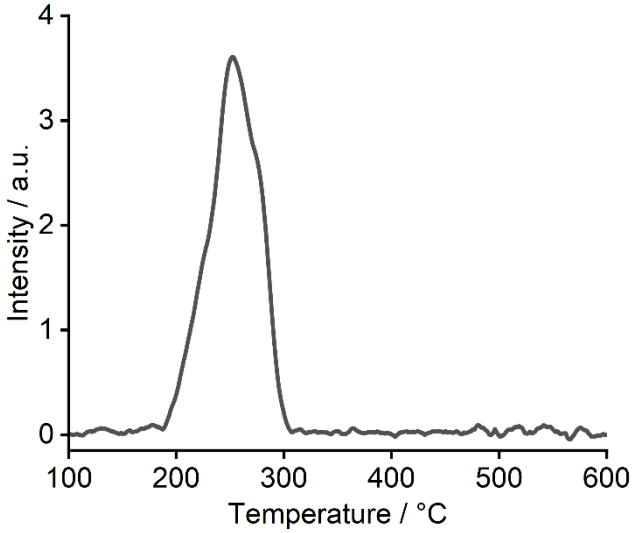

Figure 6.24: H_2-TPR profile of Cu-Au/α-Al_2O_3 after O_2 pretreatment (ramp rate 5 °C min^{-1}).

The O_2-TPD (*Figure 6.25*) of Cu-Au/α-Al_2O_3 was found to contain one peak at 350 °C, which is likely to correspond to surface-bound atomic adsorption oxygen species.[17–19] When comparing to the O_2-TPD of Cu/α-Al_2O_3 there is an increase in intensity but a decrease in width of the peak. It could be that compared to Cu/α-Al_2O_3 only, there are smaller copper particles sizes, meaning that it is more difficult to desorb the oxygen species.

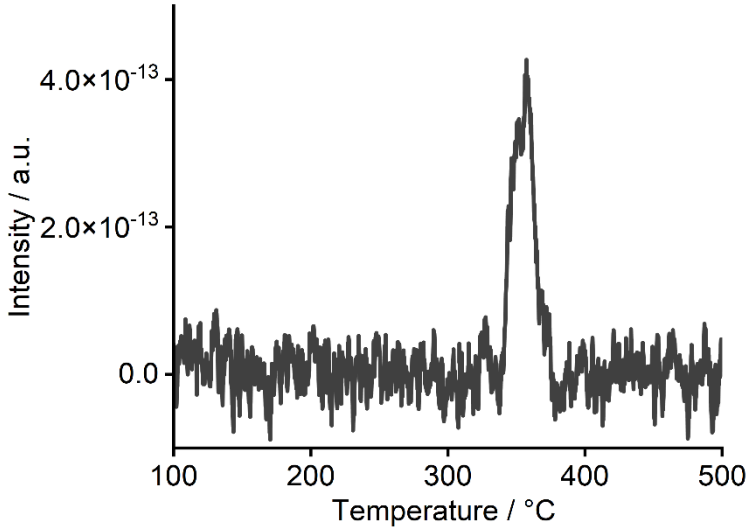

Figure 6.25: O_2-TPD profile of Cu-Au/α-Al_2O_3 after O_2 pretreatment (ramp rate 5 °C min^{-1}).

Ex situ XANES was undertaken of Cu-Au/α-Al_2O_3 before and after ethylene epoxidation to give more indication into the structure and oxidation state of Cu and Au throughout the reaction. As shown in *Figure 6.26* (Cu XANES) both fresh Cu-Au/Al_2O_3 and spent Cu-Au/Al_2O_3 correspond to CuO (Cu^{2+}), which also correlates to the H_2-TPR. As these samples are handled in air there is a possibility that exposure always leads to CuO. *Ex situ* XANES was undertaken of Cu-Au/α-Al_2O_3 before and after ethylene epoxidation to give more indication into the structure of Au throughout the reaction. As shown in *Figure 6.27,* the fresh Au/Al_2O_3 matches the Au foil and therefore shows metallic Au. A reference for $Au(OH)_3$, was found on BENTEN, the database for SPring-8.[11] The catalysts have not been oxidised as no similarities to $Au(OH)_3$ are shown. This indicates that the spent Au/α-Al_2O_3 catalyst is also metallic Au. These results from the XANES of Cu-Au/α-Al_2O_3 show similar data to the separate monometallic Cu/α-Al_2O_3 and Au/α-Al_2O_3 catalysts.

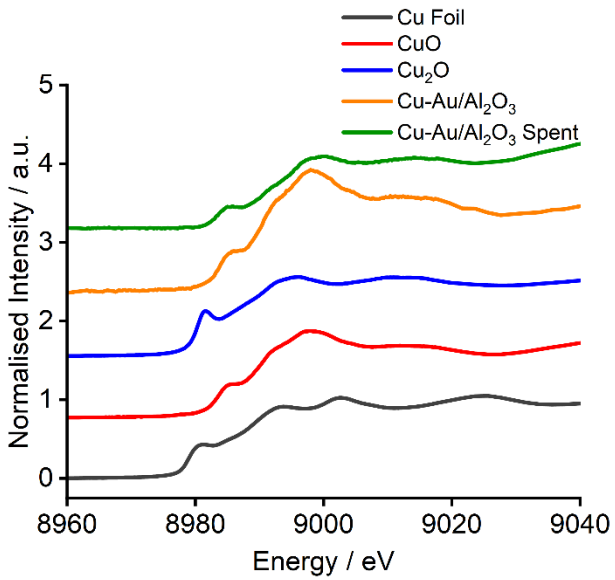

Figure 6.26: XANES at the Cu K edge of Cu-Au/α-Al_2O_3 before and after ethylene epoxidation, with references of Cu foil, CuO and Cu_2O. Spectra have been offset for clarity.

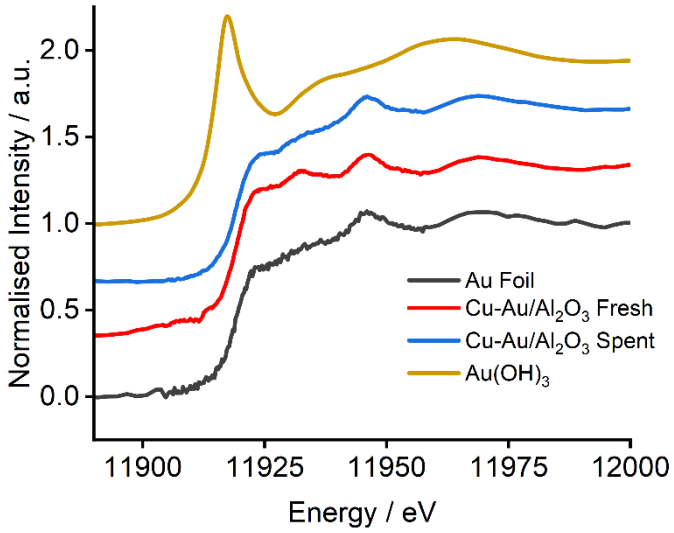

Figure 6.27: XANES at the Au L3 edge of Cu-Au/α-Al_2O_3 before and after ethylene epoxidation with references of Au foil and $Au(OH)_3$. Spectra have been offset for clarity.

As stated in **Chapter 6.3**, there is currently no experimental literature looking at Cu-Au catalysts for the use of ethylene epoxidation, however this experimental data is able to be compared to other catalysts. The efficacy of this catalyst compared to the others is likely to be a mixture of reason. When comparing this catalyst to Ag/α-Al_2O_3 there is a reduction in hydroxyl groups, likely making it more selective towards EO. However, when comparing this catalyst to Au/α-Al_2O_3 and Cu-Ag/α-Al_2O_3 there is a decrease in the average Au crystallite size indicating there is more of a dispersion of Au. When comparing this catalyst to Cu/α-Al_2O_3 it has been suggested through O_2-TPD that there are potentially more smaller copper particles on the Cu-Au/α-Al_2O_3 catalyst. It has been suggested in the literature that

copper can improve the interaction between gold and alumina, therefore allowing a stronger interaction which helps in stabilising the smaller gold and preventing them from agglomerating into less active particles.[21] Therefore, there are multiple reasons as to why the Cu-Au/α-Al_2O_3 catalyst is so selective towards ethylene epoxidation.

6.4 Investigating Cu-Ag/α-Al_2O_3 as a Catalyst for Ethylene Epoxidation

The last catalyst that was investigated was Cu-Ag/α-Al_2O_3. Compared to some of the other catalysts there are a large number of suggestions on the role and structure of Cu-Ag/α-Al_2O_3 used for ethylene epoxidation. Whilst one paper was found to show experimental data, all other papers used DFT calculations, therefore it was thought to be useful to obtain experimental data to find out more information regarding this catalyst.[22–28] Some suggestion include, Cu oxidising under reaction conditions and forming a thin Cu oxide later on top of the Ag particles which causes O_{sub} to migrate to the catalyst surface, where O_{sub} was found to weaken the bond strength of surface oxygen, therefore facilitating the binding of the C=C bond to O_{suf} to form EO.[24,25] Another suggestion is that there is a coexistence of thin CuO and AgO-CuO films on the Ag substrate, where the active oxygen species rather than the oxygen atoms chemisorbed on a metal surface are oxygen atoms which are part of an oxide layer.[28] A third suggestion is that the relative bond strength between the C-O and the O-metal bonds in the oxametallacycle (OMC) intermediate affects the selectivity to EO, where there is a volcano like relationship as a function of surface Cu content.[29] A final suggestion is that a formation of an alloy between the copper and the silver provides a selective pathway.[23]

To correspond to all the other catalysts prepared in this section, this catalyst was also prepared using 2 wt. % of Cu and 2 wt. % of Ag. To confirm that the elemental composition of the catalyst was as expected, ICP-OES was conducted. The elemental composition of the catalyst is shown in *Table 6.10*. As shown, the copper and silver contents of the catalyst were close to the expected value, with small fluctuations in value and low errors.

Table 6.10: Summary of ICP-OES results. The results reported are the average results of the duplicate samples where errors are one standard deviation calculated based on the duplicate samples for each material. Standards are run in the same batch to confirm no significant anomalies or deviations in the instrumental analysis of the samples.

Catalyst	Metal	Expected Metal Content / wt. %	Metal Content by ICP-OES / wt. %	Error in Metal Content by ICP-OES / wt. %
Cu-Ag/α-Al_2O_3	Cu	2	1.9	± 0.2
	Ag	2	1.9	± 0.1

Cu-Ag/α-Al_2O_3 was evaluated for ethylene epoxidation, with the EO selectivity in *Figure 6.28*. As shown with the comparison to Ag/α-Al_2O_3 (from Chapter 4), there is an increase in EO and AA selectivity with Cu-Ag/α-Al_2O_3.

The Cu-Ag/ZnO catalyst made by Xuan (with the same synthesis as the Cu-Ag/α-Al_2O_3 catalyst) shows a PO selectivity of 32.1%, it is well known that the difficulty in the direct epoxidation of propylene, meaning that ethylene is easier to undertake selective epoxidation compared to propylene indicating the increase here.[30,31] Barteau *et al.* also investigated the use of bimetallic Cu-Ag/Al_2O_3 for ethylene epoxidation, here they used different wt. % but they found that with Cu-Ag/Al_2O_3 the EO selectivity was increased compared to Ag/Al_2O_3.[27]

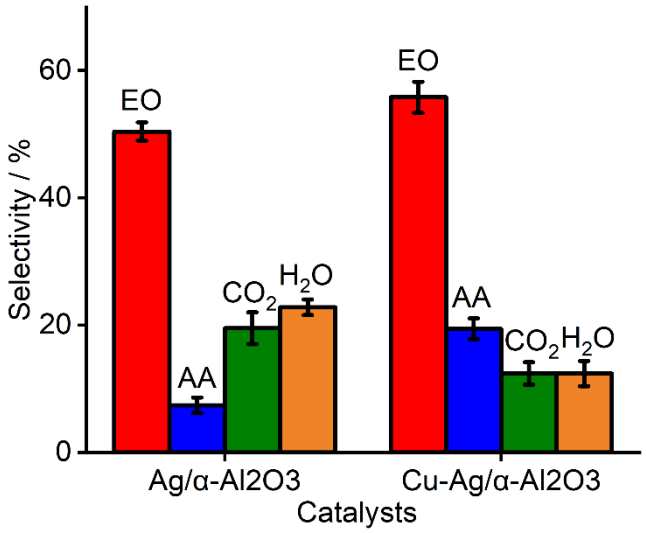

Figure 6.28: A comparison of EO selectivity between Ag/α-Al_2O_3 (from Chapter 4) and Cu-Ag/α-Al_2O_3. Errors shown are based on 3 repeat measurements

Ethylene conversion was calculated and displayed in *Table 6.11*. There is a slight decrease in the conversion between Ag/α-Al_2O_3, Cu-Au/α-Al_2O_3 and Cu-Ag/α-Al_2O_3 and an increase when comparing to Cu/α-Al_2O_3 and Au/α-Al_2O_3.

Table 6.11: A table showing the ethylene conversion and percentage error based on 3 repeat measurements for Ag/α-Al_2O_3 (from Chapter 4), Cu/α-Al_2O_3, Au/α-Al_2O_3 and Cu-Ag/α-Al_2O_3.

Catalyst	Ethylene Conversion / %	% Error
Ag/α-Al_2O_3 (from Chapter 4)	7.7	0.4
Cu/α-Al_2O_3	3.1	0.7
Au/α-Al_2O_3	5.4	0.2
Cu-Au/α-Al_2O_3	6.1	0.3
Cu-Ag/α-Al_2O_3	5.9	0.2

Therefore, this catalyst was characterised and analysed to give more information into why this catalyst is selective towards EO.

6.4.1 Particle Sizes and Morphology

XRD analysis was conducted to be able to both estimate the particle sizes of Ag and to confirm the crystallinity of the material. When looking at *Figure 6.29* the Cu reflections are unable to be identified, however the Ag reflections are. Many of the reflections from metallic silver are hidden by the α-Al_2O_3 as they overlap. The metallic Ag^0 reflections should be at 38.1 ° (1 1 1), 44.3 ° (2 0 0), 64.4 ° (2 2 0), 77.4 ° (3 1 1) and 81.5 ° (2 2 2).[32] Therefore, as expected, there is some overlap between the Ag and the α-Al_2O_3 reflections, however, pXRD can confirm that the Cu-Ag/α-Al_2O_3 catalyst contains additional reflections consistent with the presence of metallic Ag^0. Both Cu-Ag/α-Al_2O_3 and Ag/α-Al_2O_3 (from Chapter 4) show very little difference in terms of pXRD comparison. *Figure 6.32* was expanded at the Ag (2 2 0) reflection to investigate the reflection broadenings as there is no overlap of α-Al_2O_3 (shown in *Figure 6.30*).

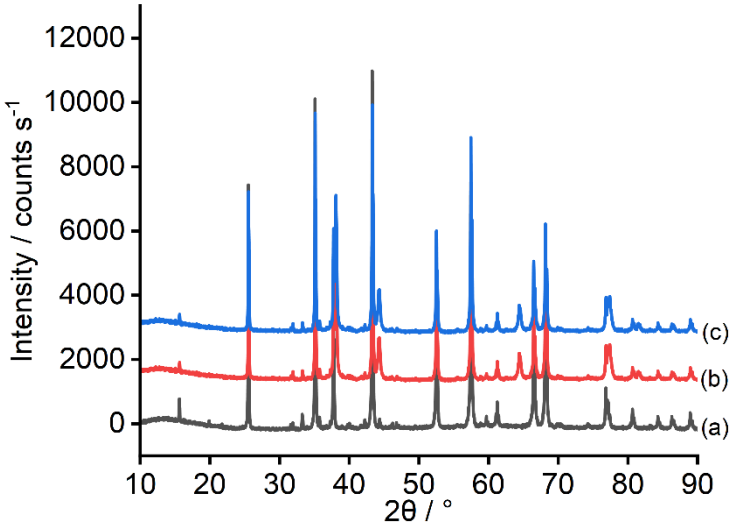

Figure 6.29: pXRD pattern for (a) α-Al_2O_3, (b) Ag/α-Al_2O_3 (from Chapter 4) and (c) Cu-Ag/α-Al_2O_3. Patterns offset for clarity.

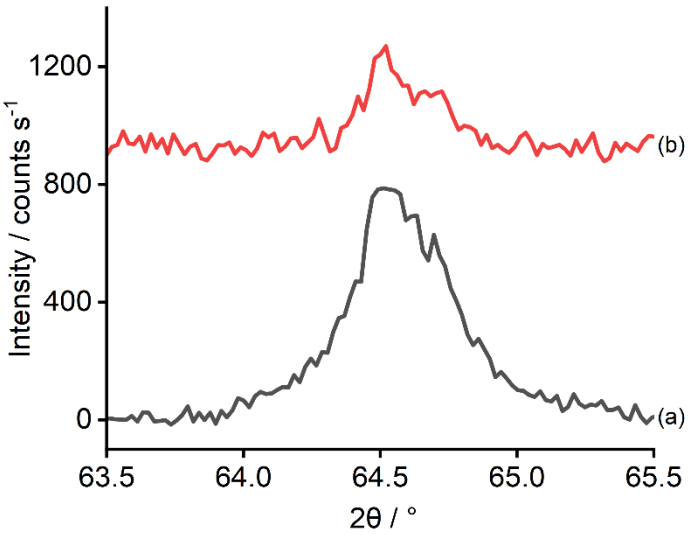

Figure 6.30: pXRD pattern for (a) is Ag/α-Al_2O_3 (from Chapter 4) and (b) is Cu-Ag/α-Al_2O_3. Patterns offset for clarity.

The size of the silver crystallite was investigated using the reflection at 64.5 ° with the Scherrer equation. The FWHM used for each catalyst and the resultant crystallite sizes are shown in *Table 6.12*. As discussed in **Chapter 1.1.2,** there have been many arguments into the sizes of the Ag crystallite.[33–37] There is a large increase in average Ag crystallite sizes from 45 nm to 74 nm indicating that Cu causes a large increase in the average Ag crystallite size. The EO selectivity data where at 2 h the selectivity is at 55.8%, however, there is a decrease to 50.8% after 10 h.

Table 6.12: Summary of FWHM and particle size estimation from pXRD data using the Scherrer equation. Errors were calculated based on the error from fitting the Gaussian functions.

Catalyst	Reflection(s) used / °	FWHM / °	Estimated Crystallite Size / nm	Error in Gaussian fit of Crystallite Size / nm
Ag/α-Al_2O_3 (from Chapter 4)	64.5	0.36	51.2	± 1.4
Cu-Ag/α-Al_2O_3	64.5	0.25	73.8	± 3.2

TEM was undertaken (shown in *Figure 6.31*), to investigate the distribution of Ag and Cu on the Al_2O_3 to see if this could be a reason as to why the Cu-Ag/α-Al_2O_3 is more selective to EO. Darker roughly spherical metal particles of copper and silver are visible on the lighter alumina support, however, there is difficulty distinguishing between the two with TEM. However, there are much larger darker particles on the light alumina support for Cu-Ag/α-Al_2O_3 compared to Ag/α-Al_2O_3.

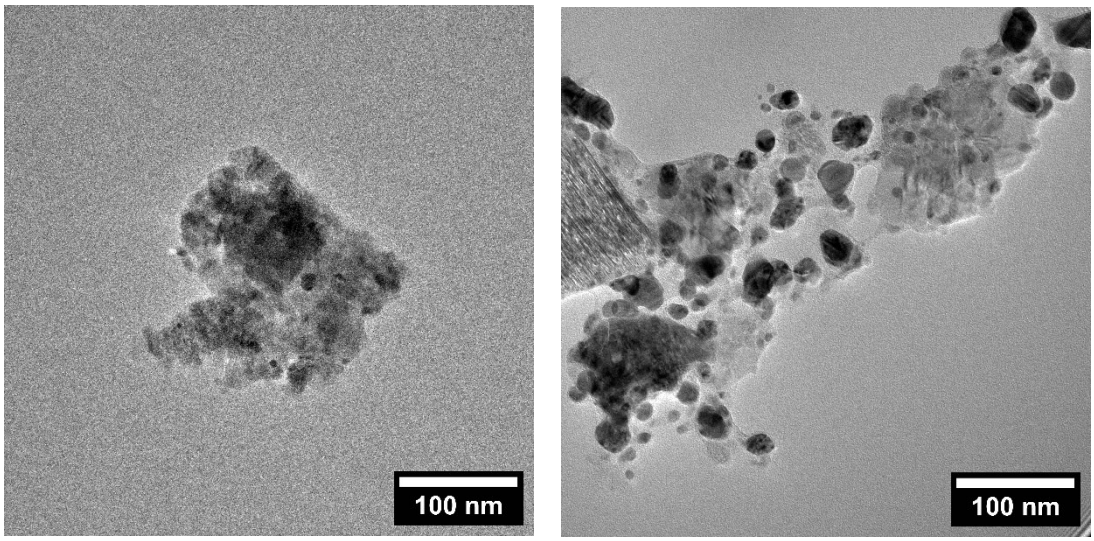

Figure 6.31: Representative TEM of Ag/α-Al_2O_3 (from Chapter 4) on the left-hand side and Cu-Ag/α-Al_2O_3 on the right-hand side.

6.4.2 Investigating Hydroxyl Groups and Acidity

The hydroxyl groups were investigated with the use of DRIFTS. As shown in *Figure 6.32*, there is very little difference between Cu/α-Al_2O_3, Au/α-Al_2O_3 and Cu-Ag/α-Al_2O_3 agreeing with the proposed idea that the higher pretreatment temperature of 450 °C used for these catalysts compared to 225 °C used for Ag/α-Al_2O_3 is likely to cause this substantial effect on the decrease in hydroxyl groups and acidity.

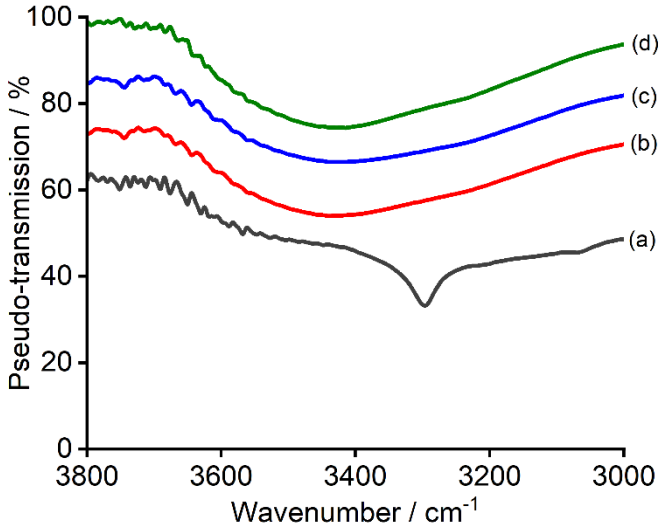

Figure 6.32: DRIFTS spectra of (a) Ag/α-Al_2O_3, (b) Cu-Au/α-Al_2O_3, (c) Au/α-Al_2O_3 and (d) Cu/α-Al_2O_3 showing the region of interest, backgrounded against KBr. Spectra have been offset for clarity.

In situ DRIFTS was undertaken by looking at the O_2 pretreatment as shown in *Figure 6.33* when comparing the Cu-Ag/α-Al_2O_3 to the other catalysts in this chapter, as expected from the *ex situ* DRIFTS, this matches the data from Au/α-Al_2O_3 and Cu/α-Al_2O_3 where there is a decrease in hydroxyl groups as the temperature of the pretreatment is increased.

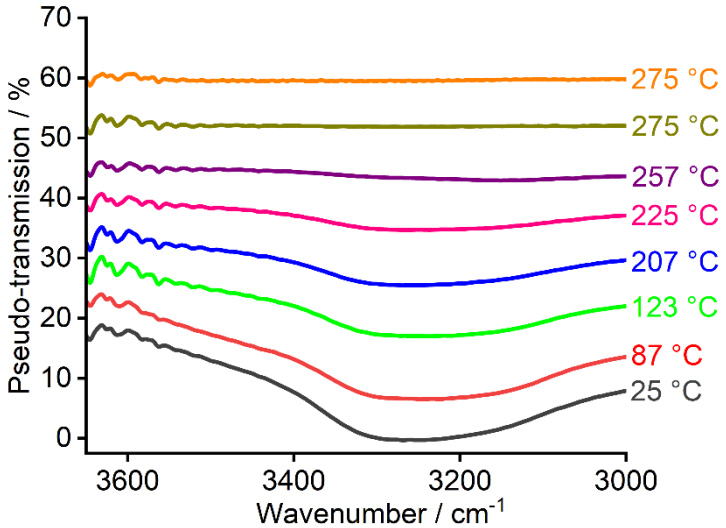

Figure 6.33: In situ O_2 pretreatment DRIFTS on (a) Ag/α-Al_2O_3 (from Chapter 4) and (b) Cu-Ag/α-Al_2O_3 backgrounded against KBr using the new DRIFTS cell. The second 275 °C shown is after 20 min of being held at 275 °C. Spectra have been offset for clarity.

In situ DRIFTS under ethylene epoxidation conditions was undertaken on Cu-Ag/α-Al_2O_3 as with Au/α-Al_2O_3, Cu/α-Al_2O_3 and Cu-Au/α-Al_2O_3 using the new DRIFTS cell however a large broad band between 880 and 1400 cm^{-1} was found to obscure bands making band assignment difficult, this result is shown in **Appendix 5**.

6.4.3 Understanding the Structure of Cu and Ag Together

As discussed above, very little experimental work has been undertaken on the Cu and Ag catalyst therefore it was thought to be useful to investigate the structure of the Cu and the Ag on the α-Al_2O_3. H_2-TPR was undertaken on the Cu-Ag/α-Al_2O_3 (Figure 6.34), as explained in **Chapter 4**, there is a large amount of difficulty in peak deconvolution on silver species, due to the multiple overlapping Ag-O interactions, therefore, there was difficulty in assigning peaks. At 270 °C a peak was observed which likely represents a mixture of copper cations being reduced to copper metal which corroborates with TPR of Cu/α-Al_2O_3, where the total hydrogen consumption was found to be 0.35 ± 0.04 H_2 molecules per copper atom, which has decreased compared to Cu/α-Al_2O_3 and Cu-Au/α-Al_2O_3, which could be due to a crossover of peaks. The peaks observed after this, are likely to be associated with the silver oxides reductions, where the total hydrogen consumption was found to be 0.79 ± 0.04 H_2 molecules per silver atom, compared to Ag/α-Al_2O_3 after O_2 pretreatment there is no change, indicating there are a similar number of oxygen atoms adsorbed.

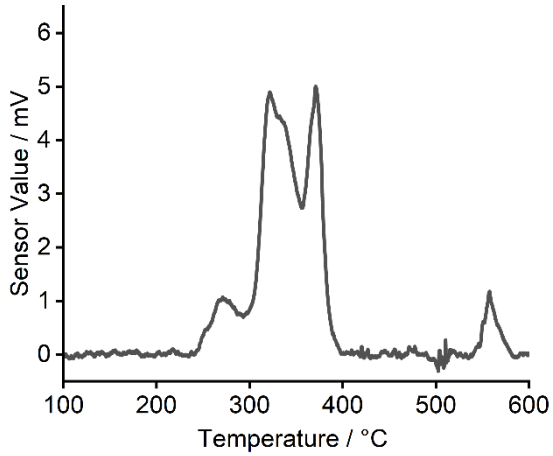

Figure 6.34: Temperature Programmed Reduction of Cu-Ag/α-Al_2O_3 after O_2 pretreatment (ramp rate 5 °C min^{-1}).

O_2-TPD was undertaken as shown in *Figure 6.35*, one peak at 370 °C was found, which is likely to correspond to surface-bound adsorbed atomic oxygen.[19] There is an increase in temperature compared to Ag/α-Al_2O_3 which can be explained by the fact that Cu binds oxygen stronger than the silver. Therefore, the presence of a Cu and Ag surface will bind the oxygen more strongly resulting in shifting of the peak towards a higher temperature.[19]

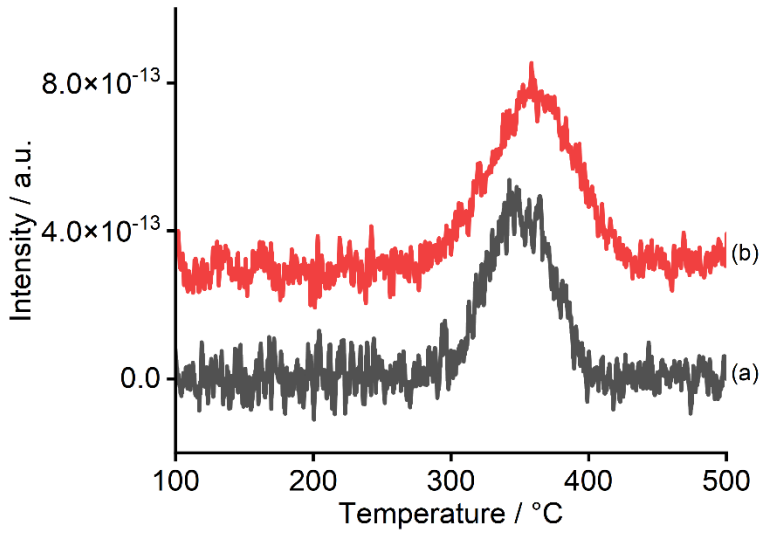

Figure 6.35: O_2-TPD profile of (a) Ag/α-Al_2O_3 and (b) Cu-Ag/α-Al_2O_3 after O_2 pretreatment (ramp rate 5 °C min^{-1}). Spectra have been offset for clarity.

Ex situ XANES was undertaken of Cu-Ag/α-Al_2O_3 before and after ethylene epoxidation to give more indication into the structure of Cu throughout the reaction. Unfortunately, on the EasyXAFS machine, Ag is unable to be investigated, therefore *Figure 6.36* shows the XANES of Cu in this catalyst, before and after ethylene epoxidation. When compared to the literature, this work gives evidence of CuO being the Cu species.

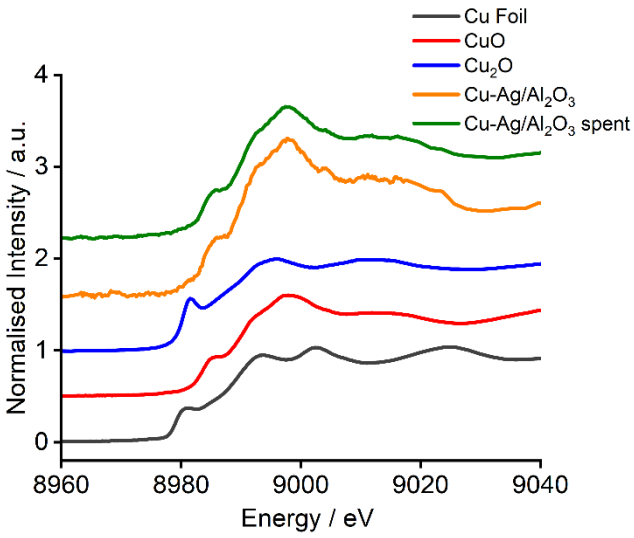

Figure 6.36: XANES at the Cu K edge of Cu-Ag/α-Al_2O_3 before and after ethylene epoxidation alongside references of CuO, Cu_2O and Cu foil. Spectra have been offset for clarity.

6.5 Conclusions

The use of Cu and Au-based catalysts for propylene epoxidation has been widely used however very little experimental data into looking at these metals for the catalysis of ethylene epoxidation has been investigated. It was thought that it would be useful to investigate to give more insight into the use of Cu and Au-based catalysts for ethylene epoxidation. These catalysts have been characterised with both *in situ* and *ex situ* techniques and the activity and selectivity profiles of these catalysts have been determined with comparison to the literature. The role of the Au and Cu both separately and together have been discussed in detail and provide information to improve the understanding of the catalysts used in ethylene epoxidation.

- All combinations of catalysts investigated are relatively active towards ethylene epoxidation.
- Au/α-Al_2O_3 was found to give similar selectivity towards EO when compared to Ag/α-Al_2O_3 (51% and 51% respectively), where the structure shows metallic Au.
- Whilst Cu/α-Al_2O_3 was shown to be moderately selective towards EO (25%), there was an increase in AA, H_2O and CO_2 selectivity compared to Ag/α-Al_2O_3.
- Cu-Au/α-Al_2O_3 showed higher selectivity (59%) towards EO when compared to Au/α-Al_2O_3 (51%) and an increase compared to Cu/α-Al_2O_3 (25%).
- Cu-Ag/α-Al_2O_3 (58%) showed an increased EO selectivity compared to Ag/α-Al_2O_3, however, there was also an increase in AA selectivity.
- The addition of Cu caused a decrease in average Au crystallite size alongside a decrease in hydroxyl groups and an increase in average Ag crystallite size in Cu-Au/α-Al_2O_3 and Cu-Ag/α-Al_2O_3, respectively.
- All catalysts showed an increase in AA selectivity compared to Ag/α-Al_2O_3.
- H_2-TPR and XAS tentatively indicate copper is present in its oxidised form whilst gold is present as a metallic Au.
- The Cu-Ag/α-Al_2O_3 indicates that surface-bound adsorbed atomic oxygen is bound more strongly on the surface of the catalyst compared to Ag/α-Al_2O_3
- The pretreatment of 450 °C is a likely reason for the decrease in hydroxyl groups on these catalysts.

Chen *et al.* used density functional theory stating that the Au nanoparticle catalyst is very selective towards ethylene epoxidation, whilst different types of Au catalysts were not tested in this thesis, the Au/α-Al_2O_3 was found to give similar selectivity towards EO when compared to Ag/α-Al_2O_3.[38,39]

The ethylene oxide selectivity over the Cu/α-Al_2O_3 was found to be 25 %, which is in agreement with the selectivity data collected by Bhattacharya *et al.*[15] Whilst no exact percentage of ethylene oxide selectivity could be identified Lambert *et al.* found that for high selectivity epoxidation both metallic copper sites and adsorbed oxygen sites are required, whereas on Cu/α-Al_2O_3 only CuO was present with adsorbed oxygen sites.[14] The Cu/α-Al_2O_3 catalyst was found to have copper in the +2 oxidation state where there was no change throughout ethylene epoxidation, this contradicts the work by Bhattacharya *et al.* who stated that Cu(I) is an active species in epoxidation and the decrease in selectivity is due to this change from Cu(I) to Cu(II).[15]

Chen *et al.* undertook a computational study where they found that Cu-Au core-shell nanoclusters are more reactive than pure Cu and Au nanoclusters, this agrees with the results where the Cu-Au/α-Al_2O_3 showed higher selectivity (59%) towards EO when compared to Au/α-Al_2O_3 (51%) and an increase compared to Cu/α-Al_2O_3 (25%).[20]

When comparing the Cu-Ag/α-Al_2O_3 catalyst to literature there are some agreements and contradictions to the literature. As stated by Nguyen *et al.* the Ag-Cu catalyst for ethylene epoxidation has been shown to yield higher selectivity towards ethylene oxide compared to pure Ag, this has been confirmed by Cu-Ag/α-Al_2O_3 (58%) showing an increased EO selectivity compared to Ag/α-Al_2O_3 (51%).[24] Stampfl and Piccinin stated that these catalysts contain surface alloys where copper oxide is formed and both Cu(I) and Cu(II) are present at the surface, however in the catalysts characterised in this thesis, no surface alloys were formed with only Cu(II) being present at the surface.[23] Scheffler *et al.* stated that there is a coexistence of thin CuO and AgO-CuO films on the Ag substrate, whilst this was not able to be identified in this thesis, a mixture of CuO and AgO was found to be present on the Cu-Ag/α-Al_2O_3 catalyst.[28] Lastly, Nguyen *et al.* stated that Cu tends to oxidise and form thin Cu oxide layers on top of the Ag particles, causing O_{sub} to migrate to the catalyst surface, whilst again this was difficult to confirm, it does agree with the Cu-Ag/α-Al_2O_3 catalyst containing Cu oxide.[24,25]

6.6 Future Work

Whilst a large amount of new experimental work has been undertaken with investigating Cu and Au-based catalyst for the use ethylene epoxidation, there are still some unanswered questions and next steps that are needed to address these.

1. What oxidation states/structure is the Cu and the Au in these catalysts and how do they interact under ethylene epoxidation conditions? – To investigate this by using more *in situ* spectroscopic techniques, including NAP-XPS, XAFS and Raman.
2. Does the pre-treatment cause this large decrease in hydroxyl groups compared to Ag/α-Al_2O_3? – To investigate this an experiment with looking at the hydroxyl groups after using the same pretreatment on Ag/α-Al_2O_3.
3. When looking at different catalysts for the use of ethylene epoxidation, different weight percentages of metal change the selectivity of ethylene oxide, does this occur with Au and Cu catalysts? – Design and synthesis more catalysts with different weight percentages of Au and/or Cu and undertake ethylene epoxidation to investigate the ethylene oxide selectivity.
4. The comparison of these 2 wt. % catalysts are being compared to a 10 wt. % Ag/α-Al_2O_3 catalysts – Synthesis a 2 wt. % Ag/α-Al_2O_3 catalyst and undertake ethylene epoxidation to compare to the other catalysts.

6.7 References

1 D. M. Minahan, G. B. Hoflund, W. S. Epling and D. W. Schoenfeld, *J. Catal.*, 1997, **168**, 393–399.
2 Z.-Q. Xuan, Cardiff University, 2009.
3 S. Krishnamurthy, A. Esterle, N. C. Sharma and S. V. Sahi, *Nanoscale Res. Lett.*, 2014, **9**, 627.
4 M. Singh, R. Kalaivani, S. Manikandan, N. Sangeetha and A. K. Kumaraguru, *Appl Nanosci.*, 2013, **3**, 145–151.
5 K. Otto, I. Oja Acik, M. Krunks, K. Tõnsuaadu and A. Mere, *J. Therm. Anal. Calorim.*, 2014, **118**, 1065–1072.
6 A. J. F. van Hoof, E. A. R. Hermans, A. P. van Bavel, H. Friedrich and E. J. M. Hensen, *ACS Catal.*, 2019, **9**, 9829–9839.
7 15.3: Spectroscopic Properties of Alcohols, https://chem.libretexts.org/Bookshelves/Organic_Chemistry/Basic_Principles_of_Organic_Chemistry_(Roberts_and_Caserio)/15%3A_Alcohols_and_Ethers/15.03%3A_Spectroscopic_Properties_of_Alcohols, (accessed 22 March 2024).
8 F. T. T. Huque and J. A. Platts, *Org. Biomol. Chem.*, 2003, **1**, 1419–1424.
9 R. Meyer, C. Lemire, Sh. K. Shaikhutdinov and H.-J. Freund, *Gold Bull.*, 2004, **37**, 72–124.
10 J. Kim, E. Samano and B. E. Koel, *Surf. Sci.*, 2006, **600**, 4622–4632.
11 BENTEN, https://benten.spring8.or.jp/login/?next=/, (accessed 22 March 2024).
12 M. T. Greiner, T. E. Jones, A. Klyushin, A. Knop-Gericke and R. Schlögl, *J. Am. Chem. Soc.*, 2017, **139**, 11825–11832.
13 M. T. Greiner, T. E. Jones, B. E. Johnson, T. C. R. Rocha, Z. J. Wang, M. Armbrüster, M. Willinger, A. Knop-Gericke and R. Schlögl, *Phys. Chem. Chem. Phys.*, 2015, **17**, 25073–25089.
14 A. K. Santra, J. J. Cowell and R. M. Lambert, *Catal Lett.*, 2000, **67**, 87–91.
15 M. Jayamurthy, P. Hayden and A. K. Bhattacharya, *J. Catal.*, 2014, **309**, 309–313.
16 Z. Wang, F. Luo, N. Wang and X. Li, *Catalysts.*, 2022, **12**, 481.
17 R. Zhou, T. Yu, X. Jiang, F. Chen and X. Zheng, *Appl. Surf. Sci.*, 1999, **148**, 263–270.
18 W. Zhou, W. Jing, H. Shen, R. Qin, S. Mo, M. Qiao, G. Fu and N. Zheng, *J Clust Sci.*, 2023, **34**, 255–260.
19 S. K. Amin, Eindhoven University of Technology, 2018.
20 J.-Y. Tseng and H.-T. Chen, *Theor Chem Acc.*, 2020, **139**, 57.
21 Q. Xiao, S. Sarina, E. R. Waclawik, J. Jia, J. Chang, J. D. Riches, H. Wu, Z. Zheng and H. Zhu, *ACS Catal.*, 2016, **6**, 1744–1753.
22 A. Kokalj, P. Gava, S. de Gironcoli and S. Baroni, *J. Catal.*, 2008, **254**, 304–309.
23 C. Stampfl and S. Piccinin, *J. Mater. Chem.*, 2010, **20**, 10521–10527.
24 N. L. Nguyen, S. de Gironcoli and S. Piccinin, *J. Chem. Phys.*, 2013, **138**, 184707.
25 N. L. Nguyen, S. Piccinin and S. de Gironcoli, *J. Phys. Chem. C.*, 2011, **115**, 10073–10079.
26 P. J. Van den Hoek, E. J. Baerends and R. A. Van Santen, *J. Phys. Chem.*, 1989, **93**, 6469–6475.
27 J. T. Jankowiak and M. A. Barteau, *J. Catal.*, 2005, **236**, 379–386.
28 S. Piccinin, S. Zafeiratos, C. Stampfl, T. W. Hansen, M. Hävecker, D. Teschner, V. I. Bukhtiyarov, F. Girgsdies, A. Knop-Gericke, R. Schlögl and M. Scheffler, *Phys. Rev. Lett.*, 2010, **104**, 035503.
29 A. Fortunelli, D. Cheng, J. Zhu, Y. Xie, Y. Nan, L. Zhu and H. Xu, *Ind. Eng. Chem. Res.*, 2019, **58**, 12996–13006.
30 R. M. Lambert, F. J. Williams, R. L. Cropley and A. Palermo, *J. Mol. Catal. A Chem.*, 2005, **228**, 27–33.
31 M. A. Barteau, *Top. Catal.*, 2003, **22**, 3–8.
32 P. Mulpur, S. Patnaik, A. Chunduri, T. M. Rattan, A. M. Rao and V. Kamisetti, *Soft Nanoscience Letters.*, 2013, **2013**, 27–31.

33 J. E. van den Reijen, S. Kanungo, T. A. J. Welling, M. Versluijs-Helder, T. A. Nijhuis, K. P. de Jong and P. E. de Jongh, *J. Catal.*, 2017, **356**, 65–74.
34 J. K. Lee, X. E. Verykios and R. Pitchai, *Appl. Catal.*, 1989, **50**, 171–188.
35 J. C. Wu and P. Harriott, *J. Catal.*, 1975, **39**, 395–402.
36 S. N. Goncharova, E. A. Paukshtis and B. S. Bal'zhinimaev, *Appl. Catal. A: Gen.*, 1995, **126**, 67–84.
37 X. E. Verykios, F. P. Stein, R. W. Coughlin and R. W. Coughlin, *J. Catal.*, 1980, **66**, 368–382.
38 H.-T. Chen, J.-G. Chang, S.-P. Ju and H.-L. Chen, *J. Phys. Chem. Lett.*, 2010, **1**, 739–742.
39 C.-C. Lee and H.-T. Chen, *J. Phys. Chem. A.*, 2015, **119**, 8547–8555.

Chapter 7 – Overall Conclusions and Future Work

7.1 All Catalytic Systems

Table 7.1 shows a comparison of all catalysts synthesised in this thesis showing their ethylene oxide selectivity and conversion.

Table 7.1: A table showing the selectivity and conversion of all of the catalytic systems synthesised in this thesis.

Catalysts	Selectivity / %	Conversion / %
Ag/α-Al_2O_3	50.4	7.7
Ag/γ-Al_2O_3	30.8	3.7
Re-Ag/α-Al_2O_3	41.9	8.0
Re-Ag/γ-Al_2O_3	25.1	3.6
Cs-Ag/α-Al_2O_3	63.3	8.8
Cs-Ag/γ-Al_2O_3	39.6	3.7
Cs-Re-Ag/α-Al_2O_3	85.1	8.6
Cs-Re-Ag/γ-Al_2O_3	40.3	4.1
Au/α-Al_2O_3	50.7	5.4
Cu/α-Al_2O_3	25.3	3.1
Cu-Au/α-Al_2O_3	58.7	6.1
Cu-Ag/α-Al_2O_3	55.8	5.9

There are some key factors that give better/poorer selectivities and conversions, these have been summarised in *Table 7.2*.

Table 7.2: A table summarising the key factors that give the better and poorer selectivities and conversions.

Key Factors That Give Better Selectivities and Conversion	Key Factors That Give Poorer Selectivities and Conversion
Using an O_2 pretreatment causes a decrease in average Ag crystallite size causing a redispersion of Ag and an increase in O_{ads}.	A reaction temperature of 275 °C causing sintering of the Ag crystallites.
Using small surface area α-Al_2O_3 compared to larger surface area γ-Al_2O_3.	Smaller Ag particles.
Smaller Ag particles.	Increase in hydroxyl groups on the surface of the catalyst.
More distributed Ag and less hydroxyl groups.	Decrease in strongly bound nucleophilic oxygen.
Increase in weakly bound electrophilic oxygen.	500 ppm of Re.
Increase in O_{ads} on the catalyst.	Lower wt. % of metal present on the catalyst.
Mixture of atomic electrophilic oxygen and hybrid atomic-molecular oxygen Ag_x-O_2.	A stronger Ag-O bond.
Thin layer of silver oxide on the surface.	
Shift to a more oxidised surface during the O_2 pretreatment and under reaction conditions.	
A weaker Ag-O bond.	
600 ppm of Cs.	
500 ppm of Re and 600 ppm of Cs.	
A higher temperature of pretreatment.	

7.2 Overall Conclusions

In summary, catalysts, promoters and oxygen species for ethylene epoxidation have been investigated. The key results are as follows:

1. An *in situ* DRIFTS cell was successfully designed and developed to provide information on the surface structure of the catalysts used for ethylene epoxidation. The main issues found during *in situ* DRIFTS experiments from literature investigation of the performance of multiple commercially available cells were gas by-passing the sample bed, inaccurate

temperature readings and difficulty in accurate backgrounding.[1] In this new DRIFTS cell, there are two beds, one is the sample bed and the other is the reference bed, and there is a translation between the two meaning that both the reference and the sample can be taken simultaneously. This means that the reference can be taken under the same conditions as the sample therefore reducing the differences in the atmosphere (CO_2 and H_2O gas phases) in the DRIFTS instrument and in turn improving the backgrounding. Issues from previous models allowed for the design of the new cell, where if the cell was compressed correctly and screwed together tightly, there was no accidental leaking of gases, the intensity increase to *ex situ* samples was achieved, translation between background and sample worked and heating could readily be achieved. The flat window with a flat cover, allows for a reduction in the dead volume and, in turn a reduction in the gas phase species in this cell, therefore improving the backgrounding due to this being removed. This also causes the IR window to get to reaction temperature, whilst this led to the problems with cracking and fogging, it did reduce the issue with high boiling point species condensing on the window. Two thermocouples, one in the cell and the other in the bed, meant that the temperature of the bed could be recorded and controlled by the thermocouple in the cell, giving accurate and correct temperature of the bed during reactions. The design of this cell allows an easy flow of gas between both beds (where the gas has to flow through the beds and not bypass) and using a new flat top screwed into the cell allows a gas-tight DRIFTS cell. Three case studies have been conducted using this new DRIFTS cell and have shown that the cell is successful under reaction conditions and has also improved the issues (gas by-passing the sample bed, inaccurate temperature readings and difficulty in accurate backgrounding) described in the literature.

2. The Ag/α-Al_2O_3 catalyst was investigated and compared to Ag/γ-Al_2O_3 where it was found to show a smaller surface area, therefore fewer acid sites leading to fewer side reactions of EO to acetaldehyde agreeing with the literature and confirming what was expected as to why α-Al_2O_3 is used as the preferred support.[2,3] Ag/γ-Al_2O_3 has lower EO selectivity and conversion compared to Ag/α-Al_2O_3 again agreeing with the literature.[4–7] Although γ-Al_2O_3 causes more distribution with smaller Ag crystallites and showed more adsorbed oxygen, DRIFTS indicated that there were more hydroxyl groups on the surface. It was found that the role of the O_2 pretreatment was to decrease the Ag crystallite sizes causing a redispersion of Ag and an increase in O_{ads}, whilst the optimum reaction temperature was at 225 °C due to sintering occurring at 275 °C. *Ex situ* XPS indicated that the amount of silver on the Ag/α-Al_2O_3 catalyst was equivalent to a thin silver oxide layer over the alumina agreeing with more recent literature that ethylene

epoxidation occurs on an oxidised silver surface and disagreeing with Linic and Barteau and the oxametallacycle.[8–11] Both XPS and Raman spectroscopy identified a hybrid atomic-molecular oxygen structure of Ag_4–O_2. This data agreed with the results from *in situ* XPS that a mixture of atomic electrophilic oxygen and Ag_x–O_2 dioxygen species were found to be present under reaction conditions. These results agree with the new literature of this hybrid species being present and agree with literature from both Wachs and Alzahrani *et al.* who have both stated that a mixture of oxygen species including both atomic and hybrid electrophilic oxygen species are present under ethylene epoxidation.[12–17] A shift in the Ag 3d XPS of Ag/α-Al_2O_3 under both O_2 pretreatment and ethylene to lower binding energy was found, indicating the Ag getting more oxidised agreeing with literature from both Artiglia and Carbonio *et al.* who stated that under oxidation and ethylene epoxidation condition, there is an increase in the oxidation of silver.[18,19] Whilst the addition of 500 ppm of Re caused a decrease in EO selectivity, it was investigated to be able to compare to the Cs-Re-Ag/α-Al_2O_3 catalyst. Re appeared to weaken the Ag-O bond, however, there was an increase in the acidity and the hydroxyl groups therefore indicating the reason as to why there is a reduction in EO selectivity. Here the Re species in Re-Ag/α-Al_2O_3 was found to be in the +7 oxidation state as an oxide cluster where the Re-O bonds changed throughout the reaction, disagreeing with Ren *et al*. who stated that the Re oxidation state is between +4 to +7 but agreeing with Dellamorte and Diao *et al.* who stated that the Re is in a +7 oxidation state. Whilst the Re species in Re-Ag/γ-Al_2O_3 were found to have a coordination of 3-4 oxygen atoms with a tetrahedral distortion bound to the surface and did not change throughout the reaction. This agrees with Hardcastle and Okal *et al*. who stated that on Al_2O_3 there are three equivalent terminal Re-O bonds and one inequivalent Re-O bond.[20–24] This has given more insight into the oxygen species and in turn the oxygen species during ethylene epoxidation whilst also giving more insight into the role of the Re promoter.

3. The addition of 600 ppm of Cs caused an increase in EO selectivity and a decrease in acetaldehyde selectivity. Here the Cs promoter was found to decrease the Ag crystallite sizes and cause more distribution of Ag, alongside causing a decrease in the acidity and therefore hydroxyl groups, reducing the side reactions of EO to AA. This agrees with Grant, Lambert and Schoenfeld *et al.* who stated that Cs neutralises the acid sites on the support that are active for the isomerisation of EO to form acetaldehyde. This agrees with Schoenfeld and Bal'zhinimaev *et al.* who stated that Cs is able to distribute the silver particles more uniformly on the support.[25,26] Whilst also agreeing with Schmal *et al.* who stated that Cs promoted the formation of very small silver particles which

increased the selectivity of ethylene oxide by increasing the contact with the reactants.[27] Cs was found to weaken the Ag-O bond which agrees with Ren *et al.* who stated that Cs decreases the adsorption strength of oxygen on Ag/weakens the adsorption of atomic oxygen.[20] Cs also was found to cause an increase in the amount of O_{ads} leading to a more selective catalyst. The structure of the Cs species was found to be a mixture of peroxide- and suboxide-like species which is likely to be distributed over both Ag and Al_2O_3 which supports the evidence given by Bukhtiyarov *et al.* who stated that there was a mixture of Cs peroxide and Cs suboxide species present.[28] Cs was found to interact with both Ag and Al_2O_3, this agrees with Minahan *et al.* who stated that Cs acts as a binder between the Ag and alumina support in ethylene epoxidation catalysts.[25] The addition of 600 ppm of Cs and 500 ppm of Re caused a large increase in EO selectivity and a decrease in acetaldehyde selectivity. pXRD and STEM confirm that when Cs and Re are added together, there is a modest decrease in the Ag crystallite size and causes more Ag dispersion, giving more sites for oxygen adsorption. Together they were found to cause a weakening of the Ag-O bond which agrees with Ren *et al.* who stated that Re and Cs together cause a higher concentration of weakly adsorbed oxygen and lower concentrations of strongly adsorbed oxygen.[20] O_2-TPD, H_2-TPR and *ex situ* O1s all indicate an increase in the O_{ads} with the addition of Cs and Re therefore causing an increase in EO selectivity by there being more electrophilic oxygen. When both Cs and Re are added together, the hydroxyl acidic groups on the support are still titrated away (as per the Cs only case) therefore reducing the isomerisation of EO to form acetaldehyde. It was found that the active oxidation state for Re was +7 whilst for Cs it was +1, where they both interact with each other as there is a slight shift in both binding energies indicative of electrons being transferred towards the Re atoms, facilitating the formation of weakly adsorbed oxygen, therefore giving a higher EO selectivity. When Re is added to the Cs-Ag/α-Al_2O_3 there is a significant amount of broadening with Cs NMR indicating that Re interacts with Cs and causes electron distortion of the Cs. Vodyankina *et al.* found the formation of a $CsReO_x$ species on the surface of a Cs-Re-Ag/α-Al_2O_3, whilst this was not found, the ss NMR found a new interaction between Cs and Re which indicates that some form of complex is present on the surface.[29] Under ethylene epoxidation conditions, the Cs species was found to be suboxide-like, and the Re species in Re-Ag/α-Al_2O_3 was found to be in the +7 oxidation state as a single Re atom oxide species where the Re-O bonds changed throughout the reaction. Whilst when supported on the higher surface area γ-Al_2O_3 the Re species in Re-Ag/γ-Al_2O_3 were found to have a coordination of 3-4 oxygen atoms with a tetrahedral distortion bound to the surface and did not change throughout the reaction. When comparing to Ag/α-Al_2O_3 under ethylene epoxidation conditions, there was no change

in the binding energy of Ag with the addition of Cs and Re. However, in the O 1s, there is an increase in the electrophilicity of the oxygen with the addition of Cs and Re under Ar and O_2 pretreatment. This agrees with Diao *et al.* who stated that Re causes the Ag binding energy to increase which means that Ag sites are more electron deficient and therefore the resulting O adsorbed on Ag more electrophilic, whilst Cs lowers the desorption energy of the EO precursor which is strongly bound.[21] This data agrees with the Ag/α-Al_2O_3 that there is a mixture of Ag_x-O_2 dioxygen species and atomic electrophilic oxygen under reaction conditions. This has given more indication into the role of both Cs alone and Cs and Re together as promoters for Ag/α-Al_2O_3 during ethylene epoxidation.

4. Whilst the use of Cu and Au-based catalysts have been widely used for propylene epoxidation, very little research has been investigated into the use of these catalysts for ethylene epoxidation. All combinations of catalysts that were investigated were relatively active towards ethylene epoxidation, Au/α-Al_2O_3 showed a selectivity of 51%, Cu/α-Al_2O_3 showed a selectivity of 25%, Cu-Au/α-Al_2O_3 showed a selectivity of 59% and Cu-Ag/α-Al_2O_3 showed a selectivity of 58%. The copper was found to be present in its oxidised form, whilst the gold was found to be present as metallic Au where there is no change in the structure before and after ethylene epoxidation. Whilst Cu/α-Al_2O_3 was shown to be moderately selective towards EO (25%), there was an increase in AA, H_2O and CO_2 selectivity compared to Ag/α-Al_2O_3. All catalysts showed an increase in AA selectivity compared to Ag/α-Al_2O_3. The addition of Cu caused a decrease in Au crystallite size for Cu-Au/α-Al_2O_3 alongside a decrease in hydroxyl groups and an increase in Ag crystallite size in Cu-Ag/α-Al_2O_3. The Cu-Ag/α-Al_2O_3 indicates that surface-bound adsorbed atomic oxygen is bound more strongly on the surface of the catalyst compared to Ag/α-Al_2O_3. All catalysts showed a large decrease in hydroxyl groups and the likely reason for this is the pretreatment of 450 °C. Chen *et al.* stated that Au nanoparticle catalysts are very selective towards ethylene epoxidation, agreeing with the data in this thesis as the Au/α-Al_2O_3 was found to give similar selectivity towards EO when compared to Ag/α-Al_2O_3.[30,31] The ethylene oxide selectivity over the Cu/α-Al_2O_3 was found to be 25 %, which is in agreement with the selectivity data collected by Bhattacharya *et al.*[32] Whilst no exact percentage of ethylene oxide selectivity could be identified Lambert *et al.* found that for high selectivity epoxidation both metallic copper sites and adsorbed oxygen sites are required, whereas on Cu/α-Al_2O_3 only CuO was present with adsorbed oxygen sites.[33] The Cu/α-Al_2O_3 catalyst was found to have copper in the +2 oxidation state where there was no change throughout ethylene epoxidation, this contradicts the work by Bhattacharya *et al.* who

stated that Cu(I) is an active species in epoxidation and the decrease in selectivity is due to this change from Cu(I) to Cu(II).[32] Chen *et al.* undertook a computational study where they found that Cu-Au core-shell nanoclusters are more reactive than pure Cu and Au nanoclusters, this agrees with the results where the Cu-Au/α-Al_2O_3 showed higher selectivity (59%) towards EO when compared to Au/α-Al_2O_3 (51%) and an increase compared to Cu/α-Al_2O_3 (25%).[34] As stated by Nguyen *et al.* Ag-Cu catalyst for ethylene epoxidation has been shown to yield higher selectivity towards ethylene oxide compared to pure Ag, this has been confirmed by Cu-Ag/α-Al_2O_3 (58%) showing an increased EO selectivity compared to Ag/α-Al_2O_3 (51%).[35] Scheffler *et al.* stated that there is a coexistence of thin CuO and AgO-CuO films on the Ag substrate, whilst this was not able to be identified in this thesis, a mixture of CuO and AgO was found to be present on the Cu-Ag/α-Al_2O_3 catalyst.[36] Lastly, Nguyen *et al.* stated that Cu tends to oxidise and form thin Cu oxide layers on top of the Ag particles, causing O_{sub} to migrate to the catalyst surface, whilst again this was difficult to confirm, it does agree with the Cu-Ag/α-Al_2O_3 catalyst containing Cu oxide.[35,37] This work therefore gives evidence to the use of Cu and or Au-based catalysts for ethylene epoxidation.

7.3 Future Work

Some suggestions for possible areas of further research, based on the key findings of this thesis are provided below.

Whilst the development and optimisation of the *in situ* DRIFTS cell was successful in solving the main three issues of gas by-passing the sample bed, inaccurate temperature readings and difficulty in accurate backgrounding, there is some future work that would be useful if undertaken. This developed DRIFTS cell can only reach 300 °C, which for many catalytic reactions this is the maximum temperature, however, if this cell is needed for more high-temperature reactions, developments need to be undertaken to improve this temperature limit. One experiment that would be interesting to investigate with this new cell would be pyridine adsorption to identify the type of acidic sites, due to only having one cell made, this was unable to be undertaken. Subsequence desorption from the cell and the pipe work would have been difficult, leading to a contaminated cell. An *in situ* DRIFTS system coupled with mass spectrometry would allow for accurate reactions to be undertaken where the results from the DRIFTS can be correlated to the results from the mass spectrometer, therefore this would be interesting to allow an improved *in situ* DRIFTS cell. Whilst KBr and CaF_2 windows were able to be used for the cell, the KBr had problems with fogginess,

therefore it would be useful to be able to solve this problem to stop this from happening allowing KBr to be used for all high-temperature long reactions.

Whilst a large amount of experimental work has been undertaken by looking at *in situ* and *ex situ* characterisation and spectroscopic techniques, no work has been undertaken with DFT calculations. Some of the proposed roles/ideas by looking at the mechanism, the oxygen species and the promoters have been investigated with the use of DFT calculations. A full understanding of all of the proposed ideas would require DFT calculations by looking at the stepped and defect sites, the energy barriers and the activation energies. These computational studies would give full insight into the mechanism, oxygen species and the promoters used in ethylene epoxidation.

Whilst XAFS analysis gave insight into the Re species throughout both the O_2 pretreatment and ethylene epoxidation, full analysis was unable to be undertaken due to a limited number of structural models. Therefore, DFT calculations to find different bond lengths throughout the Re-based catalysts would be useful to gain more insight into the structure and the position, and therefore the role of the Re in the catalysts.

Suggestions have been made that the bimetallic catalyst forms a $CsReO_x$ species (potentially a $CsReO_4$ complex).[21,29] Due to time constraints, this was unable to be investigated, however further experimental work with an investigation into this species would give more insight into the Cs-Re-Ag/Al_2O_3 catalysts.

Whilst *ex situ* Raman measurements were undertaken, *in situ* Raman experiments during both O_2 pretreatment and ethylene epoxidation would give insight into the changing of the molecular interactions, specifically the metal-oxygen interactions, which could therefore give more insight into the mechanism and oxygen species during ethylene epoxidation.

As discussed in **Chapter 1.1.2.2**, chlorine is another well-known promoter that is commonly used industrially in ethylene epoxidation. Here the chlorine is fed in in the gas phase and is more complex to do experimentally as there needs to be a low concentration of the chloride gas phase.[9] However, future work would be useful to investigate the presence/role of the chlorine promoter.

H_2 chemisorption could be employed on all the catalysts to give a quantitative measure of the Ag dispersion, giving more information and understanding of how the silver plays a role in ethylene epoxidation.

Whilst a large amount of experimental work has been undertaken with looking at Cu and/or Au catalysts, more work needs to be undertaken with investigations of these catalysts. Firstly, different wt. % need to be tested, with the Ag-based catalysts different wt. % of

promoters cause an increase or a decrease in EO selectivity therefore this could occur with Cu/Au. Analysis needs to be undertaken on Raman spectroscopy and NAP-XPS to give more information regarding the oxygen and metal species and how the interaction between these allows for an increase in EO selectivity. STEM would give insight into the positions of the metals on the surface giving more insight into the structure of the catalyst. More *in situ* reactions are needed with the investigation of Cu and/or Au catalysts to understand the structure of the catalysts during reaction conditions. To compare easily to the Cu/Au catalyst, it would be useful to have a 2 wt. % Ag catalyst under the same pretreatment conditions, to give more information into the metals for ethylene epoxidation. Another suggestion would be using silylation of the hydroxyl groups as a means to investigate their role in the catalytic reaction. Here identification and analysis of the hydroxyl group can occur giving more specific information into the hydroxyl species and whether they play a part in the Cu and Au based catalysis.

There are a large number of arguments for the role of Cu/Al_2O_3, whilst Cu^{2+} was found to be selective here, it would be useful to compare this to metallic Cu and Cu^{+} to see the difference in EO selectivity to be able to compare to the literature.

Whilst a large amount of information has been investigated into the roles of the promoters and the oxygen species for ethylene epoxidation with Ag-based catalysts, more work needs to be undertaken to understand why the Cu and Au catalysts give EO selectivity.

7.4 References

1 F. C. Meunier, *React. Chem. Eng.*, 2016, **1**, 134–141.
2 J. Lv, D. Wang, L. Peng, X. Guo, W. Ding and W. Yang, *Catalysts.*, 2023, **13**, 994.
3 V. Sanchez Escribano, G. Garbarino, E. Finocchio and G. Busca, *Top Catal.*, 2017, **60**, 1554–1564.
4 C. J. Keijzer, L. C. J. Smulders, D. Wezendonk, J. W. de Rijk and P. E. de Jongh, *Catal. Today.*, 2024, **428**, 114447.
5 S. Rojluechai, S. Chavadej, J. W. Schwank and V. Meeyoo, *Catal. Commun.*, 2007, **1**, 57–64.
6 J. E. van den Reijen, S. Kanungo, T. A. J. Welling, M. Versluijs-Helder, T. A. Nijhuis, K. P. de Jong and P. E. de Jongh, *J. Catal.*, 2017, **356**, 65–74.
7 A. Ayame, Y. Uchida, H. Ono, M. Miyamoto, T. Sato and H. Hayasaka, *Appl. Catal. A Gen.*, 2003, **244**, 59–70.
8 S. Linic and M. A. Barteau, *J. Am. Chem. Soc.*, 2002, **124**, 310–317.
9 T. Pu, H. Tian, M. E. Ford, S. Rangarajan and I. E. Wachs, *ACS Catal.*, 2019, **9**, 10727–10750.
10 G. Rovida, F. Pratesi and E. Ferroni, *Appl. Surf. Sci.*, 1980, **5**, 121–132.
11 M. O. Özbek and R. A. van Santen, *Catal Lett.*, 2013, **143**, 131–141.
12 Z. Tang, T. Chen, K. Liu, H. Du and S. G. Podkolzin, *Langmuir.*, 2021, **37**, 11603–11610.
13 H. A. Alzahrani and J. J. Bravo-Suárez, *J. Catal.*, 2023, **418**, 225–236.
14 T. Pu, A. Setiawan, B. Mosevitzky Lis, M. Zhu, M. E. Ford, S. Rangarajan and I. E. Wachs, *ACS Catal.*, 2022, **12**, 4375–4381.
15 T. Pu, A. Setiawan, A. C. Foucher, M. Guo, J.-M. Jehng, M. Zhu, M. E. Ford, E. A. Stach, S. Rangarajan and I. E. Wachs, *ACS Catal.*, 2024, **14**, 406–417.
16 C. Liu, D. P. Wijewardena, A. Sviripa, A. Sampath, D. W. Flaherty and C. Paolucci, *J. Catal.*, 2022, **405**, 445–461.
17 K.-K. Liu, S. Tadepalli, L. Tian and S. Singamaneni, *Chem. Mater.*, 2015, **27**, 5261–5270.
18 E. A. Carbonio, T. C. R. Rocha, A. Y. Klyushin, I. Píš, E. Magnano, S. Nappini, S. Piccinin, A. Knop-Gericke, R. Schlögl and T. E. Jones, *Chem. Sci.*, 2017, **9**, 990.
19 M. Guo, N. Dongfang, M. Iannuzzi, J. A. van Bokhoven and L. Artiglia, *ACS Catal.*, 2024, **14**, 10234–10244.
20 D. Ren, G. Cheng, J. Li, J. Li, W. Dai, X. Sun and D. Cheng, *Catal. Letters.*, 2017, **147**, 2920–2928.
21 W. Diao, C. D. DiGiulio, M. T. Schaal, S. Ma and J. R. Monnier, *J. Catal.*, 2015, **322**, 14–23.
22 J. C. Dellamorte, J. Lauterbach and M. A. Barteau, *Catal. Today.*, 2007, **120**, 182–185.
23 F. D. Hardcastle, I. E. Wachs, J. A. Horsley and G. H. Via, *Mol. Catal.*, 1988, **46**, 15–36.
24 J. Okal, *Appl. Catal. A: Gen.*, 2005, **287**, 214–220.
25 D. M. Minahan, G. B. Hoflund, W. S. Epling and D. W. Schoenfeld, *J. Catal.*, 1997, **168**, 393–399.
26 S. N. Goncharova, E. A. Paukshtis and B. S. Bal'zhinimaev, *Appl. Catal. A: Gen.*, 1995, **126**, 67–84.
27 M. C. N. A. Carvalho, C. A. Perez, R. A. Simão, F. B. Passos and M. Schmal, *An. Acad. Bras. Ciênc.*, 2004, **76**, 19–27.
28 E. A. Podgornov, I. P. Prosvirin and V. I. Bukhtiyarov, *J. Mol. Catal. A Chem.*, 2000, **158**, 337–343.
29 M. A. Salaev, A. A. Salaeva and O. V. Vodyankina, *Catal. Today.*, 2021, **375**, 585–590.
30 H.-T. Chen, J.-G. Chang, S.-P. Ju and H.-L. Chen, *J. Phys. Chem. Lett.*, 2010, **1**, 739–742.

31 C.-C. Lee and H.-T. Chen, *J. Phys. Chem. A.*, 2015, **119**, 8547–8555.
32 M. Jayamurthy, P. Hayden and A. K. Bhattacharya, *J. Catal.*, 2014, **309**, 309–313.
33 A. K. Santra, J. J. Cowell and R. M. Lambert, *Catal Lett.*, 2000, **67**, 87–91.
34 J.-Y. Tseng and H.-T. Chen, *Theor Chem Acc.*, 2020, **139**, 57.
35 N. L. Nguyen, S. de Gironcoli and S. Piccinin, *J. Chem. Phys.*, 2013, **138**, 184707.
36 S. Piccinin, S. Zafeiratos, C. Stampfl, T. W. Hansen, M. Hävecker, D. Teschner, V. I. Bukhtiyarov, F. Girgsdies, A. Knop-Gericke, R. Schlögl and M. Scheffler, *Phys. Rev. Lett.*, 2010, **104**, 035503.
37 N. L. Nguyen, S. Piccinin and S. de Gironcoli, *J. Phys. Chem. C.*, 2011, **115**, 10073–10079.

Appendix 1

1.1 Catlab Calibration Data

The calibrations for all the gases used are shown in *Figures A1.1, A1.3, A1.5, A1.7, A1.9* and *A1.11*. The comparison of the NIST cracking patterns and the calibration patterns used are shown in *Figures A1.2, A1.4, A1.6, A1.8, A1.10, A1.12* and A*1.13*.

Table A1.1: A table showing the m/z used for the compounds analysed on the Catlab.

Compound	m/z
Water	18
Ethylene	27 & 28
Oxygen	32
Carbon Dioxide	44
Argon	40
Acetaldehyde	29, 42, 43 & 44
Ethylene Oxide	29, 42, 43 & 44

Firstly, H_2O was calibrated, here m/z 18 was used, as shown in *Figure A1.1*.

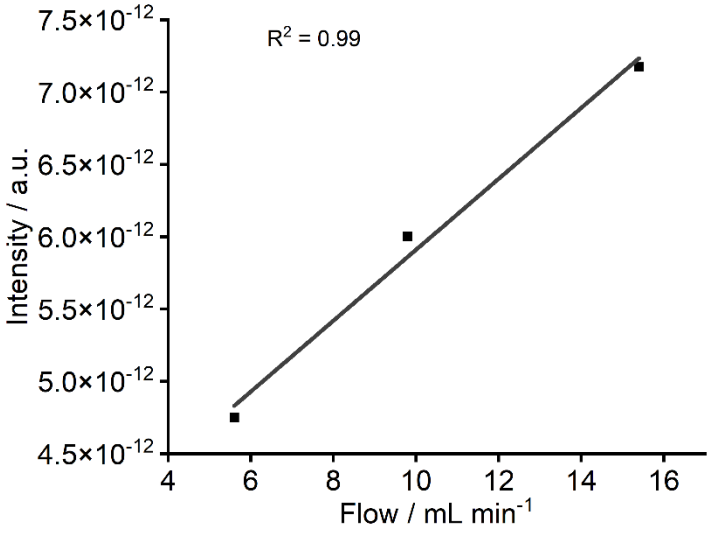

Figure A1.1: Calibration of H_2O.

As discussed in **Chapter 2** the NIST cracking pattern and the calibration pattern were compared, here H_2O is compared shown in *Figure A1.2*.

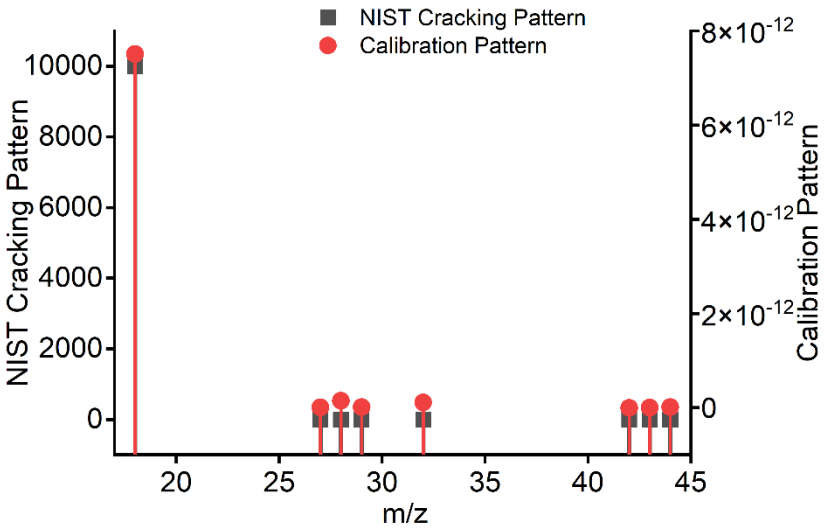

Figure A1.2: Comparison of NIST cracking pattern versus calibration pattern of H_2O.

Next ethylene was calibrated here m/z 27 and 28 were used, shown in *Figure A1.3*. As shown, in *Table A1.1*, both the m/z of 27 and 28 are used. *Figure A1.4* shows the comparison of the NIST cracking pattern versus the calibration pattern.

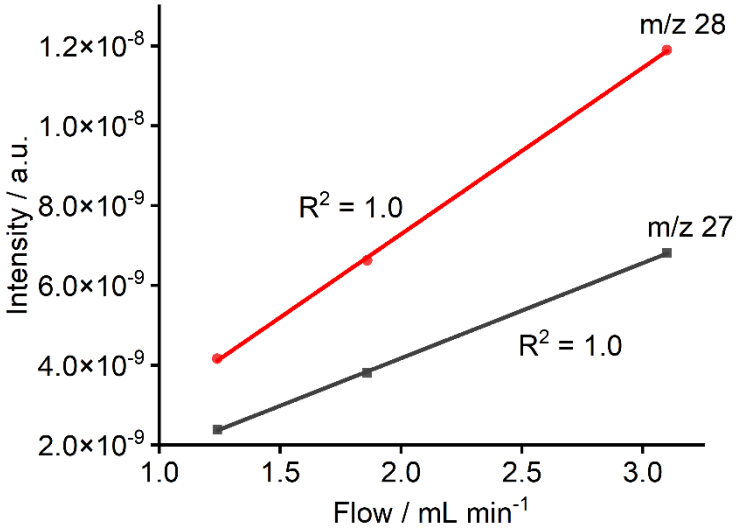

Figure A1.3: Calibration of Ethylene.

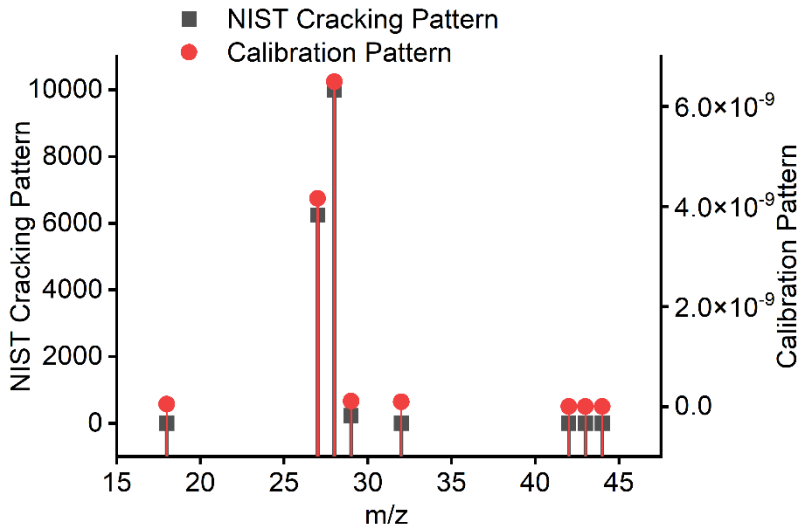

Figure A1.4: Comparison of NIST cracking pattern versus calibration pattern of Ethylene.

Next oxygen was calibrated here m/z 32 was used, shown in *Figure A1.5. Figure A1.6* shows the comparison of the NIST cracking pattern versus the calibration pattern of oxygen.

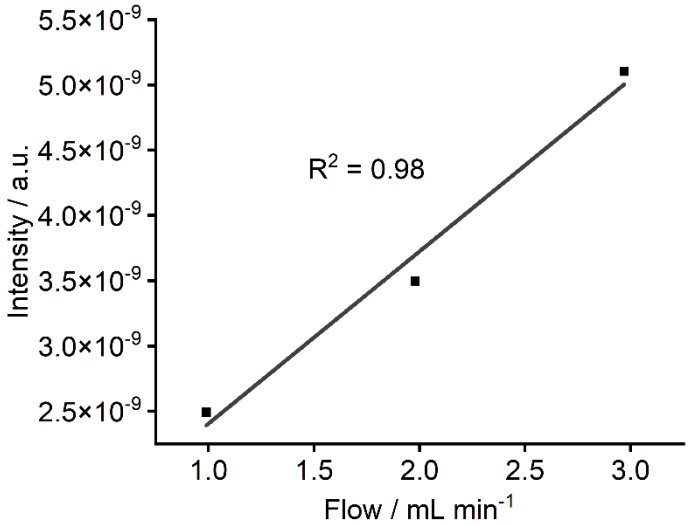

Figure A1.5: Calibration of Oxygen.

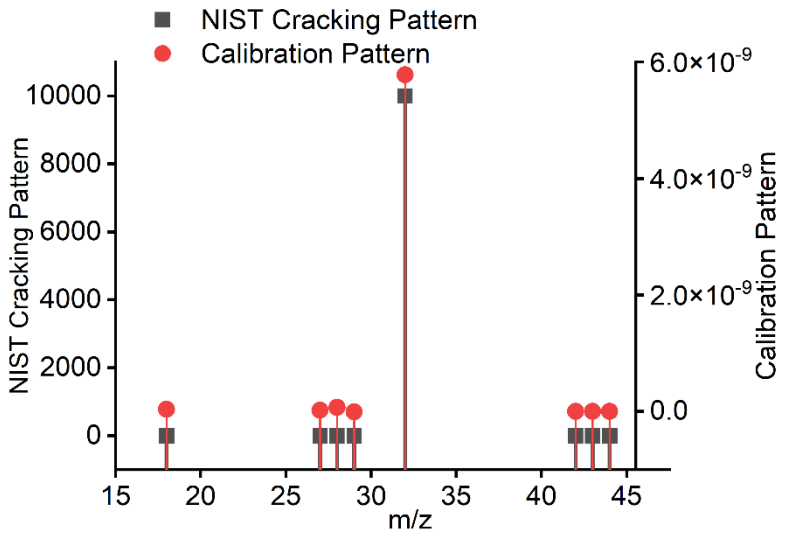

Figure A1.6: Comparison of NIST cracking pattern versus calibration pattern of Oxygen.

There is a large crossover with the m/z of 44 with CO_2, acetaldehyde and EO. CO_2 was calibrated using the m/z of 44 (shown in *Figure A1.7*) and then compared the calibration pattern to the NIST cracking pattern (shown in *Figure A1.8*).

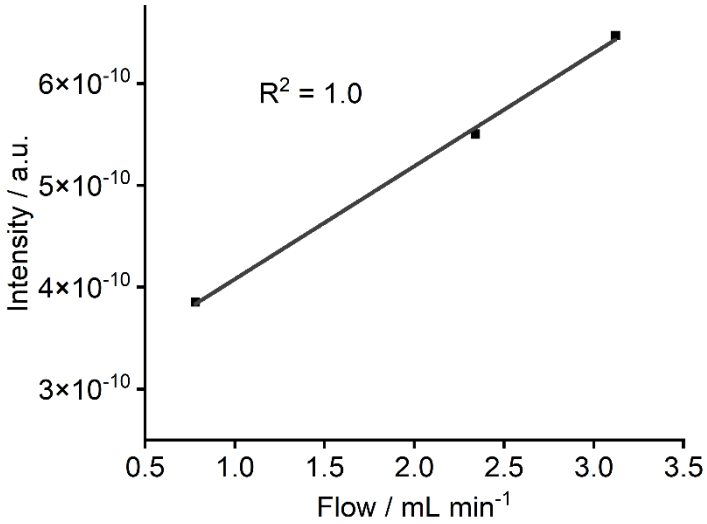

Figure A1.7: Calibration of CO_2.

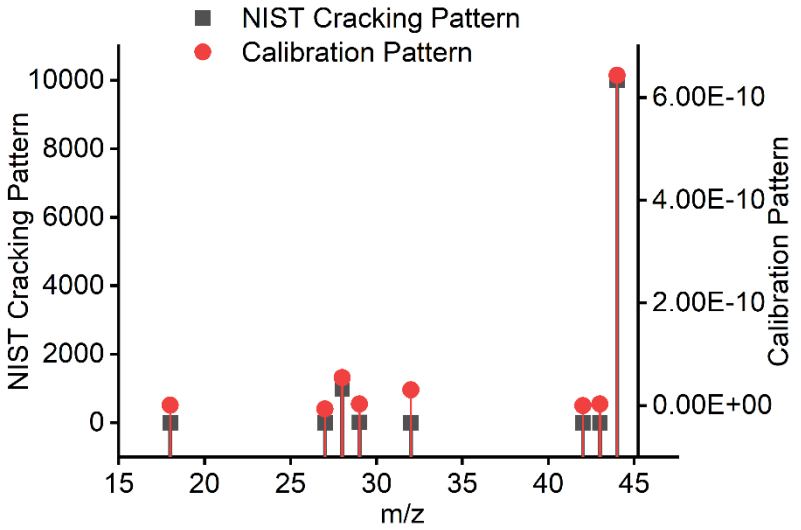

Figure A1.8: Comparison of NIST cracking pattern versus calibration pattern of CO_2.

There is no crossover of argon with any of the other compounds, however, argon was used as the carrier gas, therefore this was calibrated using m/z 40 (shown in *Figure A1.9*) and then compared to the NIST cracking pattern (shown in *Figure A1.10*).

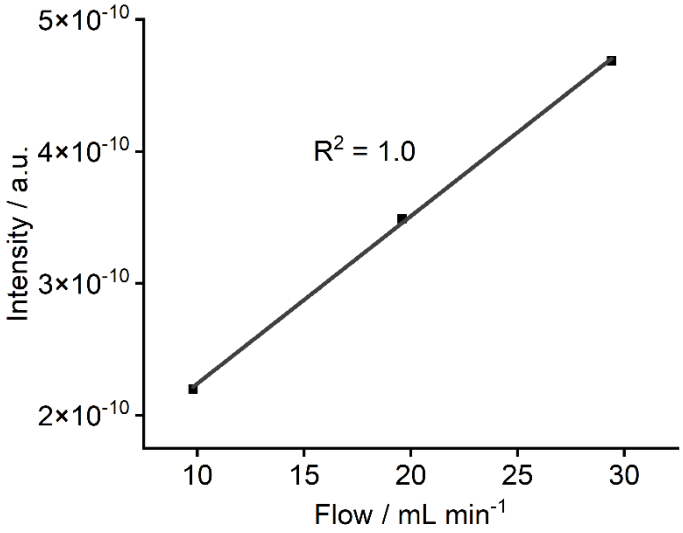

Figure A1.9: Calibration of Argon.

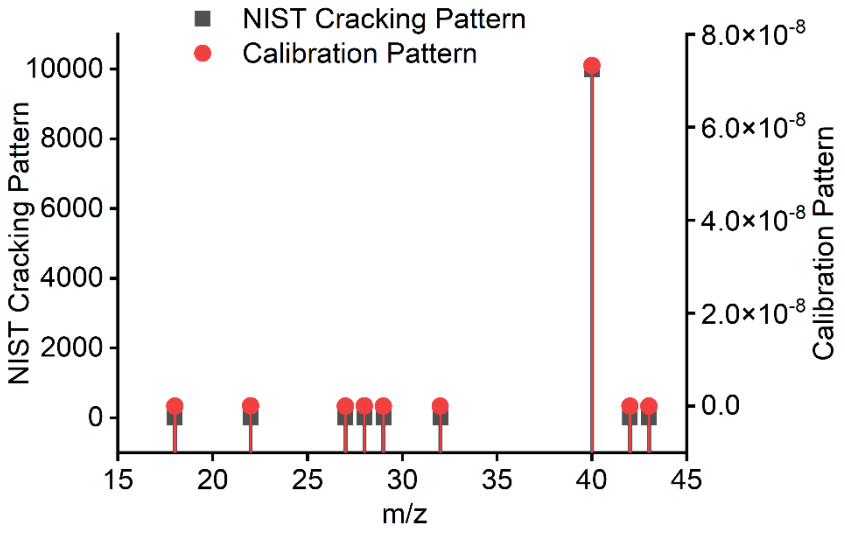

Figure A1.10: Comparison of NIST cracking pattern versus calibration pattern of Argon.

Calibration of acetaldehyde was undertaken where the m/z of 29, 42, 43 and 44 were all measured shown in *Figure A1.11*, whilst the comparison of the calibration pattern to the NIST cracking pattern is shown in *Figure A1.12*.

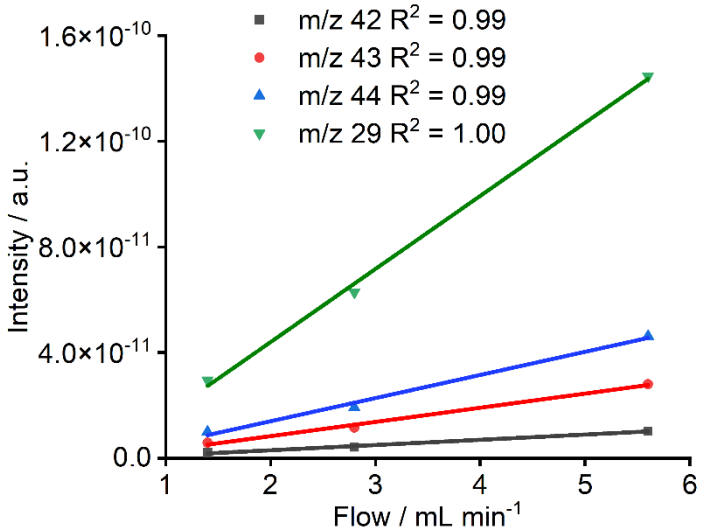

Figure A1.11: Calibration of Acetaldehyde.

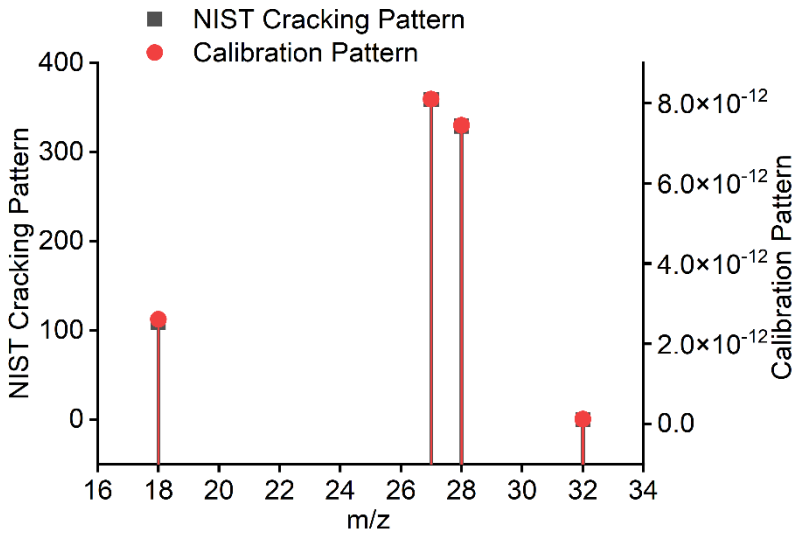

Figure A1.12: Comparison of NIST cracking pattern versus calibration pattern of Acetaldehyde.

Due to the toxicity of ethylene oxide, no calibration was undertaken. However, using the NIST cracking pattern and the calibration pattern of the acetaldehyde intensities a calibration pattern of EO was able to be found and compared to the NIST data of EO. This is shown in *Figure A1.13.*

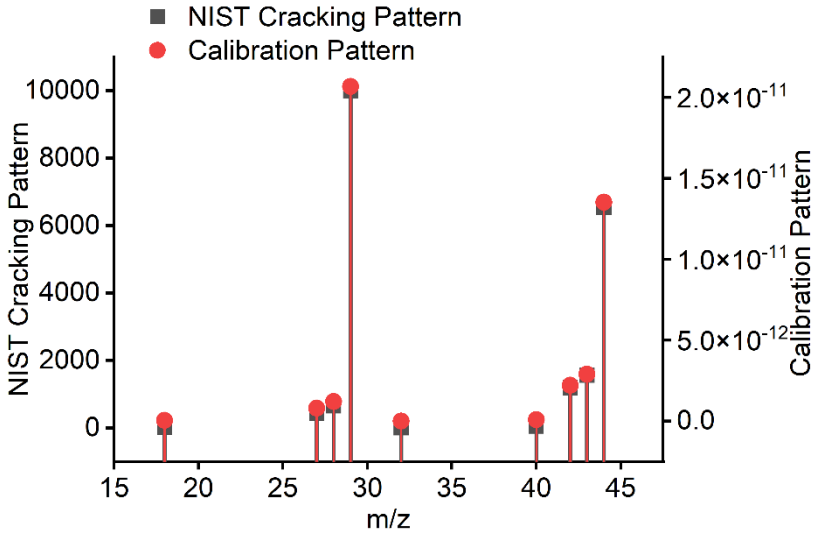

Figure A1.13: Comparison of NIST cracking pattern versus calibration pattern of EO.

1.2 Initial Optimisation of Raman Setup

1.2.1 Alignment Acquisitions

For the alignment adjustments, measurements were tried with an exposure time of 20 seconds, with 1 accumulation and a kinetic series length of 100. The kinetic series length was normally cut short once the alignment had been corrected.

1.2.2 Background and Readout Noise

Firstly, spectra to establish the background and readout noise were obtained under different conditions following the replacement of the enclosures to understand the extent to which they are light-tight or ambient lighting may contribute to signals. Spectra without laser illumination were taken when the CCD shutter was open, and lights were on and off. Spectra were also taken when the CCD shutter was closed, and lights were on and off. These are shown in *Figure A1.14*. It can be seen that there is minimal change when turning the lights on or when turning them off, this shows that the black casing structure of the enclosure around the Raman set-up does block out most of the room light. There is however a larger difference between when the shutter is closed and when the shutter is open. The reason for this is likely that when the shutter is open there is the potential for light from other parts of the spectrometer to enter but when the shutter is closed there is both thermal and readout noise.

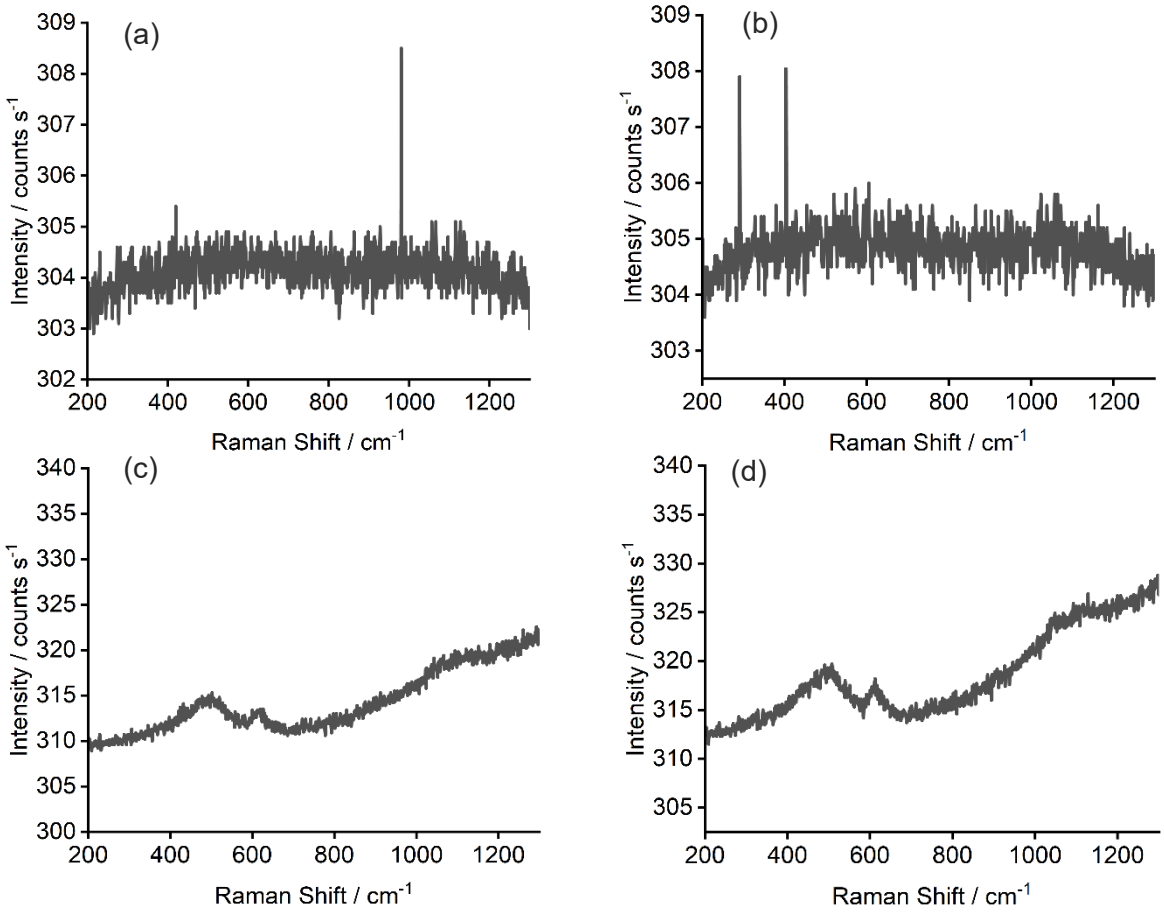

Figure A1.14: Raman spectrum of the wavelength 667-725 nm here the laser is off. Where (a) Shutter is closed and room lights are on, (b) Shutter is closed and room lights are off, (c) Shutter is open and room lights are off, (d) Shutter is open and room lights are on. Slit width = 150 μm, number of spectra = 20, length of each spectrum = 20 s.

1.2.3 Filament Lamp

To understand the intensity throughput of the spectrometer, a spectrum of a filament lamp (shown in *Figure A1.15*) in a plastic scattering sphere was also recorded under a standard set of conditions. The filament lamp functions as a black body radiation source, which in this region is expected to increase smoothly with wavelength and contain no spectral features. Given the change in the spectral region considered is expected to be small and featureless, it is adequate to assume the intensity response based on the emission profile of the radiation source should remain constant across each spectrum. Corrections in this thesis have therefore been made based on *Equation A1.1* which divides the sample spectrum (corrected for dark noise) by the reference spectral shape of the filament lamp (also corrected for dark noise, but this is small relative to the filament lamp spectra). The dark spectrum is the data from the different wavelengths where the shutter is open, and the room lights are off.

$$Corrected\ Spectrum = \frac{(Raw\ Sample\ Spectrum - Dark\ Spectrum)}{Normalised\ Filament\ Lamp\ Spectrum}$$

Equation A1.1

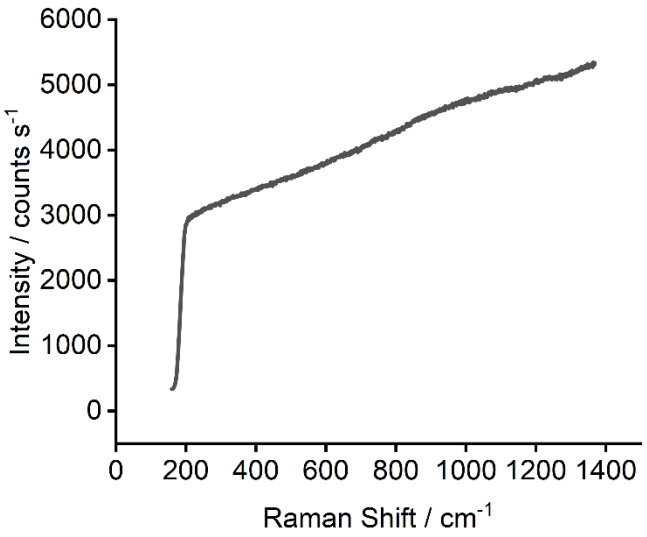

Figure A1.15: Raman spectrum of filament lamp (after applying intensity response correction and subtraction of dark signal). Where the is a wavelength of 667-725 nm, slit width = 150 µm, number of spectra = 20, and length of each spectrum = 20 s.

1.2.4 Neon Light

The spectrum of a neon light was also measured to allow for calibration of wavelength. As shown in *Figure A1.16* the black lines from the literature line up with the neon light measured from the laser 660 nm.

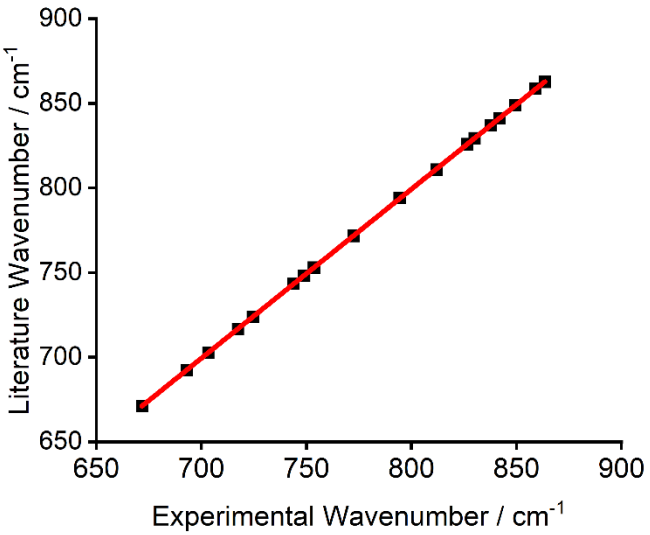

Figure A1.16: Neon lamp calibration against a literature standard, allowing correction of wavenumbers for this Raman setup. Where the is a wavelength of 667-725 nm, slit width = 150 µm, number of spectra = 20, and length of each spectrum = 20 s.

1.2.5 Cosmic Ray Removal

Cosmic ray removal was undertaken on all of the Raman results using MATLAB. This was achieved by averaging the data from accumulations without cosmic rays. To do this, outliers (more than 20 counts s^{-1} threshold distance from the median) are replaced by the median. This rejects cosmic rays of all shapes and sizes as they will always be an extreme value, rather than the median.

1.2.6 Initial Aligning of Raman System Using Silicon Wafer Sample

Due to the system being out of commission for some time and moved slightly in the work done to install a new enclosure for safety, it was necessary to first check the alignments of components not ordinarily adjusted. In particular, the positioning of the spectrograph slit with respect to the optical system. To achieve this, a silicon wafer was used to investigate if Raman spectra could be obtained, but the initial spectrum did not show anything other than background noise. Therefore, it was thought that the spectrograph slit did not align completely with the optical system. To align it, a torch was placed in the spectrograph with the light shining through the slit into the spectrograph antechamber. The setup is shown in *Figure A1.17*.

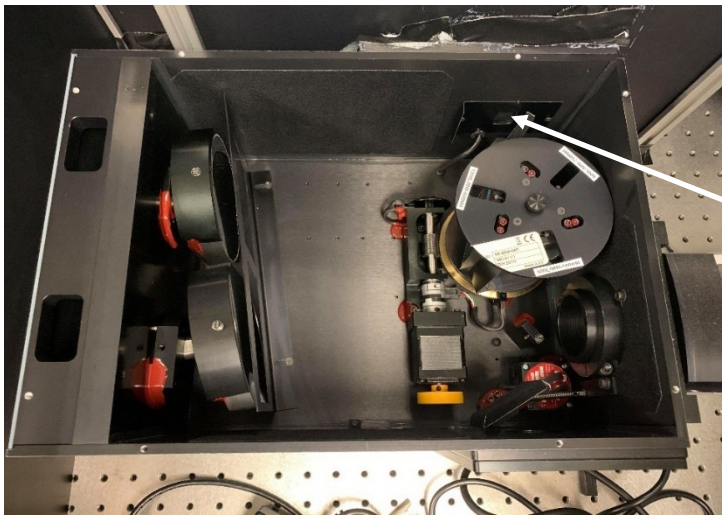

Figure A1.17: The inside of the spectrograph with any arrow where the torch was placed.

Figure A1.18 shows the light path of the torch from the spectrograph slit to the spectrograph antechamber. The spectrograph slit was moved to be able to see the torch in the spectrograph antechamber first, therefore confirming that the spectrograph had been moved, likely when the boxing was being added. The mirror was moved to get the light into the path required to be able to shine into the sample chamber. Once this was done and aligned so the light entered the sample chamber, the same alignment occurred the other way around. The light was shone from the slit in the sample chamber into the spectrograph antechamber with the movement of the mirror to align it correctly.

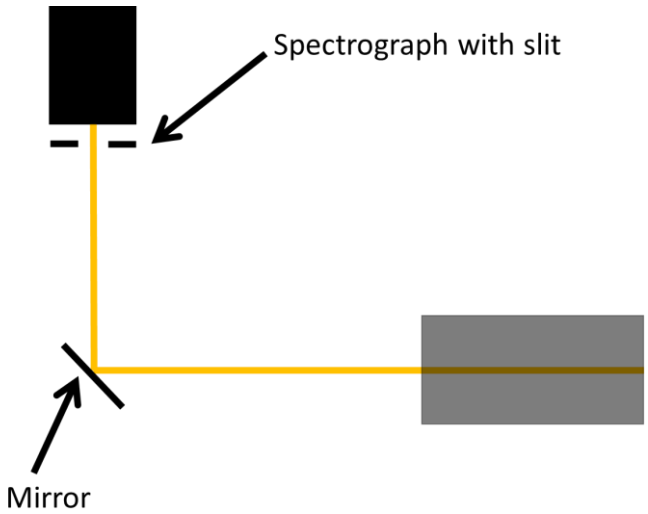

Figure A1.18: The spectrograph antechamber, where it shows the path of the light from the spectrograph slit.

Once the spectrograph was thought to be aligned, the silicon wafer was used again and a peak at approximately 520 cm^{-1} was seen as expected, shown in *Figure A1.19*.[1] There was also a very small peak between 700 – 1000 cm^{-1} which was likely to be a native oxide layer

on the surface of the silicon. This peak is broad and small which is likely due to not having many counts due to the Raman set-up not being completely aligned.

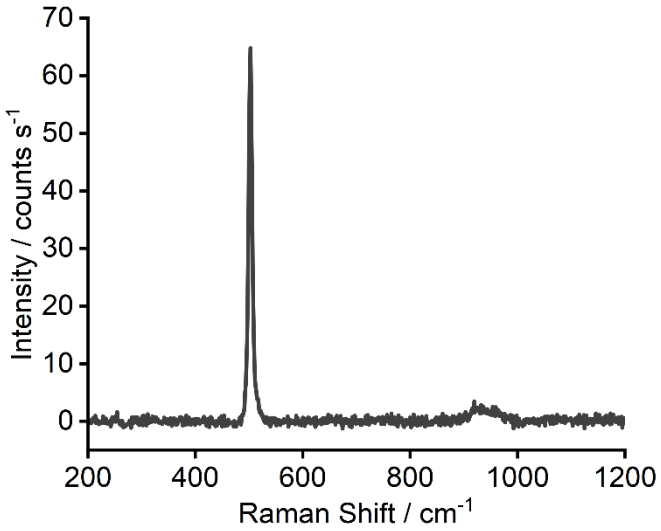

Figure A1.19: Raman spectrum of the silicon wafer after aligning the spectrograph to the optical system (after applying intensity response correction and subtraction of dark signal). Wavelength between 667-725 nm. Slit width = 80 µm, number of spectra = 10, length of each spectrum = 20 s.

Whilst the spectrograph is aligned, the Raman spectrum showed a very low intensity, particularly as the slit size is reduced the intensity of the Si Raman signal at 520 cm^{-1} appears to drop (shown in *Figures A1.20 and A1.21*). Therefore, a slit of 150 µm was used throughout the collection of Raman data.

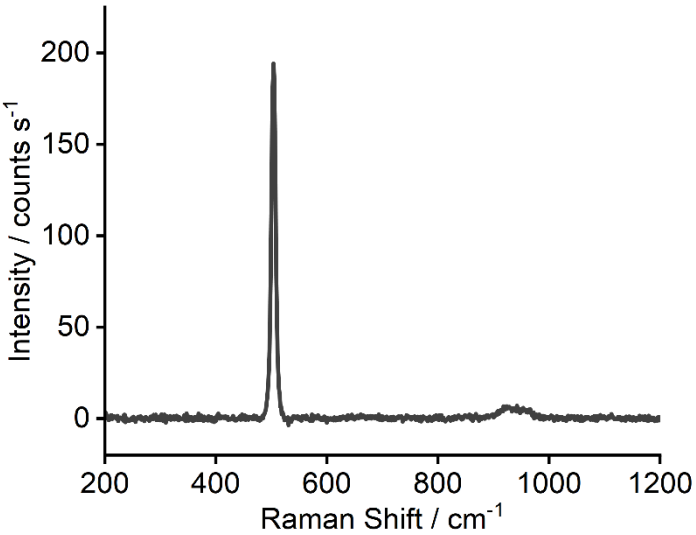

Figure A1.20: Raman spectrum of the silicon wafer after aligning the spectrograph (after applying intensity response correction and subtraction of dark signal). Wavelength between 667-725 nm. Slit width = 150 µm, number of spectra = 10, length of each spectrum = 20 s.

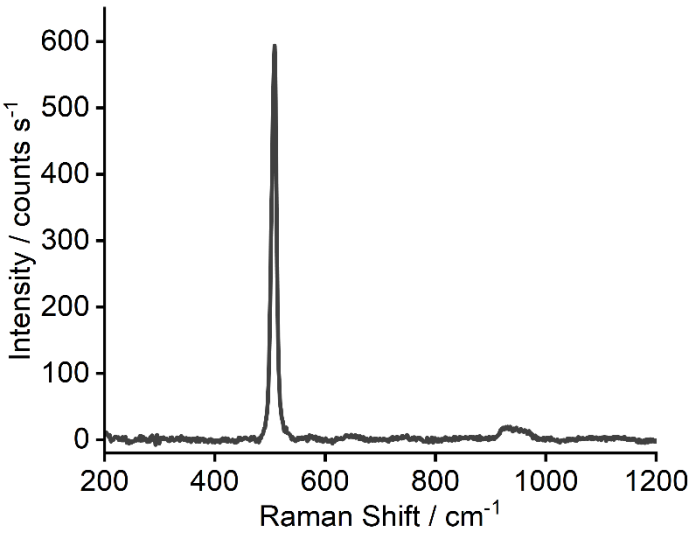

Figure A1.21: Raman spectrum of the silicon wafer after aligning the spectrograph (after applying intensity response correction and subtraction of dark signal). Wavelength between 667-725 nm. Slit width = 800 µm, number of spectra = 10, length of each spectrum = 20 s.

Two adjustments were then made, firstly the focusing lenses in the sample chamber that focus the laser beam to a tight spot on the sample. The lenses were moved to be at the correct focal point of 10 cm and 13 cm calculated before and adjusted to try and make the laser spot at the sample as small as possible. Secondly, the lens in the spectrograph antechamber that focused Raman scattered light on the spectrograph slit was also moved towards the slit by being turned clockwise (to move the focal point towards the slit). This improved the intensity of the spectrum as shown in *Figure A1.22*. This also caused a significant increase in the background, which suggests the sample may be better illuminated by the laser (producing more signal and noise) but does not improve signal and noise overall. There is an increase in the peak at 860 cm^{-1}, which is likely to be a native oxide layer on the surface of the silicon, again, therefore, confirming that the Raman setup is better aligned.[1]

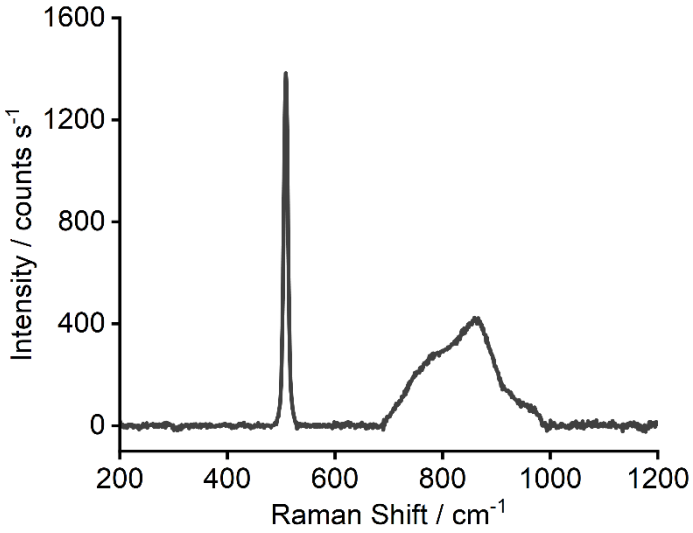

Figure A1.22: Raman spectrum of the silicon wafer after tightening and moving the lenses (after applying intensity response correction and subtraction of dark signal). Wavelength between 667-725 nm. Slit width = 150 µm, number of spectra = 10, length of each spectrum = 20 s.

Another component considered for optimisation was the iris used to carry out confocal spectroscopy, where only light from the focal point on the sample is passed through the spectrograph slit. It was found that when the iris was almost closed, no peak at 520 cm^{-1} was able to be found. The only time the peak was seen was when the iris was completely open. As a result, it was thought that the iris was out of alignment. The iris was moved so that it was lower to gain more exposure until a large signal had been detected. This was achieved once the iris was closed down whilst acquiring spectra and continuing to carefully move the iris position.

It was thought that the lens in front of the spectrograph slit could be off focus. Spectra were continuously acquired while adjusting the lens, focusing light onto the slit at different slit sizes. Initially, the issue was investigated with a slit size of 100 µm before it was later measured using other slit sizes.

As shown in *Figure A1.23*, there is an increase in the intensity of the peak, therefore reflecting that the movement of the optical components as described above was needed and that the Raman set-up is more aligned now. There is an increase in the peak around 860 cm^{-1}, which is likely to be the native oxide layer on the surface of silicon, again therefore confirming that the Raman set-up is better aligned.[1]

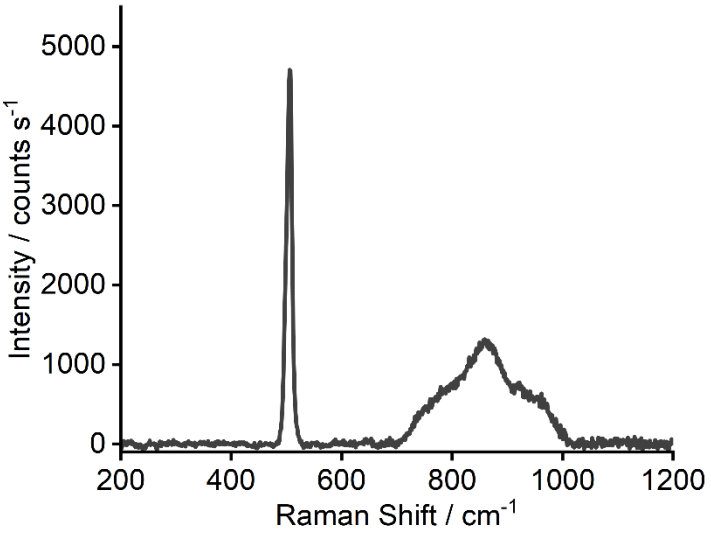

Figure A1.23: Raman spectrum of the silicon wafer after changing parameters (after applying intensity response correction and subtraction of dark signal). Wavelength between 667-725 nm. Slit width = 150 µm, number of spectra = 10, length of each spectrum = 20 s.

1.2.7 Raman Spectrum of Double-Sided Sticky Tape

Due to all samples being undertaken on double-sided sticky tape, to make sure there was no confusion with the peak assignment a spectrum was undertaken of only the double-sided sticky tape (*Figure A1.24*). Between 200 – 1000 cm^{-1} no peaks corresponded to the double-sided sticky tape.

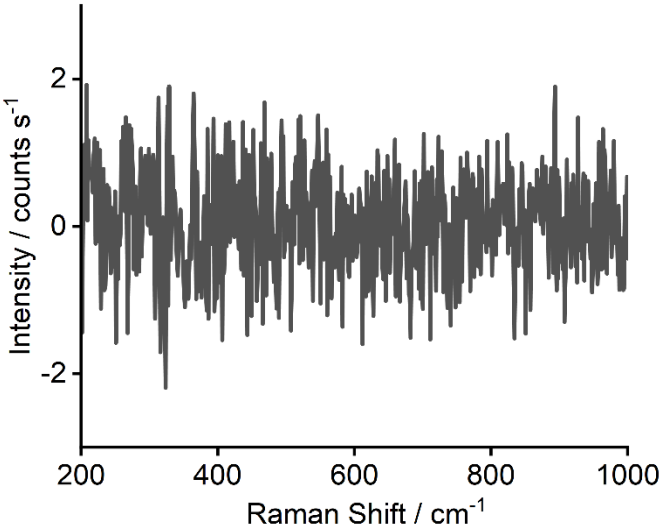

Figure A1.24: Raman spectrum of the double-sided sticky tape (after applying intensity response correction and subtraction of dark signal). Wavelength between 667-725 nm. Slit width = 150 µm, number of spectra = 10, length of each spectrum = 20 s.

1.3 Temperature Programmed Reduction (TPR) Calibration

The TPRs were calibrated using CuO, and silicon carbide was used to make the catalyst bed the same length. Silicon carbide was investigated to see if any peaks were found that could affect the CuO calibration. As shown in *Figure A1.25*, there are no peaks in the silicon carbide temperature programmed reduction.

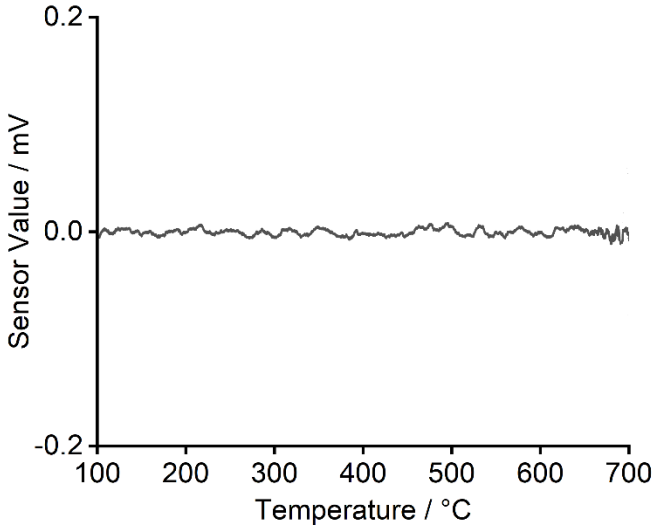

Figure A1.25: Temperature Programmed Reduction of Silicon Carbide

A mixture of CuO and silicon carbide was used to make the bed up to 100 mg of catalyst in total since very small masses of copper oxide were required to obtain peaks with areas similar to the catalysts. Since CuO consumes one mole of hydrogen during reduction as shown in *Equation A1.2*. The resulting calibration graph is shown in *Figure A1.26* and gives an equation relating peak area to molar hydrogen consumption.

$$\mathrm{CuO} + \mathrm{H_2} \longrightarrow \mathrm{Cu} + \mathrm{H_2O}$$

Equation A1.2: Reduction process of copper oxide.

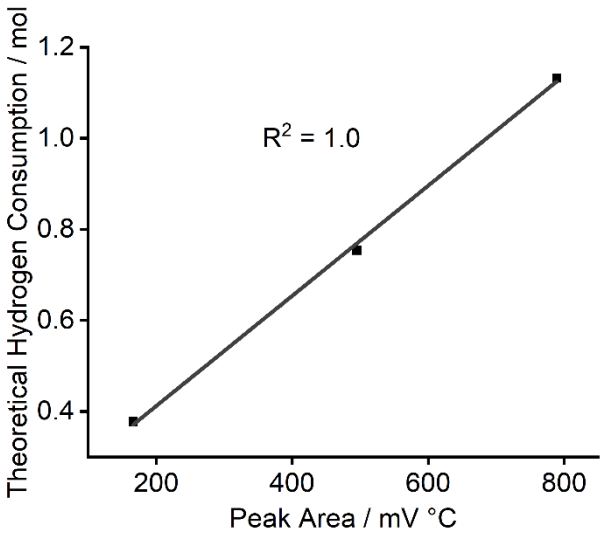

Figure A1.26: Calibration graph for the TCD in TPR setup obtained via reduction of varying masses of CuO diluted with SiC.

1.4 Time On Stream

An example of a time-on-stream graph is shown in *Figure A1.27*. This graph is Ag/α-Al_2O_3 under ethylene epoxidation conditions. Very few changes differ from the other Ag/α-Al_2O_3 and Ag/γ-Al_2O_3 based catalysts, therefore only an example has been shown.

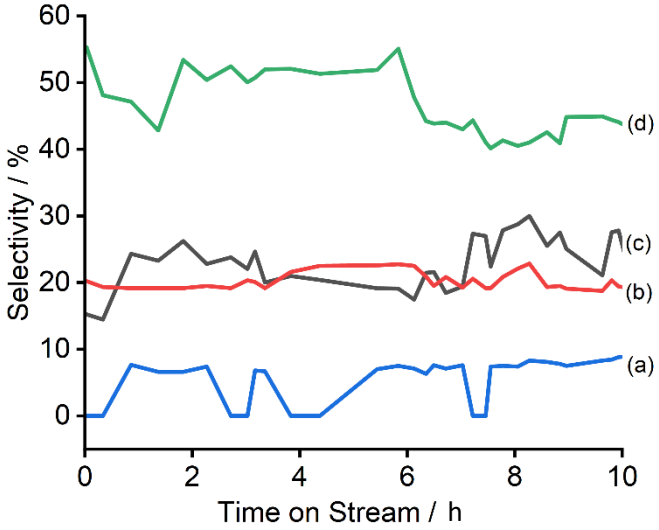

Figure A1.27: An example of a time on stream graph. This shows Ag/α-Al_2O_3 under ethylene epoxidation conditions over 10 h. Here (a) shows the selectivity of AA, (b) shows the selectivity of CO_2, (c) shows the selectivity of H_2O and (d) shows the selectivity of EO.

1.5 Ethylene Epoxidation Over α-Al_2O_3 With Varied Metal Loading Levels

Other α-Al_2O_3 based catalysts were investigated with different metal loading levels where the most selective catalysts towards ethylene oxide were used for characterisation and analysis in this thesis.

Table A1.2: Reaction data for the other catalysts synthesised for the investigation of ethylene epoxidation activity.

Catalysts wt %.			Selectivities / %			
Ag	Cs	Re	EO	AA	CO_2	H_2O
15	-	-	13.43	15.85	16.26	54.46
15	0.050	-	24.92	13.00	15.83	46.26
15	-	0.050	18.08	25.67	13.07	43.18
15	0.050	0.050	24.41	11.11	24.03	40.44
12	-	-	24.99	12.38	18.55	44.08
12	0.035	-	24.64	11.90	13.41	50.05
12	-	0.040	22.24	12.85	23.11	41.79
12	0.035	0.040	26.29	13.55	16.54	43.62
15	0.1	0.1	22.38	12.82	22.66	42.14

1.6 References

1 W.-J. Lee and Y.-H. Chang, *Coat.*, 2018, **8**, 431.

Appendix 2

2.1 DRIFTS Calibration

The calibrations for all the gases used are shown in *Figures A2.1, A2.2, A2.3* and *A2.4*.

Figure A2.1 shows the calibration of H_2 the trend of the line equation is y = 0.9993x – 0.5226. Where R^2 = 1.0.

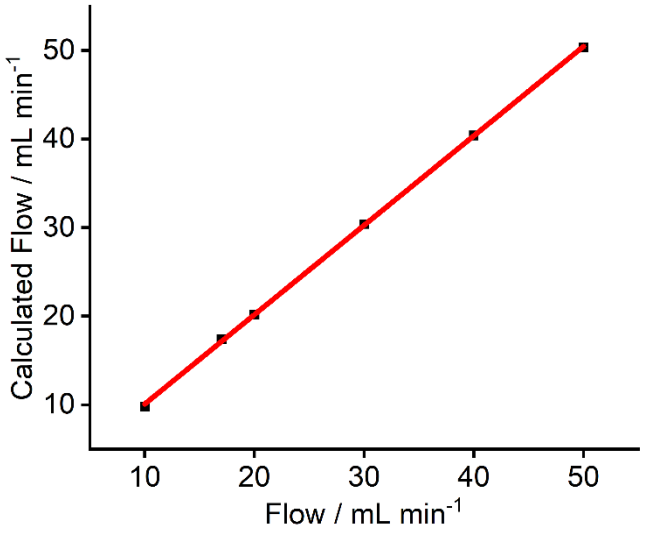

Figure A2.1: A graph showing the calibration of H_2.

Figure A2.2, shows the calibration of C_2H_4, here the trend of the line equation is y = 1.0094x – 0.0074. Where R^2 = 1.0.

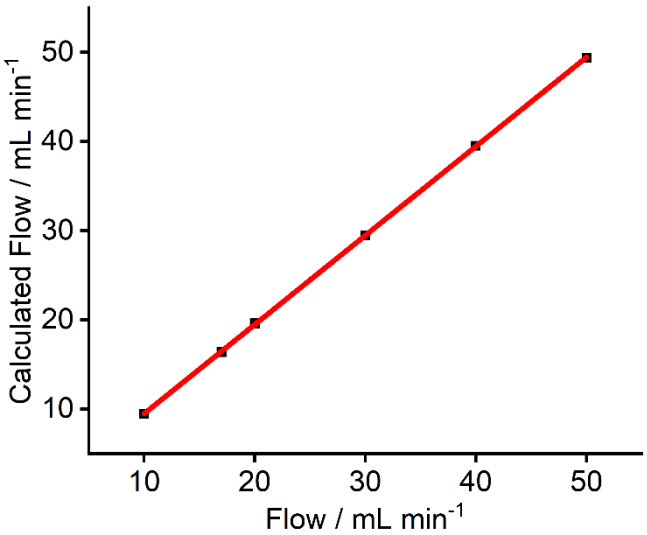

Figure A2.2: A graph showing the calibration of C_2H_4.

Figure A2.3 shows the calibration of O_2, here the trend of the line equation is y = 0.9894x + 0.1295. Where R^2 = 1.0.

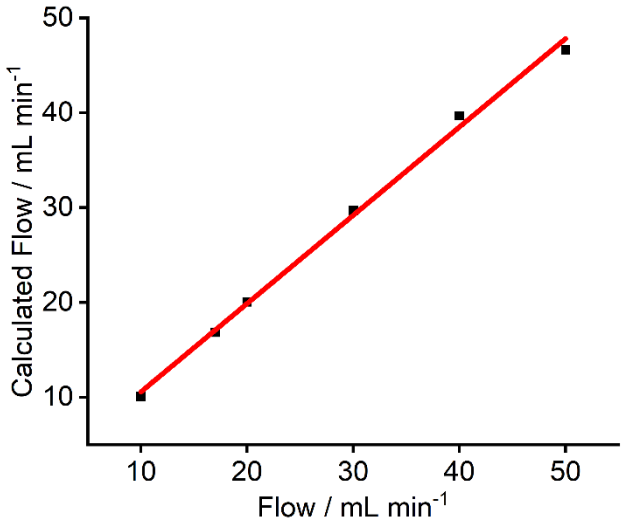

Figure A2.3: A graph showing the calibration of O_2.

Figure A2.4 shows the calibration of Ar, here the equation of the line is y = 0.9883x + 0.1774. Where R^2 = 1.0.

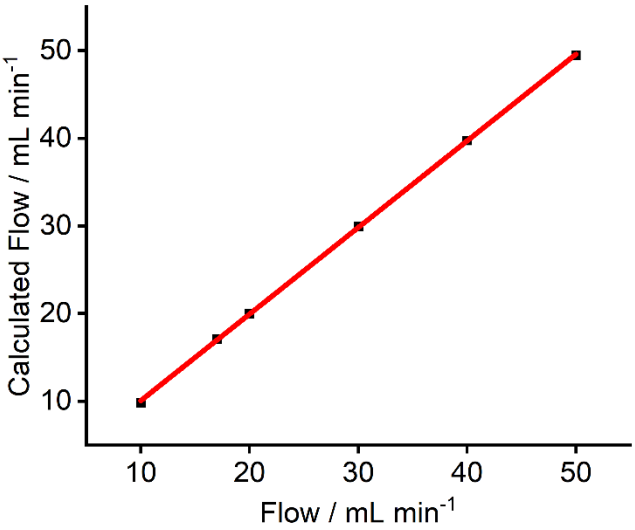

Figure A2.4: A graph showing the calibration of Ar.

Appendix 3

3.1 *Ex situ* X-ray Photoelectron Spectroscopy (XPS)

Ex situ XPS was undertaken of Al 2p for Ag/α-Al_2O_3, Re-Ag/α-Al_2O_3, Ag/γ-Al_2O_3 and Re-Ag/γ-Al_2O_3, which is shown in *Figure A3.1*. These spectra were used as references for the *ex situ* XPS results, where the reference used for Al was 74.1 eV, which corresponds to Al oxide.[1]

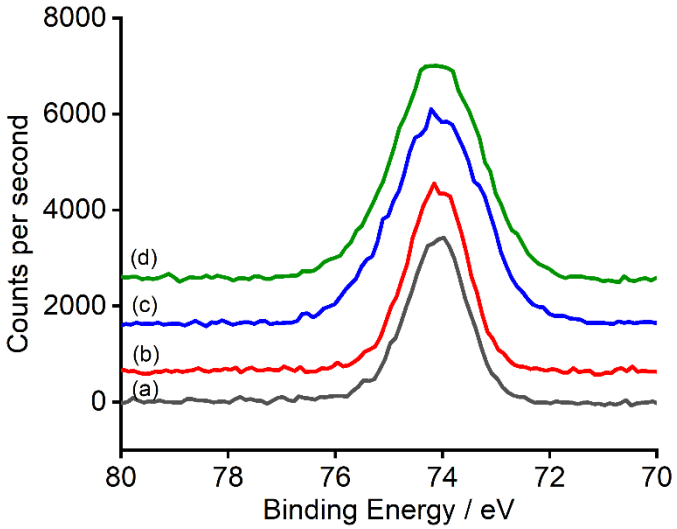

Figure A3.1: XPS spectra of all Al2p data (after applying binding energy correction verified by the shift of the Al 2p peak and after subtraction of a Shirley background). Where (a) is Ag/α-Al_2O_3, (b) is Re-Ag/α-Al_2O_3, (c) is Ag/γ-Al_2O_3 and (d) is Re-Ag/γ-Al_2O_3. Spectra have been offset for clarity.

Ex situ XPS was also undertaken of C 1s, shown in *Figure A3.2*. Carbon in XPS is often the result of adventitious carbon.[2] The intensity suggests the peaks are small with a C:Al atomic ratio of 1:2 for the α-Al_2O_3 based catalysts and 1:3 for the γ-Al_2O_3 based catalysts.

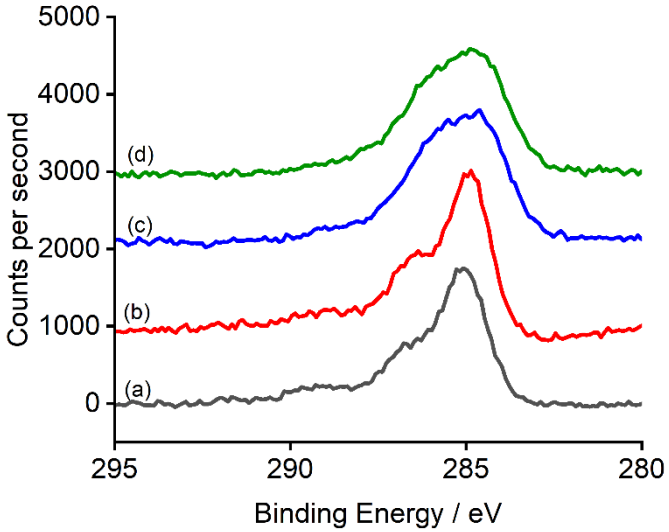

Figure A3.2: XPS spectra of all C1s data (after applying binding energy correction verified by the shift of the Al 2p peak and after subtraction of a Shirley background). Where (a) is Ag/α-Al_2O_3, (b) is Re-Ag/α-Al_2O_3, (c) is Ag/γ-Al_2O_3 and (d) is Re-Ag/γ-Al_2O_3. Spectra have been offset for clarity.

Table A3.1 shows the integral areas taken from the individual XPS spectra of the different elements from Ag/α-Al_2O_3, Ag/γ-Al_2O_3 and Re-Ag/α-Al_2O_3.

Table A3.1: A table showing the integral areas taken from the individual XPS graphs of the different elements. The table also shows the relevant cross-sections of the different elements from data by Yeh and Lindau.[3]

		Area of XPS / eV counts s^{-1}				
		C1s	**O1s**	**Ag3d**	**Al2p**	**Re4f**
Catalyst	**Ag/α-Al_2O_3**	3.54 x 10^5	8.97 x 10^6	1.51 x 10^5	7.16 x 10^5	-
	Ag/γ-Al_2O_3	4.38 x 10^5	1.75 x 10^7	4.32 x 10^4	1.28 x 10^6	-
	Re-Ag/α-Al_2O_3	3.11 x 10^5	1.12 x 10^7	1.60 x 10^5	8.04 x 10^5	1.39 x 10^4
	Cross Sections / Mb	0.013	0.04	0.2474	0.0072	0.1631

Using *Table A3.1* and the Strohmeier equation (*Equations A3.1* and A3.2), the overlayer thickness of the different samples was determined (assuming an even layer despite knowing silver is present as particles is still insightful to get a sense of the surface coverage).

$$d = \lambda_{ox} \sin\theta \ln[(\frac{N_m \lambda_m I_{ox}}{N_{ox} \lambda_{ox} I_m}) + 1]$$

Equation A3.1: Strohmeier Equation, where I_m is the relative percentage of metal, I_{ox} is the relative percentage area of oxide, λ_m is the IMFP for metal and λ_{ox} is the IMFP for metal oxide, d is the path length, θ is the take-off angle and N_m is the volume density for the metal and N_{ox} is the volume density for the metal oxide.[4]

The volume densities were calculated from *Equation A3.2*.

$$N = \frac{\rho}{M_R}$$

Equation A3.2: Volume Density, where M_R is molar (or atomic) mass and ρ is the density.[4]

Table A3.2: Calculation for the Strohmeier equation, where Ox is silver, and M is the Al_2O_3 for the α-Al_2O_3 and γ-Al_2O_3 based catalysts.

		Ag/α-Al_2O_3	**Ag/γ-Al_2O_3**	**Re-Ag/α-Al_2O_3**
Calculations	**I_m / %**	715937.5	1281556.9	803804.2
	I_{ox} / %	151110.8	42322.2	160147.1
	λ_m / nm	2.679	2.679	2.679
	λ_{ox} / nm	1.906	1.906	1.906
	θ / deg	90	90	90
	θ / radians	1.571	1.571	1.571
	N_m / g cm^{-1}	0.039	0.039	0.039
	N_{ox} / g cm^{-1}	0.097	0.097	0.097
	d / nm	0.215	0.035	0.203

3.2 *In situ* X-ray Photoelectron Spectroscopy (XPS)

One example of the Al 2p reference for the *in situ* XPS is shown in *Figure A3.3*. Here referencing was undertaken to match the *ex situ* XPS shown above.

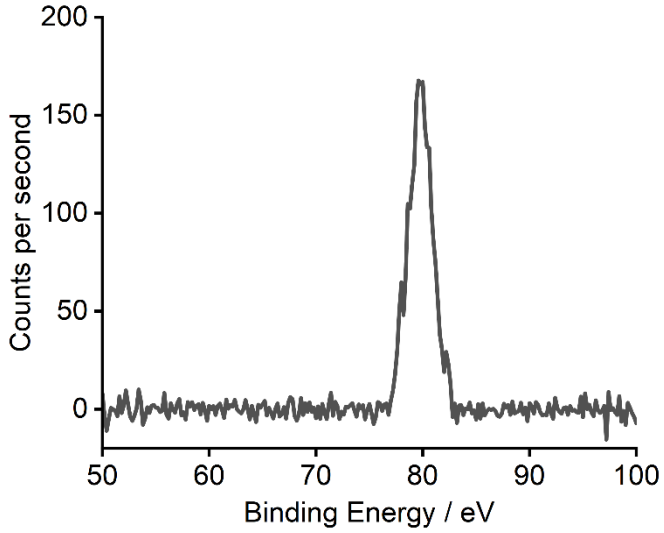

Figure A3.3: XPS spectra of an example of the Al2p data (after applying binding energy correction verified by the shift of the Al 2p peak and after subtraction of a Shirley background).

3.3 References

1 Aluminum, http://www.xpsfitting.com/2008/09/aluminum.html, (accessed 4 April 2024).
2 Carbon | XPS Periodic Table | Thermo Fisher Scientific - UK, https://www.thermofisher.com/uk/en/home/materials-science/learning-center/periodic-table/non-metal/carbon.html, (accessed 17 June 2022).
3 J. J. Yeh and I. Lindau, *At. Data Nucl. Data Tables.*, 1985, **32**, 1–155.
4 Overlayer thickness determination by XPS - HarwellXPS Guru, https://www.harwellxps.guru/knowledge-base/overlayer-thickness-determination-by-xps/, (accessed 11 May 2022).

Appendix 4

4.1 *Ex situ* X-ray Photoelectron Spectroscopy (XPS)

Ex situ XPS was undertaken of Al 2p for Cs-Ag/α-Al_2O_3, Cs-Re-Ag/α-Al_2O_3, Cs-Ag/γ-Al_2O_3 and Cs-Re-Ag/γ-Al_2O_3, which is shown in *Figure A4.1*. These spectra were used as references for the *ex situ* XPS results, where the reference used for Al was 74.1 eV, which corresponds to Al oxide.[1]

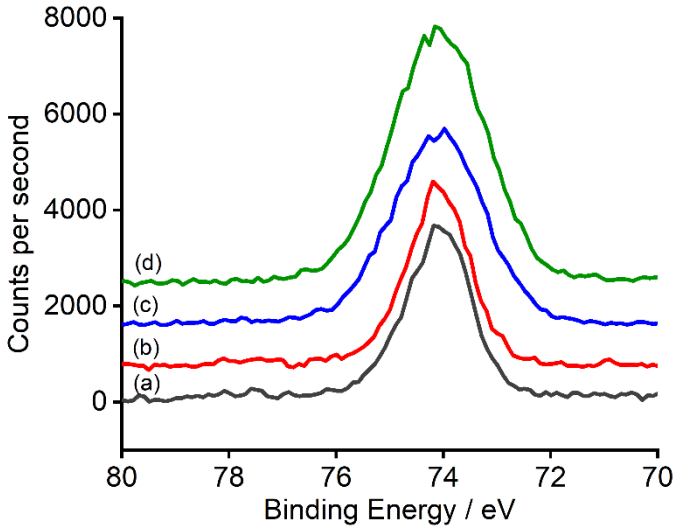

Figure A4.1: XPS spectra of all Al2p data (after applying binding energy correction verified by the shift of the Al 2p peak and after subtraction of a Shirley background). Where (a) is Cs-Ag/α-Al_2O_3, (b) is Cs-Re-Ag/α-Al_2O_3, (c) is Cs-Ag/γ-Al_2O_3 and (d) is Cs-Re-Ag/γ-Al_2O_3. Spectra have been offset for clarity.

Ex situ XPS was also undertaken of C 1s, shown in *Figure A4.2*. Carbon in XPS is often the result of adventitious carbon.[2] The intensity suggests the peaks are small with a C:Al atomic ratio of 1:2 for the α-Al_2O_3 based catalysts and 1:3 for the γ-Al_2O_3 based catalysts.

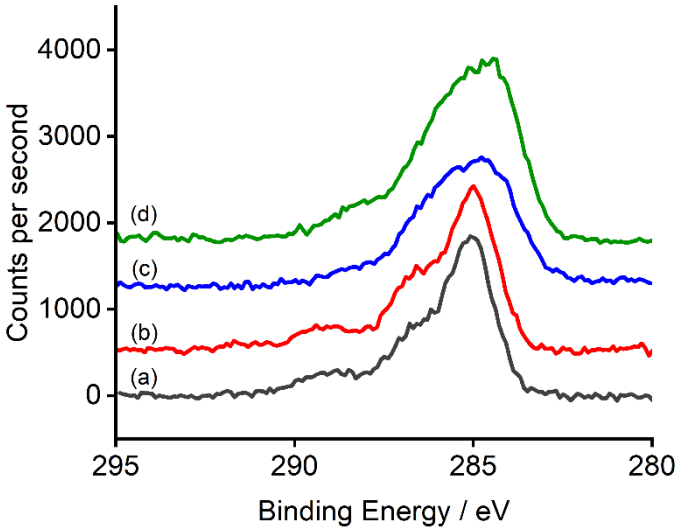

Figure A4.2: XPS spectra of all C1s data (after applying binding energy correction verified by the shift of the Al 2p peak and after subtraction of a Shirley background). Where (a) is Cs-Ag/α-Al_2O_3, (b) is Cs-Re-Ag/α-Al_2O_3, (c) is Cs-Ag/γ-Al_2O_3 and (d) is Cs-Re-Ag/γ-Al_2O_3. Spectra have been offset for clarity.

The Strohmeier equation (as described and shown in **Appendix 3**) was also used for these catalysts. *Table A4.1* shows the integral areas taken from the individual XPS spectra of the different elements from Ag/α-Al_2O_3 and Cs-Re-Ag/α-Al_2O_3. Whilst the calculations for the Strohmeier equation are shown in *Table A4.2*.

Table A4.1: A table showing the different areas taken from the individual XPS graphs of the different elements. The table also shows the relevant cross-sections of the different elements as extrapolated from data by Yeh and Lindau.[3]

		Area of XPS / eV counts s^{-1}					
		C1s	**O1s**	**Ag3d**	**Al2p**	**Cs3d**	**Re4f**
Catalyst	**Cs-Ag/α-Al_2O_3**	3.64 x 10^5	9.51 x 10^6	1.39 x 10^5	6.98 x 10^5	5.55 x 10^3	-
	Cs-Re-Ag/α-Al_2O_3	3.52 x 10^5	9.94 x 10^6	1.65 x 10^5	6.09 x 10^5	7.18 x 10^3	2.82 x 10^3
	Cross Sections / Mb	0.013	0.04	0.2474	0.0072	0.5539	0.1631

Table A4.2: Calculation for the Strohmeier equation, where Ox is silver, and M is the Al_2O_3 for the α-Al_2O_3 based catalysts.

		Cs-Ag/α-Al_2O_3	Cs-Re-Ag/α-Al_2O_3
Calculations	I_m / %	698422.2	608656.3
	I_{ox} / %	139133.4	164502
	λ_m / nm	2.679	2.679
	λ_{ox} / nm	1.906	1.906
	θ / deg	90	90
	θ / radians	1.571	1.571
	N_m / g cm^{-1}	0.039	0.039
	N_{ox} / g cm^{-1}	0.097	0.0972
	d / nm	0.203	0.271

4.2 Solid State Nuclear Magnetic Resonance Spectroscopy (ss NMR)

The local chemical environment of caesium was investigated by cross-polarisation (CP) ^{133}Cs NMR spectroscopy. Caesium-133 has 100% natural abundance, I = 7/2 and a small quadrupole moment. Caesium spectral referencing is relative to 1 M $CsNO_3$, shown in *Figure A4.3*.

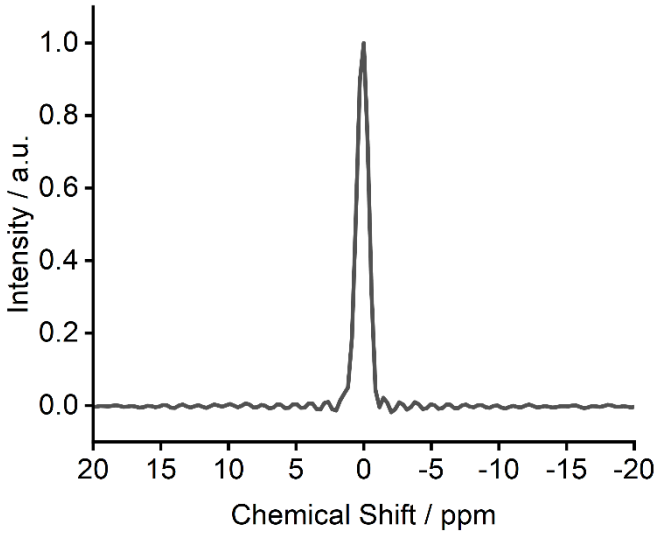

Figure A4.3: Solid State CP ^{133}Cs NMR spectrum of 1 M $CsNO_3$ reference.

4.3 *In situ* X-ray Photoelectron Spectroscopy (XPS)

One example of the Al 2p reference for the *in situ* XPS is shown in *Figure A4.4*. Here referencing was undertaken to match the *ex situ* XPS shown above.

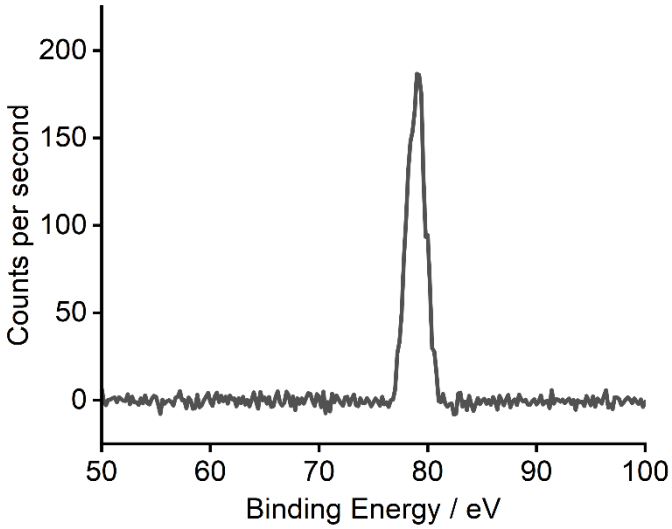

Figure A4.4: XPS spectra of an example of the Al2p data (after applying binding energy correction verified by the shift of the Al 2p peak and after subtraction of a Shirley background).

4.4 References

1 Aluminum, http://www.xpsfitting.com/2008/09/aluminum.html, (accessed 4 April 2024).
2 Carbon | XPS Periodic Table | Thermo Fisher Scientific - UK, https://www.thermofisher.com/uk/en/home/materials-science/learning-center/periodic-table/non-metal/carbon.html, (accessed 17 June 2022).
3 J. J. Yeh and I. Lindau, *At. Data Nucl. Data Tables.*, 1985, **32**, 1–155.

Appendix 5

5.1 *In situ* DRIFTS

In situ DRIFTS under ethylene epoxidation conditions of Cu/α-Al_2O_3, Au/α-Al_2O_3, Cu-Au/α-Al_2O_3 and Cu-Ag/α-Al_2O_3 using the new DRIFTS cell are shown in *Figure A5.1*.

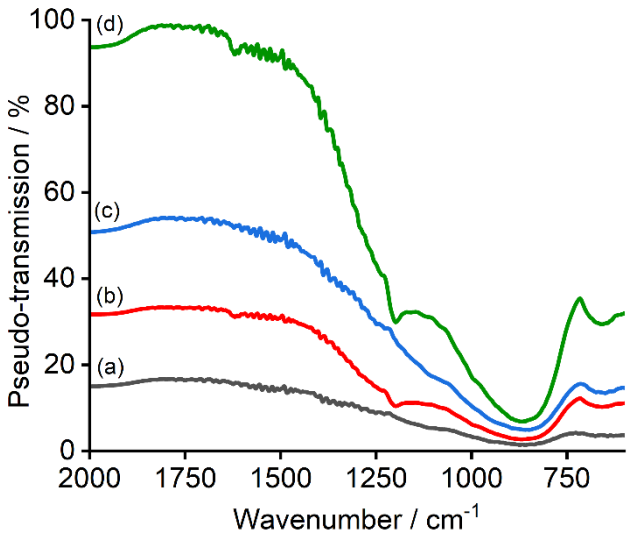

Figure A5.1: In situ DRIFTS of ethylene epoxidation reaction on (a) Au/α-Al_2O_3, (b) Cu/α-Al_2O_3, (c) Cu-Au/α-Al_2O_3 and (d) Cu-Ag/α-Al_2O_3 after 2 hr of exposure to ethylene at 225 °C backgrounded against KBr. The O_2:C_2H_4 ratio in all cases is 2:1. Spectra have been offset for clarity.